Functional grading of steel structures via wire arc additive manufacturing
Microstructural Evolution and Mechanical Performance

Galán Argumedo, J.L.

DOI
10.4233/uuid:04bf27e6-41e8-47b5-9ab7-e608929ba43a

Publication date
2026

Document Version
Final published version

Citation (APA)
Galán Argumedo, J. L. (2026). *Functional grading of steel structures via wire arc additive manufacturing: Microstructural Evolution and Mechanical Performance*. [Dissertation (TU Delft), Delft University of Technology]. https://doi.org/10.4233/uuid:04bf27e6-41e8-47b5-9ab7-e608929ba43a

FUNCTIONAL GRADING OF STEEL STRUCTURES VIA WIRE ARC ADDITIVE MANUFACTURING

Microstructural evolution and mechanical performance

J.L. GALÁN ARGUMEDO

FUNCTIONAL GRADING OF STEEL STRUCTURES VIA WIRE ARC ADDITIVE MANUFACTURING

Microstructural Evolution and Mechanical Performance

FUNCTIONAL GRADING OF STEEL STRUCTURES VIA WIRE ARC ADDITIVE MANUFACTURING

Microstructural Evolution and Mechanical Performance

DISSERTATION

for the purpose of obtaining the degree of doctor
at Delft University of Technology
by the authority of the Rector Magnificus, Prof.dr.ir. H. Bijl,
Chair of the Board for Doctorates

to be defended publicly on
Thursday, 22nd of January, 2026 at 12.30h

by

José Luis GALÁN ARGUMEDO

This dissertation has been approved by the promotors.

Composition of the Doctoral Committee:

Rector Magnificus,	chairperson
Prof.dr. V.A. Popovich,	Delft University of Technology, *promotor*
Dr.ir. M.J.M. Hermans,	Delft University of Technology, *promotor*

Independent Members

Prof.dr. M. Veljkovic	Delft University of Technology
Prof.dr.ir. R.C. Alderliesten	Delft University of Technology
Prof.dr.ir N. Moelans	Katholieke Universiteit, Leuven. Belgium.
Prof.dr.techn.dipl.-ing. P. Mayr	Technische Univeristät München. Germany.
Dr. P. Dey	Delft University of Technology, *reserve member*

This project has been financed by the program of research and innovation Horizon2020 of the European Union under the Grant Agreement No. 862017.

Keywords: Direct energy deposition; wire arc additive manufacturing; functional grading; mechanical properties; fatigue crack propagation; fracture

Cover image: Through the thesis, consistent colour coding is used to present results. Blue refers to the HSLA steel material volume, amber to the ASS steel material volume, and green to the bi-metallic interface between the former two. The cover artistically represents this bi-material cross section, following the mentioned colour convention. The different shades of green represent the heterogeneity found in the interface layer.

Printed by: Ridderprint www.ridderprint.nl

ISBN 978-94-6537-148-1

An electronic copy of this dissertation is available at:
https://repository.tudelft.nl

"The first principle is that you must not fool yourself, and you are the easiest person to fool"

R. Feynman, in his Caltech's 1974 commencement speech entitled *Cargo Cult Science*

[Page intentionally left blank]

TABLE OF CONTENTS

SUMMARY

The increasing demand for efficient manufacturing of specialized large-scale metallic components in critical sectors such as maritime, energy, and heavy industry underscores the limitations of traditional fabrication methods, as they are often constrained by cost, low production volumes, and complex logistics. Additive manufacturing (AM) presents a promising alternative, offering geometric flexibility, material efficiency, and supply chain simplification. However, many AM technologies remain unsuitable for large-scale applications due to low deposition rates, high material costs, and build size limitations. Wire Arc Additive Manufacturing (WAAM), by contrast, leverages arc welding technologies to produce near-net-shape, fully dense components at high deposition rates, without inherent size restrictions. This makes WAAM a leading candidate for large-scale metal part production.

A key innovation enabled by WAAM is functional grading: the ability to spatially tailor microstructural or compositional features across a part. This work focuses specifically on compositional grading between High-Strength Low-Alloy (HSLA) steel and austenitic stainless (AS) steel, a material pairing with industrial relevance due to their complementary properties. Despite growing interest in such bi-material systems, significant challenges persist in controlling the resulting microstructure, especially at the chemically graded interface, where microstructural gradients can lead to unpredictable mechanical performance. This research addresses these challenges through a systematic investigation of interface microstructure and mechanical response, guided by three primary objectives: (1) to understand microstructural evolution at the interface, (2) to assess deformation and fracture behaviour, and (3) to evaluate fatigue performance of WAAM-fabricated AS steel–HSLA steel bi-metal components.

To achieve these aims, a comprehensive experimental programme was implemented. Representative mono-material and bi-material blocks were fabricated using Cold Metal Transfer (CMT)-assisted WAAM, with consistent deposition parameters to ensure comparability. The bi-material blocks featured AS steel deposited onto a previously-deposited HSLA steel material volume, creating a chemically diluted interface. Microstructural characterization was conducted across multiple length scales using optical

microscopy, SEM, EBSD, EPMA, TEM, and TKD. These techniques enabled detailed investigation of solidification features, phase transformations, and chemical segregation. The insights drawn were further supported by CALIPHAD simulations of microstructural development. Mechanical testing included quasi-static tensile tests supported by DIC, fracture toughness evaluation using custom J-integral formulations via FEA modelling, and fatigue crack propagation studies under constant-load and constant-ΔK conditions.

The results reveal that the interface formed during WAAM is highly heterogeneous, shaped by partial mixing and thermal gradients. Multiscale characterization identified a complex structure involving intrusions of unmixed material, phase segregation, and metastable austenite capable of transforming into ε- and α'-martensite. Under quasi-static loading, the interface layer exhibited enhanced work hardening and delayed failure due to the activation of a Transformation Induced Plasticity (TRIP) mechanism. While this effect contributed positively to tensile performance, fracture toughness testing revealed variability due to brittle martensitic regions that act as crack initiators. Fatigue testing further confirmed the dual nature of the interface: TRIP initially slowed crack propagation, but once transformation was exhausted, propagation rates increased sharply in regions containing pre-existing allotropic martensite. These results highlight the importance of local microstructural control in determining the mechanical reliability of bi-material WAAM structures.

This thesis makes several key contributions to understand the process-microstructure-property relationship of additively-manufactured, functionally-graded components. It demonstrates that controlled heterogeneity can be beneficial in functionally graded steels, provided that metastable phases are stabilized and effectively leveraged. It emphasizes the critical role of local thermal conditions during deposition and the need to design process parameters that account for heat flow and dilution effects. Beyond the specific AS steel-HSLA steel system, these findings support broader efforts to establish qualification pathways for functionally graded materials in additive manufacturing. They underscore the importance of localized property assessment, microstructural validation, and real-time process monitoring as foundational elements for reliable design and certification. By offering a comprehensive case study of dissimilar metal WAAM, this work contributes both fundamental insights and practical guidance for the development and qualification of advanced graded structures in industrial settings.

LIST OF ABBREVIATIONS AND SYMBOLS

UPPER-CASE ABBREVIATIONS

AM	Additive Manufacturing
AS	Austenitic Stainless
BD	Build Direction
BM	Bi-material
BMAS	Bi-material additively manufactured structure
CMOD	Crack-mouth opening displacement [mm]
CMT	Cold Metal Transfer
DIC	Digital Image Correlation
DCPD	Direct Current Potential Drop
EBSD	Electron Back-Scatter Diffraction
EPMA	Electron Probe Microanalysis
FCGR	Fatigue Crack Growth Rate
FGM	Functionally-Graded Materials
FFT	Fast Fourier Transform
HSLA	High Strength Low Alloy
HV	Hardness Vickers
IQ	Image Quality
IPF	Inverse Pole Figure
KAM	Kernel Average Misorientation
K-S	Kurdjumov-Sachs
LENS	Laser-Engineered Net Shaping
LPBF	Laser Powder-Based Fusion
MDF	Misorientation distribution function
MM	Mono-material
N-W	Nishiyama-Wasserman
OA	Overlapping Area
ODF	Orientation Distribution Function
OR	Orientation Relationship
PAG	Parent Austenite Grain
RA	Remelted Area
SEM	Scanning Electron Microscopy
SDAS	Secondary Dendrite Arm Spacing
TEM	Transmission Electron Microscopy
TKD	Transmission Kikuchi Diffraction
TRIP	Transformation-Induced Plasticity
TWIP	Twinning-Induced Plasticity
WAAM	Wire Arc Additive Manufacturing

LOWER-CASE ABBREVIATIONS

bcc	body-centred cubic
bct	body-centred tetragonal
fcc	face-centred cubic
hcp	hexagonal close-packed

UPPER-CASE SYMBOLS

B Sample thickness, before grooving [mm]

B_n Sample thickness, after grooving [mm]

B_e Effective sample thickness [mm]

$C(a/W)_{FEM,BM}$ Relative crack depth as a function of compliance, as derived from linear-elastic FEM results [mm/mm]

$C(a/W)^E_{Analyt,MM}$ Relative crack depth as a function of CMOD compliance, as derived from analytical relationships [mm/mm]

C_{LL} Load-line compliance [mm/N]

C_m Crack-mouth opening displacement compliance [mm/N]

$C_{m,analyt}$ Analytical description of crack-mouth opening displacement compliance [mm/N]

$CMOD_{Analyt}$ Analytical description of crack-mouth opening displacement [mm]

$CMOD_{BM}$ Numerical description of crack-mouth opening displacement for a bi-material sample [mm]

$CMOD_{FEM}$ Numerical description of crack-mouth opening displacement, as obtained by FEM [mm]

$CMOD_{MM}$ Numerical description of crack-mouth opening displacement for a mono-material sample [mm]

E Elastic modulus [MPa]

G_I Elastic energy per unit area of crack extension [kJ/m^2]

G^E_{MM} Elastic energy per unit area of crack extension for a mono-material sample of elastic modulus E [kJ/m^2]

$J_{I,el}$, J_{el} Elastic component of J-integral [kJ/m^2]

J_{Ic} Classified, size-insensitive plane strain fracture toughness

$J_{el,BM}$ Numerical description of elastic component of J-integral for a bi-material sample [kJ/m^2]

J_{pl} Plastic component of J-integral [kJ/m^2]

J_Q Unclassified (provisional) plane strain fracture toughness

K_I, K Stress intensity factor [MPa·m$^{0.5}$]

P Load [N]

S Span between supports [mm]

W Sample width [mm]

$Z(BM)$ Position of bi-material dissimilar fusion line, as measured from the same reference plane as a [mm]

LOWER CASE SYMBOLS

a	Crack length [mm]
a_p	Final crack length before final tear-out [mm]
a_0	Initial crack length after pre-fatigue [mm]
b_0	Remaining tendon ahead of a_0 [mm]
e	Engineering strain [-]
e_m	Relative error function between $CMOD_{Analyt}$ and $CMOD_{FEM}$ [-]
$e_{a/W}$	Inverse function of e_m [-]
$f\left(\frac{a}{W}\right)$	Geometry-specific function relating P and K [-]
i	Counter variable indicating a given load-unload cycle
s	Engineering stress [MPa]
u	Function-specific substitution variable [-]
v_{LL}	Load-line displacement [mm]
v_m	Crack opening displacement at measure point [mm]

GREEK SYMBOLS

α	bcc phase
α'	bct phase
Δa	Crack extension [mm]
Δa_Q	Crack extension value at J_Q [mm]
δ	Delta-ferrite
γ	fcc pahse
ε	True strain [-]
ϵ	hcp martensite
Γ_J^E	Correction function relating numerical and analytical solutions of J-integral, as a function of reference elastic modulus [kJ/m^2]
Γ_C^E	Correction function relating numerical and analytical solutions of elastic compliance, as a function of reference elastic modulus [kJ/m^2]
ν	Poisson's ratio [-]
σ	True stress [MPa], sigma phase
Θ	Strain-hardening rate [MPa]

[Page intentionally left blank]

1. INTRODUCTION

1.1. ADDITIVE MANUFACTURING OF LARGE-SCALE METALLIC COMPONENTS

There is a clear need for the development of an efficient additive manufacturing (AM) process for large-scale metallic components. Industries, such as maritime [1], [2], energy [3], and heavy manufacturing [4], rely on large-scale components like propellers for large vessels, heavy punch-die moulds, and turbine hold rings for hydroelectric power generation. However, low production volumes and geometrical complexity of these components make traditional manufacturing routes inefficient, cost prohibitive, and dependant of complex logistic chains. Additive manufacturing offers a viable solution by enabling the production of customized large-scale components with minimal material waste, while simplifying manufacturing logistics [5]. Still, most AM technologies face significant challenges, including reliance on expensive material stocks, low deposition rates, and overall size constraints [6], [7]. These challenges restrict widespread adoption for large scale additive manufacturing. Yet, a family of additive-manufacturing processes is currently maturing to bridge these constraints at an industrial scale.

Wire arc additive manufacturing (WAAM) presents a viable and efficient solution for producing large-scale metal components [8], [9]. Falling under the category of direct-energy deposition AM technologies, WAAM is particularly distinguished for its ability to achieve near-net shaping with exceptional deposition rates. This capability is achieved by integrating well-established wire-and-arc fusion-welding technologies. With advanced computer-controlled robotic manipulators, power sources, and in-process control systems, this technology promises the production of high-quality, fully dense, near-net shape metal parts. Moreover, unlike many conventional additive manufacturing methods, WAAM is not limited by size constraints; the dimensions of the parts produced are restricted only by the reach of the robot arm holding the welding tool [10]. This makes it possible to fabricate components with previously unachievable dimensions, addressing a critical limitation in the AM of large-scale parts. As an outstanding example, the aerospace industry is currently employing a WAAM system capable of manufacturing full-size rocket fuel containers with the aid of a robot standing on a travelling elevator and an accompanying workpiece manipulator [11], [12], [13]. Figure 1-1 provides two examples of WAAM demonstrators that have been completed, namely a holding ring – a critical component for control valves within hydroelectric power plants -, and a boat propeller.

Figure 1-1 (a) Naval Group's WAAM'ed holding ring, part of a cut-off valve in a dam's hyrdropower plant, (b) Ramlab's WAAM'ed propeller, a world's first, class-approved ship propeller, and (c) an illustrative example of the two extra-large, geometrically complex parts being manufactured through WAAM (with human scale).

The introduction of new manufacturing technologies, such as wire-arc additive manufacturing, brings significant challenges. For industry acceptance, AM parts must consistently achieve performance levels comparable to those of conventionally manufactured components. Ensuring this reliability depends on the predictability qualification of the manufacturing process [14], which necessitates a comprehensive

understanding of the complex physical phenomena involved in AM. These processes are inherently intricate and difficult to predict accurately without empirical data derived from detailed characterization of the resulting microstructure and functional properties. Consequently, extensive characterization efforts are driving the broader industrial adoption and diverse applications of additive manufacturing, including WAAM. These efforts are also paving the way for further innovations, such as functional grading.

1.2. FUNCTIONAL GRADING THROUGH WAAM

Wire-arc additive manufacturing offers a unique opportunity to exploit its layer-by-layer deposition process to tailor the microstructure, chemical composition, or physical features of the part being produced [10], [15]. This concept, known as functional grading, enables the deliberate control and tuning of characteristics such as grain size, chemical composition, the presence of precipitates, and void density across the part's volume. By achieving this level of (micro-) structural control, it becomes possible to optimize the local functional performance of specific regions within a component and extend the realm of possibilities in terms of part design. For example, void density can be tuned for lightweight structural applications, ensuring optimal material distribution; or hardening precipitates can be concentrated near deformation-critical contact surfaces to enhance wear resistance. These strategies enable functional grading to mitigate the performance trade-offs commonly observed in major alloy families, paving the way for parts that are both highly specialized and high performing. The realm of possibilities is immense; hence, it is important to concentrate in one specific form of functional grading.

In this work, functional grading through compositional grading is of particular interest. This is due to its potential to tailor material properties across a component. Compositional grading is achieved by altering the alloy composition being deposited during the additive manufacturing process. This can be done by leveraging the layer-by-layer build process, during which the consumable material is changed between successive layers [15], [16]. Figure 1-2 shows a successful attempt to functional grade through this method, by integrating different alloy consumables in a single metal holding ring of large dimensions. This method requires the fusion welding of two distinct alloy compositions within a single melt pool, inevitably leading to dilution and interaction of the primary alloying elements. While this offers exciting opportunities for designing materials with graded properties, it also introduces significant challenges in controlling the microstructural and functional properties of the compositional gradient.

Functional grading through compositional variation presents significant challenges, especially at the interface where alloys of different compositions merge. The microstructural evolution in this region is influenced by the interplay of local thermal and chemical conditions. Additionally, turbulent flow within the melt pool causes heterogeneous mixing of the alloys [17], resulting in an unpredictable distribution of elements. Consequently, the microstructure that forms upon solidification is subject to considerable uncertainty, making accurate prediction of microstructure and properties a scientifically intriguing challenge. While not all alloy combinations are feasible, certain combinations offer distinct advantages that are highly relevant for industrial applications [18], [19], [20].

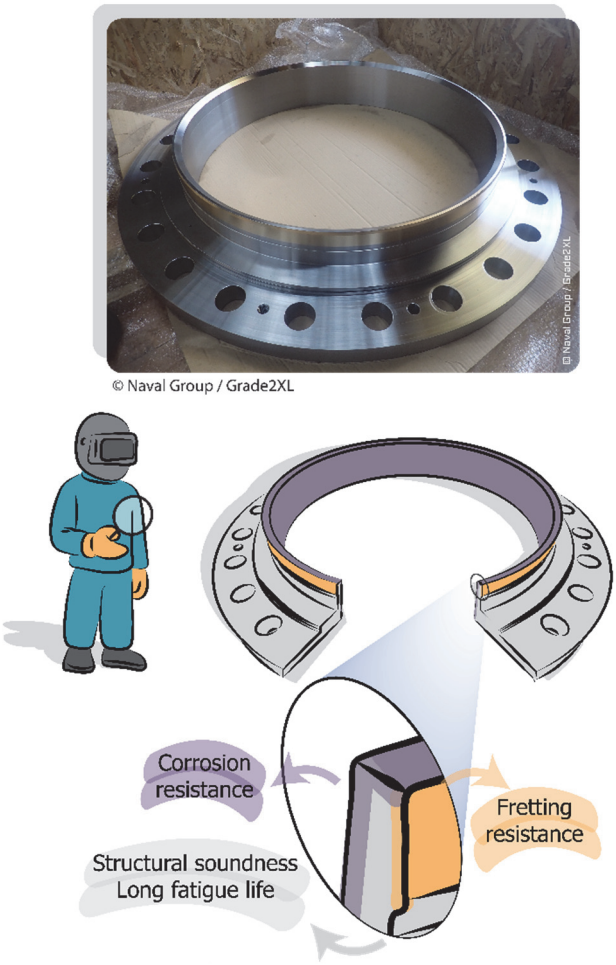

Figure 1-2 Example of location-specific properties required on a large-scale holding ring that can be tackled through compositional grading during the additive manufacturing process.

This work focuses on the compositional grading of austenitic stainless (AS) and high-strength low-alloy (HSLA) steels. Combining these two alloy families aims to leverage the strengths of each: the excellent strength and toughness of HSLA steel, and the corrosion resistance, ductility, and performance under cryogenic and high-temperature conditions of austenitic stainless steel. Low-alloy steel cladded with austenitic stainless steel has potential applications in marine and offshore environments[21], nuclear installations [22], and petrochemical reactors [23]. Through WAAM, mechanically loaded components such as propellers, moulds, and complex pressurized vessels could be additively manufactured, overcoming the limitations of conventional methods. However, uncertainties regarding the functional performance of the bi-material interface pose challenges for structural applications. To address this, extensive empirical evidence is needed to establish the mechanical performance of this bi-material combination and understand the underlying mechanisms controlling its behaviour.

1.3. RESEARCH MOTIVATION AND OBJECTIVES

Despite its potential, achieving reliable functional grading of HSLA and AS steel via WAAM presents significant challenges. While some studies have explored the interface characteristics of HSLA-ASS combinations [24], a comprehensive understanding of their microstructural development and resulting functional properties remains elusive. This work aims to address this gap by investigating the microstructural and mechanical properties of HSLA-AS steel bi-metal structures using WAAM, with a particular focus on the interface layer. The following objectives are established to achieve this goal:

- To develop a comprehensive understanding of microstructural evolution at the interface layer, which is crucial for correlating microstructural features with the mechanical performance of bi-material components.
- To investigate the quasi-static deformation and fracture behaviour of the bi-material part, combining mechanical testing and microstructural analysis to elucidate the mechanisms driving plastic deformation and failure, while addressing challenges in testing anisotropic specimens.
- To characterize the fatigue behaviour of the bi-material couple for reliable application, focusing on the relationship between the interface microstructure and fatigue crack propagation, and establishing reliable performance levels for bi-material components.

1.4. THESIS OUTLINE

To achieve the research motivation outlined in the previous section, this thesis is structured in 7 chapters:

- **Chapters 1 (present) and 2** introduce the research objectives and provides insights into the state of the art on the microstructural development of the parent materials as obtained through WAAM.
- **Chapter 3** addresses the microstructural development at the diluted interface layer, establishing the framework for microstructural characterization in subsequent chapters.
- **Chapter 4** explores the deformation mechanisms governing quasi-static deformation, focusing on tensile loading and fracture toughness.
- **Chapter 5** provides insights into the fatigue crack propagation behaviour across the bi-metal part, building on the established deformation mechanisms of the interface layer.
- **Chapters 6 and 7** offer a general discussion of the results presented in this thesis, including comprehensive conclusions and recommendations for future research on the functional grading for large-scale additive manufacturing.

1.5. CHAPTER REFERENCES

[1] A. Taşdemir and S. Nohut, "An overview of wire arc additive manufacturing (WAAM) in shipbuilding industry," 2020, *Taylor and Francis Ltd.* doi: 10.1080/17445302.2020.1786232.

[2] A. Queguineur, G. Rückert, F. Cortial, and J. Y. Hascoët, "Evaluation of wire arc additive manufacturing for large-sized components in naval applications," *Welding in the World*, vol. 62, no. 2, pp. 259–266, Mar. 2018, doi: 10.1007/s40194-017-0536-8.

[3] J. G. Rafferty, D. Gill, and R. Kapur, "Disrupting the Metallics Domain in Pressure Vessel and Piping Manufacture-Advanced Manufacturing in the Oil and Gas Sector," in *Volume 5: High-Pressure Technology; ASME Nondestructive Evaluation, Diagnosis and Prognosis Division (NDPD); SPC Track for Senate*, American Society of Mechanical Engineers, Jul. 2017, pp. 1–7. doi: 10.1115/PVP2017-65840.

[4] L. Yan, "Wire and Arc Additive Manufacture (WAAM) reusable tooling investigation," Cranfield University, 2013. [Online]. Available: uri: http://dspace.lib.cranfield.ac.uk/handle/1826/12308

[5] D. Frey, J. Palladino, J. Sullivan, and M. Atherton, "Part count and design of robust systems," *Systems Engineering*, vol. 10, no. 3, pp. 203–221, Sep. 2007, doi: 10.1002/sys.20071.

[6] C. R. Cunningham *et al.*, "Cost Modelling and Sensitivity Analysis of Wire and Arc Additive Manufacturing," in *Procedia Manufacturing*, Elsevier B.V., 2017, pp. 650–657. doi: 10.1016/j.promfg.2017.07.163.

[7] M. Baumers, P. Dickens, C. Tuck, and R. Hague, "The cost of additive manufacturing: Machine productivity, economies of scale and technology-push," *Technol Forecast Soc Change*, vol. 102, pp. 193–201, 2016, doi: 10.1016/j.techfore.2015.02.015.

[8] B. Wu *et al.*, "A review of the wire arc additive manufacturing of metals: properties, defects and quality improvement," Oct. 01, 2018, *Elsevier Ltd*. doi: 10.1016/j.jmapro.2018.08.001.

[9] S. W. Williams, F. Martina, A. C. Addison, J. Ding, G. Pardal, and P. Colegrove, "Wire + Arc additive manufacturing," *Materials Science and Technology (United Kingdom)*, vol. 32, no. 7, pp. 641–647, Jun. 2016, doi: 10.1179/1743284715Y.0000000073.

[10] R. Zhang, F. Jiang, L. Xue, and J. Yu, "Review of Additive Manufacturing Techniques for Large-Scale Metal Functionally Graded Materials," Jun. 01, 2022, *MDPI*. doi: 10.3390/cryst12060858.

[11] "Relativity Space announces 4th generation of its Stargate metal Additive Manufacturing platform," Metal AM. Accessed: May 08, 2025. [Online]. Available: https://www.metal-am.com/relativity-space-announces-4th-generation-of-its-stargate-metal-3d-printing-platform/

[12] S. Davies, "Relativity unveils Stargate 4th Generation metal 3D printer with horizontal printing capability," TCT Magazine. Accessed: May 08, 2025. [Online]. Available: https://www.tctmagazine.com/additive-manufacturing-3d-printing-news/metal-additive-manufacturing-news/relativity-unveils-stargate-4th-generation-metal-3d-printer-/

[13] C. Schwaar, "WAAM! What Is Wire Arc Additive Manufacturing?," All3DP. Accessed: May 08, 2025. [Online]. Available: https://all3dp.com/1/waam-what-is-wire-arc-additive-manufacturing/#google_vignette

[14] G. Moroni, S. Petrò, and H. Shao, "On Standardization Efforts for Additive Manufacturing," 2020, pp. 156–172. doi: 10.1007/978-3-030-46212-3_11.

[15] A. Reichardt *et al.*, "Advances in additive manufacturing of metal-based functionally graded materials," *International Materials Reviews*, vol. 66, no. 1, pp. 1–29, Jan. 2021, doi: 10.1080/09506608.2019.1709354.

[16] K. Sanjeeviprakash, A. R. Kannan, and N. S. Shanmugam, "Additive manufacturing of metal-based functionally graded materials: overview, recent advancements and challenges," May 01, 2023, *Springer Science and Business Media Deutschland GmbH*. doi: 10.1007/s40430-023-04174-1.

[17] T. Soysal, S. Kou, D. Tat, and T. Pasang, "Macrosegregation in dissimilar-metal fusion welding," *Acta Mater*, vol. 110, pp. 149–160, May 2016, doi: 10.1016/j.actamat.2016.03.004.

[18] J. Wang *et al.*, "Characterization of wire arc additively manufactured titanium aluminide functionally graded material: Microstructure, mechanical properties and oxidation behaviour,"

Materials Science and Engineering: A, vol. 734, pp. 110–119, Sep. 2018, doi: 10.1016/j.msea.2018.07.097.

[19] T. A. Rodrigues *et al.*, "Steel-copper functionally graded material produced by twin-wire and arc additive manufacturing (T-WAAM)," *Mater Des*, vol. 213, Jan. 2022, doi: 10.1016/j.matdes.2021.110270.

[20] B. Wu *et al.*, "Enhanced interface strength in steel-nickel bimetallic component fabricated using wire arc additive manufacturing with interweaving deposition strategy," *J Mater Sci Technol*, vol. 52, pp. 226–234, Sep. 2020, doi: 10.1016/j.jmst.2020.04.019.

[21] D. Wang, X. Sun, Y. Jiang, X. Chang, and X. Yonglei, "Review on the application of stainless-clad bimetallic steel in the marine environment," *Anti-Corrosion Methods and Materials*, vol. 71, no. 2, pp. 132–142, 2024, doi: 10.1108/ACMM-06-2023-2832.

[22] H. T. Wang, G. Z. Wang, F. Z. Xuan, and S. T. Tu, "Fracture mechanism of a dissimilar metal welded joint in nuclear power plant," *Eng Fail Anal*, vol. 28, pp. 134–148, Mar. 2013, doi: 10.1016/j.engfailanal.2012.10.005.

[23] N. Switzner and Z. Yu, "Austenitic stainless steel cladding interface microstructures evaluated for petrochemical applications," *Weld J*, vol. 98, no. 2, pp. 50S-61S, Feb. 2019, doi: 10.29391/2019.98.004.

[24] M. R. U. Ahsan, A. N. M. Tanvir, T. Ross, A. Elsawy, M. S. Oh, and D. B. Kim, "Fabrication of bimetallic additively manufactured structure (BAMS) of low carbon steel and 316L austenitic stainless steel with wire + arc additive manufacturing," *Rapid Prototyp J*, vol. 26, no. 3, pp. 519–530, 2019, doi: 10.1108/RPJ-09-2018-0235.

[Page intentionally left blank]

2. A STATE-OF-THE-ART: DIRECT ENERGY DEPOSITION OF HIGH STRENGTH LOW ALLOY STEELS AND AUSTENITIC STAINLESS STEELS

Select topics are presented on microstructural development after fusion-arc welding and direct energy deposition (DED) processes of HSLA and AS steels. This background discussion is necessary to understand the expected microstructural development for each material volume, and to identify potential problems that literature indicates may arise through their mixing. The discussion first addresses the microstructural characteristics of both alloy families. It is then followed by a review on the microstructural and mechanical properties as obtained through DED of representative consumables, mostly concentrating on WAAM of the alloys ER70S-6 and ER316L.

2.1. HIGH STRENGTH LOW ALLOY STRUCTURAL STEELS

The modern development of high-strength low-alloy (HSLA) steels focuses on achieving elevated mechanical performance with minimal alloying content. This is intended to obtain good mechanical performance and excellent weldability while keeping production costs low [1]. For fusion welding applications, a variety of electrodes have been designed, with ER70S-XX and ER80S-XX being the most widely used consumables in gas metal arc welding (GMAW) processes. The differences in electrode denomination between both alloys is derived from their mechanical performance, as inherited from their microstructural constitution.

The mechanical properties of these consumables depend on the formation of refined microstructures. In particular, acicular ferrite (AF) is a preferred morphology due to its excellent combination of strength and ductility. Although AF is often used as an umbrella term, it typically encompasses a mixture of small ferrite needles mixed with Widmanstätten ferrite, bainite, and smaller fractions of other microphases alongside disperse oxides [2], [3]. Commercial welding consumables are alloyed in such way that these later oxides promote the intergranular formation of the ferritic and bainitic plates. Examples of typical morphologies of ferrite and martensite in low-alloy, low carbon weldments are presented in Figure 2-1.

The choice for acicular ferrite as a main microstructural constituent is founded on its favourable morphological characteristics. Small ferrite grains form a weave-like pattern, with a high density of high-angle grain boundaries and an elevated dislocation density [4]. These characteristics improve strength and hinder crack initiation and propagation, as illustrated through the fracture toughness obtained from impact test results and summarized in Figure 2-2.

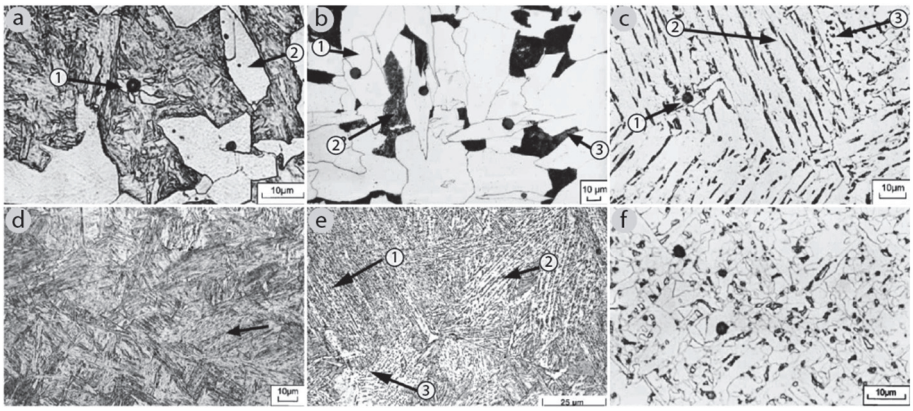

Figure 2-1 Common ferrite morphologies found in low-alloy steel weldments, including (a) 1 – idiomorphic ferrite (PF(I)); 2 - allotriomorphic ferrite (PF(G)). Fig. (b) 1 – PF(I); 2 – ferrite-carbide aggregate (FC); 3 – pearlite (FC(P)). Fig. (c) 1 - PF(I); 2 and 3 – Prior austenite grain boundary Widmanstätten ferrite (WS(GB)). Fig. (d) Lath Martensite (M(L)). Fig. (e) 1 – lower bainite (FC(LB)); 2 – upper bainite (FS(UB)); and 3 – bainitic ferrite (FS(NA)). Fig. (f) acicular ferrite (AF). Classification follows the International Institute of Welding system (2003) [2].

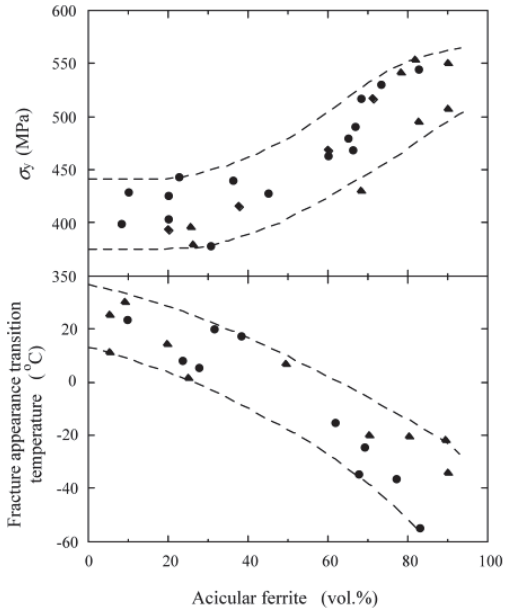

Figure 2-2 Variation of yield strength, σ_y, and the ductile to brittle transition temperature with relation to the proportion of acicular ferrite for C-Mn-Nb weld metals [5].

2.1.1. DED of HSLA steel

It is well established that the high heat input associated with welding processes can cause coarsening of ferrite grains in steels. This phenomenon is commonly attributed to recrystallization or abnormal austenite-to-ferrite phase transformations [6], [7] and often results in softening of the heat-affected zone (HAZ) and a reduction in its toughness. In wire arc additive manufacturing (WAAM), this issue is even more critical due to the inherently multi-pass nature of the process [8]. As such, adopting variants of gas metal arc welding (GMAW) or gas tungsten arc welding (GTAW) with rapid cooling characteristics can improve the HAZ toughness of WAAM-fabricated HSLA steels.

Rafieazad et al. [8] investigated the suitability of ER70S-6 in WAAM. The study involved fabricating a 135 mm × 150 mm coupon with a six-bead width using a 1.6 mm wire, 320 A arc current, 28 V arc voltage, 104 mm/s wire feed rate, and a scan speed of 5 mm/s. Pure argon was used as the shielding gas at 45 L/min. To minimize heat input and surface defects, the authors employed Surface Tension Transfer (STT), a current-controlled short-circuiting arc transfer mode. STT technique achieves approximately 80% of the heat input associated with conventional arc modes [9], [10] thereby limiting HAZ softening and enhancing bead geometry.

Microstructural analysis of the deposited wall, presented in Figure 2-3, reveals the as-deposited structure across various zones—from regions near the fusion line to the centre of the melt pool (top-left of the in Figure 2-3 (a)) and overlapping HAZ regions (bottom-right). The dominant microstructure in each fusion region consists of fine polygonal ferrite (F) as the primary phase and a minor fraction of lamellar pearlite (P) located primarily at ferrite grain boundaries. This configuration aligns with previous findings for WAAM-fabricated ER70S-6 components [8]. Additionally, micrographs near the melt-pool boundary show localized regions of acicular ferrite and bainite (AF + B), attributed to additional uptake of oxygen near fusion lines.

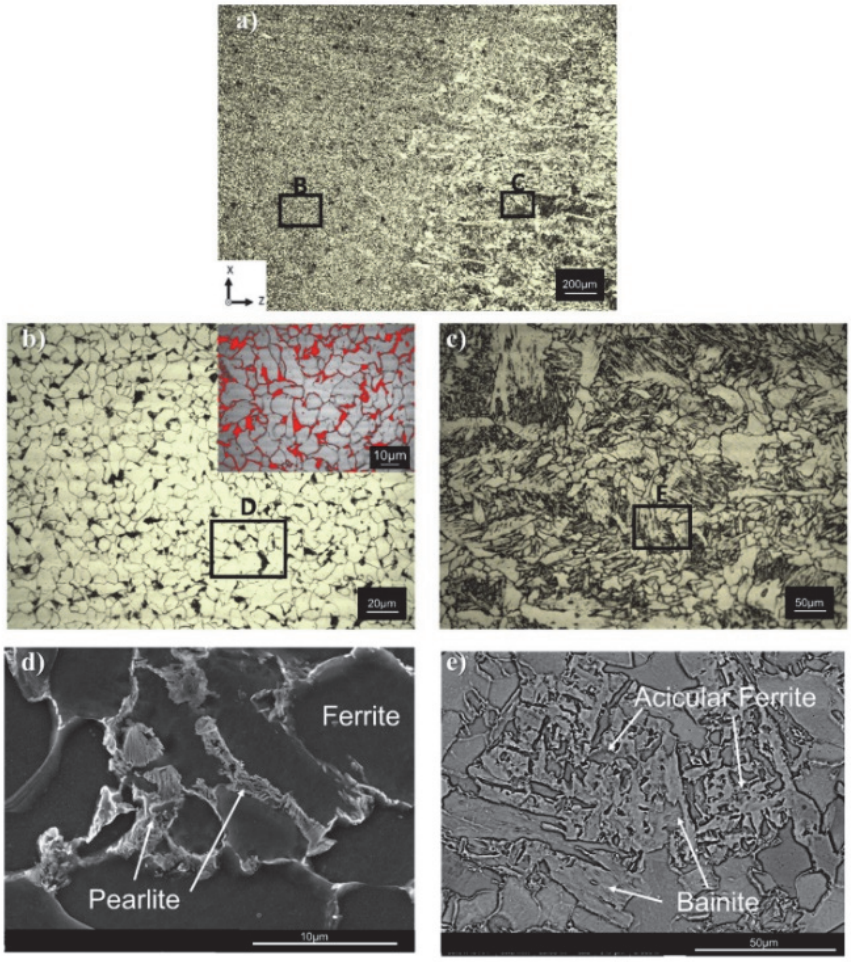

Figure 2-3 Optical micrographs of (a) a WAAM-ER70S-6 steel wall showcasing the etched microstructure at the fusion line and centre of the melt pool, and accompanying details under higher magnification of (b) the centre of the weld metal and (c) a region close to the fusion line. Microstructural details in the latter two micrographs are further enhanced under SEM on (d) and (e). The inset on (b) shows perlite regions in red [8].

The authors attribute the observed microstructural variation to the thermal gradients between overlapping deposited beads. As the fusion boundaries cool more rapidly than the melt pool centre, non-equilibrium phases such as AF and bainite preferentially form near these interfaces [8], [11]. Similar observations were reported by Haselhuhn et al. [12]. The pearlite phase volume fraction was estimated at 12.54 ± 0.56%, while the volume fractions of AF and bainite at the fusion boundaries were comparable. Despite

localized heterogeneity within individual beads, the overall microstructure was found to be relatively uniform across the build, owing to the application of a 10-minute interlayer cooling period. This thermal management strategy minimized heat accumulation and suppressed microstructural variation along the build direction.

However, under rapid cooling conditions brittle phases may form. In the absence of sufficient carbon or austenite-stabilizing elements—as is the case for ER70S-6—the reverted austenite may transform into martensite–austenite (MA) constituents, forming localized brittle zones (LBZs) in the inter-critical HAZ (ICHAZ) [13]. These MA regions compromise toughness by reducing the deformation capacity of the surrounding matrix and by promoting debonding at phase boundaries [14]. Figure 2-4 illustrates the presence of such LBZs, where the MA phase nucleates within a bainitic lamellar structure. Although the volume fraction of MA is low, its presence can still significantly affect mechanical behaviour, particularly in the build direction.

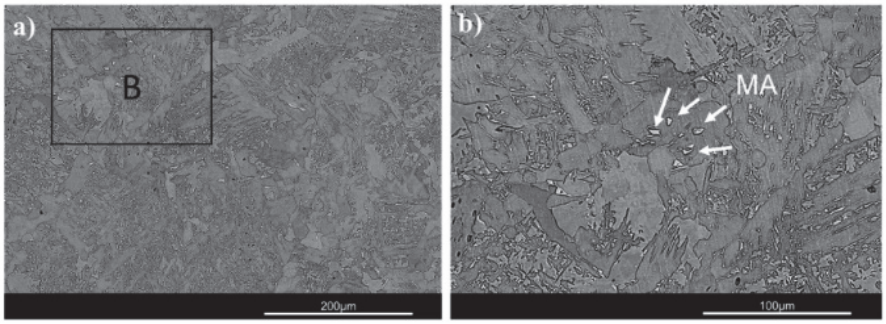

Figure 2-4 (a) SEM micrograph taken from thermally treated overlap region of WAAM-ER70S-6 and (b) this region under higher magnification showing the formation of MA phase between coarse bainite lamellas [8].

Grain morphology analysis using inverse pole figure (IPF) maps and statistical measurements of grain size and aspect ratio indicate a predominantly equiaxed grain structure (aspect ratio < 3) with an average grain size of ~7.30 µm, as shown in Figure 2-5 by Rafiezad et al. [8]. However, the grain structure is heterogeneous. Coarse grains averaging 15.76 ± 2.34 µm were identified near the melt pool boundaries, whereas finer grains averaging 4.94 ± 1.26 µm were found in the melt centre. These microstructural differences are attributed to the layer-by-layer nature of WAAM: each new layer thermally treats the preceding one, promoting recrystallization, grain boundary migration, and grain growth. Such inhomogeneities can introduce anisotropic mechanical behaviour in the final component. As shown in Figure 2-5, approximately 80% of grains have areas below 100

μm², indicating a generally fine-grained structure. Misorientation distribution analysis Figure 2-6 further confirms a narrow distribution of grain boundary angles (0°–4°), suggesting an overall uniform crystallographic orientation.

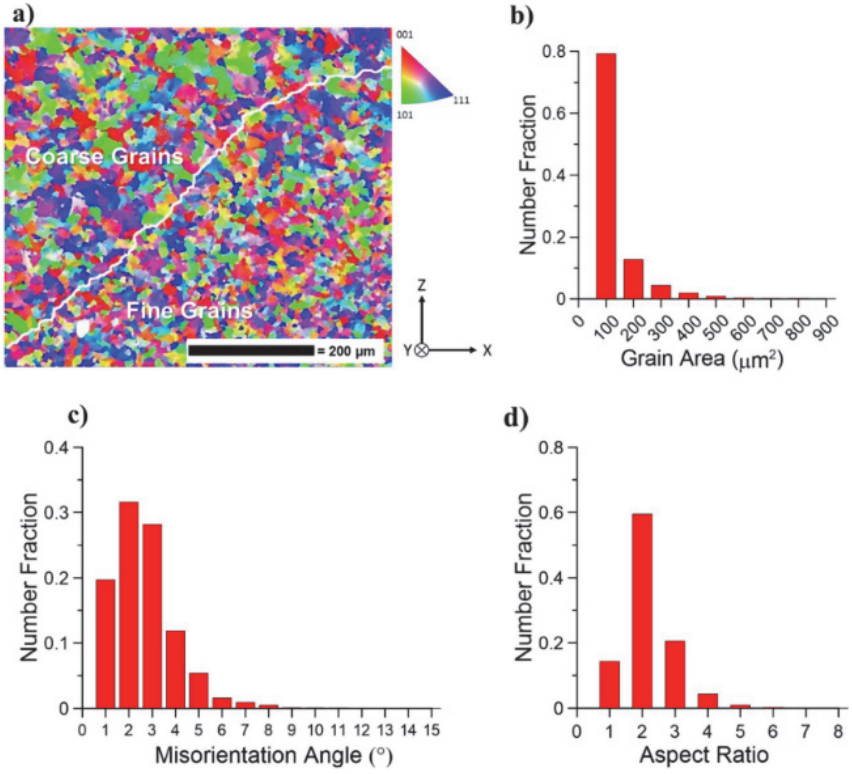

Figure 2-5 (a) EBSD inverse pole figure map of as-printed ER70S-6 sample, and the corresponding histogram distribution of (b) grain area, (c) misorientation angle, and (d) grain aspect ratio [8]. Coarse grained area belongs to the HAZ of the previously deposited material; fine grained area belongs to the subsequently deposited layer.

Texture analysis using {100}, {110}, and {111} pole figures, Figure 2-6, shows a very weak texture with a maximum intensity of 3.08, indicating mostly random grain orientations. The build direction is normal to the pole figure plane, with longitudinal (Y) and transverse (X) directions indicated. X-ray diffraction (XRD) analysis confirms that the as-deposited structure is dominated by α-iron (body-centred cubic, BCC), with no austenite (face-centred cubic, FCC) phase. This suggests either the absence of retained austenite or a volume fraction below the XRD detection threshold.

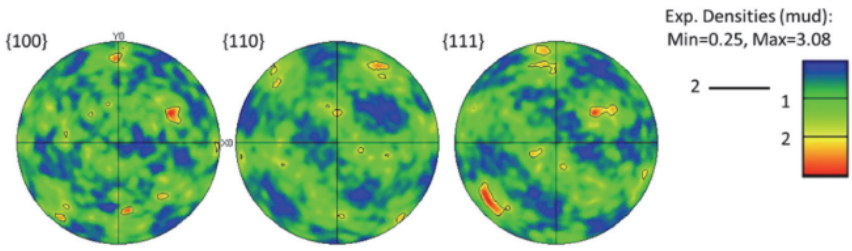

Figure 2-6 Pole figures from WAAM-ER70S-6 single layer wall [8].

2.1.2. Mechanical properties

The as-printed WAAM-ER70S-6 sample exhibited an overall average microhardness of 160 ± 7 HV across the entire build height, indicating a uniform hardness distribution along the build direction. The hardness values measured by Rafiezad et al. [8] are presented on Figure 2-7. This uniformity reflects the consistency of the microstructure throughout the deposited wall and is generally desirable, as it suggests a more homogeneous and isotropic mechanical response [15]. The relatively small deviation in microhardness (±7 HV) is attributed to variations in microstructural constituents and inclusions, which differ in volume fraction across the melt-pool boundaries.

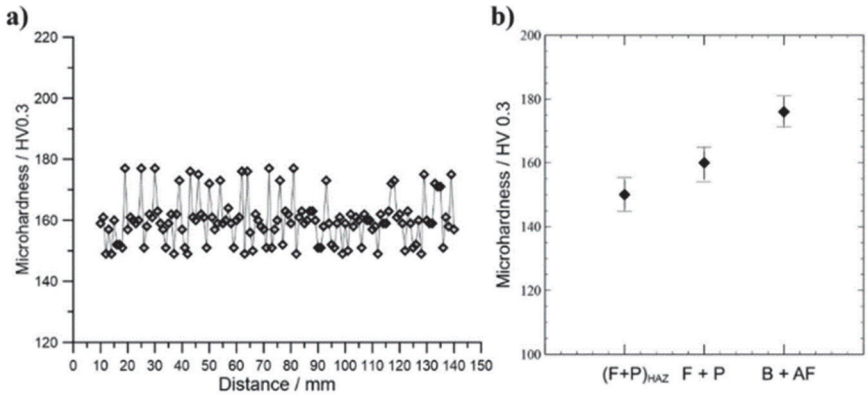

Figure 2-7 (a) Vickers microhardness distribution along the build direction, and (b) average measured microhardness on different constituents in the microstructure (F – Ferrite, P – Pearlite, B – Bainite, AF – Acicular Ferrite, HAZ – Heat Affected Zone). Error bars indicate one standard deviation [8].

Mechanical testing further confirmed the isotropic nature of the material in terms of strength. The average yield strength (YS) and ultimate tensile strength (UTS) for

specimens extracted in both horizontal and vertical orientations were approximately 396 ± 26 MPa and 503 ± 21 MPa. These values indicate that the tensile strength of the additively manufactured wall is nearly identical in both plane directions, consistent with previous findings on low-alloy steels processed by WAAM [15], [16], [17].

However, despite the observed strength isotropy, a marked anisotropy was evident in ductility. As shown in Figure 2-8, the elongation to failure for vertical specimens was significantly lower than that of their horizontal counterparts, with average values of 12 ± 3% and 35 ± 2%, respectively. This pronounced directional difference in ductility and toughness is a well-documented characteristic in additively manufactured components, reported across a wide range of metals and alloys [18], [19], [20]. The authors attribute this mechanical anisotropy in ductility to several possible factors: (1) the presence of manufacturing defects or discontinuities, such as lack of fusion or porosity, often concentrated at interlayer regions; (2) grain coarsening within the HAZ, particularly along the build direction; and (3) the localized formation of brittle martensite–austenite (MA) constituents within bainitic lamellar structures. Although these potential causes are identified, they were not quantitatively examined in the cited study.

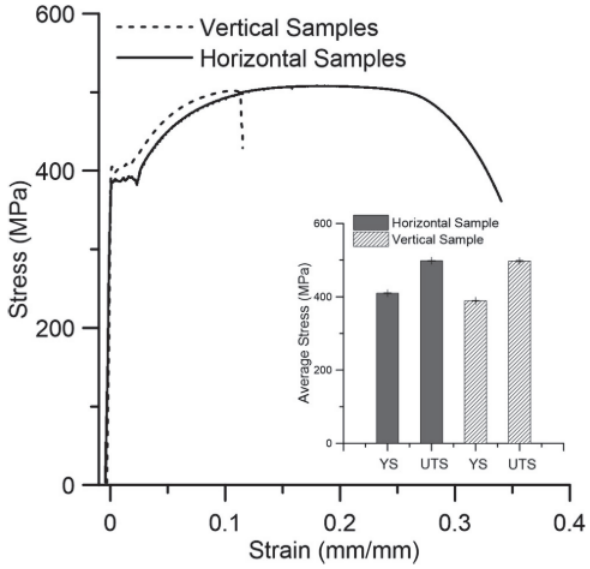

Figure 2-8 Stress-strain curves and their corresponding tensile properties for two perpendicular orientations. [8]

2.2. STAINLESS STEELS

2.2.1. Stainless steel families

Stainless steel refers to a broad family of high-alloy steels primarily composed of iron (Fe), chromium (Cr), nickel (Ni), and carbon (C), with a minimum chromium content of 10.5 wt%. The relatively high proportion of chromium ensures the formation of a chromium oxide passive barrier that protects the alloy from further oxidation and corrosion.

In general, the physical properties of stainless steels are governed by the relative proportions of their main microstructural constituent. These are tuned through the careful balancing of ferrite promoting elements against austenite promoting elements, as well as the speed at which solidification and further cooling occur. The different combinations lead to differences in the major microstructural constituent formed, it typically being either austenite, ferrite, or martensite, along with the presence of carbides and oxides. Due to the complex multicomponent nature of these alloys, phase diagrams can become unpractical or simply insufficient for predicting the final microstructure. Consequently, significant research has focused on developing predictive models based on elemental tendencies toward ferrite or austenite formation.

A landmark contribution to this field was made by Schaeffler in 1948, whose diagram remains widely used to estimate phase fractions in stainless steel welds [21]. The Schaeffler diagram introduces the concepts of chromium-equivalent and nickel-equivalent to quantify the ferrite- and austenite-forming tendencies of alloying elements. This diagram is shown on Figure 2-9, mapping in it the approximate location of many commercial austenitic stainless alloys. It includes iso-ferrite lines that predict ferrite content in the as-solidified structure. Most common welding alloys fall within the fully austenitic region or slightly above the 20% ferrite boundary. For example, alloy 316L is shown with in the figure with a predicted ferrite content of ~10%, based on its standard composition, after the American Iron and Steel Institute (AISI). The formation of this austenite matrix accompanied by ferrite under fusion-weld additive manufacturing is introduced in the following section.

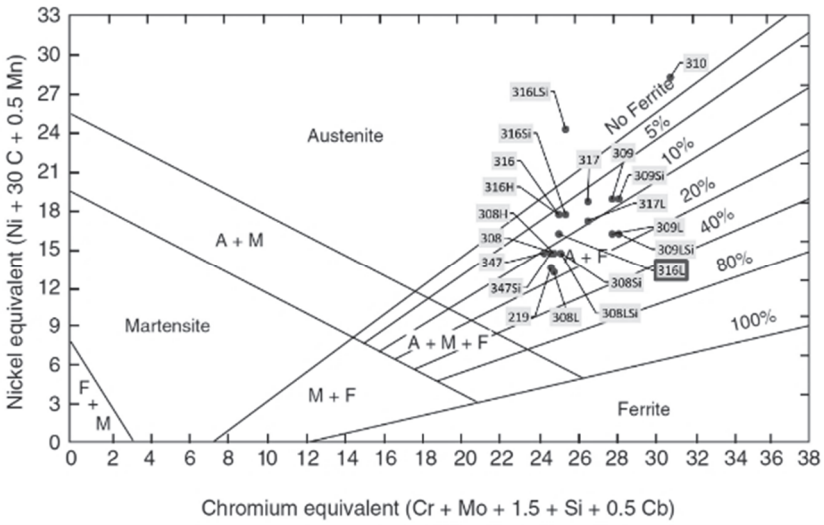

Figure 2-9 Schaeffler modified constitution diagram and ferrite content prediction for common GMAW standard welding consumables [21]

2.2.2. DED of AS Steels

In the context of wire arc additive manufacturing (WAAM), the deposition of austenitic stainless steel 316L has been studied extensively due to its favorable corrosion resistance and weldability. Zhang et al. [22] distinguished between two regions in WAAM-fabricated 316L components based on their solidification modes: an inner layer area, characterized by ferrite-austenite (FA) solidification, and a partial melting area, exhibiting austenite-ferrite (AF) solidification. In a related study, Chen et al. [23] observed that during subsequent thermal cycles, δ-ferrite phases redissolved into austenite, while intermetallic σ-phases formed at γ/δ interfaces. These δ and σ phases typically appeared in the HAZ with columnar morphologies, differing from the finer structure observed in the remainder of the build.

Wang et al. [24] conducted a separate study using the Cold Metal Transfer (CMT) process to deposit 316L. A 1.0 mm diameter wire was used with an arc current of 150 A, arc voltage of 14.1 V, wire feed rate of 11 m/min, scan speed of 0.7 m/min, and a 40% overlapping rate. A shielding gas mixture of Ar + 2% O_2 was supplied at 20 L/min. CMT relies on controlled retraction of the electrode wire, allowing droplet transfer with minimal spatter. During metal transfer, current briefly drops near zero, then is re-initiated, enabling stable, low-heat deposition [25].

The microstructure of the deposited component exhibited a multi-layered morphology in both the build and transverse directions. Wang et al. [24] identified two key zones: the re-melted area (RA), corresponding to the fusion zone of a single pass, and the overlapping area (OA), where adjacent passes intersect. In the same study, EBSD and optical microscopy analyses revealed alternating zones of dispersed and concentrated grain orientations along the transverse direction and the plane perpendicular to the build direction. Dispersed grain orientations correlated with re-melted areas at semicircular fusion lines. Fusion lines subdivided the structure into discrete layers, though similar grain orientations were maintained between layers.

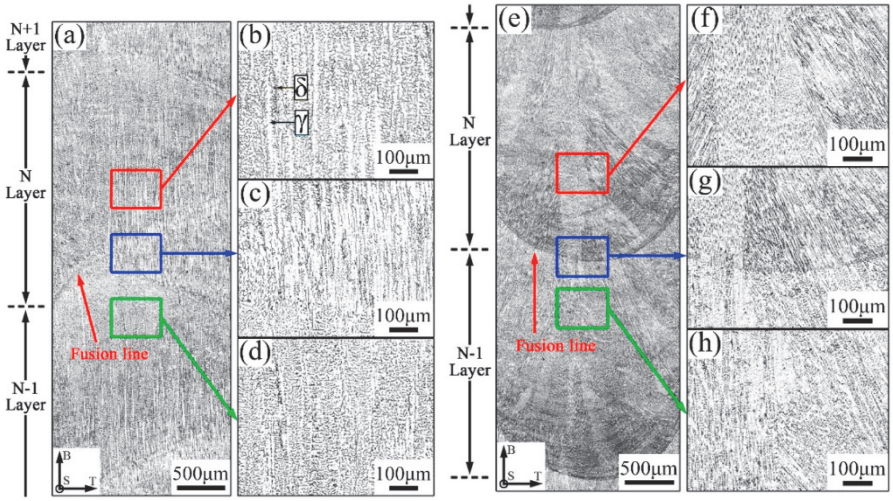

Figure 2-10 (a – d) Microstructure of overlap regions on the transverse plane, including three subsequent layers (e – h) microstructure of re-melted region on the transverse plane BOT, including three subsequent layers [24]

Figure 2-10 shows the microstructure in OA and RA regions, respectively. In the OA, austenite dendrites grow along the build direction, while ferrite appears in skeletal morphology at the base and transitions into lath ferrite higher in the bead. In RA regions, austenite dendrites grow perpendicular to fusion lines, and ferrite transitions from granular/acicular forms to coarse lath ferrite along bead height. This morphology is symmetric on either side of each bead and demonstrates periodic changes in ferrite structure along both the build direction and interlayer planes.

Figure 2-11 shows EBSD results for a cross-section perpendicular to the deposition direction. Below the fusion lines indicated as white dotted lines in the figure, columnar

austenite grains are observed growing epitaxially toward the center of the melt pool. In the OA, grains display a strong <001> texture, with 99.7% alignment in the build direction. The texture includes 83.8% Goss {110}<001> and 10.5% cubic {100}<001> components. Grain boundaries are classified by misorientation: white lines indicate low-angle grain boundaries (3°–15°) and black lines mark high-angle boundaries (>15°). A higher density of low-angle boundaries was observed in OA regions, correlating with the strong texture. According to Wang et al. [26], a higher frequency of high-angle grain boundaries enhances recrystallization, strength, and toughness—suggesting that RA regions may display superior mechanical properties.

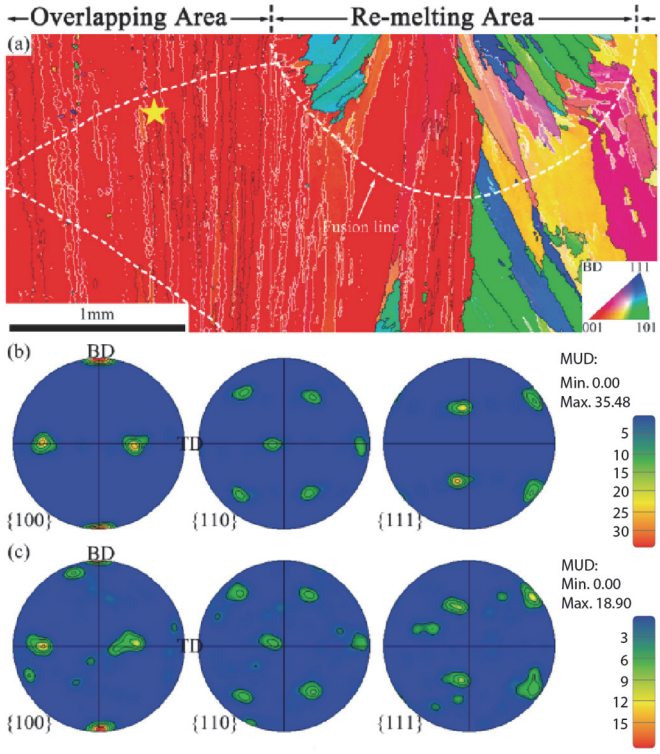

Figure 2-11 (a) EBSD inverse pole map with <001> plotted parallel to the building direction, and equal area projection pole figures of the (b) overlap and (c) re-melted regions for FCC phase [24]. Star indicates the point measurement of Euler angles, φ_1: 86.2°, Φ: 42.9°, φ_2: 4.9°.

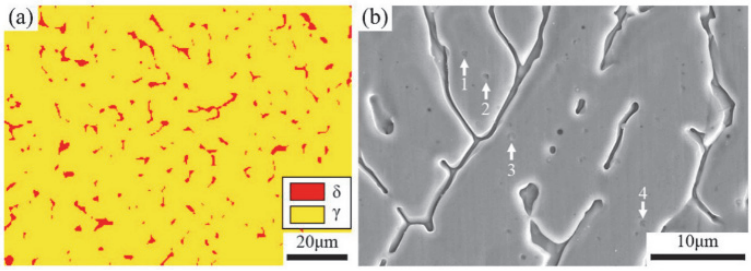

Figure 2-12 (a) EBSD phase map, and (b) SEM micrographs of as-built 316L part. Arrows indicate the location of silicate particles, as reported by the study's authors [24].

Figure 2-12 presents EBSD and SEM micrographs of the as-built sample. The microstructure primarily consists of austenite (γ) and δ-ferrite, with no σ-phase detected. The low carbon content of 316L inhibited carbide formation. Spherical particles (~1 μm) distributed throughout the austenite matrix were identified via EDS as Si-Mn-O-rich silicate oxides or inclusions.

Wang et al. [27] further explored how the arc mode affects the microstructure and mechanical properties of WAAM-deposited 316L. Figure 2-13 offers an overview of the hardness values found across layers, while Figure 2-14 shows the tensile curves obtained in the same study. The authors focused on secondary dendrite arm spacing (SDAS), a key indicator of solidification rate and grain refinement. Smaller SDAS generally correlates with improved mechanical properties.

Two arc modes were compared.

- SpeedPulse: A non-short-circuiting pulse process using projected spray transfer
- SpeedArc: A traditional CMT arc mode with lower heat input

Both modes operated at equal deposition rates, however SpeedArc WAAM consistently produced smaller SDAS at both bottom and top layers. This was attributed to lower heat input, smaller melt pools, and higher cooling rates compared to SpeedPulse. Two factors explained the SDAS variation across layers: (1) Upper layers experience reduced heat loss due to heat accumulation and diminished conductive paths to the substrate. (2) The base plate and lower layers dissipate heat more efficiently, enabling faster cooling and finer microstructures at the bottom of the build [27], [28]. The SDAS values confirm that SpeedArc WAAM promotes a finer solidification structure in both lower and upper layers, which is advantageous for improving component strength and uniformity.

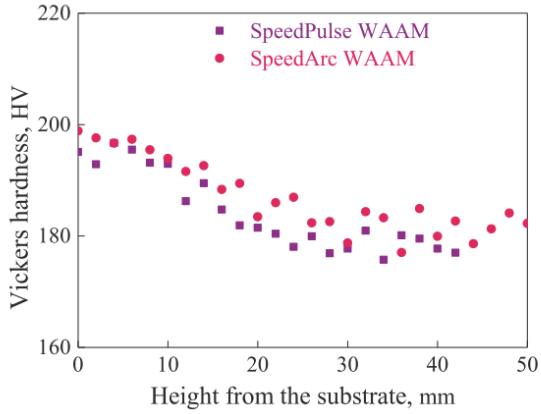

Figure 2-13 Vickers hardness of the SpreedPulse and SpeedArc additive manufactured components [24].

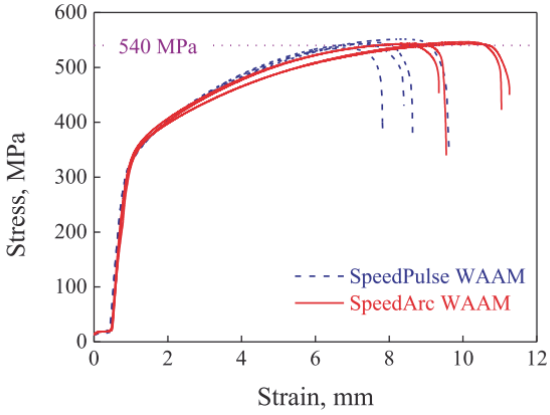

Figure 2-14 Stress-strain curves of the SpeedPulse and SpeedArc additive manufactured tensile specimens along the build direction [24].

Table 2-1 Experimentally measured and previously reported tensile properties of additively manufactured 316L stainless steel, as well as wrought material [24].

Metal Transfer Mode	**Yield Strength [MPa]**	**UTS [MPa]**
SpeedPulse	418	550
SpeedArc	418	553
CMT WAAM	235	533
Wrought	255-310	525-623

2.2.3. Mechanical properties

The mechanical behaviour of austenitic stainless steel 316L produced by WAAM is known to exhibit directional dependence due to the anisotropic nature of the solidification and thermal cycling inherent to the process. Several studies have investigated the tensile properties of CMT-WAAM and other arc-based additive manufacturing methods, with varying conclusions depending on build orientation, deposition strategy, and alloy behaviour. Rodriguez et al. [29] evaluated the tensile properties of 316L fabricated via Cold Metal Transfer (CMT)-WAAM, reporting that the yield strength along the build direction was lower than that along the bead (scanning) direction. This reduction was attributed to epitaxial grain growth, which promotes a preferential crystallographic orientation aligned with the thermal gradient, leading to weaker resistance to deformation along the growth axis. Conversely, Wu et al. [30] studied 316L samples fabricated by Metal Inert Gas Additive Manufacturing (MIG-AM) and found that both yield and ultimate tensile strengths were higher in the build direction compared to the scanning direction. These results suggest that although mild, mechanical anisotropy in WAAM-fabricated stainless steel is dependent on process parameters and thermal history. Tabernero et al. [31] also investigated CMT-deposited 316L and observed comparable tensile strengths in different directions. However, they reported that yield strength and elongation were lower along the build direction than in the scanning direction. These observations further emphasize the complexity of mechanical property anisotropy in arc-based additive manufacturing processes.

The underlying causes of anisotropy in mechanical behaviour are closely linked to the non-equilibrium solidification and thermal cycling experienced during deposition. However, a concrete correlation between microstructural features and mechanical response remains unresolved [32]. For Most of the available data are derived from thin-walled structures, which raises concerns about their representativeness in bulk or block-fabricated components. The mechanical response of thick sections may vary significantly due to interlayer heat accumulation, weaving strategies, and differential heat dissipation across the build volume.

Stainless steel undergoing DED additive manufacturing often displays orientation-dependant elastic properties. A phenomenological approach was carried out Laghi et al. [33] clearly highlighting the dependencies in mechanical properties per orientation on a 304L stainless steel thin wall. Dedicated studies on textured polycrystal materials shows a

clear correlation between the relationship of crystal orientation and Voigt elastic constants [34], [35]. The difference in measured elastic constants has shown to vary from circa 70 GPa for C_{44} to circa 270 GPa for C_{11} for selective laser melted austenitic stainless steel 316L [36]. These values resemble those obtained from single crystal Fe-19Cr-10Ni alloy (AINSI 304), showing values of C_{44} = 126.2 GPa, C_{11} = 204.6 GPa and C_{12} = 137.7 GPa [37], translating to elastic moduli E of 93.8 GPa in the [100] direction, 193.5 GPa in the [110] direction and 299.8 GPa in the [111] direction [35], [38]. Additive manufacturing of FCC alloys often allows for a strong [001] texture parallel to the build direction; the stronger the crystallographic texture, the higher the resemblance of macroscopic properties to that of single crystals. These results give thus an hint to the origin of the often reported orthotropic behaviour in mechanical properties of textured FCC stainless steel alloys obtained through WAAM.

The thermal history in metal AM is inherently complex, characterized by rapid heating and cooling cycles, directional solidification, steep thermal gradients, and partial re-melting of previous layers. These factors influence microstructure evolution—such as grain growth direction, texture formation, and phase transformations—and are expected to affect the mechanical properties of the final component [39]. Understanding and controlling these parameters are essential for tailoring the mechanical performance of WAAM-fabricated 316L stainless steel parts for structural applications.

2.3. HSLA TO SS STEEL DISSIMILAR JOINING THROUGH WAAM

HSLA-AS bi-material steel offers significant advantages for engineering applications. While traditional cladding methods such as hot rolled bonding, friction welding, and explosive welding are effective manufacturing options for long and flat bi-metal products, they are limited in geometric flexibility. These limitations restrict design innovations that could potentially improve part performance, ease of assembly, and reliability [40]. WAAM offers a viable solution to overcome these limitations by enabling the production of custom geometries. This approach even allows for the fabrication of mechanically loaded components like propellers [41], integrated pressurized vessels [42], [43], and other intricate designs that are impractical or cost-prohibitive with alternative methods. As such, additive manufacturing (AM) opens new possibilities for designing high-performance components tailored to demanding engineering environments. However, a clear challenge is to establish adequate reliability levels on the mechanical performance of these

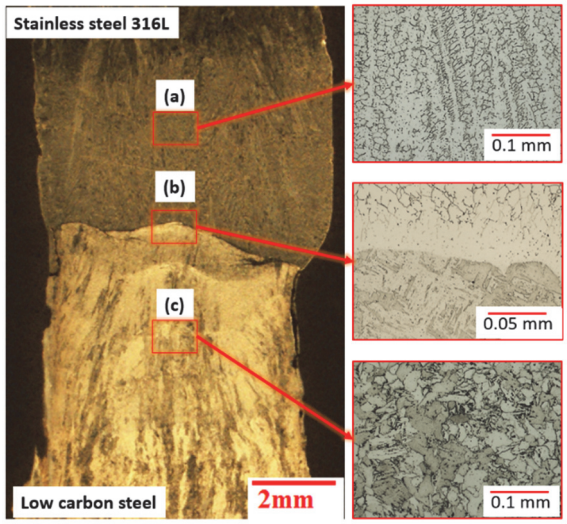

Figure 2-15 Low magnification and accompanying micrographs at (a) stainless steel 316L, (b) the interface, and (c) low carbon steel material volumes, as provided by [50] .

components, given the uncertainty derived from the diluted interface layer obtained through dissimilar fusion welding between the two alloys.

Previous work has given indications of the challenges related to combining these two alloys and their effect on the mechanical properties. Under arc-welding processes, the two materials will be diluted by each other in a single weld-pool. The degree of dilution will depend on the deposition parameters. However, the dilution of a chromium-rich austenitic stainless steel onto a ferritic steel consistently leads to the formation of martensite along the fusion line [44], or in the form of martensite islands [45], as predicted in the Schaeffler diagram. Mukherjee and Pal [46] showed that the amount of martensite formed and its effect on mechanical properties will depend on the local chemistry and heat input. Moreover, this alloy combination is susceptible to the formation of Type-II boundaries [47]. These Type-II boundaries are formed due to allotropic transformations at elevated temperatures, which lead to the formation of a compatible austenite phase between the dissimilar base metal and the weld metal. However, such boundaries can compromise mechanical strength [48] and may lead to cracking [49].

As a means of addressing the challenges associated with this dissimilar joint, heat treatment has yielded inconsistent outcomes. Ahsan et al. [50] reported important

increments in strength and ductility of bi-material specimens by heat-treating their WAAM coupon to 950 °C for one hour followed by quenching. Nonetheless, the authors contribute this increase in performance to the microstructural refinement obtained at the heat affected zone on the HSLA steel, not to refinement of the microstructure at the interface layer. Longer heat treatments lead to carbon migration from the low alloy steel to the austenite phase across the fusion line [44], [51], causing hardness spikes in the austenite alongside ferrite decarburization and softening. Hence, a defect-tolerant approach to the design of these bi-material components might be a necessary alternative to heat treatment.

2.4. FATIGUE AND FRACTURE OF FUNCTIONALLY-GRADED PARTS

Recent advances in additive manufacturing have enabled the production of functionally graded parts, including those composed by mechanically mismatched alloys. This has sparked interest in understanding their fatigue and fracture performance, especially where cracks may propagate across interfaces with significant differences in strength, ductility, or toughness [52], [53], [54], [55], [56]. Studies on bi-material joints and Functionally-graded materials (FGM's) have shown that crack-tip behaviour is profoundly influenced by the orientation and direction of crack propagation across dissimilar joints. Notably, retardation of fatigue crack growth rates and elevated fracture toughness are consistently observed when cracks propagate from a softer to a stronger region in terms of yield strength, due to shielding effects induced by plastic mismatch [57]. This has been demonstrated experimentally in copper-steel and stainless-steel-based FGM's, where the crack driving force at the interface was lower than in monolithic materials despite the presence of residual stresses [58].

Microstructure plays a defining role in dictating the crack path and resistance in FGM's. Anisotropy in grain orientation, phase distribution, and solidification structures strongly influence local crack growth behaviour [59]. For instance, in Laser Powder-Based Fusion (L-PBF)-produced Inconel 718 FGM's, vertically built specimens showed consistent fatigue crack growth rates, while horizontally built specimens exhibited a rising growth rate with increasing crack length; the difference is attributed to grain orientation and microstructural constitution at melt pool boundaries [56]. In dissimilar austenitic stainless steel welds, cracks tended to propagate along ferrite regions or deflect at ferrite-austenite boundaries, leading to tortuous paths that enhanced energy dissipation [60]. Moreover, functionally graded joints obtained through additive manufacturing often contain a complex mix of

columnar and equiaxed grains and heterogeneous microstructures, as obtained from the specific combination of material's, processing parameters and post-processing treatment [52], [53].

Key considerations when assessing fatigue and fracture in FGMs include not only the mechanical contrast between adjacent materials, but also the influence of residual stresses, porosity, and interface quality. Studies have shown that while residual stresses affect crack-tip constraint and driving force, their influence may be secondary to that of the elastic-plastic mismatch in determining crack deflection or arrest [58]. Nonetheless, they can exacerbate local yielding or promote early crack initiation in the presence of defects [59]. The formation of intermetallic phases or Laves phase precipitates, as seen in heat-treated 316L/IN718 AM parts, can lead to ductility-dip cracking and local embrittlement [52]. Additionally, crack closure mechanisms may also be relevant in AM components due to their intrinsic microstructural metastability [59] and heterogeneity [56].

Direct studies on the HSLA steel – AS steel material combination within the context of additive manufacturing are scarce. In terms of fatigue, Ayan et al. [26] showed that HSLA-AS bi-material parts maintain satisfactory performance under bending loads, with failure initiating in the HSLA volume. In terms of fracture, useful literature can be found on the dissimilar welded joint literature. Salem et al. [61] showed that the joint may display low toughness values after heat treatment, due to the carburization / decarburization phenomenon briefly introduced in the section 2.3. Yet, detailed studies on crack propagation in the context of additively-manufactured functionally-graded parts are lacking. This is a critical gap, as the deformation mechanisms active ahead of a propagating crack tip through a chemically and mechanically graded interface are likely distinct from those in either parent alloy.

Collectively, these findings highlight the importance of designing functionally graded AM parts with a comprehensive understanding of microstructure-property relationships. Beyond conventional property gradients, the orientation of layers, crack growth path, and interaction between phases at interfaces must be carefully considered in performance-critical applications.

2.5. CHAPTER SUMMARY AND CONCLUSIONS

Across this background discussion, the alloy families studied in this thesis are briefly introduced. Modern HSLA steel welding consumables typically rely on a combination of different microstructural constituents, designed to favour the formation of intergranular acicular ferrite. Microstructural and mechanical properties are discussed for this alloy family within the context of direct-energy deposition, demonstrably showing the material's high mechanical performance.

The discussion is then followed by a description of the microstructural development and mechanical properties of austenitic stainless steels. The factors driving the formation of this austenitic matrix were briefly presented, including the models used to predict the microstructural proportions obtained after solidification and cooling, such as the values Cr_{eq} and Ni_{eq},. These are used to build empirical models like the Schaeffler diagram, which provide a practical tool to predict the effect of alloy composition for the AS steel alloy family. Moreover, the concept of columnar grain formation across multiple layers during direct energy deposition is introduced, and the influence of texture on mechanical properties is discussed.

Finally, the combination of HSLA-AS steel for the purpose of bi-material functional grading is addressed. A few recent publications have dealt with this question, offering some insights into the macroscopic performance of this bi-material couple as well as complimenting these observations with microstructural observations and possible post-weld heat treatment routes. The documentation of the microstructural constitution at the diluted interface layer is however scarce, and the documentation of the mechanical performance at this specific region is up to this point not sufficient. This is especially important, as it is shown that the diluted region will likely deviate from the properties of the parent alloys, and will potentially have a significant impact in the quasi-static and fatigue performance of the overall part.

The development and processing of HSLA and AS steels via WAAM shows promising potential for producing high-performance components. Although some steps have been taken in the right direction, an understanding of the microstructural development at the interface of a bi-metal component and its mechanical performance is still pending. The success of such bi-metallic structures hinges on a deep understanding of solidification behaviour, phase evolution, and defect susceptibility, particularly at the dissimilar interface. This will also dictate the performance of the bi-material joint, as the mechanical

mismatch between both alloys further demands the production of a high quality interface, capable of overcoming the mechanical demands set by the conditions developed during additive manufacturing and throughout the part's lifetime. Chapters 3 through 5 bridge that gap by systematically investigating the microstructural development and mechanical performance of HSLA–ASS components produced via WAAM, with a specific emphasis on the diluted interface layer.

2.6. A NOTE ON CONVENTION: THE INTERFACE LAYER

Functional grading through additive manufacturing is a gigantic realm of opportunities, hence it is important to funnel down the scope into a specific subject of study. Through this thesis, functional grading is carried out by cladding layers of the austenitic steel alloy onto the underlaying, previously deposited high-strength low alloy steel. Changing the material composition from one layer to the next produces a special case of gradient, namely a maximal gradient step happening across a single layer. Chapter 3 focuses on the detailed description of this layer, which becomes an interface of distinct composition and properties, as it is shown throughout the length of this thesis.

The significance of this approach onto the broader realm of functional grading through additive manufacturing is discussed further in Chapter 6.

2.7. CHAPTER REFERENCES

[1] F. J. Winsor and W. Consultant, "Welding of Low-Alloy Steels," in *ASM Handbook 6 - Welding, Brazing and Soldering*, 2nd ed., vol. 6, Park, OH: ASM Inter, 1993, ch. Welding of, pp. 662–676. doi: 10.1361/asmhba000.

[2] G. Thewlis, "Classification and quantification of microstructures in steels," *Materials Science and Technology*, vol. 20, no. 2, pp. 143–160, Feb. 2004, doi: 10.1179/026708304225010325.

[3] S. S. Babu, "The mechanism of acicular ferrite in weld deposits," *Curr Opin Solid State Mater Sci*, vol. 8, no. 3–4, pp. 267–278, 2004.

[4] T. Zhang *et al.*, "Global progress on welding consumables for HSLA steel," 2014, *Iron and Steel Institute of Japan*. doi: 10.2355/isijinternational.54.1472.

[5] D. S. Sarma, K. A.V., and P. G. Jönsson, "On the role of non-metallic inclusions in the nucleation of acicular ferrite in steels," *ISIJ international*, vol. 49, no. 7, pp. 1063–1074, 2009.

[6] S. Gook, A. Gumenyuk, and M. Rethmeier, "Hybrid laser arc welding of X80 and X120 steel grade," *Science and technology of welding and joining*, vol. 19, no. 1, pp. 15–24, 2014.

[7] R. Alagesan and T. S. Kumar, "Optimization of welding cycle time by establishing full GMAW process (STT and P-GMAW) through a newly designed semi-automatic welding positioner," *Int J Res Eng Technol*, vol. 3, 2014.

[8] M. Rafieazad, M. Ghaffari, A. Vahedi Nemani, and A. Nasiri, "Microstructural evolution and mechanical properties of a low-carbon low-alloy steel produced by wire arc additive manufacturing," *The International Journal of Advanced Manufacturing Technology*, vol. 105, no. 5–6, pp. 2121–2134, Dec. 2019, doi: 10.1007/s00170-019-04393-8.

[9] B. D. DeRuntz, "Assessing the benefits of surface tension transfer welding to industry," *Journal of Industrial Technology*, vol. 19, no. 4, pp. 2–8, 2003.

[10] E. K. Stava, "The surface tension transfer power source, new, low spattering of metal in CO_2 welding with a short arc," *Welding Production*, pp. 26–27, 1980.

[11] P. A. Colegrove *et al.*, "Microstructure and residual stress improvement in wire and arc additively manufactured parts through high-pressure rolling," *J Mater Process Technol*, vol. 213, no. 10, pp. 1782–1791, 2013.

[12] A. S. Haselhuhn, B. Wijnen, G. C. Anzalone, P. G. Sanders, and J. M. Pearce, "In situ formation of substrate release mechanisms for gas metal arc weld metal 3-D printing," *J Mater Process Technol*, vol. 226, pp. 50–59, 2015.

[13] Y. Li and T. N. Baker, "Effect of morphology of martensite--austenite phase on fracture of weld heat affected zone in vanadium and niobium microalloyed steels," *Materials Science and Technology*, vol. 26, no. 9, pp. 1029–1040, 2010.

[14] X. Li, X. Ma, S. V Subramanian, C. Shang, and R. D. K. Misra, "Influence of prior austenite grain size on martensite--austenite constituent and toughness in the heat affected zone of 700 MPa high strength linepipe steel," *Materials Science and Engineering: A*, vol. 616, pp. 141–147, 2014.

[15] N. Sridharan, M. Gussev, and S. Babu, "Tailoring plasticity mechanisms in compositionally graded hierarchical steels fabricated using additive manufacturing," *Sci Rep*, vol. 11, no. 1, pp. 1–9, 2021, doi: 10.1038/s41598-021-98205-3.

[16] S. Suryakumar, K. P. Karunakaran, U. Chandrasekhar, and M. A. Somashekara, "A study of the mechanical properties of objects built through weld-deposition," *Proc Inst Mech Eng B J Eng Manuf*, vol. 227, no. 8, pp. 1138–1147, 2013.

[17] C. V. Haden, G. Zeng, F. M. Carter, C. Ruhl, B. A. Krick, and D. G. Harlow, "Wire and arc additive manufactured steel: Tensile and wear properties," *Addit Manuf*, vol. 16, pp. 115–123, 2017, doi: 10.1016/j.addma.2017.05.010.

[18] B. E. Carroll, T. A. Palmer, and A. M. Beese, "Anisotropic tensile behavior of Ti--6Al--4V components fabricated with directed energy deposition additive manufacturing," *Acta Mater*, vol. 87, pp. 309–320, 2015.

[19] L. Thijs, M. L. M. Sistiaga, R. Wauthle, Q. Xie, J.-P. Kruth, and J. Van Humbeeck, "Strong morphological and crystallographic texture and resulting yield strength anisotropy in selective laser melted tantalum," *Acta Mater*, vol. 61, no. 12, pp. 4657–4668, 2013.

[20] Q. Zhang, J. Chen, Z. Zhao, H. Tan, X. Lin, and W. Huang, "Microstructure and anisotropic tensile behavior of laser additive manufactured TC21 titanium alloy," *Materials Science and Engineering: A*, vol. 673, pp. 204–212, 2016.

[21] J. C. Lippold and D. J. Kotecki, *Welding Metallurgy and Weldability of Stainless Steels*, 1st ed. John Wiley & Sons, 2005.

[22] X. Zhang *et al.*, "Study on microstructure and tensile properties of high nitrogen Cr-Mn steel processed by CMT wire and arc additive manufacturing," *Mater Des*, vol. 166, p. 107611, Mar. 2019, doi: 10.1016/j.matdes.2019.107611.

[23] X. Chen, J. Li, X. Cheng, B. He, H. Wang, and Z. Huang, "Microstructure and mechanical properties of the austenitic stainless steel 316L fabricated by gas metal arc additive manufacturing," *Materials Science and Engineering A*, vol. 703, no. January, pp. 567–577, 2017, doi: 10.1016/j.msea.2017.05.024.

[24] C. Wang, T. G. Liu, P. Zhu, Y. H. Lu, and T. Shoji, "Study on microstructure and tensile properties of 316L stainless steel fabricated by CMT wire and arc additive manufacturing," *Materials Science and Engineering A*, vol. 796, no. June, 2020, doi: 10.1016/j.msea.2020.140006.

[25] S. Selvi, A. Vishvaksenan, and E. Rajasekar, "Cold metal transfer (CMT) technology - An overview," *Defence Technology*, vol. 14, no. 1, pp. 28–44, 2018, doi: 10.1016/j.dt.2017.08.002.

[26] Q. Wang *et al.*, "Microstructure evolution and EBSD analysis of a graded steel fabricated by laser additive manufacturing," *Vacuum*, vol. 141, pp. 68–81, 2017, doi: 10.1016/j.vacuum.2017.03.021.

[27] L. Wang, J. Xue, and Q. Wang, "Correlation between arc mode, microstructure, and mechanical properties during wire arc additive manufacturing of 316L stainless steel," *Materials Science and Engineering A*, vol. 751, no. February, pp. 183–190, 2019, doi: 10.1016/j.msea.2019.02.078.

[28] W. Hofmeister, M. Griffith, M. Ensz, and J. Smugeresky, "Solidification in direct metal deposition by LENS processing," *Jom*, vol. 53, no. 9, pp. 30–34, 2001, doi: 10.1007/s11837-001-0066-z.

[29] N. Rodriguez, L. Vázquez, I. Huarte, E. Arruti, I. Tabernero, and P. Alvarez, "Wire and arc additive manufacturing: a comparison between CMT and TopTIG processes applied to stainless steel," *Welding in the World*, vol. 62, no. 5, pp. 1083–1096, 2018, doi: 10.1007/s40194-018-0606-6.

[30] W. Wu, J. Xue, L. Wang, Z. Zhang, Y. Hu, and C. Dong, "Forming process, microstructure, and mechanical properties of thin-walled 316L stainless steel using speed-cold-welding additive manufacturing," *Metals (Basel)*, vol. 9, no. 1, 2019, doi: 10.3390/met9010109.

[31] I. Tabernero, A. Paskual, P. Álvarez, and A. Suárez, "Study on Arc Welding Processes for High Deposition Rate Additive Manufacturing," *Procedia CIRP*, vol. 68, no. April, pp. 358–362, 2018, doi: 10.1016/j.procir.2017.12.095.

[32] J. L. Prado-Cerqueira *et al.*, "Analysis of favorable process conditions for the manufacturing of thin-wall pieces of mild steel obtained by wire and arc additive manufacturing (WAAM)," *Materials*, vol. 11, no. 8, 2018, doi: 10.3390/ma11081449.

[33] V. Laghi, M. Palermo, L. Tonelli, G. Gasparini, L. Ceschini, and T. Trombetti, "Tensile properties and microstructural features of 304L austenitic stainless steel produced by wire-and-arc additive manufacturing," *The International Journal of Advanced Manufacturing Technology*, vol. 106, no. 9–10, pp. 3693–3705, Feb. 2020, doi: 10.1007/s00170-019-04868-8.

[34] H. J. Bunge, R. Kiewel, T. Reinert, and L. Fritsche, "Elastic properties of polycrystals—influence of texture and stereology," *J Mech Phys Solids*, vol. 48, no. 1, pp. 29–66, Jan. 2000, doi: 10.1016/S0022-5096(99)00020-4.

[35] H. B. Huntington, "The Elastic Constants of Crystals," 1958, pp. 213–351. doi: 10.1016/S0081-1947(08)60553-6.

[36] Mason Hayward, "Ultrasonic Characterization of Elastic Properties of Additively Manufactured 316L Stainless Steel," University of Louisiana at Lafayette, Lafayette, 2024.

[37] H. M. Ledbetter, "Monocrystal-Polycrystal Elastic Constants of a Stainless Steel," *Physica Status Solidi (a)*, vol. 85, no. 1, pp. 89–96, Sep. 1984, doi: 10.1002/pssa.2210850111.

[38] Y. Li and R. B. Thompson, "Relations between elastic constants Cij and texture parameters for hexagonal materials," *J Appl Phys*, vol. 67, no. 5, pp. 2663–2665, Mar. 1990, doi: 10.1063/1.345479.

[39] J. Ge, J. Lin, H. Fu, Y. Lei, and R. Xiao, "A spatial periodicity of microstructural evolution and anti-indentation properties of wire-arc additive manufacturing 2Cr13 thin-wall part," *Mater Des*, vol. 160, no. 100, pp. 218–228, 2018, doi: 10.1016/j.matdes.2018.09.021.

[40] D. Frey, J. Palladino, J. Sullivan, and M. Atherton, "Part count and design of robust systems," *Systems Engineering*, vol. 10, no. 3, pp. 203–221, Sep. 2007, doi: 10.1002/sys.20071.

[41] A. Taşdemir and S. Nohut, "An overview of wire arc additive manufacturing (WAAM) in shipbuilding industry," 2020, *Taylor and Francis Ltd.* doi: 10.1080/17445302.2020.1786232.

[42] K. Lipiäinen *et al.*, "Manufacturing and mechanical performance of a large-scale stainless steel vessel fabricated by wire-arc direct energy deposition," *Mater Des*, vol. 243, no. May, 2024, doi: 10.1016/j.matdes.2024.113044.

[43] J. G. Rafferty, D. Gill, and R. Kapur, "Disrupting the Metallics Domain in Pressure Vessel and Piping Manufacture-Advanced Manufacturing in the Oil and Gas Sector," in *Volume 5: High-Pressure Technology; ASME Nondestructive Evaluation, Diagnosis and Prognosis Division (NDPD); SPC Track for Senate*, American Society of Mechanical Engineers, Jul. 2017, pp. 1–7. doi: 10.1115/PVP2017-65840.

[44] J. N. DuPont and C. S. Kusko, "Technical note: Martensite formation in austenitic/ferritic dissimilar alloy welds," *Welding Journal (Miami, Fla)*, vol. 86, no. 2, 2007.

[45] Z. H. Wang, B. Y. Xu, and C. Q. Ye, "Study of the Martensite Structure at the Weld Interface and the Fracture-Toughness of Dissimilar Metal Joints," *Weld J*, vol. 72, no. 8, pp. S397–S402, 1993.

[46] M. Mukherjee and T. K. Pal, "Influence of Heat Input on Martensite Formation and Impact Property of Ferritic-Austenitic Dissimilar Weld Metals," *J Mater Sci Technol*, vol. 28, no. 4, pp. 343–352, 2012, doi: 10.1016/S1005-0302(12)60066-8.

[47] T. W. Nelson, J. C. Lippold, and M. J. Mills, "Investigation of boundaries and structures in dissimilar metal welds," *Science and Technology of Welding and Joining*, vol. 3, no. 5, pp. 249–255, 1998, doi: 10.1179/stw.1998.3.5.249.

[48] Q. Wang *et al.*, "Study of type-II boundary behavior during SA508-3/EQ309L overlay weld interfacial failure process," *J Mater Process Technol*, vol. 247, no. December 2016, pp. 64–72, 2017, doi: 10.1016/j.jmatprotec.2017.04.009.

[49] T. W. Nelson, J. C. Lippold, and M. J. Mills, "Nature and evolution of the fusion boundary in ferritic-austenitic dissimilar metal welds - Part 2: on-cooling transformations," *Welding Journal (Miami, Fla)*, vol. 79, no. 10, 2000.

[50] M. R. U. Ahsan *et al.*, "Heat-treatment effects on a bimetallic additively-manufactured structure (BAMS) of the low-carbon steel and austenitic-stainless steel," *Addit Manuf*, vol. 32, pp. 1–25, 2020, doi: 10.1016/j.addma.2020.101036.

[51] G. Ben Salem, S. Chapuliot, A. Blouin, P. Bompard, and C. Jacquemoud, "Brittle fracture analysis of Dissimilar Metal Welds between low-alloy steel and stainless steel at low temperatures," *Procedia Structural Integrity*, vol. 13, pp. 619–624, 2018, doi: 10.1016/j.prostr.2018.12.102.

[52] M. S. Duval-Chaneac *et al.*, "Fatigue crack growth in IN718/316L multi-materials layered structures fabricated by laser powder bed fusion," *Int J Fatigue*, vol. 152, Nov. 2021, doi: 10.1016/j.ijfatigue.2021.106454.

[53] M. S. Duval-Chaneac *et al.*, "Effect of heat treatment on fatigue crack growth in IN718/316L multiple-materials layered structures fabricated by laser powder bed fusion," *Int J Fatigue*, vol. 160, Jul. 2022, doi: 10.1016/j.ijfatigue.2022.106852.

[54] Y. Ayan and N. Kahraman, "Fabrication and characterization of functionally graded material (FGM) structure containing two dissimilar steels (ER70S-6 and 308LSi) by wire arc additive manufacturing (WAAM)," *Mater Today Commun*, vol. 33, no. September, p. 104457, 2022, doi: 10.1016/j.mtcomm.2022.104457.

[55] Y. Ayan and N. Kahraman, "Fabrication and Fatigue Properties of Dissimilar Steel Functionally Graded Material Structure Through Wire Arc Additive Manufacturing," *J Mater Eng Perform*, vol. 32, no. 24, pp. 11285–11295, 2023, doi: 10.1007/s11665-023-07914-5.

[56] S. Ghorbanpour *et al.*, "Effect of microstructure induced anisotropy on fatigue behaviour of functionally graded Inconel 718 fabricated by additive manufacturing," *Mater Charact*, vol. 179, no. July, p. 111350, 2021, doi: 10.1016/j.matchar.2021.111350.

[57] J. D. Pribe, T. Siegmund, and J. J. Kruzic, "The roles of yield strength mismatch, interface strength, and plastic strain gradients in fatigue crack growth across interfaces," *Eng Fract Mech*, vol. 235, Aug. 2020, doi: 10.1016/j.engfracmech.2020.107072.

[58] M. Velu and S. Bhat, "Experimental investigations of fracture and fatigue crack growth of copper-steel joints arc welded using nickel-base filler," *Mater Des*, vol. 67, pp. 244–260, Feb. 2015, doi: 10.1016/j.matdes.2014.11.026.

[59] U. Zerbst *et al.*, "Review on fracture and crack propagation in weldments - A fracture mechanics perspective," *Eng Fract Mech*, vol. 132, pp. 200–276, Dec. 2014, doi: 10.1016/j.engfracmech.2014.05.012.

[60] Y. B. Shang, H. J. Shi, Z. X. Wang, and G. D. Zhang, "In-situ SEM study of short fatigue crack propagation behavior in a dissimilar metal welded joint of nuclear power plant," *Mater Des*, vol. 88, pp. 598–609, Dec. 2015, doi: 10.1016/j.matdes.2015.08.090.

[61] G. Ben Salem, S. Chapuliot, A. Blouin, P. Bompard, and C. Jacquemoud, "Brittle fracture analysis of Dissimilar Metal Welds between low-alloy steel and stainless steel at low temperatures," *Procedia Structural Integrity*, vol. 13, pp. 619–624, 2018, doi: 10.1016/j.prostr.2018.12.102.

3. MICROSTRUCTURAL CHARACTERIZATION OF A BI-METAL INTERFACE

This study examines the interface layer between a high-strength low-alloy steel and an overlaying austenitic stainless steel as deposited through Wire Arc Additive Manufacturing in a bi-metal block. By utilizing optical and electron microscopy techniques, and accompanied by phenomenological and thermodynamic modeling, the work elucidates on the nature of the distinct microstructural features at a new level of detail. Results showcase martensite in the form of a band along the fusion line of the first dissimilar layer, as well as in segregated islands. Within the same bead, yet away from the fusion line, an austenite matrix is identified alongside a large phase fraction of primary ferrite and sparse bainite. These findings enhance our understanding of the nature of the heterogeneous microstructure at the interface of a bi-metal build and establish empirical evidence for future modeling of microstructural development. Supplementary characterization reveals the impact of these microstructural heterogeneities on bulk mechanical performance. Hardness indents exhibit varied results along the interface, peaking at martensite islands with values up to 370$HV_{0.2}$, surpassing the neighboring matrix by 50%. Under quasi-static tensile loading, bi-metallic specimens display strain partitioning across the dissimilar fusion line, as confirmed by Digital Image Correlation. The additional work-hardening capacity at the interface leads to necking and failure away from this region. These results help predict the structural performance of bi-metal parts, and build a base for further research in more intricate loading scenarios, such as crack propagation processes.

This chapter is an adaptation from the publication Galán Argumedo, J. L., Mahmoudiniya, M., Reinton, T. E., Kestens, L. A. I., Hermans, M. J. M., & Popovich, V. A. (2024). Functional grading of low alloy steel to 316 L by wire arc additive manufacturing – Microstructural and mechanical characterization of bi-metal interface. *Journal of Materials Processing Technology*, *325*, 118305. https://doi.org/10.1016/j.jmatprotec.2024.118305

3.1. INTRODUCTION

The overall quality of the functionally graded bi-metal component will depend in large on the performance of the graded interface. This imposes an important problem when considering alloys that are dissimilar in nature. Problems such as solidification cracking are commonplace, as presented by Sridar et al. [1] in the context of Inconel cladding on pipe steel. Certain material combinations are susceptible to liquid-metal embrittlement, as shown by Wang et al. [2] in the context of combining bronze and steel. A final example is offered in the context of copper and titanium dissimilar welding resulting on unwanted intermetallic CuTi phases [3]. Solutions to these problems might be as straightforward as the selection of adequate deposition parameters, or as intricate as requiring transition material, such as buttering layers. Nonetheless, available knowledge drawn from welding literature [4] shows that a defect-free joint between low-alloy steels and austenitic stainless steels is within reach, with the caveat of an often-occurring martensite phase fraction forming at the bi-metal fusion boundary. For carbon steels, post-weld heat treatment may lead to decarburization of the low alloy steel immediately adjacent to the dissimilar fusion line, leading to a detrimental effect on mechanical properties in this region [5].

Recent attempts for HSLA-AS steel combinations have been carried out within the context of WAAM. Alloys ER70S-6 (HSLA steel) and ER316L (AS steel) are good candidates for arc-based additive manufacturing due to their excellent weldability and availability. In the context of single bead walls, [6] studied the effects of dissimilar deposition of these two alloys and the microstructural development at the bi-metal fusion boundary. They found a defect-free interface populated by what is reported to be acicular ferrite, although this finding is only supported by observations done through optical microscopy. The interface is nonetheless found to respond adequately to transverse tensile testing. Further studies by the same authors [7] demonstrate that a post-process heat treatment can yield additional deformation capacity at the interface region, as well as strength enhancement. Additional work by Rani et al. [8] shows similarly a defect-free interface, elucidating the differences in residual stress development for their single-bead geometry. The literature so far gives an indication of the microstructural constitution and bulk behavior of the bi-material interface layer. However, the indication of acicular ferrite is non-trivial, as the mixed chemistry is distinct from that of the surrounding material. This observation thus requires further support through detailed characterization of the microstructural

constitution at the interface, including composition as well as phase morphology and distribution.

By committing to understand the microstructural constitution of the interface layer, the question of the geometry of the part becomes relevant. The geometry of the deposited coupon significantly influences heat dissipation during the deposition of the bi-metal part. With increasing material volume, the size of the mass acting as a heat sink grows, impacting the cooling rate. Significant evidence on the differences between multi-bead and single-bead depositions appears to lay in the microstructural development of the bi-metal interface, as observed through the presence of martensite along the fusion line. [9] attribute the martensite layer to limited liquid diffusion and negligible convection, resulting in a boundary region favoring martensite transformation. As substrate temperature increases, this boundary region expands, leading to a larger martensite band. [7] demonstrate a clear dilution effect in single-bead WAAM, with an interface region of high hardness ranging from 300 HV to 350 HV, linked to higher Cr concentrations. Despite using lower arc power, their conditions, including high inter-pass temperature and low heat extraction capacity, foster prolonged solidification, aiding dilution, and forming a large martensite volume. Considering the apparent effect of heat accumulation in the bi-metal interface, it is concluded that depositing a thick section is advantageous for enhanced microstructural control in the bi-metal product. This higher heat extraction capacity should lead to a limited martensite phase fraction at the dissimilar fusion boundary.

Thus, the scientific gap addressed throughout this work is the need for in-depth characterization of the ferritic phases in the diluted interface layer that may lead to a mechanistic understanding of the microstructural development in the interface layer. This research gap is addressed with the methods described in the following section, encompassing the deposition of a thick-section bi-metal HSLA-AS steel structure by WAAM, and the in-depth characterization of the interface layer through thermodynamic modelling, optical and electron microscopy. A detailed characterization of the phases formed in the dissimilar interface is carried out, including a crystallographic analysis and transmission electron microscopy. This is done to understand the mechanisms controlling the microstructural development of the phases observed and their nature. Microstructural characterization is lastly complemented with mechanical testing, to provide a connection between the results obtained and the mechanical performance of the bi-metal part.

3.2. MATERIALS AND METHODS

3.2.1. Wire Arc Additive Manufacturing

The consumables selected for deposition are proprietary to the Voestalpine Boehler 3Dprint welding consumables brand [10], [11]. The nominal compositions of both electrodes as stated by the manufacturer are shown in Table 3-1, and the properties at room temperature are shown in

Table 3-2 3-2. These comply with the commercial specifications AWS A5.9 [12] ER316L and AWS A5.18 [13] ER70S-6. In both cases, a 1.2 mm diameter wire was used. The additive manufacturing process was carried out with a Fanuc M710iC/12L series robot. The Cold Metal Transfer (CMT)-capable power source, wire feeder, controller and cooling unit area are proprietary Fronius systems.

Table 3-1 Chemical composition of wire materials as stated by manufacturer, in wt%

	C	**Si**	**Mn**	**Cr**	**Ni**	**Mo**	**N**	**Fe**
3Dprint AM 46 (HSLA steel)	0.1	1.00	1.7	-	-	-	-	Bal.
3Dprint AM 316L (AS steel)	0.015	0.45	1.6	18.5	12.0	2.6	0.04	Bal.

Table 3-2 Average physical properties at room temperature of as-deposited all-weld metal per material used [10], [11]. All values obtained from the manufacturer of the wire consumables except where references are indicated.

	Elastic Modulus E [GPa]	**Min. Yield Strength σ_y [MPa]**	**Min. Tensile Strength σ_u [MPa]**	**Min. Elongation Δ/L0 [%]**	**Coefficient Thermal Expansion α [m/m/°C]**
3Dprint AM 46 (HSLA steel)	209-221 [14]	480	580	24	13.6 E-6 [15]
3Dprint AM 316L (AS steel)	112-139 [16]	≥320	≥510	≥25	16.6 E-6 [17]

A DL750 Yokogawa ScopeCorder was used to record the CMT current and voltage at a sampling frequency of 2 kHz; the consumable 3D print AM 316L was deposited using the Fronius CMT929+P(V1.0.0.5.4) welding program, corresponding to a CMT+Pulsed deposition mode; 3D print AM 46 was deposited with a typical CMT arc mode corresponding to the Fronius CMT963(V2.3.5.2) welding program. In all cases, the welding position was perpendicular to the work piece (PA welding position). Table 3-3 shows the summary of deposition parameters, including target voltage (U) and current (I) set on the Fronius user interface, wire feed speed (WFS), travel speed (TS), contact-tip-to-workpiece distance (CTWD) and estimated heat input (HI). Heat input is evaluated as the average value over the length of any given deposited bead utilizing the specification mentioned in the ISO/TR 18491 [18] technical report and corrected by the estimated efficiency:

$$HI = \eta \cdot \frac{U(t) \cdot I(t)}{TS} \qquad (Eq. 3.1)$$

where HI is the instantaneous heat input [J/mm], η is the process efficiency [-], U(t) is the measured instantaneous potential [V], and I(t) is the instantaneous measured current [A]. Process efficiency is assumed to be 80% [19] for simplification. To shield the AS steel deposit, a mixture of Ar35He2CO_2 was used for the austenitic stainless steel, whilst for the high-strength low-alloy steel Ar20He12CO_2 was selected. In both cases, a gas flow was set of 15 L/min.

Table 3-3 Wire Feed Speed (WFS), Travel Speed (TS) Contact Tip Working Distance (CTWD) Heat Input (HI), and Interpass Temperature (Int. Temp.) deposition parameters for the different wire consumables used.

	target U	**target I**	**WFS**	**TS**	**CTWD**	**HI**	**Int. Temp.**
	V	A	m/min	mm/s	mm	kJ/mm	°C
3Dprint AM 46 (HSLA steel)	21.1	143	7.5	10	17	0.27	50-120
3Dprint AM 316L (AS steel)	13.2	214	5.0	10	17	0.22	<140

The substrate used for welding is a commercial S690QT high-strength steel. The net shape of the coupon to be characterized is a block of 205 mm x 127 mm x 91 mm, as shown in Figure 3-1. The first 54 mm height consists of 16 layers of 3D print AM 46. In this case, each layer consisted of 33 beads of 205 mm length and approximately 3.5 mm height. For each layer, all beads were deposited in the same direction with a 25% bead width overlap, and in the opposite orientation for the subsequent layer, as it is schematically represented in the figure. Since the start/stop regions tend to bulk-up for the given welding parameters, after the HSLA steel layers were deposited, the top beads were machined flat to begin welding the subsequent 37 mm block height of 3D print AM316L material. The effect of this procedure on microstructural development is included in the discussion. The latter layers were completed with 26 beads per layer and 16 layers in total, averaging a total height per layer of about 2 mm.

3.2.2. Microstructural Characterization

Several techniques were used to characterize the microstructural properties of the interface region for later correlation with the mechanical properties. For Optical Microscopy, Scanning Electron Microscopy (SEM), Electron Back Scatter Diffraction (EBSD) and Transmission Electron Microscopy (TEM), specimens were extracted from the center of the block, as it is schematically represented on Figure 3-1. To extract the specimens, the block was sectioned, mounted in conductive resin (with exception of TEM specimens), ground with SiC paper grits #80 through #2000, and finally polished with 3 μm and 1 μm diamond suspensions. EBSD specimens where further polished with colloidal silica suspension (OP-S) for a minimum of 45 minutes. Etching was done with 5% Nital to reveal microstructural features within the HSLA steel portion of each specimen; Kalling's No. 2 etchant was used to visualize interdendritic ferrite, carbides, and oxides on the AS steel portion. For specimens containing the interface and the material close to its proximity, etching was carried out only for macrographic inspection following the sequence of Nital and then Kalling's No 2. This was nevertheless avoided for further microstructural characterization due to galvanic effects between both materials, leading in every case to poor delimitation of microstructural features, and partial etching at best.

Optical microscopy was carried out using a Keyence VHX-600 microscope under epi illumination. Scanning Electron Microscopy was carried out with a JEOL JSM-6500F Field-Emission Gun Scanning Electron Microscope at an accelerating voltage of 10 kV. Backscatter Electron Imaging was used complementarily with a Deben 5th generation 4

quadrant detector. EBSD mapping was made by a FEI® SEM-Quanta FEG 450 SEM with integrated EBSD detector. EBSD scans were carried out at a 70° tilt, 20 kV accelerating voltage. A varying step size between 70 nm for fine detail and up to 3 μm for multi-bead scans was necessary to overcome the differences in dimensional scale between features. In every case, step size is specified in each image caption, and step sizes are kept constant within the extent of each map. EBSD measurements were post-processed with EDAX-OIM Analysis™ software ver. 8.6. Stitching of large maps was performed with the aid of physical indentation marks on the specimen's surface and the stitching tools available in the mentioned software. With exception of texture analysis, a clean-up procedure consisting of a level 5 Neighbour Orientation Correlation was used with a grain tolerance angle of 5°, restricted to clean-up points with a confidence index lower than 0.1 and a minimum grain size of 4 points. Texture analysis was done by constructing the Orientation Distribution Function (ODF) through Harmonic Series Expansion with a Series Rank (L) equal to 16 and a Gaussian Half-Width of 5°. No symmetry (triclinic) was assumed. Parent Austenite Grain (PAG) reconstruction maps were carried out assuming a Nishiyama-Wasserman $\{111\}_{fcc}||\{110\}_{bcc}$ and $<11\text{-}2>_{fcc}||<110>_{bcc}$ orientation relationship, given the well-established fcc to bcc transformation path [20]. For the latter analysis, an iterative orientation relationship refinement was performed, for which a tolerance angle of 5 deg. was deemed acceptable. Slight differences were observed from maps reconstructed based on Bain, Kurdjumov-Sachs and Greninger-Troiano orientation relationships; these differences are discussed briefly in the discussion section 3.3.3.

Electron Probe Microanalysis (EPMA) measurements were performed with a JEOL JXA 8900R microprobe using an electron beam with energy of 10 keV and beam current of 100 nA employing Wavelength Dispersive Spectrometry. The composition at each analysis location of the specimen was determined using the X-ray intensities of the constituent elements after background correction relative to the corresponding intensities of reference materials. The obtained intensity ratios were processed with a matrix correction program CITZAF.

Additional care was taken to prepare specimens for Transmission Electron Microscopy (TEM) characterization. Specimens of approximately 1 mm thickness were extracted with a cooled diamond cutter, and further mechanically polished to about 40 μm thickness. Disks of 2.3 mm diameter were punched out of the specimens at the bi-material interface region, glued on a 3 mm copper ring, and ion milled to electron transparency at their center. A cubed C_s image-corrected FEI Titan was used for analysis. Elemental mapping

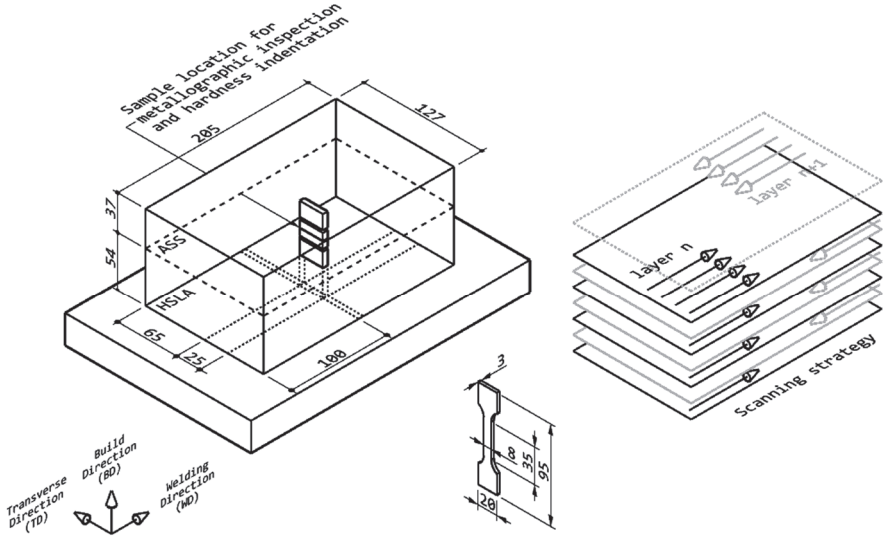

Figure 3-1 Deposition strategy and dimensions of bi-material block, conventions on orientations and dimensions of tensile specimens. Specimen location for microstructural characterization and microhardness is indicated.

in STEM mode was done using the super-X in the ChemiSTEM ™ configuration. HREM Lattice images were collected on a Thermo Scientic Ceta ™ 16M.

3.2.3. Mechanical Characterization

Hardness indentations were used to obtain a measure of the local variation in mechanical properties at the interface. Vickers Hardness was measured with a load of 200 grams-force and a center-to-center distance between indents and free edges of 500 μm, in agreement with minimum distance specifications by ASTM standard E92-17 [21]. Indentation contact was performed at a speed of 0.07 mm/s and dwell time was kept at 14 s. The indentations were performed along the build direction on the specimens used for optical microscopy.

Additionally, Digital Image Correlation (DIC) was carrier out on flat coupons loaded under quasistatic tensile testing. Six tensile specimens were extracted with the dimensions shown in Figure 3-1. To extract the specimens, the block was sawn and the resulting slices where machined flat; water jet cutting was used to extract the final dog-bone geometry. The specimens are oriented along the build direction, across the interface layer. Single-material specimens were extracted also for the HSLA steel and AS steel deposits for a

comparative benchmark. During testing, a relative deformation rate of 0.005 s^{-1} was applied to the specimens at ambient temperature and humidity. The universal testing rig was controlled by crosshead displacement. Indications for zero-point setting, gripping and post-mortem calculations are done according to the ISO standard EN-ISO 6892-1:2019 [22]. Complementary to the strain calculations, DIC was used to obtain local strain measurements in the region surrounding the bi-metal interface. The DIC system is a commercial LIMESS Q400-3D stereo camera set-up fitted with a 40 mm focal length and operating at an acquisition rate of 0.5 Hz. Speckle pattern used on the specimens was achieved with aerosol paint. The images were post-processed using LIMESS ISTRA 4D software, with which local engineering strain was estimated by a virtual gauge line of approximately 2.5 mm.

3.2.4. CALPHAD Simulations

Thermodynamic simulations were performed with ThermoCalc2023a. The database used for the prediction of thermodynamically stable phases included v.12. of the Steels / Fe Alloys. However, Continuous Cooling Transformation (CCT) diagrams and Scheil calculations require additional mobility data. In such cases, the v.7.0. of the Mobility database for Steel and Ferrous Alloys was used. Phases considered for CCT diagrams construction include Liquid, Ferrite, Bainite, Pearlite and Martensite. Lastly, Scheil solidification calculations were performed with the classical mode, considering carbon as a fast diffuser.

3.3. RESULTS AND DISCUSSION

The results and discussion section are divided in six distinct sub-sections to guide the reader through the intricacies of a highly heterogeneous interface layer. The description of microstructural features starts with an overview based on the observations under optical microscopy, chemical analysis, and thermodynamic modelling. As it is discussed throughout the length of these sections, the distinction of certain features is only achievable through additional supporting methods. The discussion is thus complemented by an in-depth characterization through electron microscopy-based methods. A correlation is finally established between the features observed and the performance of the interface through hardness mapping and quasi-static tensile testing.

3.3.1. Macroscopic inspection

Figure 3-2 shows the macroscopic features of the interface layer, also understood as the material volume of the first AS steel layer. This distinction is made from the rest of the block due to its unique microstructural features. The image is taken from a section plane normal to the welding direction. Starting with the overall geometry of the beads deposited, the distance between the two weld roots shown of the austenitic stainless steel is 5 mm. The thickness of the interface layer varies between 1.1 mm on the narrowest section and extends up to 2.2 mm, as measured between subsequent fusion lines identified through etching. Above and below the interface layer, typical microstructural features are found when considering the nature of the materials being used. In a region above the interface layer, Figure 3-2b highlights the features typically found within an austenitic stainless steel weld deposit. The dark-etched regions show the interdendritic ferrite. As it has been reported in previous studies [23], the material's tendency to form large columnar grains is made evident through the parallel orientation of the primary dendrites. Opposingly, on a region below the interface layer, the HSLA steel layer 16 displays a fine microstructure of acicular ferrite surrounded by grain boundary ferrite, as it is highlighted on Figure 3-2f. The approximate shape and size of the Parent Austenite Grains are distinguishable through the light tonal differences, characterized by their columnar nature oriented towards each respective weld-pool center. The HSLA steel material in the immediate vicinity of the fusion line shows microstructural features typical for the Heat Affected Zone (HAZ), and are exemplified on the lower half of Figure 3-2e. At this location, the individual Parent Austenite Grains are indistinguishable from each other. The region displays a mixture between allotriomorphic ferrite and smaller laths of acicular ferrite.

Although the bulk of the material deposited matches the microstructural development documented in previous studies [6], [7], the interface layer distinguishes itself by its different microstructural development. The material belonging to the interface layer immediately adjacent to the fusion line appears un-etched on Figure 3-2e. This effect is most likely originating from the nature of the etching process, where the low-alloy steel was preferentially attacked. Nonetheless, an area containing mostly martensite is observed. It is distinguished through mild etching of some of the martensitic lath packages.

The most distinct microstructural features are found in the middle of the interface beads, as they are shown in Figure 3-2d. The selected etchant darkens alternating bands

of a second acicular phase, undistinguishable at this magnification. These features are clustered as columnar cells and engulfed by an un-etched austenitic matrix. A detailed study of these features is presented in section 3.3.3. Figure 3-2 (c) shows the sharp boundary between the interface layer (first AS steel layer) and the second AS steel layer. The dark-etching features are discontinued abruptly and replaced by typical interdendritic ferrite. These dendrites suggest a parallel orientation relationship between the grains formed on the second AS steel layer and the underlying mixed layer. The features observed in the second AS steel layer are typical for additively manufactured AS steel 316L, suggesting a depreciable level of mixing for this and all layers above. This observation is further confirmed by EPMA measurements and shown in Figure 3-3.

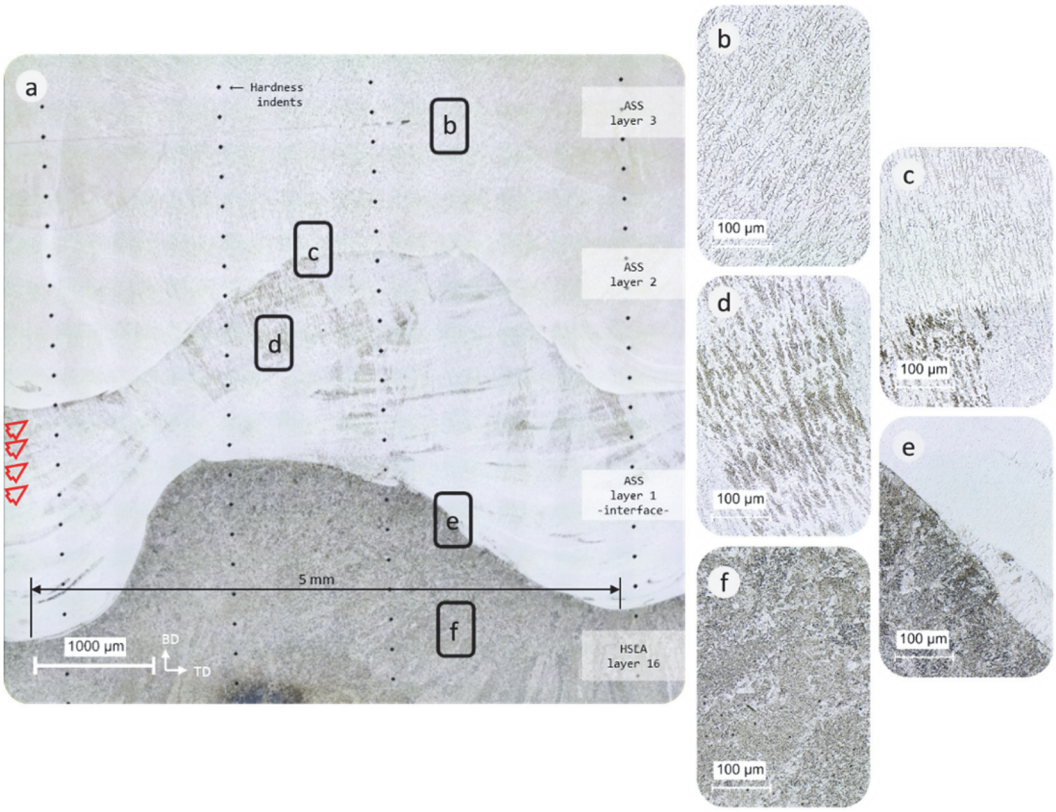

Figure 3-2 (a) The 16th HSLA steel layer, and layers 1 through 3 of AS steel, obtained with Kalling's No. 2 etchant as observed under optical microscopy including locations of hardness indents. Arrows indicate a few examples of bands formed by high amounts of ferrite. Locations of representative features under higher magnification are shown for (b) AS steel matrix, (c) boundary between AS steel layer 1 and 2, (d) ferritic phases within the interface layer, (e) fusion line between AS steel layer 1 and HSLA steel layer 16, and (f) HSLA steel matrix.

The unique features of the interface layer are not typical for the microstructural development of either material used. The approach to understand their distinct origin is taken through the investigation of the material's chemistry. Figure 3-3 shows the chemical profile as obtained through EPMA analysis. There are not only evident differences in composition between the interface layer and its surroundings, but also local differences between individual features within each layer. The region left of point 1 represents the last layer of HSLA steel. Point 1 indicates the austenite matrix immediately above the fusion line, about 50 µm into the interface layer. It shows the location with highest alloying of the bead, where Cr reaches a maximum value of 18.5 wt% and Ni 12.5 wt%. By contrast, point 2 gives an indication of the chemical composition of a martensite island close to the fusion boundary. At this location, a clear depletion of the major alloying components is observed, displaying Cr values as low as 7.9 wt% and Ni down to 4.9 wt%. Points 3 through 7 show locations of ferritic bands, where the difference with the rest of the material is less pronounced. Finally, points 8, 9 and 10 show the differences in chemical composition about the fusion boundary between the interface and the second AS steel layer. While point 8 shows a slight depletion of Cr right below this fusion line, points 9 shows an increase in the weight fraction of alloying components, followed by a decrease at point 10 and subsequent stabilization. In average, across the diluted layer, an average value of 13.9% Cr content is accounted, which roughly indicates a 74.9% dilution of its major alloying component across the first AS layer.

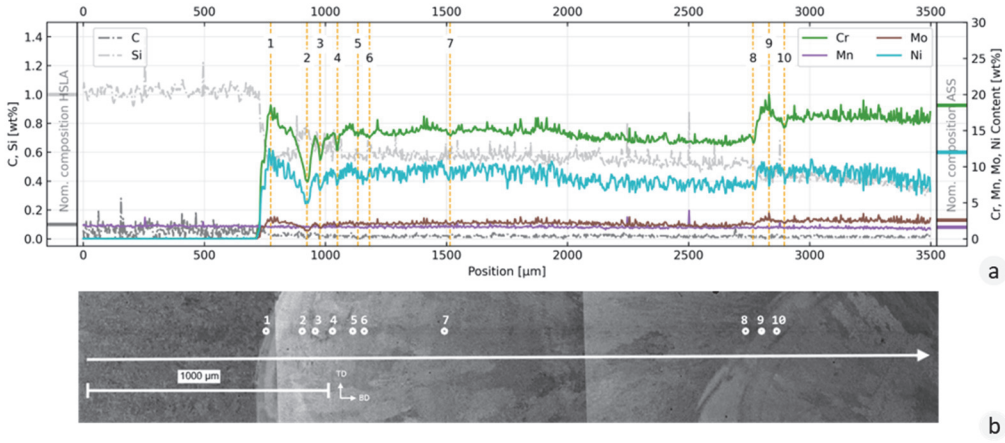

Figure 3-3 (a) Chemical profile obtained employing Electron Probe Micro-analysis (EPMA) excluding Fe. (b) Location along which measurement was performed. Locations of interest 1 through 10 are shown. Note: measurement location was realized along the mildly visible dark horizontal band. White arrow is offset from measurement location but represents accurately length and direction of line scan.

A relevant phenomenon to highlight at this point is the occurrence of segregated bands across the interface layer. This is made evident through the microstructural features observed under optical microscopy in combination with the variations in chemical composition. They are indicative of segregation; whereby un-mixed or partially mixed zones form and solidify before fully mixing with the rest of the filler material. They are easily identifiable in Figure 3-2, where some of the segregated bands are highlighted by red arrows. The heterogeneities naturally translate into scatter of the functional performance, measured through hardness in section 3.3.5. Their occurrence suggests an important effect on the mechanical performance of the interface [24]. [25] gave a first indication of an 'unmixed region' between the filler material and the substrate, described solely as a zone of melted base metal.

The mechanism driving this segregation in the region away from the fusion boundary is slightly more complex. This can be attributed to a combination of convection and incomplete mixing at the fusion boundary, as demonstrated by Kou et al. [26] and modelled by Zhang et al. [27] in the context of dissimilar arc welding. The key criterion dictating the formation of segregated regions is a lower liquidus temperature of the stainless steel weld metal compared to that of the underlaying HSLA steel layers. The effect of these chemical heterogeneities on the microstructural development of the interface region are studied in further detail in the following section.

3.3.2. Phenomenological and thermodynamical modeling

The distinction by optical microscopy of the different phases found at the interface is not a straightforward task. Thus, additional tools are utilized, and their results are discussed. These tools include the use of empirically constructed diagrams, such as the Schaeffler Diagram, as well as thermodynamic calculations.

In Figure 3-4, a Schaeffler diagram [28] is presented. Through this empirical tool, it is possible to determine the effect that dilution of an austenitic stainless steel with a low alloy steel will have on the microstructural development. The three distinct features drawn on the diagram are now discussed. Firstly, the Cr and Ni equivalent values are indicated for the nominal compositions of the selected HSLA steel and AS steel alloys. Under un-mixed solidification conditions, the HSLA steel alloy is predicted to solidify as ferrite and martensite, whereas the AS steel is predicted to solidify primarily as austenite with about 10 % volume percentage ferrite. Secondly, the effect of dilution between both alloys is approximately represented by the straight line joining the coordinates of the nominal

compositions. This line crosses the regions predicting both martensite (M) and a combination of austenite and martensite (A+M). The indication of ferrite and martensite is naturally limited to the context of the Schaeffler diagram, where other occurring phases are omitted. Thirdly, the cloud of colored points represents the composition measured through EPMA at each individual position as shown in Figure 3-4. For each position, the Cr_{eq} and Ni_{eq} coordinates were calculated, and then plotted on the Schaeffler diagram. The color indicates the estimated martensite start temperature (M_s) as predicted by Self et al. [29]. The temperature may be determined with the color bar drawn next to the diagram. The relationship used to determine the M_s temperature [30] is enunciated as follows:

$$M_s = 526 - 354 \cdot C - 29.7 \cdot Mn - 31.7 \cdot Si - 12.5 \cdot Cr - 17.4 \cdot Ni - 20.8 \cdot Mo \\ -1.34 \cdot (Cr \cdot Ni) + 22.4 \cdot (Cr + Mo) \cdot C \qquad (Eq. 3.2)$$

For ease of identification, the points that show an M_s value above 0 °C are delineated by red edges.

The Schaeffler diagram proves itself as a useful tool for the identification of the observed microstructural features. This is mostly recognized through the confirmation of martensite prediction along the diluted layer. A small variation in the Cr_{eq} and Ni_{eq} for compositions closely approximating that of the HSLA steel entails the formation of a microstructure entirely composed by martensite. These regions of limited dilution closely describe the chemistry and phase transformation occurring at the fusion boundary, as well as the segregated islands along the interface layer. The diagram does not predict the formation of bainite. This is expected, as its intended use is for high-alloy stainless steels.

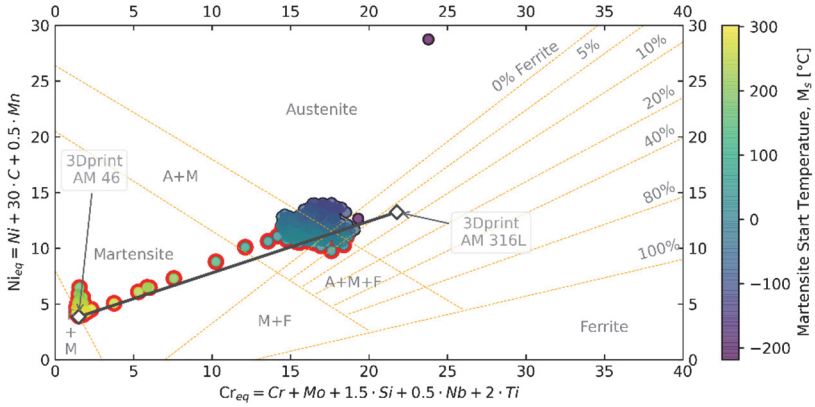

Figure 3-4 Schaeffler diagram including Cr_{eq} and Ni_{eq} of values obtained from a line scan as measured by EPMA, see Figure 3b. Color indicates M_s temperature. Red outlining indicates M_s temperature above 0 °C.

Additionally supporting the findings drawn through the Schaeffler diagram, the results obtained from thermodynamic calculations are presented on Figure 3-5. Phase volume fractions expected under thermodynamic equilibrium are shown in Figure 3-5 (a), c and e for dilution levels of HSLA steel in AS steel ratios equal to 1.0, 0.8 and 0.0. The selection of these specific dilution levels was done based on both nominal compositions of the alloys selected (dilution ratios 1.0 and 0.0) and a dilution level approximating the highest fcc start temperature, as shown in Figure 3-5g.

Figure 3-5 (a) shows the results obtained for the HSLA steel alloy. Firstly, above 865 °C, the only phase predicted is austenite, as it is expected for most low alloy steels. Secondly, between, 693 °C and 865 °C, the phases described under thermodynamic equilibrium include solely ferrite and austenite; these temperatures correspond to the expected A1 and A3 limits. Lastly, the plot describes a matrix composed by a large amount of ferrite, accompanied by a trace volume of pearlite for all temperatures below 693 °C. Pearlite, although not explicitly represented on the diagram, is indicated in part by the small volume fraction of cementite. The presence of pearlite, although not observed for the deposition parameters used for this study, have been reported by other authors [31]. Within the same temperature range, complex carbides are also expected to precipitate, such as M_5C_2 and M_7C_3.

Studying the anticipated phases is valuable; however, it's essential to recognize that the conditions needed for thermodynamic equilibrium differ significantly from those observed during the solidification and cooling of a weld pool. Thus, a CCT diagram is presented to illustrate the solid-state phase transformations under para-equilibrium conditions. Such diagram is presented in Figure 3-5 (b) for the nominal composition of the HSLA steel alloy. A reasonable range of cooling rates is shown for stable arc-welding processes on the diagram, namely between 10 °C/s and 100 °C/s. Contrasting itself from thermodynamic equilibrium, the diagram predicts a lower ferrite start temperature approximating 730 °C. This same effect is also evident for the pearlite start temperature, demonstrably appearing at a temperature closer to 580 °C. Nevertheless, the most relevant difference is the indication of a bainite start temperature. As it is expected, bainite appears at higher cooling rates than pearlite. Finally, martensite start temperatures are predicted above 430 °C for the highest cooling rates, but drastically drops for the cooling rates that represent arc welding process conditions.

A mixture of 0.8 [HSLA steel] and 0.2 [AS] naturally yields important differences in terms of thermodynamic equilibrium. This mixture is modelled on Figure 3-5 (c). Pearlite is no longer predicted under this chemistry and cooling range, but the presence of additional alloying components enables the formation of intermetallic phases. Laves, sigma and the complex $M_{23}C_6$ carbide are predicted in this case. The two intermetallic phases appear at a temperature range up to 519 °C and 392 °C respectively, whereas the carbide is predicted to precipitate within a broader range, up to 768 °C. A very small volume fraction of a lesser-known G-phase is also predicted. As a short reference, the latter is formed by a stoichiometry $(Fe)_{16}(Mn)_6(Fe,Si)_7$ belonging to the cubic crystal system [32]. Although the appearance of these phases could be of concern for the adequate performance of the material, their prediction is expected to be relevant only for long thermal treatments. Arguably more relevant within the context of this study is the effect of these additional alloying elements on the formation of ferrite and austenite. Naturally, the given proportion of alloying components influences the start temperature of ferrite formation. Compared to the nominal composition of HSLA steel, austenite is predicted to be stable down to 757 °C. Further cooling rapidly enables austenitic transformation to ferrite, although austenite is expected to remain within the mix of stable phases down to 371 °C.

To provide a similar comparison between thermodynamically stable and para-equilibrium conditions, a CCT diagram for the same 0.8 [HSLA steel] : 0.2 [AS steel] composition ratio is presented in Figure 3-5 (d). The plot distinctly lacks the indication of the ferrite start temperature, distinguishing itself from the prediction of thermodynamically stable phases. Even though bainite is predicted, this phase is not expected to be relevant for the cooling rates of interest. A bainite start temperature is foreseen only for the very slow cooling rates. The effect of additional alloying elements is thus evident. This specific composition stabilizes austenite down to 318 °C. This is also the predicted start temperature of martensite, noticeably lower than the one predicted for the nominal composition of the HSLA steel. Given that the prediction of phase transformations (or lack thereof) is accurate, it is understood that the material represented by this chemistry would appear as martensite at room temperature. This prediction extends for all mixing ratios ranging approximately between that corresponding to 0.3 [HSLA steel] : 0.7 [AS steel] and up to 0.8 [HSLA steel] : 0.2 [AS steel]. Within the studied cooling ranges, austenite is expected to be the only phase stable under the para-equilibrium conditions of arc welding, until the martensite start temperature is reached.

Finally, the thermodynamically stable phases of the nominal AS steel alloy composition are brought into discussion. The thermodynamically stable phases and CCT diagram are shown in Figure 3-5e and Figure 3-5f. Within the temperature range studied, a small phase fraction of primary ferrite is expected at any temperature above 1112 °C. Down to 592 °C, most of the material is expected to remain as austenite. Below this point, only a fraction of austenite is expected to be stable throughout all cooling transformations. Precipitated ferrite is expected to be stable under thermodynamic equilibrium at temperatures below 590 °C. Also, a significant fraction of sigma and laves phases are foreseen for temperatures below 1000 °C. The appearance of both phases is strongly detrimental, even for small volume fractions. However, ferrite transformation into sigma or laves phases is only possible through an extended thermal treatment [33], due to the sluggish kinetics [34]. For the range of temperatures considered, a CCT diagram only shows a stable austenite phase, thus no boundaries are visible for the precipitation of transformation phases.

So far, the results presented do not deal with the effect of dilution on the solidification and austenite transformation temperatures. For these transformations, Scheil-Gulliver calculations are preferred, as this modelling approach is extensively used to capture the fast solidification conditions in welding and AM of steel [35], [36], [37], and has been show to provide an adequate framework for the estimation of solidification phases in functionally-graded parts [38], [39]. This modelling is done to include the effects of solute re-distribution and rapid solidification. Figure 3-5g shows the expected liquidus, solidus, austenite start temperature, as well as the martensite start temperature for all degrees of dilution. The effect of additional alloying elements in the AS steel alloy becomes obvious [40], as the liquidus line reaches below 1450 °C for the nominal composition of this alloy. Opposingly, the HSLA steel alloy shows the highest liquidus temperature, approximately 1510 °C [41]. Regardless of the location of the liquidus line, primary ferrite is expected to be the first phase to nucleate. However, for all dilution levels the austenite start temperature is predicted to lie between the solidus and liquidus lines. This observation indicates that regardless of the local chemical effect of partial dilution, austenite will appear before solidification is completed. Between 1.0 [HSLA steel] : 0.0 [AS steel] and 0.4 [HSLA steel] : 0.6 [AS steel] combination ratios, the fcc start temperature also indicates the full transformation of the readily nucleated delta ferrite into austenite. This is not the case for the rest of the compositions considered, where ferrite remains a stable phase throughout subsequent solid-state transformations as a product of segregation.

To understand the mechanisms driving solidification at the dissimilar fusion boundary, it is important to study the nucleation and initial phase transformations in detail. As it was discussed, the initial phase nucleated at 1425 °C from the liquid is a ferrite phase for the AS steel. At this same temperature, the HSLA steel is transformed entirely to austenite. Assuming a situation where there is no mixing between both alloys, such conditions would lead to the conclusion that no epitaxial growth is possible [42], [43]. Nevertheless, before fully solidifying, the AS steel also nucleates austenite at the dendrite tips of the primary solidified ferrite [44]. The nucleation of a peritectic austenite phase is apparently true for the mixing range between 0 and 0.8, as indicated by Scheil-Gulliver calculations used to build Figure 3-5. This primary austenite phase distinguishes itself form the later occurring austenite produced through solid-state transformation of the primary ferrite while cooling. Moreover, it has been demonstrated by Inouse et al. [45], that for primary ferritic solidification modes, planar austenite first grows from the base metal. This phenomenon would naturally resolve the conditions necessary for the AS steel weld composition to solidify under crystallographic agreement from its underlying substrate. The observations made by Inoue and Nelson are nevertheless indirect, either through crystallographic measurements or thermodynamic modelling, thus requiring further confirmation.

3.3.3. Microstructural characteristics of interface region

Having completed a detailed description of the chemical and thermodynamic characteristics of the interface, it is now appropriate to describe the unique features found at the bi-metal interface layer in further detail. Optical microscopy images are shown in Figure 3-2. Nonetheless, as it was described in section 3.3.1, traditional metallographic procedures lead to poor feature outlining. This effect may be attributed to the difference in galvanic properties between both alloys. Thus, back-scattered electron imaging is used to avoid any misinterpretation caused by partial etching of the two materials. Figure 3-6 (a) shows a low magnification image of the dissimilar interface. The features described in section 3.3.1 match with those observed in this figure. Bands of a low image-quality phase, in this case assumed to be ferritic, are engulfed by a larger matrix of austenite. In the context of EBSD image quality (IQ) mapping, darker features correspond to lower IQ values. The density of features with low image quality increases at the shoulder of the bead and appears to be lowest at its root.

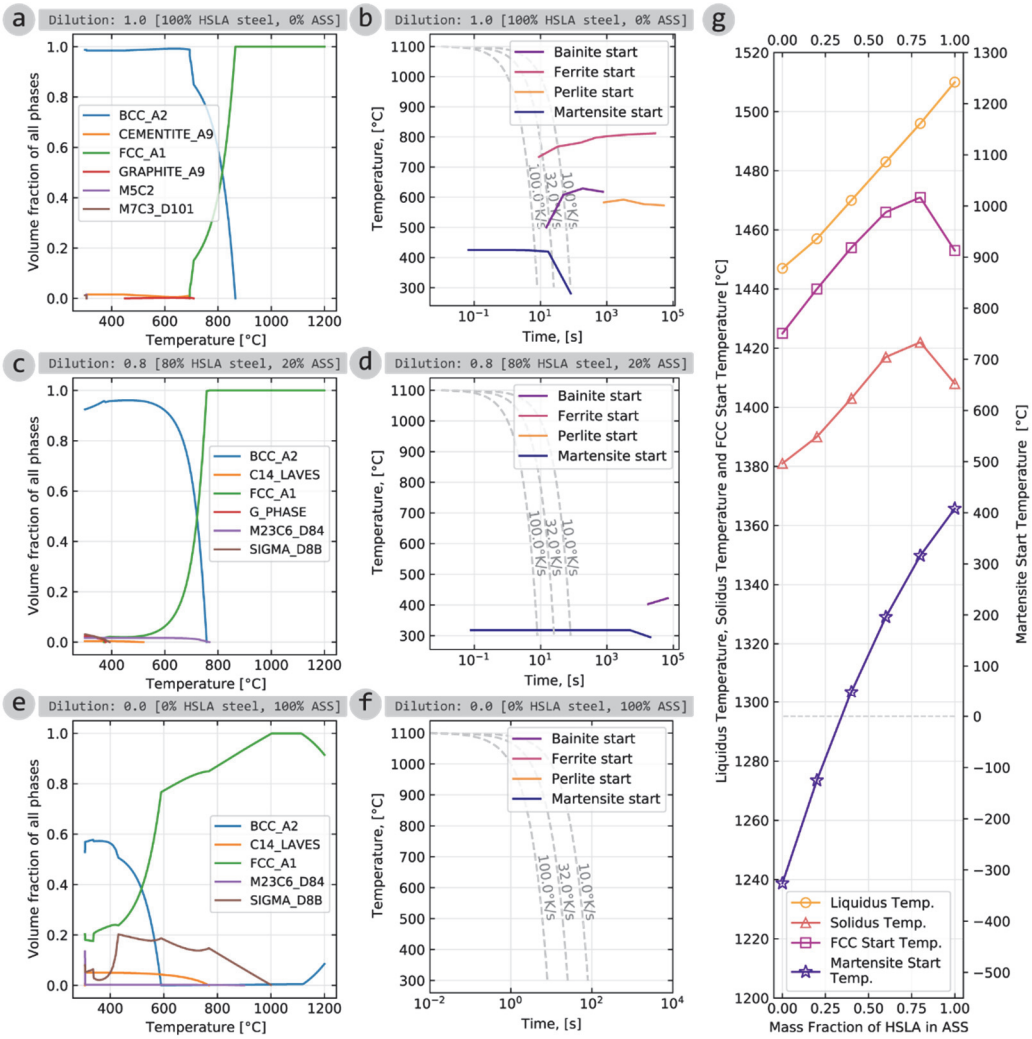

Figure 3-5 (a) Volume fraction of all thermodynamically stable phases as a function of temperature, and (b) CCT diagram for the nominal HSLA steel alloy composition. (c) Volume fraction of all stable phases as a function of temperature, and (d) CCT diagram for an alloy consisting of 0.6 [HSLA steel]: 0.4 [AS steel] (e) Volume fraction of all stable phases as a function of temperature, and (f) CCT diagram for the nominal composition of the AS steel alloy. (g) Liquidus, solidus, fcc start temperature, as determined by Scheil calculations, and Martensite start temperature as a function of the degree of mixing between the nominal compositions of [HSLA steel] in [AS steel]. In this case, 0.0 means a nominal composition of AS steel, whereas 1.0 means a nominal composition of the HSLA steel.

To gain a better understanding of the microstructural features at the interface, higher magnification images are also presented. Markers b and c in Figure 3-6 (a) indicate the approximate locations where Figure 3-6 (b) and Figure 3-6 (c) are located. The value of characterizing this region with backscatter electrons becomes clear, as several features can be identified. The boundary region between the last HSLA steel and the AS steel layer 1 is shown in Figure 3-6 (b). On the one hand, marker B highlights the location of a Type I boundary. Some small fractions of martensite form a tortuous transition between the underlying low alloy steel into the austenite matrix. From the fusion boundary, the austenite grain grows towards the center of the weld pool. Its length development is interrupted only by the martensite island highlighted by marker A. Marker C, on the other hand, shows the location of an elongated ferrite grain running parallel to the fusion boundary. Martensite is found continuously along the fusion line at this location. Across the fusion line, a grain with low IQ is observed to have developed parallel to its substrate. These features correspond with a Type II boundary. As a reference, the label Type I is assigned to those fusion boundaries where epitaxial growth proceeds from the underlying crystal substrate. From this nucleation site, growth continues perpendicular to the fusion boundary in the direction of the bead centerline. Type II boundaries, by contrast, are those where grains from the dissimilar material solidify parallel to the fusion line along the dissimilar boundary [46].

The features observed at the boundary region do not represent those observed along the rest of the interface layer. Thus, the region away from the dissimilar fusion line is given in Figure 3-6 (c) in the form of an IQ map. While marker D distinguishes the austenite matrix, marker G points at the location of acicular ferrite. A few distinct lath packages may be identified, ranging between 12 to 19 μm in length and 2 to 3 μm in width at this specific location. Smaller constituents are identified alongside these lath packages, highlighted with marker F. These microconstituents are on average more equiaxed and about an order of magnitude smaller than the neighboring acicular ferrite. Marker E highlights the location of a porosity, as it becomes clear under such magnification. Due to their potentially detrimental effect on the mechanical properties of the interface, quantifying its occurrence is deemed necessary. Utilizing manual counting methods [47], it is estimated that the porosity observed represents no more than 0.6 % of the surface fraction, with pores not exceeding 1.5 μm in diameter.

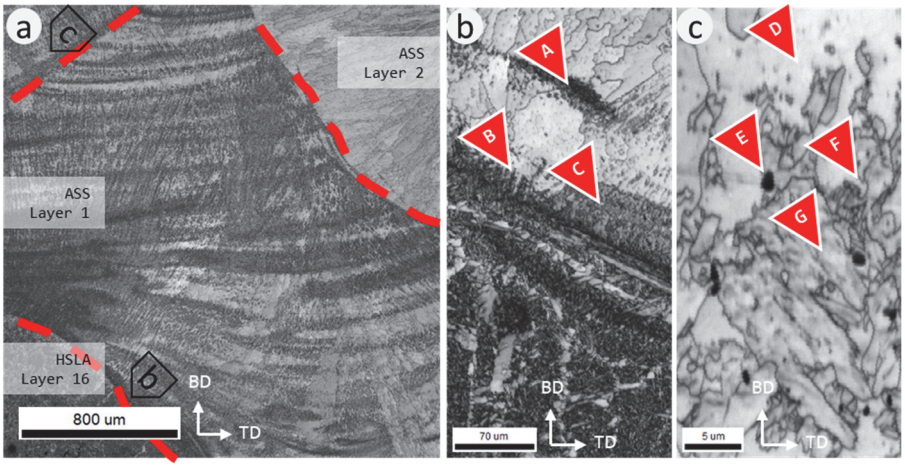

Figure 3-6 (a) Low magnification EBSD Image Quality (IQ) map of HSLA steel layer 16, AS steel layer 1 and AS steel layer 2. (b) High magnification of the region around the dissimilar fusion boundary. (c) High magnification of bainitic / ferritic phase within the AS steel layer 1 and away from the dissimilar fusion boundary

The relationship between the different microstructural features may be best described through their crystallographic traits. Consequently, EBSD measurements were carried out across the interface layer. Figure 3-7 presents the IPF, KAM and Phases maps of this region. As a quantitative description of the texture and phase fraction follows, it is important to indicate what is considered as the interface layer. For ease of identification, the interface layer is outlined with a dashed white line in Figure 3-7 (a). The values presented in all legends belong to the entire map shown, including phase fractions and grain size distribution. By isolating the interface boundary, a 0.6 phase fraction of austenite phase is found, complemented by a 0.4 fraction of ferritic phases identified as 'iron-alpha'. Within these ferritic phases, martensite, bainite and ferrite are expected. Their spatial distribution is shown in Figure 3-7 (c). Alongside the phase distribution, this figure also shows the boundaries that match the Nishiyama-Wasserman (N-W) orientation relationship (OR) within a 4° tolerance. This tolerance encompasses all Bain-like relationship, thus also possibly includes Kurdjumov-Sachs, Greninger-Toriano and Pitsch OR [48]. These orientation relationships describe the possible orientation variations a daughter bcc phase may display with respect to the parent fcc phase. As it is clear from this map, all ferrite-austenite boundaries comply with this criterion.

The maps shown in Figure 3-7 (a) gives an indication of the crystal orientations, grain shapes, and sizes within and around the interface. The IPF map is obtained with respect

to the build direction (BD) to easily identify texture components along this direction. Columnar grain development is clear, even across the ferritic constituents found all throughout the layer. As it has been identified that the orientation of the ferritic phase within any given austenite grain is coherent (Bain-like), all ferrite features within the same grain appear to have the same inverse pole orientation. Nonetheless, a preferential crystallographic orientation of <001> aligned with the build direction is not recognizable, although it is typical for fcc materials in the context of AM. KAM mapping accentuates the differences between the austenitic and ferritic phases, even as intertwined as they appear within the dissimilar interface. Grain Average KAM values (also known as 'AMIS' [49]) for ferritic phases included exclusively within the interface layer display an average value of 1.62°. Opposingly, the austenite fraction displays a value of 1.04° under the same metric. This may be qualitatively confirmed through the color mapping shown in Figure 3-7 (b).

Although low magnification maps reveal useful information about the interface layer, the dissimilar boundary is best studied locally under higher magnification in Figure 3-8. Thus, the description of the crystallographic features continues with a detailed analysis of the HSLA-AS steel dissimilar fusion boundary. In section 3.3.4, this characterization is complemented with Transmission Electron Microscopy. These results are useful to elucidate the nature of all the phases identified as bcc, given that the distinction between martensite, bainite and acicular ferrite is non-trivial. The location mapped coincides with the one shown in Figure 3-6 (b). As the identification of specific features may be troublesome within the map, labels are provided for the identification of Type I and Type II boundaries, as well as the outlining of the corresponding crystals.

For the region identified as Type I boundary, two relevant features are identified. Firstly, martensitic packages are observed populating the fusion line. These packages are shown closely oriented to <100> on the IPF map in Figure 3-8 (a). They are distinguished being martensite due to their high misorientation values. The martensite laths show a 1.47° grain average kernel misorientation and grow up to 15 μm beyond the fusion line. As a comparative reference, the austenite crystal immediately adjacent shows a value of 0.52°. The second feature of interest is the OR between the martensite phase and the austenite crystal. As it is shown in Figure 3-7 (c), the N-W OR shown in orange describes accurately the boundary between both phases within a 4° tolerance. This is true not only for the martensite found at the fusion line, but also for the martensite island found detached from said region. PAG reconstruction further clarifies the origin of this observed orientation relationship. Both the martensite found at the fusion line and the one found in

the detached island have originated from the same parent grain. Moreover, the ferritic phases immediately below the fusion boundary show a coherent PAG orientation with respect to the austenite crystal. This result reveals crystallographic agreement and growth of the austenite grain across the fusion boundary.

The boundary region identified as Type II distinguishes itself from the Type I boundary through a few key features. Alongside the dissimilar boundary, a ferritic grain is observed. This grain is nevertheless not homogeneous, as it is populated with smaller features. Along the fusion line, lath martensite is found oriented towards the center of the weld bead, alongside few isolated inclusions of retained austenite. The remaining features within the ferritic grain display a high value of KAM, where the observed value of grain average misorientation is estimated to be 0.82°. Nonetheless, the Image Quality is higher than the austenite matrix, yet not as high as that of martensite. It is important to point out that Image Quality is a measure of the relative quality of the Kikuchi patterns, which in part vary due to microstructural imperfections. This observation suggests that the nature of the ferritic phase is either idiomorphic ferrite or bainite [50]. PAG reconstruction indicates that the ferritic and martensitic constituents may have originated from the same parent grain, which only partially transformed to the grain observed at room temperature. The austenite retained within the grain matches the orientation of the parent grain. This reconstruction map thus reveals that such grain and all its internal features may come in crystallographic agreement with its prior-austenite substrate and partially transformed to three different phases.

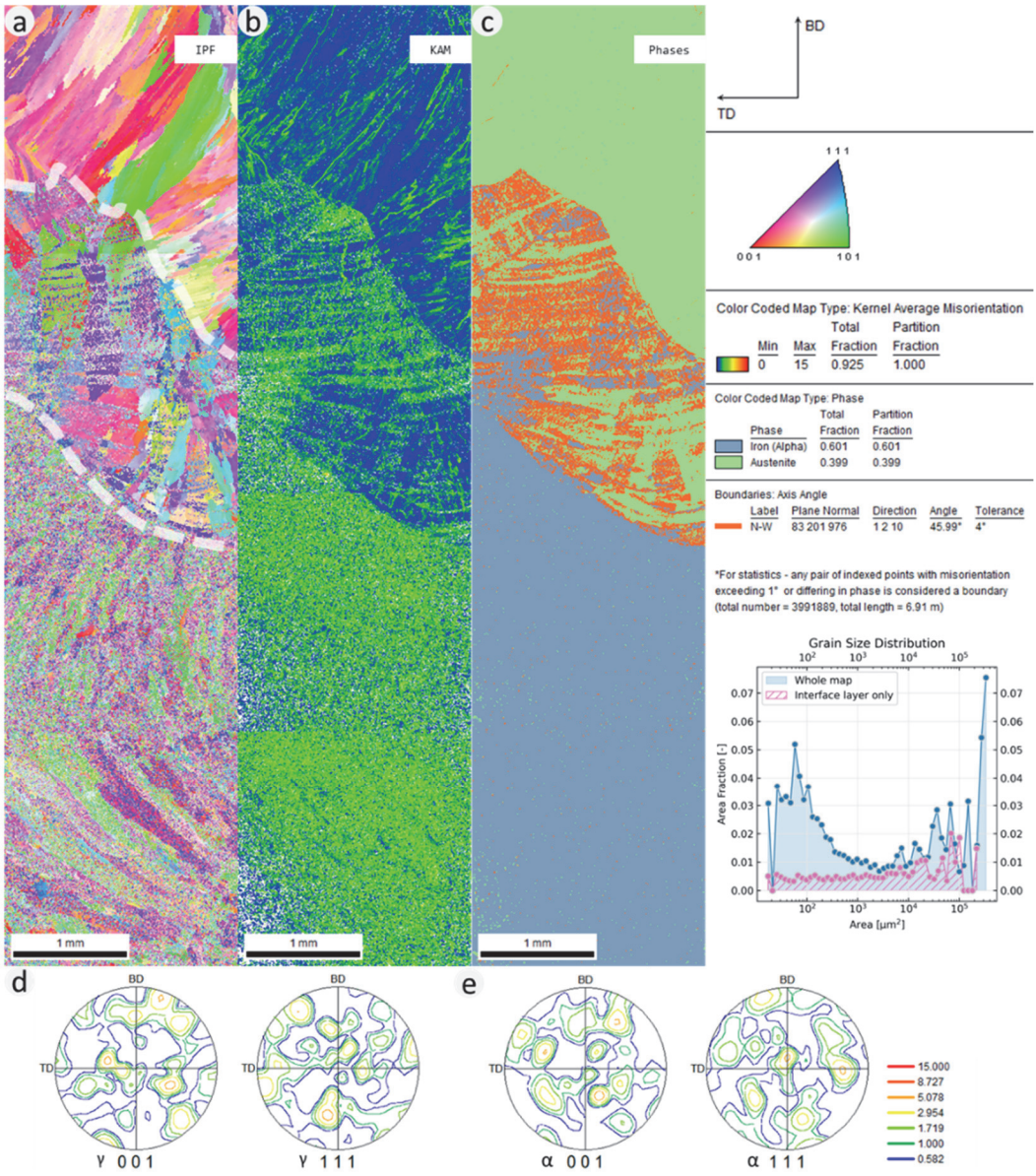

Figure 3-7 (a) Inverse Pole Figure (IPF) mapping of multiple beads around the dissimilar interface obtained with a step size of 3000 nm. (b) Kernel Average Misorientation (KAM). (c) Phases map, where white pixels represent points indexed with a confidence interval lower than 0.1. Pole figures showing stereographic representation of ODF as measured at the interface layer are provided for (d) the fcc phase and (e) the bcc phase. Pole figures are obtained from the region delimited by white dashed line on figure a. Legend includes reference axis to maps, IPF, KAM, Phase map color legend, and grain size as a function of area fraction for the entire map shown.

The existence of a Type I boundary alongside a Type II boundary is an observation that demands further discussion. The Type I boundary follows the conventional austenite-ferrite dissimilar fusion boundary, as presented by Ornath et al. [9]. Due to the friction between the liquid and the solid phase, fluid flow is reduced at the weld pool boundary [51]. Thus, a small material volume of scarcely mixed base metal can still exist. Under the condition of limited mixing, the chemical composition favors the formation of martensite, as it has been demonstrated and discussed in section 3.3.2. This same mechanism leading to limited mixing at the fusion boundary may also promote the reduction of the solidification temperature, at an intermediate temperature between that of the base material and that of the layer being deposited. Thus, this scarcely mixed region may re-solidify before the rest of the weld-pool.

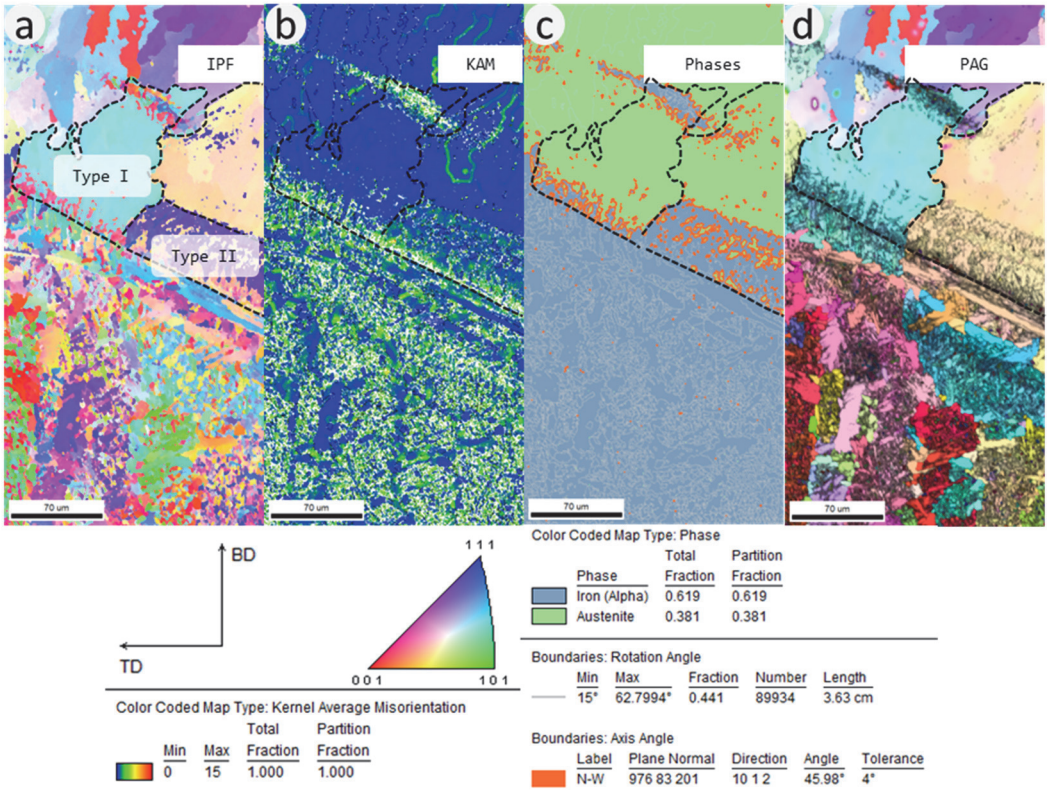

Figure 3-8 (a) Inverse Pole Figure (IPF) of boundary region between last layer of HSLA steel and the interface layer, obtained with a step size of 700 nm. (b) Kernel Average Misorientation (KAM). (c) Phase map showing grain boundaries larger than 15° in white and boundaries that match the N-W orientation relationship. (d) Parent austenite grain reconstruction overlayed on the Image Quality map. Legend includes reference axis to maps, IPF, KAM, Phase map color legends and large angle grain boundary length.

Kuo and Yang [26] further extended this macro-segregation mechanism by indicating the effect of convection within the weld pool. Their work indicates that the partially mixed volume fraction could be lifted behind the weld pool, forming either peninsulas or islands. A peninsula is understood as a volume of unmixed (or scarcely mixed) base material that is lifted through convection but remains in continuous contact with the fusion boundary. An island, by distinction, refers to that material volume that completely detaches from the fusion boundary and yet retains a scarcely mixed composition. This convection mechanism may thus give an explanation between the different boundary types observed alongside the fusion boundary.

Continuing with the description of the unique features within the interface, the crystallographic description of the region captured in Figure 3-6 (c) are illustrated on Figure 3-9. The IPF map on Figure 3-9 (a) gives a clear indication of the closely matching orientations of the major laths observed. This observation confirms that the feature observed is indeed a single lath package. The acicular microconstituents, nonetheless, display high angle boundaries when compared to the bainitic laths. The high angle boundaries are found to match a rotation angle close to either 52° or 59°, falling within the most typical ranges of acicular ferrite [52]. Low angle boundaries help distinguish the different lath packages within the feature. Point-to-origin misorientation mapping across one of the larger laths reveals that it is made up by 4 distinct packages of approximately 1.5 μm in width. These packages are in turn divided by a boundary misorientation between 0.5 to 3°. Kernel Average misorientation mapped in Figure 3-9 (b) shows a very low density of relevant features at this magnification. Even so, the grain average misorientation highlights the differences for all three constituents present. While the austenite matrix displays a value of 0.27°, the large bainite laths show a grain average misorientation of 0.52°. Notwithstanding the largest value observed, the neighboring microconstituents reach an average value of 1.1°. Alongside the IPF and KAM maps, the reader is provided with the phase map in Figure 3-9 (c). This includes high angle boundaries drawn for ease of identification of the microconstituents. The boundaries matching the axis-angle criterion of N-W OR are highlighted in orange. These boundaries illustrate the Bain-like relationship between fcc-bcc phase constituents belonging to the same parent grain, including those of bainitic nature.

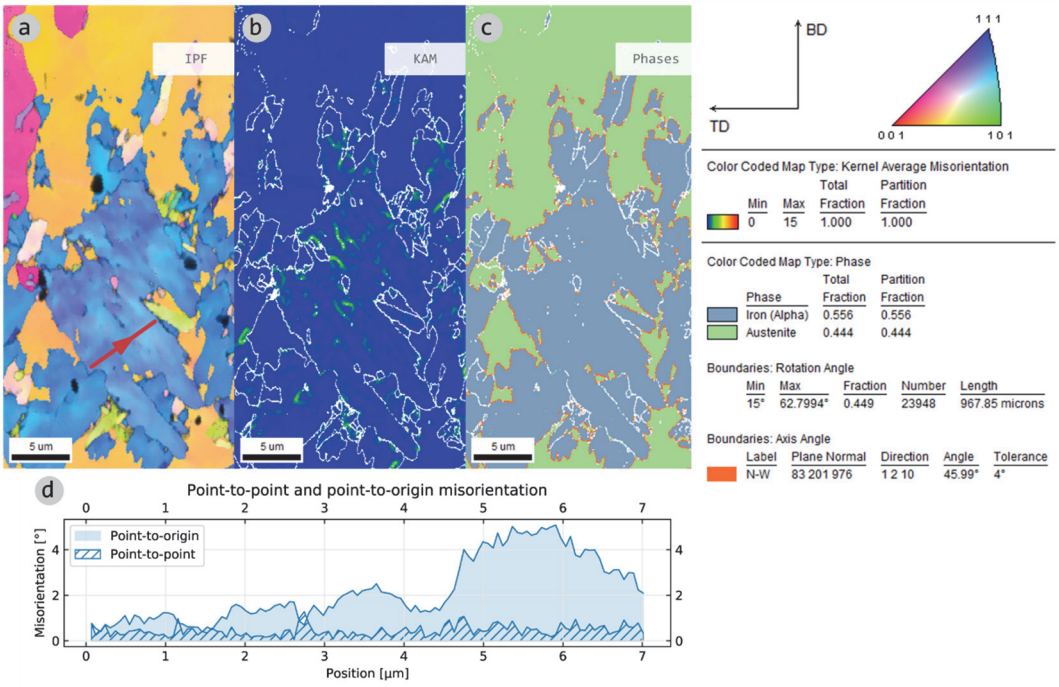

Figure 3-9 (a) Inverse Pole Figure (IPF) of bainitic island within interface layer obtained with a step size of 70 nm. (b) Kernel Average Misorientation (KAM) showing grain boundaries larger than 15° in white. (c) Phase map highlighting boundaries that match with N-W orientation relationship. (d) Point-to-point and point-to-origin misorientation profile at location marked in (a). The legend includes reference axis to maps, IPF, KAM and Phase map color legends, as well as total grain length density of boundaries matching the orientations of interest.

The possible identification of acicular ferrite within the interface layer delineates the degree at which segregation might occur. Para-equilibrium calculations discussed in section 3.3.2 indicate the range at which bainitic transformation is expected. Departing from the nominal composition of the HSLA steel filler wire, any mixing larger than 10% of the AS steel into the HSLA steel composition leads to sufficient austenite stabilization to overcome any transformation other than martensite. The orientation relationship between the ferritic phase and the austenite matrix matches throughout its entire periphery by a Bain-like rotation. This naturally indicates the precipitation of this ferritic phase from the parent austenite grain. The ferrite constituents contained within the same austenite grain share the same crystallographic orientation as the ferritic phase shown in Figure 3-9. The lack of obvious martensite laths in its vicinity suggests the lack of a mixed alloy composition described in previous sections. Thus, an alternative mechanism must be

controlling the solid-state phase transformations. For this, TEM characterization is carried out to confirm the description of phases observed.

3.3.4. TEM characterization

As it has been shown throughout the methods employed up to this point, the interface layer presents a large variety of phases of different morphologies. These may range from the austenite matrix to a mix of ferrite constituents, including products of the partial solid-state transformations of the stainless steel, bainite, allotriomorphic ferrite, idiomorphic ferrite as well as martensite. Most of these phases are identifiable through the distinction of their etching, through their crystal characteristics, or through traits shown by a combination of methods. Nevertheless, acicular ferrite, also understood as intragranular bainite [53], and martensite both form laths and packages that could easily be mis-identified through either method. The most adequate way to confirm the presence of both phases is thus through Transmission-Electron Microscopy (TEM). TEM analysis is also used to confirm the size and frequency of occurrence of important nanostructures relevant for the adequate mechanical properties of the alloy, such as dislocation structures and small precipitates.

As a first step, the features typical for the austenite matrix within the interface layer are introduced. Figure 3-10 (a) shows a location alongside the foil edge including two different grains separated by a low angle boundary. A high-density network of tangled dislocations is immediately recognizable. The average size of these cells is estimated to lie between 0.41 and 0.54 μm in diameter. Dislocation cell walls are observed to occur independent of any spatial chemical segregation.

An important effect yet to be understood is the development of a higher dislocation density when carrying out depositions of thick sections. Bertsch et al. [54] derived this conclusion from a systematic study on thermomechanical constraints during Laser Engineered Net Shaping, a form of Direct Energy Deposition. This dislocation development has a direct consequence on the material's mechanical performance, as it has been established that dislocation pile-ups moderate the twinning of austenite [55]. The authors state that this mechanism improves the yield behavior of the alloy without compromising its ductility. Nonetheless, the pileups observed are not spatially correlated neither with the dendrite structures nor with any elemental segregation like those observed by Bertsch et al. [54], leading to an un-organized cell structure. This important difference can be

attributed to the slower cooling rates of WAAM compared to LENS [56], resulting in a different solidification mode and also a less dense dislocation build-up.

Additional features may be observed under even further magnification. Appearing within the austenite matrix, high resolution imaging reveals a high density of planar dislocation arrays. These features are pointed by markers on Figure 3-10 (b), and have been correlated with the accommodation of small plastic strain [57]. As the density of stacking faults is closely related to the composition of the alloy [58], it is important to note that their density will vary along the variations of chemistry across the interface layer. The largest density of stacking faults is thus expected in the regions of highest Ni and Mn concentration [58]. Moreover, stacking faults will aggregate in the close vicinity of precipitates with a mis-matching lattice, such as the oxides found in the austenite matrix.

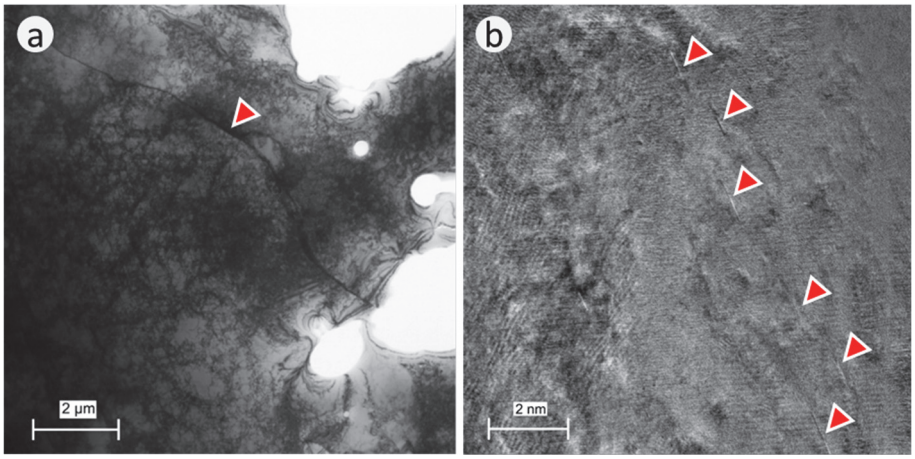

Figure 3-10 (a) Transmission Electron Microscope (TEM) Bright Field (BF) image of austenite matrix including a low angle grain boundary. (b) High-Resolution TEM (HREM) image showing a group of planar dislocation arrays in the austenite matrix.

Some phases and particles typically present in the volume fraction of the AS steel are found alongside the fcc matrix within the interface layer. A feature that has not been highlighted so far is the interdendritic ferrite. An example of this phase constituent is shown in Figure 3-11 (a). EDS line scanning in Figure 3-11b reveals the well-known segregation of Cr into the interdendritic spaces during solidification. Features both within the interdendritic ferrite and the austenite matrix are visible, highlighting thus their close orientation relationship. The zone axis matches bcc [110] for this image, clearly highlighting the high dislocation density found within this ferritic phase. Alongside the ferrite constituents, Si-Mn oxides are found. The oxides are located both in the austenite

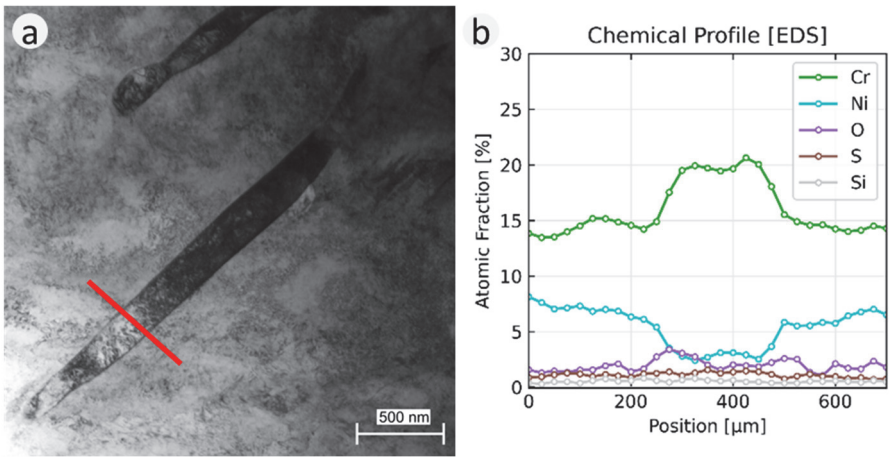

Figure 3-11 (a) TEM-BF image showing interdendritic bcc phase entirely contained within an fcc matrix indicating the location of the EDS chemical profile shown in (b).

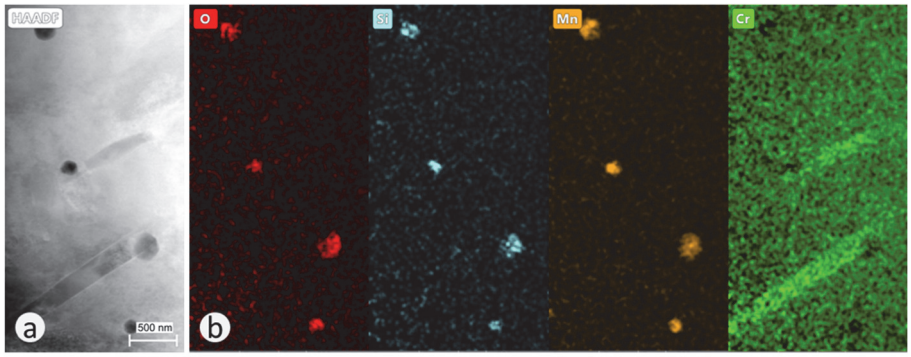

Figure 3-12 (a) High-Angle Annular Dark Field Imaging (HAADF) showing (b) the compositional maps of the same region including from left to right oxygen, silicone, manganese, and chromium. These images are obtained at the same location as Figure 3-11 in the interface layer

matrix and along the ferrite precipitate. The composition of these particles is identified through the EDS elemental maps provided in Figure 3-12. Their size is estimated between 0.15 and 0.25 µm in diameter, and the distance to the nearest neighbor particle observed ranges between 0.85 and 1.4 µm.

The last features to be described are those of acicular nature, exemplified by those features seen in Figure 3-6c and again in Figure 3-9. Under TEM imaging, bainite laths are easily identifiable. An example of these bainite laths is shown in Figure 3-13 (a), where 8 plates are visible and numbered. The plates are contoured by the austenite film which

matches in crystallographic orientation with the rest of the matrix observed. The austenite film between them appears dark, as it originates from a dislocation cell wall. The plates display an average thickness of 0.09 µm, and the whole lath has a total width of 0.97 µm. Contrastingly, lenticular plates are shown crossing a location of high dislocation density in Figure 3-13 (b). These features are much longer and thinner, possibly indicating the location of lenticular martensite. The plate thickness varies from 10 up to 80 nm. The dislocation density found within the lenticular plates is negligible when compared with the austenite matrix within which it is found. This observation serves as an indication of the possible driving mechanisms leading to the formation of this phase. The fcc austenite

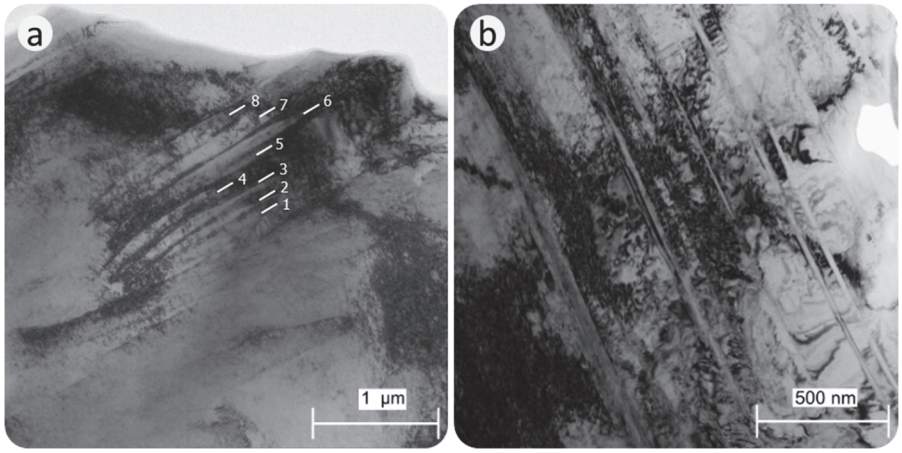

Figure 3-13 (a) TEM-BF image showing lath-like cells enclosed alongside dense dislocation clusters. (b) TEM-BF image showing an alternative example of lamellar twins within the austenite matrix at a different location.

matrix, a bcc phase and a fraction of a lenticular plate are shown near each other in Figure 3-14. The twin nature of the lenticular plate is made evident under this high-resolution image shown in Figure 3-14 (b). The orientation relationship between the bcc and the fcc phases is illustrated through the FFT transformation of the image, which in turn simulates the selected area diffraction pattern of both crystal lattices. Under the 100_{bcc} // 011_{fcc} zone axis, a corresponding orientation relationship is apparent between both phases.

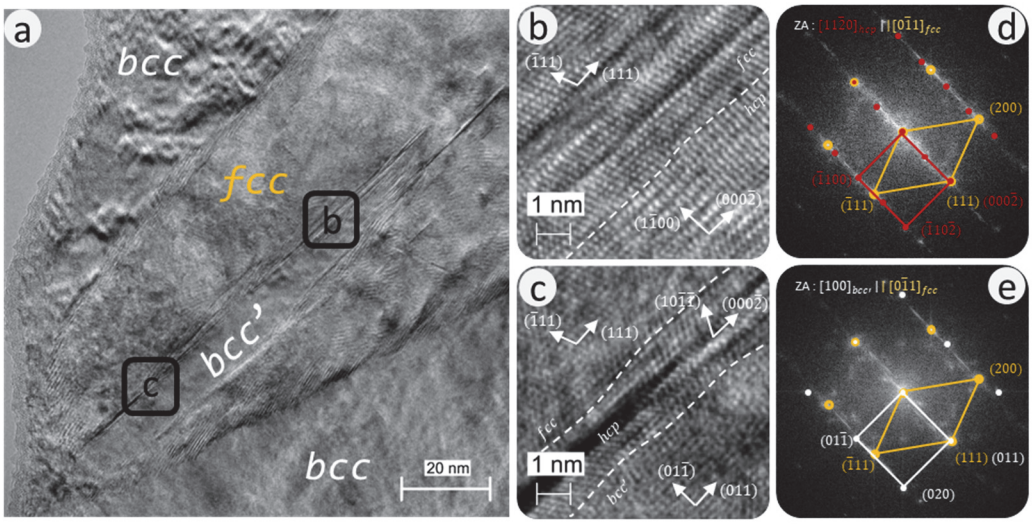

Figure 3-14 (a) HREM of bcc phases surrounding the austenite phase with a martensite plate originating from its grain boundary, Zone Axis [001] bcc || [011] fcc. (b) Higher magnification region including hcp martensite (c) Higher magnification region including bcc martensite, hcp transition region and fcc matrix (d) FFT of region b (e) FFT of region c.

3.3.5. Mechanical performance

As an indirect measure of local mechanical performance, Vicker's hardness measurements were carried out. Their locations are shown in Figure 3-2 (a). The interface shows microstructural features which are discontinuous. This includes Type I and type II boundaries, as well as occasional martensite islands within the austenite matrix. To overcome this problem, the hardness values were obtained at several locations along the dissimilar interface, noting their relative distance from the dissimilar fusion line. These results are presented graphically on Figure 3-15. The aggregation of results in a single error bar plot highlights the variation in hardness in the proximity of the fusion boundary. The highest value observed is measured within a martensite island 250 µm away from the fusion boundary, reading a value of 371 $HV_{0.2}$. Nonetheless, without the presence of a hard face like martensite, indents at the same location yield a hardness of 220 $HV_{0.2}$. The highest variability is observed between 750 µm below the interface and 1250 µm above it. This region corresponds to the coarse-grained HAZ of the last HSLA steel layer, the fusion boundary, and the lower half of the interface layer. Although martensite was

observed at the fusion boundary, the largest variability arises from the detached martensite islands.

The differences in hardness observed through the interface only give a first indication of its mechanical behavior. Tensile tests are thus conducted to understand the deformation behavior of the bi-metal component under tensile loading. To overcome the limitations posed by the relative size of the region of interest, DIC is used to monitor the deformation of the diluted interface. Figure 3-16 (a) shows the load-deformation curves of the 6 tensile specimens examined in this work. The apparent low stiffness shown in the curves is expected since the displacement measurements are taken from the crosshead of the testing rig. Nonetheless, an important phenomenon is highlighted in the zoom-in insert included in the figure. After a gradual deviation from linear-elastic behavior through relaxation, all specimens show a slight and sudden increase in stiffness at about 8.5 kN.

This inflection point is then followed by substantial work hardening up to the maximum tensile strength and subsequent specimen failure. The position of the kink is indicated by the red arrow in the inset of Figure 3-16.a.

With the help of the DIC system, it is possible to identify the origin of the observed inflection point and sudden increase in stiffness. Figure 3-16.c shows the strain distribution maps of the uniaxial engineering strain. At lower load levels the strain is distributed homogeneously all throughout. Further loading is accompanied by deformation in the vicinity of the fusion boundary of the first and second AS steel layers and is shown as such at stress level of 464 MPa. Further on, shear deformation takes place within the first and

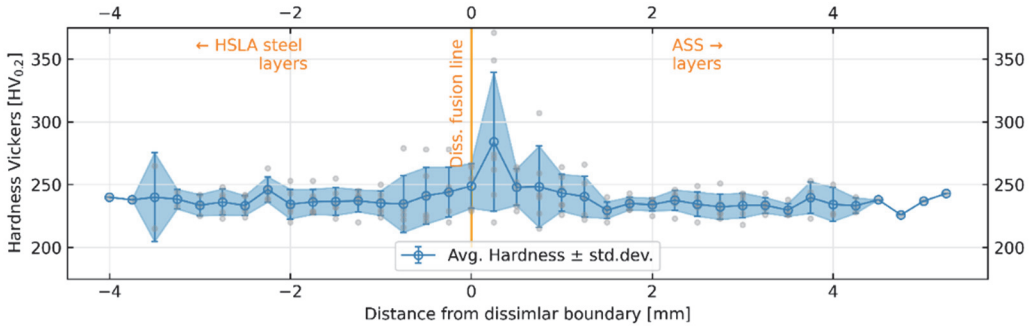

Figure 3-15 Average and error measurement of Hardness Vickers measurements in the vicinity of the dissimilar fusion line. The vertical orange line at value 0 indicates the position of the interface relative to every indentation made. Positive values indicate measurements in the AS steel layers. Negative values indicate measurements in the HSLA steel layers.

second AS steel layers, until both material volumes develop substantial plastic deformation. It is at this point, that differences start to appear between the layers of AS steel. From 580 MPa onward, the strain distribution map shows a large cluster of highly deformed material at the second AS steel layer, which continues to elongate down to necking and final failure.

It is through this strain distribution map that a reasonable relationship can be established between the microstructural and the mechanical properties of the diluted material. As the fusion boundary of the first diluted layer is partially populated by martensite, strain may be localized on the austenite matrix in its immediate vicinity. Moreover, the higher degree of ferrite content in the diluted AS steel layer, as well as a higher density of high angle boundaries between crystals may help to constraint the development of plastic deformation in the diluted layer. The comparatively high volume of ferrite content may restrict the dislocation motion in the large austenite grains. Comparatively, the neighboring layer of AS steel with almost nominal composition displays a low yield point and a large work-hardening behavior. As tensile deformation progresses, most elongation is expressed as plastic deformation of the 2nd layer of AS steel until final necking and breaking. At such point, the 1st AS steel layer is also heavily deformed, showing local strains of above 20% relative elongation. Further analysis of the quasistatic tensile properties is provided in Chapter 4, where an in-depth analysis of the origin of the additional work-hardening behavior is elucidated.

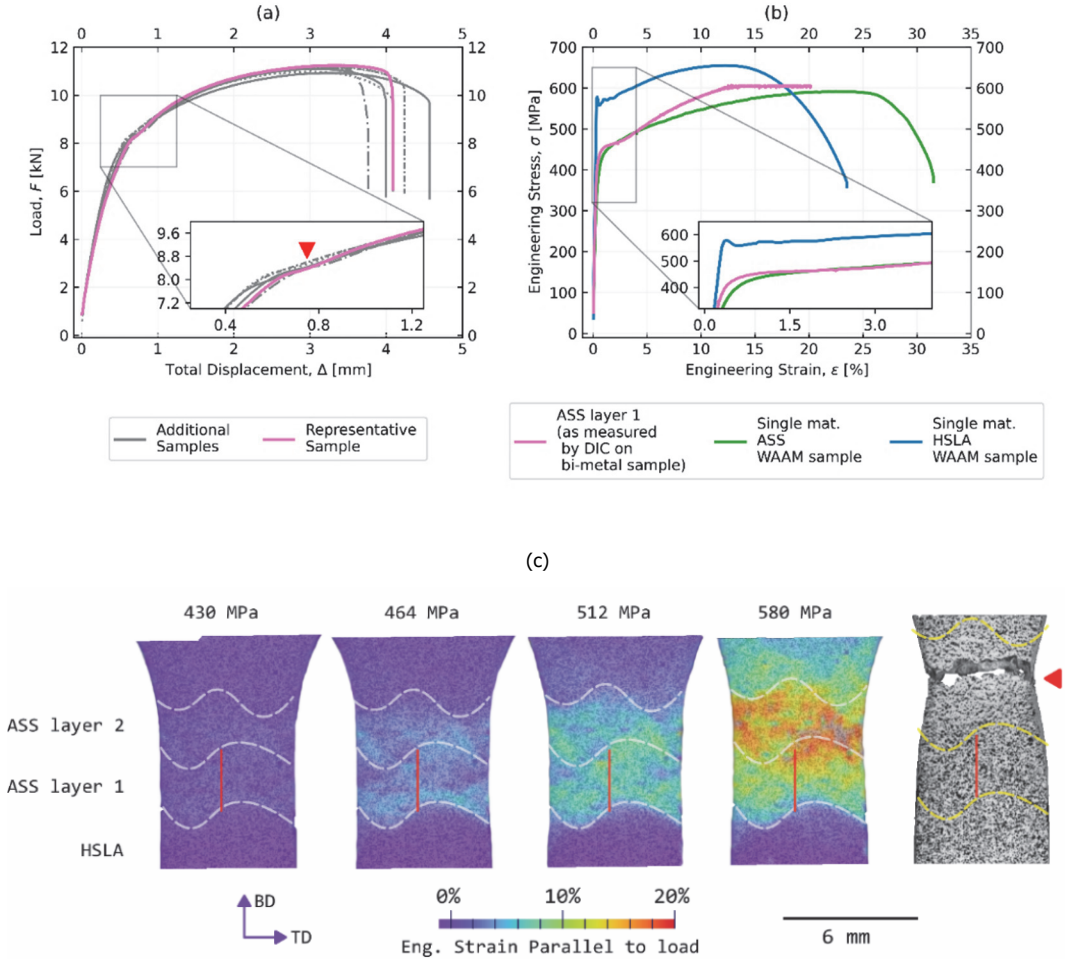

Figure 3-16 (a) Load-Displacement curves of bi-metal tensile coupons, with inset showing position of inflection point as highlighted by the red marker. (b) Stress-Strain curves for the interface layer (AS steel layer 1) obtained from DIC measurements with a virtual gauge length such as the one shown in red in (c). Reference curves for mono-material specimens are included for AS steel and HSLA steel. Strain distribution maps in (c) indicate engineering strain component in the direction of the tensile load. Approximate location of AS steel layers 1 and 2 are delimited with dashed lines. Failure location is highlighted with a red marker.

3.4. CHAPTER CONCLUSIONS

Additive manufacturing establishes a path to producing functionally graded components. A clear challenge when attempting to do so is the mixing of dissimilar alloys, and the consequences therefrom. Throughout this chapter, functional grading of a High-Strength Low-Alloy (HSLA) steel with an Austenitic Stainless Steel (AS steel) is carried out

by manufacturing a bi-metal structure through Wire Arc Additive Manufacturing (WAAM). While there has been prior research on this material combination, it is yet to be adequately described the nature of the microstructure observed. A comprehensive analysis of the microstructure of this highly heterogeneous interface is essential to establish an adequate correlation with its observed functional performance. Thus, the work provides a detailed description of the microstructural features observed at the dissimilar interface layer. It does so in a holistic approach, including phase constitution, chemical composition, crystallography and complemented by thermomechanical modeling and characterization of its bulk mechanical properties. After in-depth characterization at macro-, micro- and nano- length scales of the interface between both alloys, the following conclusions are made:

- Macroscopic examination of the interface layer revealed the formation of ferritic bands alongside austenite. EPMA analysis detected chromium and nickel segregation, matching the spatial location of the ferritic bands. For the heat input used (0.22 kJ/mm), the cladding austenitic stainless steel reaches a level of dilution of 25% from its original composition, as measured by the average chromium value across the diluted layer.
- The Schaeffler diagram is useful to predict mixed AS steel layer microstructure. However, the chosen deposition parameters yield heterogeneous mixtures in the melt pool, leading to chemical composition variations at the fusion boundary and within the weld metal.
- Bainitic ferrite coexists with martensite at the HSLA steel and first-deposited AS steel fusion line. Crystallographic analysis shows a Bain-like orientation relationship in all ferrite phases with the surrounding austenite matrix. Parent Austenite Grain (PAG) reconstruction supports crystallographic alignment of primary austenite grains during solidification, confirming grain boundary migration and growth of the austenite phase across the fusion boundary.
- Beyond the fusion boundary, the interface layer contains stratified ferrite alongside an austenite matrix. Most ferrite within austenite grains have the same crystallographic orientation. Some ferritic islands exhibit bainitic features with an acicular morphology containing smaller parallel lath packages.
- Multi-bead depositions behave as a large heat sink during the solidification and cooling of the deposited material. Although solidification and cooling

rates may be high in multi-bead deposits, and even more so when deposited using Cold-Metal Transfer, they are not high enough to form organized dislocation cell walls of segregated elemental composition in the AS steel matrix, as those observed in laser-DED methods.

- Hardness indentations reveal the effect of islands within the first AS steel layer up to 250 μm away from the fusion boundary. In these islands hardness may reach 371 $HV_{0.2}$, or about 50% higher than the surrounding material.
- Digital image correlation during tensile testing reveals a comparable quasi-static behaviour of the first AS steel interface layer with that behaviour displayed by the neighbouring AS steel layers. At lower stress levels, deformation concentrates in the region of the dissimilar fusion boundary, but further deformation localizes within the 2nd AS steel layer all throughout necking and failure.

Through the extent of this work, a better link between the alloys chosen, the microstructure formed after deposition and the local mechanical properties is provided. The microstructural characterization presented is a necessary empirical study for the further prediction of the mechanical and functional performance of large-scale HSLA-AS steel bi-metal components produced by additive manufacturing. Subsequent chapters delve into the mechanical properties at and around the interface will be characterized and correlated with the microstructural features observed in this study.

3.5. CHAPTER REFERENCES

[1] S. Sridar, N. Sargent, X. Wang, M. A. Klecka, and W. Xiong, "Determination of Location-Specific Solidification Cracking Susceptibility for a Mixed Dissimilar Alloy Processed by Wire-Arc Additive Manufacturing," *Metals (Basel)*, vol. 12, no. 284, 2022, doi: https://doi.org/10.3390/met12020284.

[2] S. Wang, C. Chen, J. Ju, J. Zhou, and F. Xue, "Suppression of LME cracks in Sn bronze-steel system based on multi-material additive manufacturing," *Mater Lett*, vol. 335, no. December 2022, p. 133775, 2023, doi: 10.1016/j.matlet.2022.133775.

[3] A. Mishra, A. R. Paul, M. Mukherjee, R. Kumar, and A. Kumar Sharma, "Evaluation of Cu-Ti dissimilar interface characteristics for wire arc additive manufacturing process," *Rapid Prototyp J*, vol. 29, no. 2, pp. 366–377, 2023, doi: 10.1108/RPJ-05-2022-0142.

[4] J. N. DuPont and C. S. Kusko, "Technical note: Martensite formation in austenitic/ferritic dissimilar alloy welds," *Welding Journal (Miami, Fla)*, vol. 86, no. 2, 2007.

[5] F. Mas *et al.*, "Heterogeneities in local plastic flow behavior in a dissimilar weld between low-alloy steel and stainless steel," *Materials Science and Engineering A*, vol. 667, pp. 156–170, 2016, doi: 10.1016/j.msea.2016.04.082.

[6] M. R. U. Ahsan, A. N. M. Tanvir, T. Ross, A. Elsawy, M. S. Oh, and D. B. Kim, "Fabrication of bimetallic additively manufactured structure (BAMS) of low carbon steel and 316L austenitic stainless steel with wire + arc additive manufacturing," *Rapid Prototyp J*, vol. 26, no. 3, pp. 519–530, 2019, doi: 10.1108/RPJ-09-2018-0235.

[7] Md. R. U. Ahsan *et al.*, "Heat-treatment effects on a bimetallic additively-manufactured structure (BAMS) of the low-carbon steel and austenitic-stainless steel," *Addit Manuf*, vol. 32, no. October 2019, p. 101036, 2020, doi: 10.1016/j.addma.2020.101036.

[8] K. U. Rani *et al.*, "Wire Arc Additive Manufactured Mild Steel and Austenitic Stainless Steel Components: Microstructure, Mechanical Properties and Residual Stresses," *Materials*, vol. 15, no. 20, 2022, doi: 10.3390/ma15207094.

[9] F. Ornath, J. Soudry, B. Z. Weiss, and I. Minkoff, "Weld Pool Segregation During the Welding of Low Alloy Steels With Austenitic Electrodes.," *Welding Journal (Miami, Fla)*, vol. 60, no. 11, pp. 1227–1230, 1981.

[10] "3Dprint AM 46," 2018, *Böhler Welding by Voestalpine*.

[11] "3Dprint AM 316L," 2019, *Böhler Welding by Voestalpine*.

[12] AWS, *AWS A5.9/A5.9M:2012 Specification for Bare Stainless Steel Welding Electrodes and Rods*. Miami, USA: AWS A5.9/A5.9M:2012, American Welding Society, 2012.

[13] AWS, *AWS A5.18/A5.18M:2005 Specificaiton for Carbon Steel Electrodes and Rods for Gas Shielded Arc Welding*. Miami, USA: ANSI, 2005.

[14] A. Ermakova, A. Mehmanparast, S. Ganguly, J. Razavi, and F. Berto, "Investigation of mechanical and fracture properties of wire and arc additively manufactured low carbon steel components," *Theoretical and Applied Fracture Mechanics*, vol. 109, no. May, p. 102685, 2020, doi: 10.1016/j.tafmec.2020.102685.

[15] O. D. Acevedo, "Assessing Mechanical Performance of Dissimilar Steel Systems Made Via Wire-Arc Additive Manufacturing," University of Tennessee, 2021.

[16] V. Laghi *et al.*, "Experimentally-validated orthotropic elastic model for Wire-and-Arc Additively Manufactured stainless steel," *Addit Manuf*, vol. 42, no. February, p. 101999, 2021, doi: 10.1016/j.addma.2021.101999.

[17] F. Armao, L. Byall, and D. Koteckl, *Gas Metal Arc welding: Product and Procedure Selection*. Cleveland, OH: Lincoln Global Inc., 2014.

[18] ISO, *ISO/TR 18491 Welding and allied processes - Guidelines for measurement of welding energies*. Geneva: ISO, 2015.

[19] J. N. DuPont and A. R. Marder, "Thermal efficiency of arc welding processes," *Welding Journal (Miami, Fla)*, vol. 74, no. 12, pp. 406-s, 1995.

[20] H. K. D. H. Bhadeshia, *Worked examples in the Geometry of Crystals*, 2nd ed. Brookfield, USA: The Institute of Materials, 2006.

[21] ASTM, *ASTM E92-17 Standard Test Methods for Vickers Hardness and Knoop Hardness of Metallic Materials*. West Conshohocken, USA.: ASTM International, 2017. doi: 10.1520/E0092-17.2.

[22] NEN-ISO, *EN-ISO 6892-1:2019 Metallic materials - Tensile Testing - Part 1: Method of test at room temperature*, no. december 2019. Belgium, 2019.

[23] C. Wang, T. G. Liu, P. Zhu, Y. H. Lu, and T. Shoji, "Study on microstructure and tensile properties of 316L stainless steel fabricated by CMT wire and arc additive manufacturing," *Materials Science and Engineering A*, vol. 796, no. June, 2020, doi: 10.1016/j.msea.2020.140006.

[24] A. K. Maurya, C. Pandey, and R. Chhibber, "Influence of heat input on weld integrity of weldments of two dissimilar steels," *Materials and Manufacturing Processes*, vol. 38, no. 4, pp. 379–400, 2023, doi: 10.1080/10426914.2022.2075889.

[25] W. F. Savage, E. F. Nippes, and E. S. Szekeres, "Study of Weld Interface Phenomena in a Low Alloy Steel.," *Welding Journal (Miami, Fla)*, vol. 55, no. 9, 1976.

[26] S. Kou and Y. K. Yang, "Fusion-boundary macrosegregation in dissimilar-filler welds," *Welding Journal (Miami, Fla)*, vol. 86, no. 10, pp. 303–312, 2007.

[27] Q. Zhang *et al.*, "Predictions of solute mixing in a weld pool and macrosegregation formation during dissimilar-filler welding of aluminum alloys: Modeling and experiments," *Journal of Materials Research and Technology*, vol. 9, no. 6, pp. 12080–12090, 2020, doi: 10.1016/j.jmrt.2020.08.109.

[28] J. C. Lippold and D. J. Kotecki, *Welding Metallurgy and Weldability of Stainless Steels*, 1st ed. John Wiley & Sons, 2005.

[29] J. A. Self, D. L. Olson, and G. R. Edwards, "The stability of austenitic weld metal," in *Proceedings of IMCC*, Kiev, Ukraine, 1984.

[30] J. Self, "Effects of composition upon martensite transformation temperature of austenitic steel welds," Colorado School of Mines, Golden, Colorado, 1986.

[31] C. Huang, P. Kyvelou, R. Zhang, T. Ben Britton, and L. Gardner, "Mechanical testing and microstructural analysis of wire arc additively manufactured steels," *Mater Des*, vol. 216, p. 110544, 2022, doi: 10.1016/j.matdes.2022.110544.

[32] T. Sourmail, "Precipitation in creep resistant austenitic stainless steels," *Materials Science and Technology*, vol. 17, no. 1, pp. 1–14, 2001, doi: 10.1179/026708301101508972.

[33] A. F. Padilha, D. M. Escriba, E. Materna-Morris, M. Rieth, and M. Klimenkov, "Precipitation in AISI 316L(N) during creep tests at 550 and 600 °C up to 10 years," *Journal of Nuclear Materials*, vol. 362, no. 1, pp. 132–138, 2007, doi: 10.1016/j.jnucmat.2006.12.027.

[34] C.-C. Hsieh and W. Wu, "Overview of Intermetallic Sigma (σ) Phase Precipitation in Stainless Steels," *ISRN Metallurgy*, vol. 2012, no. 4, pp. 1–16, 2012, doi: 10.5402/2012/732471.

[35] J. Smith, W. Xiong, J. Cao, and W. K. Liu, "Thermodynamically consistent microstructure prediction of additively manufactured materials," *Comput Mech*, vol. 57, no. 3, pp. 359–370, Mar. 2016, doi: 10.1007/s00466-015-1243-1.

[36] P. Schaffnit, C. Stallybrass, J. Konrad, F. Stein, and M. Weinberg, "A Scheil–Gulliver model dedicated to the solidification of steel," *Calphad*, vol. 48, pp. 184–188, Mar. 2015, doi: 10.1016/j.calphad.2015.01.002.

[37] J. Smith *et al.*, "Linking process, structure, property, and performance for metal-based additive manufacturing: computational approaches with experimental support," *Comput Mech*, vol. 57, no. 4, pp. 583–610, Apr. 2016, doi: 10.1007/s00466-015-1240-4.

[38] B. Bocklund, L. D. Bobbio, R. A. Otis, A. M. Beese, and Z.-K. Liu, "Experimental validation of Scheil–Gulliver simulations for gradient path planning in additively manufactured functionally graded materials," *Materialia (Oxf)*, vol. 11, p. 100689, Jun. 2020, doi: 10.1016/j.mtla.2020.100689.

[39] Z. Yang, A. Richter, H. Sun, Z.-K. Liu, and A. M. Beese, "Circumventing cracking in grading 316L stainless steel to Monel400 through compositional modifications in directed energy deposition," *Materialia (Oxf)*, vol. 38, p. 102283, Dec. 2024, doi: 10.1016/j.mtla.2024.102283.

[40] P. Pichler, B. J. Simonds, and J. W. Sowards, "Measurements of thermophysical properties of solid and liquid NIST SRM 316L stainless steel," *J Mater Sci*, vol. 55, no. 9, pp. 4081–4093, 2020, doi: 10.1007/s10853-019-04261-6.

[41] E. E. Soderstrom, K. M. Scott, and P. F. Mendez, "Calorimetric Measurement of Droplet Temperature in GMAW," *Weld J*, vol. 90, no. 4, pp. 77–84, 2011.

[42] T. W. Nelson, J. C. Lippold, and M. J. Mills, "Nature and evolution of the fusion boundary in ferritic-austenitic dissimilar weld metals, Part 1 - nucleation and growth," *Welding Journal (Miami, Fla)*, vol. 78, no. 10, pp. 329-s, 1999.

[43] T. W. Nelson, J. C. Lippold, and M. J. Mills, "Nature and evolution of the fusion boundary in ferritic-austenitic dissimilar metal welds - Part 2: on-cooling transformations," *Welding Journal (Miami, Fla)*, vol. 79, no. 10, 2000.

[44] J. W. Elmer, S. M. Allen, and T. W. Eagar, "Microstructural development during solidification of stainless steel alloys," *Metallurgical Transactions A*, vol. 20, no. 10, pp. 2117–2131, 1989, doi: 10.1007/BF02650298.

[45] H. Inoue, T. Koseki, S. Ohkita, and M. Fuji, "Formation mechanism of vermicular and lacy ferrite in austenitic stainless steel weld metals," *Science and Technology of Welding and Joining*, vol. 5, no. 6, pp. 385–396, 2000, doi: 10.1179/136217100101538452.

[46] T. W. Nelson, J. C. Lippold, and M. J. Mills, "Investigation of boundaries and structures in dissimilar metal welds," *Science and Technology of Welding and Joining*, vol. 3, no. 5, pp. 249–255, 1998, doi: 10.1179/stw.1998.3.5.249.

[47] ASTM, *Standard test method for determining volume fraction by systematic manual point count*. E562-19. ASTM International, 2020. doi: 10.1520/E0562-19E01.2.

[48] P. Thome, M. Schneider, V. A. Yardley, E. J. Payton, and G. Eggeler, "Crystallographic Analysis of Plate and Lath Martensite in Fe-Ni Alloys," *Crystals (Basel)*, vol. 12, no. 2, pp. 11–13, 2022, doi: 10.3390/cryst12020156.

[49] D. N. Githinji, S. M. Northover, P. J. Bouchard, and M. A. Rist, "An EBSD study of the deformation of service-aged 316 austenitic steel," *Metall Mater Trans A Phys Metall Mater Sci*, vol. 44, no. 9, pp. 4150–4167, 2013, doi: 10.1007/s11661-013-1787-7.

[50] M. S. Baek, K. S. Kim, T. W. Park, J. Ham, and K. A. Lee, "Quantitative phase analysis of martensite-bainite steel using EBSD and its microstructure, tensile and high-cycle fatigue behaviors," *Materials Science and Engineering A*, vol. 785, no. April, 2020, doi: 10.1016/j.msea.2020.139375.

[51] S. Kou, "Macrosegregation in the Fusion Zone," in *Welding Metallurgy*, Hoboken: John Wiley & Sons, In., 2021.

[52] S. L. Shrestha, A. J. Breen, P. Trimby, G. Proust, S. P. Ringer, and J. M. Cairney, "An automated method of quantifying ferrite microstructures using electron backscatter diffraction (EBSD) data," *Ultramicroscopy*, vol. 137, pp. 40–47, 2014, doi: 10.1016/j.ultramic.2013.11.003.

[53] G. I. Rees and B. H.K.D.H., "Thermodynamics of acicular ferrite nucleation," *Materials Science and Technology*, vol. 10, no. 5, pp. 353–358, 1994.

[54] K. M. Bertsch, G. Meric de Bellefon, B. Kuehl, and D. J. Thoma, "Origin of dislocation structures in an additively manufactured austenitic stainless steel 316L," *Acta Mater*, vol. 199, pp. 19–33, 2020, doi: 10.1016/j.actamat.2020.07.063.

[55] L. Liu *et al.*, "Dislocation network in additive manufactured steel breaks strength – ductility trade-off," *Materials Today*, vol. 21, no. 4, pp. 354–361, 2018, doi: 10.1016/j.mattod.2017.11.004.

[56] M. Izadi, A. Farzaneh, M. Mohammed, I. Gibson, and B. Rolfe, "A review of laser engineered net shaping (LENS) build and process parameters of metallic parts," *Rapid Prototyp J*, vol. 26, no. 6, pp. 1059–1078, 2020, doi: 10.1108/RPJ-04-2018-0088.

[57] M. Bayerlein, H. J. Christ, and H. Muchrabi, "Plasticity-induced maretensitic transofrmation during cyclic deformaton of AISI304 stainless steel," *Material Science and Engineering*, vol. 114, pp. L11–L16, 1989, doi: https://doi.org/10.1016/0921-5093(89)90871-X.

[58] J. Lu *et al.*, "Stacking fault energies in austenitic stainless steels," *Acta Mater*, vol. 111, pp. 39–46, 2016, doi: 10.1016/j.actamat.2016.03.042.

4. QUASISTATIC AND FRACTURE BEHAVIOR OF A FUNCTIONALLY GRADED BI-METAL INTERFACE

Wire arc additive manufacturing (WAAM) offers a novel approach to fabricate functionally graded components. By changing the wire consumable between layers, chemical grading can be used to obtain specific properties across a part's volume. This is an interesting approach to design large metal components that achieve unconventional performance in demanding engineering applications, such as sulphide-resistant pressure vessels or sea ballast piping with extended lifetime. However, challenges derived from dissimilar material combinations draw the need to study the effect of compositional grading on the mechanical properties. This study focuses on the deformation and fracture toughness behaviour of WAAM-fabricated high-strength low-alloy (HSLA) and austenitic stainless (AS) steel bi-material specimens, particularly examining the diluted interface layer obtained during deposition. Tensile testing results indicate that the elastic modulus at the interface matches that of un-diluted AS steel (157 ±17 GPa) along the build direction. Fracture toughness showed a lower J_{IC} (180 kJ·m^{-2}) when compared to the undiluted AS steel (459 ±69 kJ·m^{-2}) and HSLA steel (408 ±25 kJ·m^{-2}). Scanning electron microscopy and electron backscatter diffraction are used to establish a connection between the microstructure at the interface and the observed mechanical properties. It is concluded that deformation at the interface is in large controlled by the deformation-induced martensitic transformation of metastable austenite. These results underline the influence of chemical dilution on the deformation mechanisms and fracture behaviour of HSLA and AS steel bi-material parts, which needs to be accounted for in the design of parts composed by this bi-metal couple.

This chapter is an adaptation from the publication Galán Argumedo, J. L., Riemslag, A. C., Hermans, M. J. M., & Popovich, V. A. (2025). Fracture behaviour of functionally graded bi-material interface produced by wire arc additive manufacturing. *Materials Science and Engineering: A*, *928*(February). https://doi.org/10.1016/j.msea.2025.148034

4.1. INTRODUCTION

Useful reference work has been published on the mechanical properties of individual alloys in the context of WAAM. Both AS and HSLA steel alloys typically show high fracture toughness. On the one hand, Dirisu et al. [1] showed that ER70S-6 yields an average value of J_Q = 453 kJ·m^{-2}. The superior toughness of this alloy compared to other higher grade HSLA steels is attributed to the refined, non-equiaxed, woven nature of acicular ferrite and the minimal presence of martensite-austenite constituents. These values are consistent with those reported by Ermakova et al. [2] for the same alloy. On the other hand, a large dispersion of values is cited for fracture toughness of AS steel. Kumar et al. [3] reported toughness results for WAAM'ed ER316L to be 160 kJ·m^{-2}. However, this result suggests lower toughness than previous all-weld tests, with typically reported values between 400 and 450 kJ·m^{-2} [4], [5]. Kumar et al. [3] observed nonetheless that the formation of mechanical twins and eventual fracture is affected by the dislocation structure and grain boundary density of additively manufactured parts. It has been demonstrated that the work hardening mechanism governing the deformation of austenitic alloys with low stacking fault energy (SFE) is dependent on local chemistry, environment, and strain rate [6]. This is an important effect to be considered when discussing the deformation behaviour of a diluted austenitic alloy, such as the interface layer, and for the prediction of the mechanical behaviour of bimetal components.

Considering a defect-tolerant approach to the manufacturing of an AS-HSLA steel component, it is relevant to study the deformation and toughness behaviour of the interface layer in detail. Fracture toughness testing of bi-material specimens conveys nonetheless its own set of challenges. Standard testing specifications require testing specimens to described through a single elastic modulus [7], [8]. Much work has been carried out to further extend the formulations of J-integral to overcome the constraints of elastic homogeneity set by Rice [9] in his original formulation. Jin and Noda [10] postulated solutions for the problem of J-integral formulation across several inhomogeneous situations, including a non-constant elastic modulus along the crack path. Alternative solutions were offered by several authors [11], [12], [13], as functional grading became more popular. These solutions rely however on smooth continuous functions of the elastic modulus. A formulation for the J-integral in the vicinity of sharp boundaries between phases was proposed by Weichert and Schulz [14]. The authors point out that their solution can only be implemented when sharp boundaries are contained within the contour integral considered, making it cumbersome to implement. A practical approach

was implemented by Ghorbanpour et al. [15] through finite element analysis. The authors defined a sample-specific stress-intensity function by using the conventional J-integral formulation at incremental crack extension steps.

Having established the potential benefits and challenges of functional grading through wire arc additive manufacturing, the aim of this chapter is defined. Through a combination of quasi-static tensile loading, fracture toughness testing, and microstructural evaluation, the fracture toughness and deformation behaviour of the interface layer is to be studied. The results provide evidence on the deformation mechanisms governing the plastic strain and final fracture. Complimentary FEM analysis is implemented to bridge the gap between the available standard procedure of fracture toughness testing and the specific requirements set by testing non-isotropic specimens.

4.2. MATERIALS AND METHOD

4.2.1. Wire arc additive manufacturing and consumables

To obtain the specimens necessary for mechanical testing, a functionally graded block and two complimentary mono-material blocks were additively manufactured using WAAM. All blocks had approximate dimensions of 210 x 90 x 60 mm^3 and were built on a low-alloy high strength steel plate substrate. The wire consumables, deposition parameters, overlap

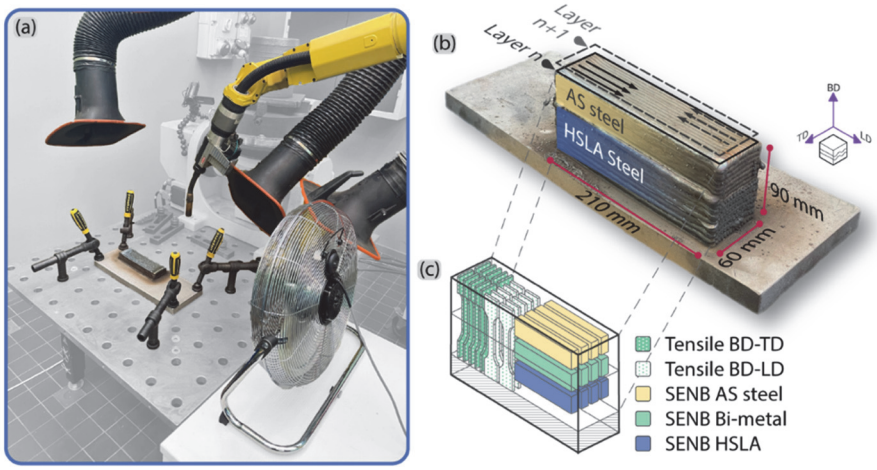

Figure 4-1 (a) Wire arc additive manufacturing setup, (b) bi-material block with schematic of building strategy and (c) schematic indicating approximate sample orientation and location within bi-material block.

geometry and substrate characteristics are identical to the ones described in section 3.2 of this thesis. The AM setup, finished bi-material block and disposition of mechanical samples extracted from the bi-material block are shown in Figure 4-1.

4.2.2. Tensile testing and in-situ digital image correlation

To evaluate the mechanical properties of both mono-material and the bi-material blocks, quasi-static tensile testing was conducted. Four sets of tensile specimens were manufactured for this purpose. The first two sets consisted of bi-material specimens extracted from two plane orientations along the build direction (BD), as illustrated in Figure 4-1 (c). These orientations were chosen to assess the effects of strain concentration caused by the geometry of the interface layer. Dog-bone specimens were extracted from flat slabs with a thickness of 3 ±0.02 mm. The final shape was achieved through waterjet cutting, featuring a constant width of 6 ±0.03 mm and a gauge length of 35 ±0.15 mm. The surface quality was maintained as obtained by machining operations. The remaining two sets of specimens were extracted from mono-material blocks with similar dimensions to those depicted in Figure 4-1. The specimens were machined and turned to obtain a cylindrical cross-section of Ø 6 ±0.03 mm along a gauge length of 35 ±0.15 mm.

Tensile testing was carried out using a Zwick Z100 universal testing rig operating under crosshead displacement control. Load was measured with a cell rated for 100 kN. The test was performed at a displacement rate of 0.005 $mm \cdot s^{-1}$ under ambient conditions. The zero-point setting, gripping, and post-mortem calculations were conducted in accordance with EN-ISO 6892-1:2019 [16]. For mono-material specimens, strain measurements up to 5% were obtained using a clip-on Zwick Digiclip extensometer with a 20 mm gauge length; beyond this strain value, the extensometer was removed, and strain was derived from an adjusted crosshead displacement. For bi-material specimens, strain was measured through DIC around the interface layer. A commercial LIMESS Q400-3D stereo camera system was employed for this purpose, featuring a 40 mm focal length and a 5 MPixel camera sensor operating at a 0.5 Hz acquisition rate. Specimen surfaces were prepared with speckle patterns using aerosol paint. The captured images were post-processed using LIMESS ISTRA 4D software. Tensile stress-strain curves were obtained by measuring local engineering strain along the interface by an average of five parallel digital strain gauge lines.

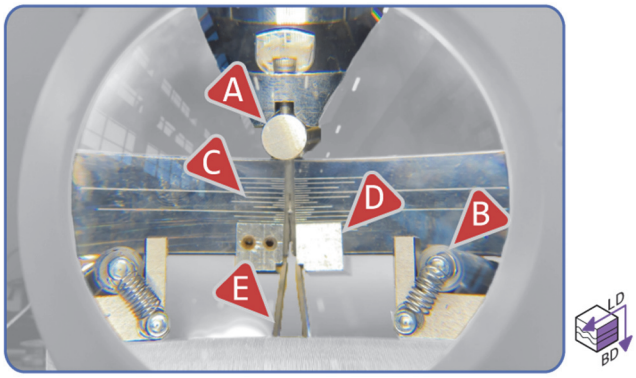

Figure 4-2 Experimental fracture toughness set-up. Markers highlight bend-test fixtures (A and B), pre-fatigued and grooved SENB sample with 0.5 mm markings (C), demountable knife edges (D), and legs of the attached clip-on crack opening displacement (COD) gauge (E).

4.2.3. Fracture toughness measurements

Fracture toughness measurements were carried out using SENB specimens subjected to three-point bending, following the specifications set by the relevant ASTM standard [8]. For this purpose, the sample size consisted of 4 specimens per location along the height of the bi-metal block. The specimens were machined from the bi-material block at the locations indicated in Figure 4-1 (c). Cutting and machining operations to extract testing specimens generally relieves the material, especially if the specimen is small compared to their parent part (Jiang et al. 2013). Specimens are thus designed as small as possible to benefit from stress relaxation. Specimens had a width (W) of 20 mm and a thickness (B) of 10 mm. Bi-material specimens were machined in such way such that the interface layer can be found at a position $Z(BM)/W$ ranging between 0.45-0.6. Roller pin supports of Ø 12 mm were set at 80 mm centre-to-centre distance to conform with standard specifications. A starting notch of 0.4 mm width was created on each specimen using electrical discharge machining (EDM) to a depth of 3 mm. Specimen pre-fatigue was performed from a starting ΔK of 25.3 MPa·m$^{0.5}$, reduced every 0.5 mm of crack extension down to 12.7 MPa·m$^{0.5}$, until the pre-fatigue crack reached a length of 9 mm. This procedure followed an exponentially decreasing ΔK-gradient C:-0.23 mm^{-1} by increasing $K_{\min}$. Pre-fatigue crack length was monitored visually with position markings on the specimens' side faces. After pre-fatiguing, side-grooving was performed on all specimens to obtain a reduced thickness of B_n of 8 ±0.03 mm. An illustration of a specimen and key elements of the experimental setup are depicted in Figure 4-2.

As mostly stable tearing is expected, the testing procedure follows the process to construct R-curves from single specimens. For this purpose, an Instron Electroplus E20000 testing bench was used and controlled with the Bluehill Fracture software. Load was measured with a cell suitable for ±15 kN. Specimens were loaded under displacement control at a consistent rate of 0.2 mm·min^{-1}, typically reaching the target load P_m within 40 to 50 seconds. Load-unload cycles were employed every 50 µm of crack mouth opening displacement (CMOD), with an unloading range of 1 kN and no hold time. CMOD was recorded using an Epsilon 3541 clip-on gauge extensometer with a 3 mm gauge length and a maximum extension of 2.5 mm. The gauge was attached to the specimen via detachable knife edges, secured with screws tightened onto the specimen's surface. Since the tip of the clip-on COD gauge was positioned 2 mm above the sample surface, adjustments to the CMOD readings were necessary following NEN-ISO 12135:2021 [7].

Special considerations were made to derive the crack-length extension measurements. For mono-material specimens, this parameter was estimated from the CMOD compliance through established standard relationships [7], [8]. Nevertheless, a special case is considered for the bi-material specimens. To account for the sharp change in elastic modulus, the elastic compliance is corrected proportionally by the results obtained through FEM.

4.2.4. Special considerations for J_{el} and elastic compliance of a bi-material SENB specimen

Standardized test procedures provide a framework to reliably obtain comparable material properties. However, international standards do not foresee testing bi-material specimens for fracture toughness. This is especially relevant when considering a bi-material specimen with heterogeneous elastic properties. Additional considerations are required to capture the interface effect of a bi-material sample. To bridge the dependency of standard testing procedures on a single elastic modulus E, a numerical approach is used. This is done following the procedure proposed by Ghorbanpour [17] for functionally-graded SENB specimens. A linear-elastic Finite Element Analysis of a bi-material specimen was used to capture the effect on J_{el} and elastic compliance. This FEM model definition and result analysis is explained in detail in Annex B. In short, a solution space for J_{el} and the elastic compliance are obtained by varying the length of a modelled crack a, and the position of the bi-material interface layer $Z(BM)$. Correction functions are used to capture the difference between the numerical results and the analytical expressions available in

standard testing procedures. These functions are later used to translate the experimentally captured data into results useful for analysis of a bi-material sample. The first correction function is defined as follows:

$$\Gamma_J^E = \frac{J_{el,FEM,BM}}{G^E_{Analyt,MM}} \qquad (Eq.4.1)$$

where $J_{el,FEM,BM}$ is the FEM solution of the elastic component of the J-integral for a bi-material sample and $G^E_{Analyt,MM}$ is the analytical description of elastic energy per unit area of crack extension for a mono-material sample with elastic modulus E. A superscript ^{E} denotes that this function definition depends on the reference value of elastic modulus E used. The function is used to determine $J_{el(i)}$ for bi-material specimen, such that:

$$J_{el(i)} = \Gamma_J^E \cdot \frac{K^2_{(i)} \cdot (1-\nu^2)}{E}. \qquad (Eq.4.2)$$

where $K_{(i)}$ is the stress intensity factor, which is in turn dependent on the load, geometry of the specimen and crack length, and, ν is the Poisson's ratio. The subscript (i) is used to indicate a load-reload cycle in the single-specimen fracture toughness test procedure.

The second function bridges the difference between the mono-material and the bi-material specimen compliance. Given that CMOD measurements are used to estimate the crack length during testing, it is necessary to later derive the crack extension values per load-unload cycle Δa. This function is defined as follows:

$$\Gamma_C^E = e_{a/W} \cdot \frac{C(a/W)_{FEM,BM}}{C(a/W)^E_{Analyt,MM}}. \qquad (Eq.4.3)$$

where $C(a/W)$ is the function that relates crack length for a SENB specimen and the CMOD-load compliance. The function $e_{a/W}$ describes the inverse of the fitted error function encountered between the analytical and numerical compliance values for mono-material specimens. This function is explained in detail in Eq. C1 through C3 in Annex C. The subscript FEM, BM denotes the a/W values obtained through FEM modelling of a bi-material sample, and the subscript *Analyt, MM* indicates the a/W values obtained from the analytical expression presented in Eq. B6 in Annex B. The compliance relationship presented in Eq. C1 in Annex C and the correction function Γ_C^E are used to predict the crack size during testing through the following relationship:

$$C(a/W)_{BM,(i)} = \Gamma_C^E \cdot C(a/W)^E_{Analyt,MM(i)}. \qquad (Eq.4.4).$$

Note that the solution of $C(a/W)$ is dependent on the elastic modulus of the material at which the crack front is found. This modification is sufficient to evaluate the relationship between the specimen compliance and the crack length for every i-th load-unload cycle using the standard procedures.

4.2.5. Fractographic analysis

To carry out the post-mortem inspection, the tested SENB specimens were cracked open under cryogenic conditions. To avoid corrosion of the fracture surface caused by de-icing, the cracked specimens were warmed up in water at room temperature, followed by a short submersion in isopropanol and final drying in air. The AS steel mono-material specimens were heat-stained at 370 °C for 15 minutes and left to cool down to room temperature and cracked open thereafter.

Macroscopic characterization was carried out with a VHX-7000N Keyence digital microscope equipped with optical shadow effect mode. Microscopic characterization was carried out with a Thermo Fisher Helios G4 PFIB UXe Dual Beam Microscope. Images were obtained with an ETD secondary electron detector at an accelerating voltage of 10 kV.

4.2.6. Crystallographic analysis

SENB specimens were used for crystallography characterization at the crack flanks by means of electron back-scatter diffraction (EBSD). The surfaces mapped coincide with the longitudinal centreline of each specimen. Standard metallographic preparation included sanding up to #2000 paper grit, polishing with 0.3 µm and 0.1 µm diamond suspensions, and a final step of polishing with an active oxide suspension (OPS).

The camera and software used for crystallographic mapping were proprietary of AMETEK EDAX integrated into the Thermo Fischer Helios equipment. Mapping was done under 15 kV accelerating voltage and a current of 13 nA. Step size was adjusted depending on the size of the region of interest and it is indicated on the caption under each map shown in the results and discussion sections. Inverse Pole Figure (IPF) maps are shown with <001> || BD. Clean-up was done cautiously to avoid incurring in large biases: Neighbour orientation correlation with a grain tolerance angle of 5° was used to clear points with a confidence index lower than 0.1. Kernel average misorientation (KAM) values were obtained for the 1st nearest neighbour with a maximum misorientation of 5°. Grain boundary texture was calculated as a harmonic series expansion of rank 16, with a

Gaussian half-width of 5° and misorientation boundaries between 5° and 180°. The grain boundary misorientation distribution function (MDF) encompasses a [0°-65°] misorientation range, [0°-45°] azimuthal range, and a [0°-55°] polar range. Only correlated MDF values were considered.

4.3. RESULTS

4.3.1. Tensile testing and in-situ digital image correlation

To investigate the effect of dilution at the interface layer, digital image correlation (DIC) is used to measure deformation during quasi-static tensile loading. The results are useful to describe two specific phenomena: the elastic behaviour and the work-hardening behaviour of the bi-material interface. The former is necessary for the description of the stress concentration effect in a bi-material 3-point bending SENB sample. The latter is used to describe the effect of dilution on the work-hardening mechanisms of the interface layer.

The elastic portion and early yielding stages of the quasi-static tensile curves are presented in Figure 4-3. The figure shows the engineering stress-strain relationship measured on the BD-TD plane in Figure 4-3 (a), and the BD-LD plane in Figure 4-3 (b). For comparison, stress-strain relationships are provided for AS and HSLA steel mono-material samples in Figure 4-3 (c) and (d) respectively. In favour of clarity, the strain-stress relationship of a representative sample is plotted in colour per orientation, while test repetitions are shown in grey. For the two chosen specimens, corresponding DIC maps are shown along the line for the indicated load levels.

Despite the overall similarity in tensile response of all measured specimens, a difference is observed through strain localization. This difference is made evident through the DIC map insets. Strain maps are shown at two strain levels for each plane measured in Figure 4-3 (a-b). Strain partitioning is observed at the fusion lines between the different materials volumes for the specimens mapped in the BD-TD plane. Given an averaged 0.55 % engineering strain, local values register 1.2 % strain localized at the fusion lines bounding the diluted interface layer. This comes in contrast with the centre of the sample, where the diluted interface layer is located, and values are registered to match with the bulk behaviour. For the BD-LD plane, the specimens display a clearly different behaviour with regards of strain partitioning. At an engineering strain level of 0.55 %, the mapped surface shows shear banding. These bands extend through the fusion line between the

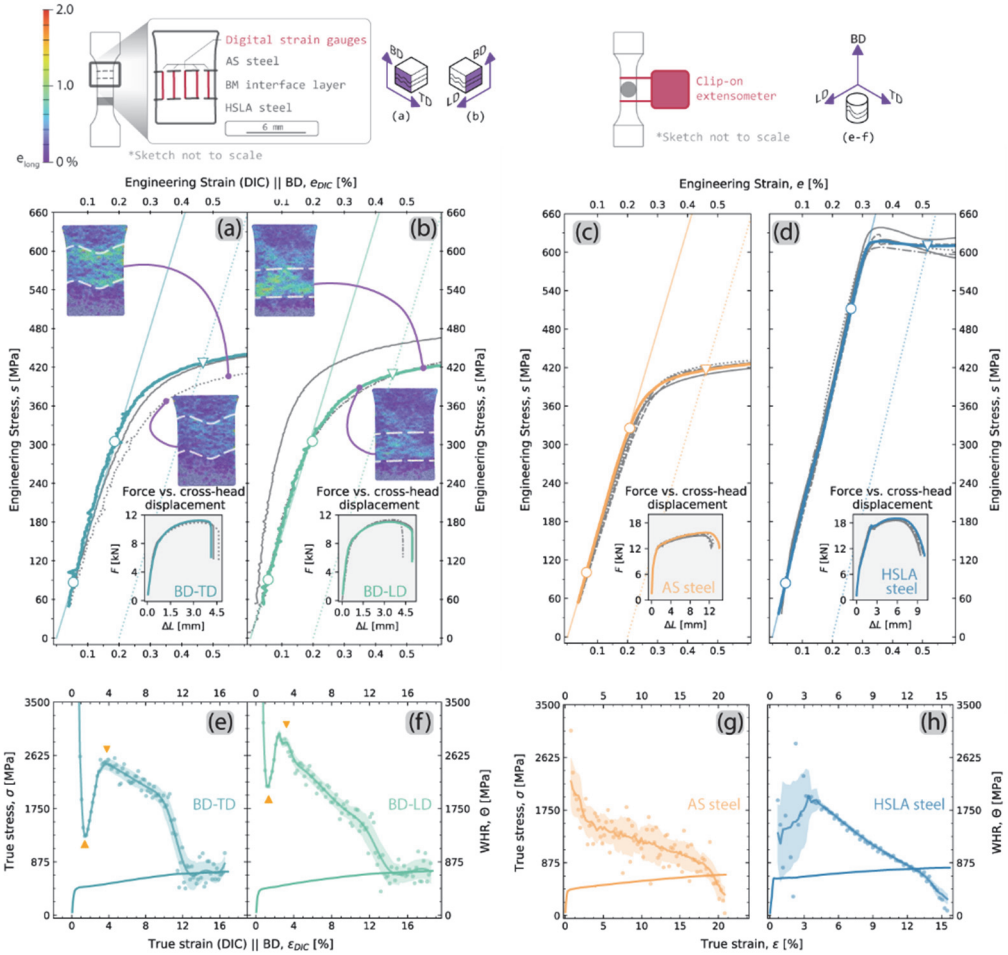

Figure 4-3 Elastic modulus and yield behaviour as obtained through DIC measurements for (a) BD-TD and (b) BD-LD bi-material sample groups, and as obtained through physical strain gauge measurements for (c) AS steel and (d) HSLA steel specimens. The yield values are obtained through a 0.2 % intercept proof strength. An example of true-strain, true stress and work-hardening rates are shown for (e) BD-TD and (f) BD-LD specimens, and (g) AS steel and (h) HSLA steel specimens.

interface layer and the AS steel material volume. Despite the differences in localized strain, the averaged elastic modulus measured across the diluted interface is consistent on both planes. The most relevant quasi-static properties derived from these results are presented in Table 4-1.

True stress-true strain relationships and work-hardening rates are shown on in Figure 4-3 (e) and (f). A detailed elaboration on the auxiliary relationships used to obtain these values and the computation of the average line and error bands are explained in the Annexes. The work-hardening rate (WHR) shows a non-linear relationship with respect to true strain ε. This relationship is shown in Figure 4-3 (e) and (f), contrasting with the WHR behaviour of both AS and HSLA steels shown in (g) and (h). The data shows a valley within $\varepsilon < 2$ %, followed by a subsequent crest, regardless of the orientation of the sample measured. The position of the crest typically lies between 3 % < ε < 4.5 %. Values of WHR measured at the crest vary substantially, yielding Θ = 2255 MPa with a standard deviation of 433 MPa if both specimen orientations are considered. Notwithstanding the variability of results, the overall trend remains consistent: an assisting work-hardening mechanism controls the plastic deformation of the diluted interface layer, different from that of the undiluted material. For metastable austenitic stainless steels, this observation has been associated with either the twinning induced plasticity (TWIP) or the transformation induced plasticity (TRIP) effect, depending on the local chemistry and temperature. This is addressed in detail in section 4.4.

Table 4-1 Mechanical properties for the bi-material interface and undiluted WAAM'ed AS and HSLA steels.

	Elastic Modulus E	**Yield Strength $s_{0.2}$**	**Tensile Strength s_u**	**Avg. strain-hardening exponent n**
	GPa	MPa	MPa	log(MPa)
Mono-material AS steel	154 ±8	418 ±5	548 ±4	0.197 ±0.011
Diluted interface	157 ±17	412 ±13	592 ±11	0.210 ±0.020
Mono-material HSLA steel	197 ±6	608 ±7	683 ±9	0.122 ±0.009

4.3.2. Fracture toughness and R-curve determination

Fracture toughness testing on both mono-material and bi-material SENB specimens adhered to the established standards [8]. This section presents the results obtained from single-specimen testing methodology. A standard procedure was followed for mono-

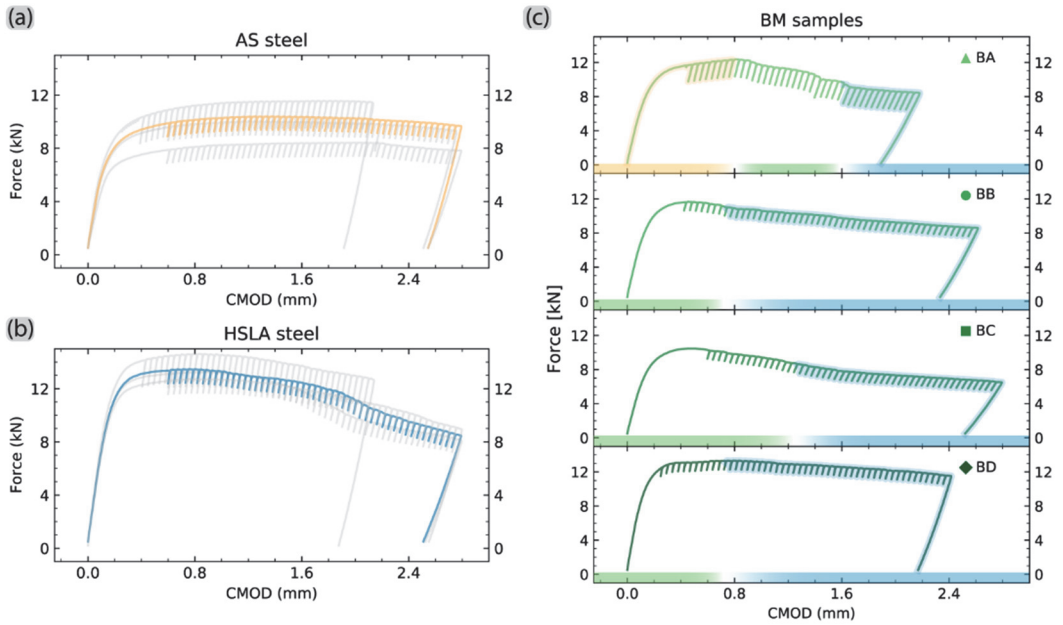

Figure 4-4 CMOD-force curves for mono-material (a) AS steel, (b) HSLA steel, and for (c) bi-material specimens. For (a) and (b), repetition tests are shown in grey. In (c), yellow highlights the load-unload cycles where the crack front is estimated to lie within the undiluted AS steel, blue highlights those cycles within HSLA steel, and the bare green line represents the diluted interface layer.

material specimens. The formulations presented on the previous section are used to correct the standard analytical solutions for the specific case of a bi-material specimen.

The load-CMOD curves for all test specimens are presented in Figure 4-4. Figure 4-4 (a) and (b) show mono-material results, highlighting the load-displacement behaviour of a sample arbitrarily chosen. Figure 4-4 (c) shows the load-CMOD values for bi-material specimens. The four bi-material specimens are identified individually with labels BA through BD to easily correlate the resistance curve (R-curve) results and features found through fractography and crystallography. For each sample presented, coloured highlighting is used to denote different material volumes through which the crack extends; yellow highlighting denotes undiluted AS steel, whilst blue indicates HSLA steel. The bare green line is thus the domain of interest, as it denotes the diluted interface layer.

Using the results obtained from the load-CMOD curves, it is possible to construct the resistance curves for the specimens tested. For mono-material specimens, the standard relationships to obtain J and Δa [8] are used. The R-curves of these sample groups are

shown in Figure 4-5 (a) and (b) for the AS steel and the HSLA steel. The numerical results for J_Q, Δa_Q, and proposed values for J_{IC} are tabulated in Table 4-2. Benchmark reference values are provided compare the obtained J_{IC} values with comparable literature.

Figure 4-5 (c) presents the R-curves taking into consideration the relationships established by Eq. 4.2 and Eq. 4.4. The results are presented with a slight modification: all values of Δa are shown relative to the position of the bi-material interface $Z(BM)$. This is done to highlight the similarities in the $J-\Delta a$ given each material domain, and discriminate the differences caused by the position of the initial crack length a_0. The inset in this figure presents the R-curves without such modification for the specimens BB and BD. These specimens were chosen, as they comply with the minimum number of valid $J-\Delta a$ data pairs necessary for determination of J_Q obtained solely along the diluted interface. These valid data pairs (points) are encircled in Figure 4-5 (c) for ease of identification.

The position of a_0 at the start of the test has a clear effect on the values of J for bi-material specimens. As mentioned before, sample BA in Figure 4-5 (c) shows the special condition, where a_0 lies within the material domain of AS steel. For the nine Δa increments registered within this domain, a larger accumulated value of J is obtained. This result gives an indication of the behaviour of a bimetal part but conveys biased values of J if the behaviour of the diluted interface is to be quantified. For the rest of the specimens, more points become available for statistical analysis as the value of $Z(BM)-a_0$ increases. This also conveys in turn higher values of J_{el} when the crack crosses the dissimilar fusion line.

The R-curves shown in Figure 4-5 reveal important specimen-specific differences between the diluted interface layer and its surroundings. Except for sample BA, a drop of J is observed at the position where $\Delta a = a_0 - Z(BM)$ for every bi-metal sample. Also, specimens BA trough BC display locations where large increments of Δa were measured for small corresponding increments of J. Both specimens BA and BB show one of these large Δa steps within the last 0.5 mm ahead of the dissimilar fusion line between the interface layer and the HSLA steel. This observation exemplifies the variability in crack-propagation behaviour across the interface layer.

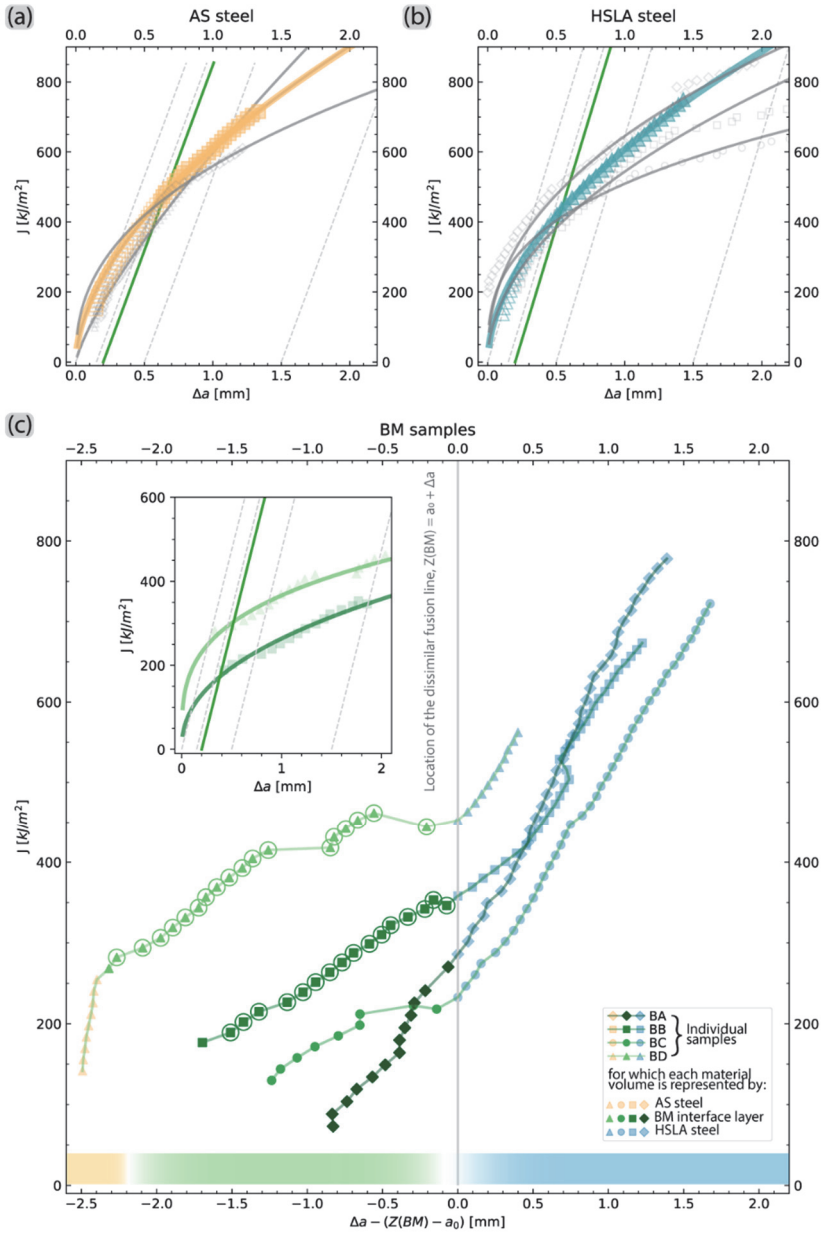

Figure 4-5 Representative R-curves for (a) AS steel specimens and (b) HSLA steel specimens, with valid data -pairs available for regression shown as filled markers. Repetition test shown in grey. (c) Bi-material specimens R-curves plotted relative to the position of the bi-material fusion line. Data points qualifying for further J_Q analysis are circled and shown in inset with corresponding exponential regression results.

Table 4-2 Overview of fracture toughness results. Error values are defined as ± one standard deviation.

Sample group	J_Q	Δa_Q	J_{IC}	Literature reported J_{IC}
	kJ/m²	mm	kJ/m²	kJ/m²
AS Steel	463 ±57	0.66 ±0.07	459 ±69	400-450 †
Bi-material	236 ±78	0.46 ±0.06	180 *	-
HSLA steel	436 ±59	0.54 ±0.05	408 ±26	420 ±73 ‡

* Result obtained from a single valid specimen

† All-weld GMAW or GTAW metal as reported by different sources [4], [18]

‡ [2], [19]

4.3.3. Post-mortem inspection of the fracture surface

Fractographic inspection is used to determine relevant geometrical and fracture features. Figure 4-6 shows the location of a_0, a_p, and $Z(BM)$ for selected specimens. With exception of sample BA, a_0 resides within the material volume of the diluted interface layer as shown in Figure 4-6 (a-c). Considerable variations of the initial a_0 and final a_p crack positions are observed. This is true not only for the bi-material specimens, but also for the AS steel specimens shown in Figure 4-6 (d-f) and the HSLA steel specimens shown in Figure 4-6 (g-i). These deviations are evaluated against a limiting deviation value of $0.1 \cdot (b_o \cdot B_n)^{1/2}$ as detailed in the standard test method [8]. Specimens that did not comply with this criterion were excluded from statistical considerations of J_{IC} cited on Table 4-2.

Alongside the position and geometry of the crack front at a_0 and a_p, distinct macroscopic fracture structures are observed. On Figure 4-6 (a), markers A, B and C indicate the zones corresponding to pre-fatigue, stable tearing, and final fracture. The prefatigued zone shows a faceted fracture surface obtained across the AS steel. This topography changes at a_0, where the driving crack propagation behaviour changes from fatigue to steady tear. The small regions of undiluted AS steel and HSLA steel deformed by steady tear show a very similar topographic character than that of the mono-material specimens. There, the corresponding fracture surfaces show indications of ridges and large plastic deformation obtained by tearing. By comparison, the region belonging to the diluted bi-material interface shows a less faceted fracture surface than that of the

undiluted counterparts. However, a feature common to all bi-material specimens is indicated by marker D. At this location, the fusion line between the diluted interface layer and the HSLA steel is outlined by a small region which shows signs of low deformation capacity.

A few relevant microscopic fracture features obtained from the bi-material specimens are presented in Figure 4-7. Figure 4-7 (a-d) show typical traits as obtained through the stable tearing process, including detail areas for the undiluted AS steel in Figure 4-7 (b), the diluted interface layer in Figure 4-7 (c) and HSLA steel in Figure 4-7 (d). Both the AS steel and the diluted interface layer fracture surfaces show dimple diameters within the range of a couple of microns, although dimple sizes appear to be marginally larger in the diluted material. In both cases, second phase particles inhabit many of the dimples pictured, suggesting a coupled void nucleation effect during the early tearing process. Figure 4-7 (c) shows with red markers disperse locations of quasi-cleavage fracture. Figure 4-7 (d) on the other hand shows a large band of quasi-cleavage fracture alongside the dissimilar fusion line, matching the features observed under macroscopic inspection. This region matches that of martensite obtained after allotropic transformations occurring after solidification and cooling, hereon referred to as allotropic martensite. Enlarged dimples in varying directions and secondary crack features about $Z(BM)$ are shown in both Figure 4-7 (a) and (d). These suggest complex tearing interactions leading to the fracture of this material volume.

Continuing with the microscopic fractography, Figure 4-7 (e-f) present traits that suggest sources of low local tear resistance. Marker A in Figure 4-7 (e) shows an alternative location of a band of quasi-cleavage fracture, like that at $Z(BM)$. This band is nevertheless not commonly found elsewhere. Additional features include the brittle deformation structures occasionally observed at the bead roots of the diluted interface layer. These are pointed by markers D in Figure 4-7 (f) and marker E in Figure 4-7 (g), as found on specimens BD and BA correspondingly. A combination of ductile and cleavage fracture is observed in the depth of these faults, suggesting a complex interaction of several different local structures. An additional example of secondary cracking is pointed by marker C. This last feature is fully populated by dimple structures, showing otherwise no signs of brittle deformation.

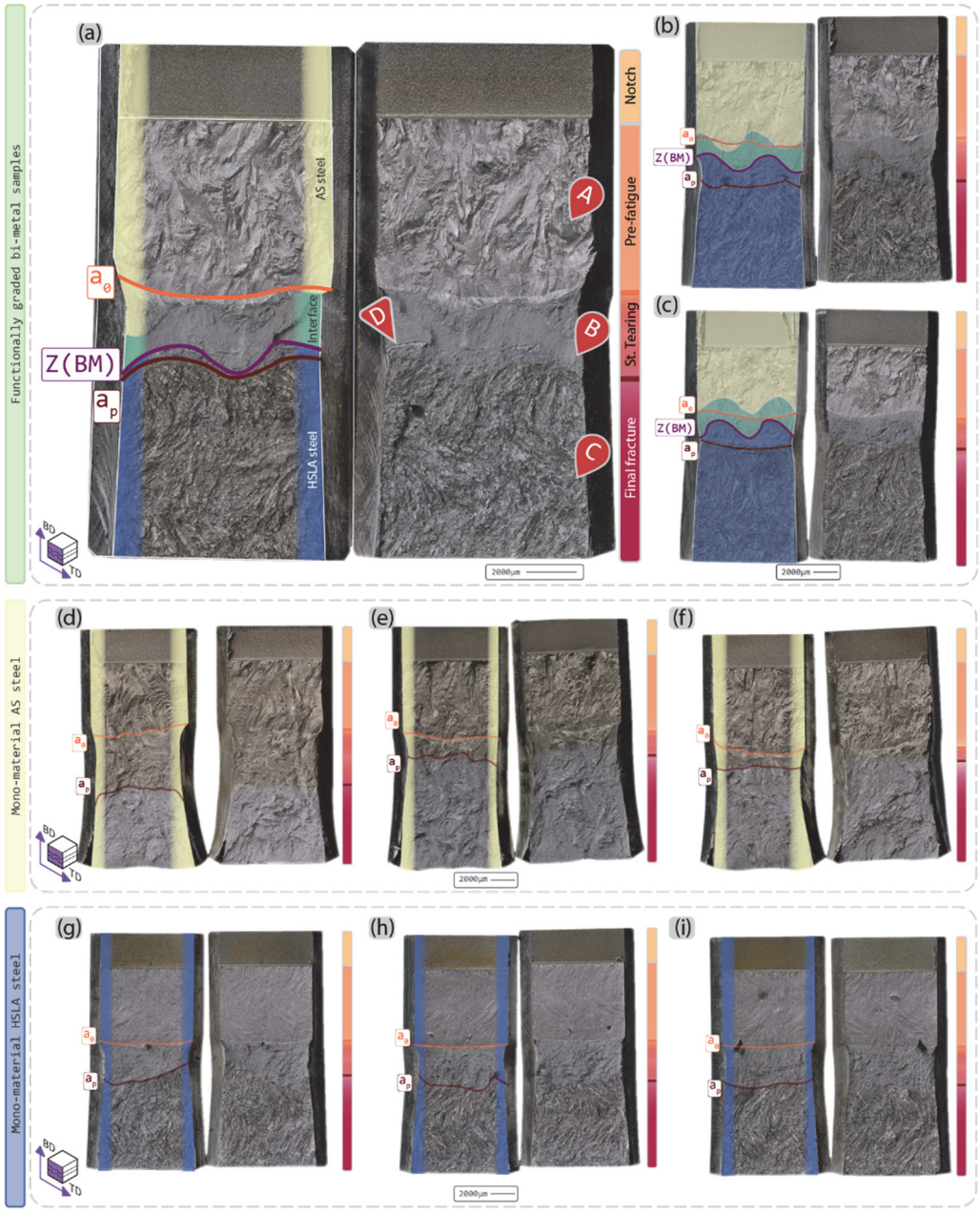

Figure 4-6 Post-mortem macroscopic fractographic images of specimens (a) BA, (b) BB and (c) BD. (d-f) Fracture surfaces of AS steel specimens and (g-i) fracture surfaces of HSLA steel specimens. Features between two fracture surfaces of the same sample appear mirrored.

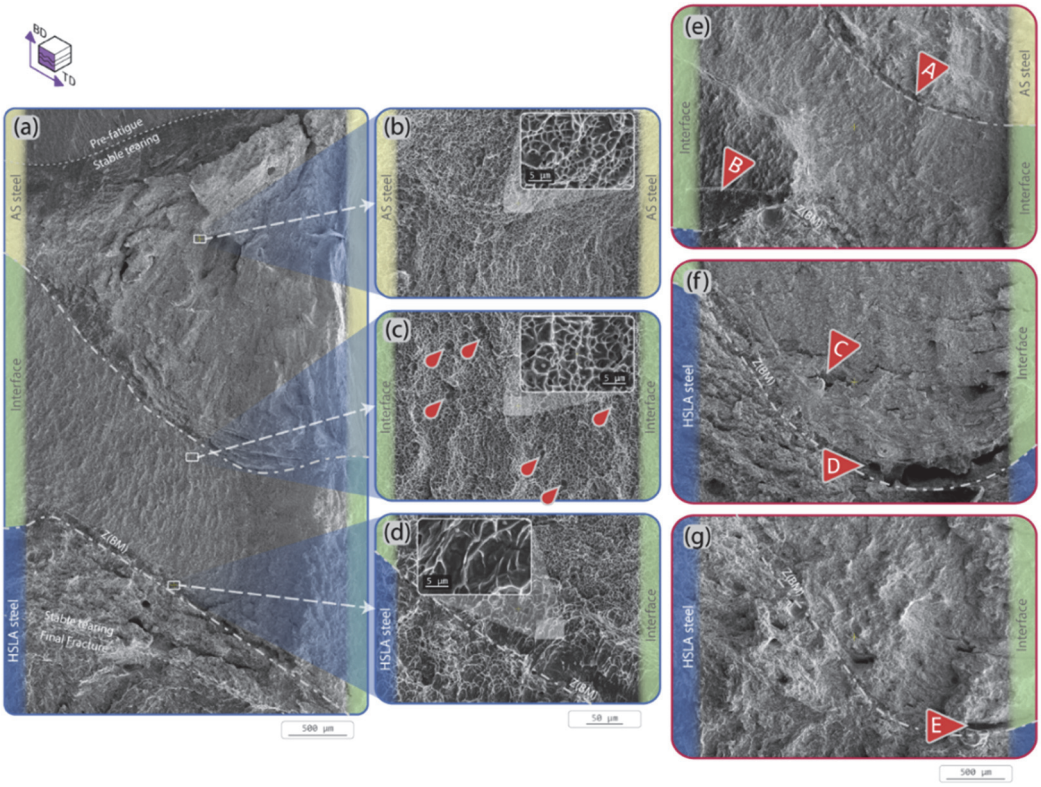

Figure 4-7 Features observed under microscopic fractographic inspection of bi-material specimens. Micrographs include the (a - d) typical fracture features encountered along the stable tear region of a bi-material sample in the (b) AS steel, (c) diluted interface material volumes and (d) the vicinity of the dissimilar fusion line. Micrographs (e-g) display examples of features encountered sporadically on different bi-material specimens, such as (e) signs of brittle fracture at the fusion boundary between the diluted interface layer and the undiluted AS steel (f) secondary crack formation perpendicular to the primary crack plane and (g) heterogeneous deformation along the dissimilar fusion line.

4.3.4. EBSD mapping of fracture profile

The investigation of the fracture surface through microscopy provides detailed information of the stable tearing process. Nonetheless, plastic deformation can largely dissipate strain energy and restrict crack extension. To understand the plastic deformation mechanisms, it is useful to study the crack flanks and their microstructural features. Chapter 3 shows that the chemistry and microstructure at the interface better resemble those of an austenitic stainless steel alloy and less so to those of a HSLA steel alloy. A comparative benchmark is thus provided in detail for the stainless alloy to easily discuss the peculiarities of the interface layer. For this, EBSD mapping is utilized. For the latter

alloy, the reader is referred to the study of Costin et al. [20], which provides an in-depth analysis of deformation mechanisms during fracture of acicular ferrite.

The crack flanks of a mono-material AS steel sample are studied as a baseline reference. This is done to compare how plastic strain is accommodated for this material volume in an undiluted condition. Figure 4-8 (a) shows a low-magnification IPF map. The map is composed by IPF orientation mapping with a grey-scale overlay of the Image Quality (IQ) values. The IQ greyscale overlay is used to highlight defects on crystal lattice, such as grain boundaries and regions of high dislocation density. Assuming adequate sample preparation and indexing parameters, shear bands, twin boundaries, as well martensite characteristically show low indexing values as well.

Detailed mapping for the pre-fatigue and the steady tear crack flank domains are provided in Figure 4-8 (b-d) and Figure 4-8 (e-g). At each location IPF, KAM and phase maps are included. The location of the crack flank presented in Figure 4-8 (b-d) shows minimal lattice misorientation within individual grains. This indication of low deformation is accompanied by low first-neighbour KAM values, and a typical FCC fraction for this welding consumable. These values contrast with the location of the crack flank presented in Figure 4-8 (e-g). There, high lattice rotations within the deformed grains are found, alongside high KAM values, suggesting a high density of geometrically necessary dislocations. At a_0, a dense network of shear bands is appreciated. The density of shear bands as well as the KAM values decrease in the lower portion of the map. Within the region mapped the FCC fraction remains constant, nonetheless, indicating that the dominant deformation mechanism does not include the transformation of austenite into α' martensite under the chosen testing conditions. It is useful to note that the first value of Δa for this sample is estimated to be 146 µm; the second load-unload cycle is expected to be located out of range beneath the region mapped.

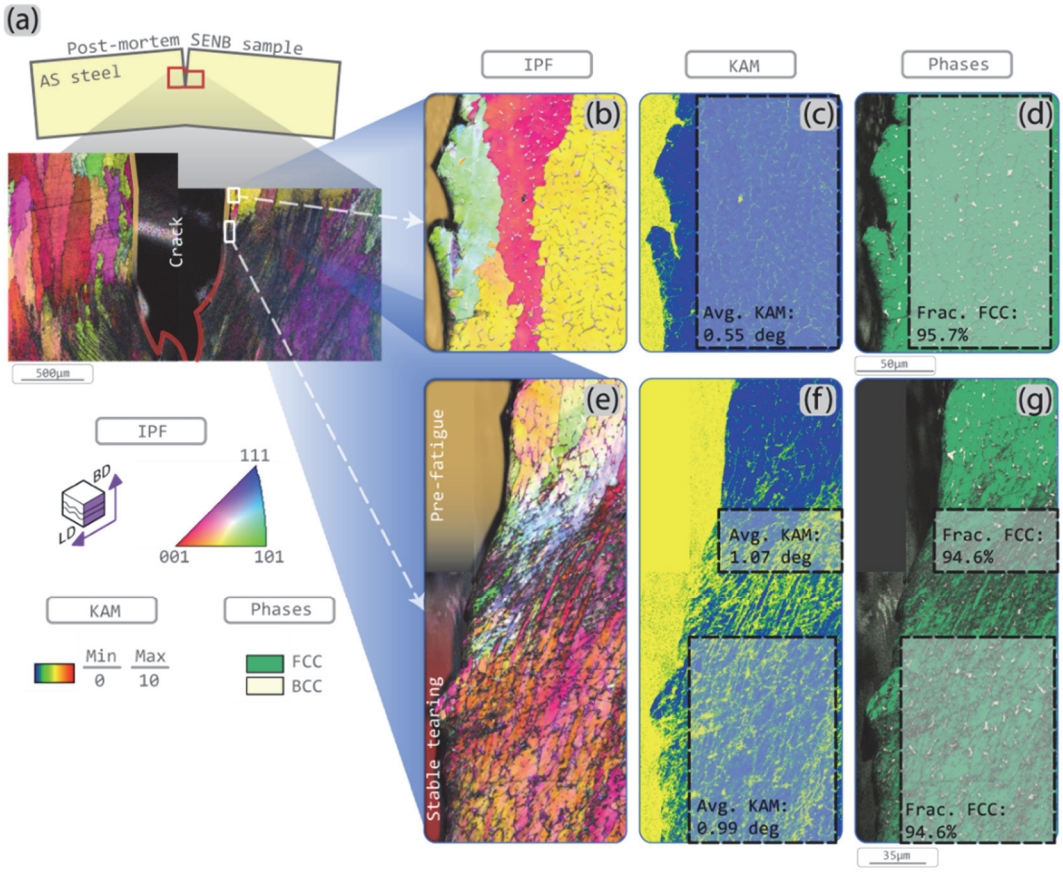

Figure 4-8 EBSD map of crack flanks on an AS steel sample. (a) IPF map stitched at a low resolution and 5 µm step size showing both crack flanks about a_0. (b-d) IPF, KAM and phase maps of a crack flank in the region of pre-fatigue mapped with a step size of 0.1 µm. (e-g) IPF, KAM and phase maps stitched along the crack flank at a_0, mapped with a step size of 0.1 µm. For IPF maps, <001> || BD.

Having established a baseline of values and identified some deformation mechanisms in the undiluted AS steel, it is possible to characterize by comparison those traits found in the diluted interface layer. The crack flanks of a bi-material sample are mapped in Figure 4-9. Figure 4-9 (a) shows a low-magnification IPF mapping of both crack flanks. Following the same representation method, image quality maps are superimposed as greyscale. On this occasion, martensite bands are identified along the lower region of the diluted interface layer. They are pointed by the red markers on the left flank, although they may be found on either side of the crack. They are confirmed to be martensite by inspection of their morphology in un-deformed regions and are considered to originate

from the local chemistry when the diluted layer solidified. For this reason, due to the high content of ferrite and martensite phase fractions in the region mapped, IQ cannot be attributed to the deformation of the crystal lattice.

A detailed map of the region where the crack flank and this martensite band converge is shown under higher resolution in Figure 4-9 (c-e). Although a clear distinction cannot be made between α' and α through this indexing method due to the minute differences between both lattice parameters, the lath packaging morphology of martensite is clearly apparent in Figure 4-9 (c). Also, Figure 4-9 (e) indicates that only a small portion of this

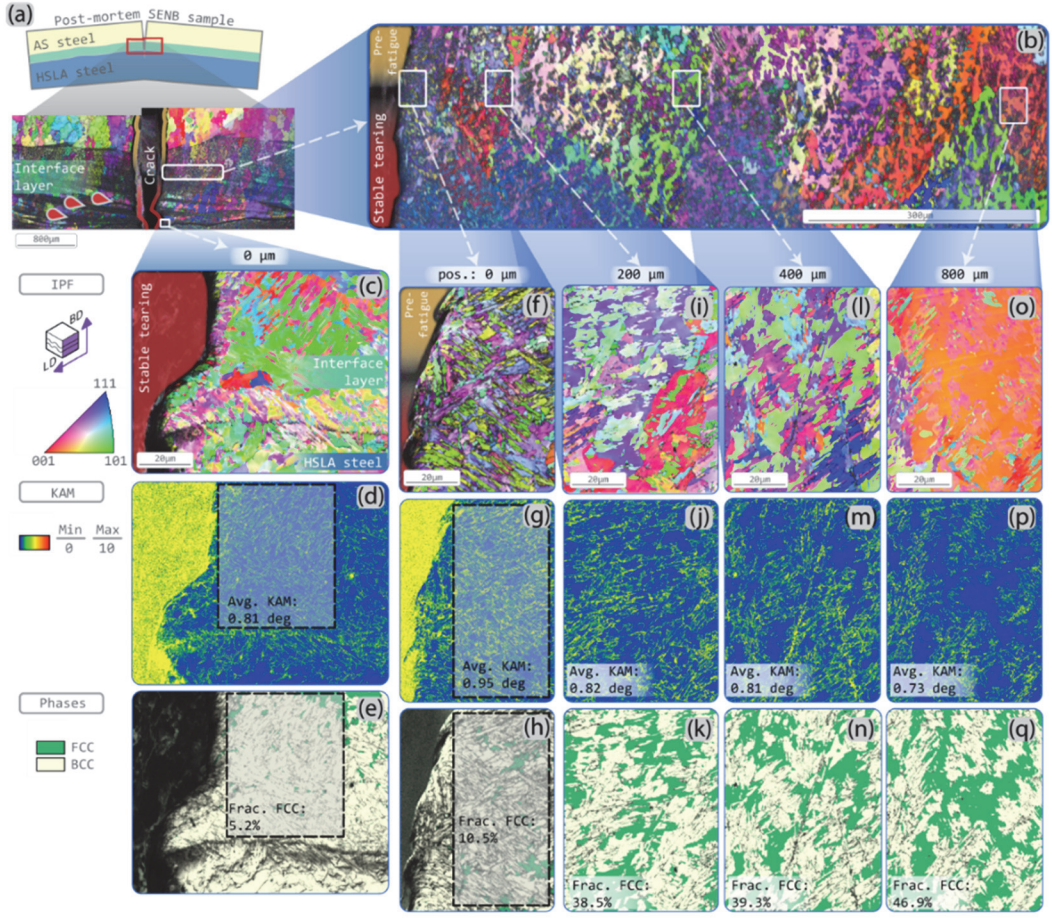

Figure 4-9 EBSD mapping of crack flanks of a bi-material sample. (a) IPF map stitched at a low resolution and 5 µm step size showing both crack flanks at a_0. (b) (c) A low magnification map of the region next to the a_0 point. (c-e) IPF, KAM and phase maps of the crack flank region in vicinity of the dissimilar fusion boundary. Detailed maps found within (b) alongside a_0 at the crack flank (f-h), as well as 100 µm (i-k), 400 µm (l-n), and 800 µm (o-q) away from the flank. For all IPF maps, <001> || BD.

region of interest is retained austenite. This detail belongs to a volume fraction that cannot accommodate large plastic deformation, as confirmed by geometry of the crack flanks surrounding this region. This is visible, as the adjacent material above and below shows large deformation into the crack plane.

It is the case that a_0 lies within the diluted interface layer in this sample and section plane observed. This location develops large amounts of plastic strain to accommodate crack blunting and eventual crack extension. To distinguish the effect of different levels of strain imposed on the microstructure, it is useful to study the features observed as a function of distance from the crack flank. Detailed maps have been set at 0, 200, 400 and 800 µm for this purpose. The specific locations of these maps are shown in Figure 4-9 (b).

A distinction between allotropic martensite and that obtained through large deformation is required. Directly on the crack flank, Figure 4-9 (f-h) shows the effect of the largest expected strain acting at the crack front. Like the microstructure found at the dissimilar fusion line, the crack flank at this location is mostly populated by martensite. This is identified by its morphology, high KAM values and primarily BCC phase indexation. However, the KAM values and the fraction of FCC for the region of interest indicated in both Figure 4-9 (g) and (h) suggest a fundamental difference between this location and the one adjacent to the dissimilar fusion line Figure 4-9 (c) and (d). The KAM values of martensite are not expected to increase due to plastic strain, and KAM values obtained from allotropic martensite are measured at about 0.8 °. Thus, the martensite observed in Figure 4-9 (f) is considered to originate in large from a different driving force, namely, the strain-induced transformation of metastable austenite.

At more distant positions away the crack plane and into the crack flank, the distinction of martensite becomes less straightforward. The morphology of the BCC grains as observed in Figure 4-9 (i-o) does not suggest clear martensitic characteristics. Nevertheless, FCC fraction appears to increase as a function of distance, and KAM values gradually decrease. Both these values are indicated for the maps in Figure 4-9 (j-p) and Figure 4-9 (k-q). These values provide an undirect quantitative measure derived from the mechanisms accommodating plastic strain.

4.4. DISCUSSION

4.4.1. Accounting for bi-material interface in fracture toughness testing

The effect of a sharp change in E-modulus across the bi-material interface has a clear impact in the numerical solution of the J-integral. As the solution for J_{el} on a bi-material specimen is demonstrably discontinuous, the numeric correction factor Γ_J^E introduces a discontinuity as well. The effect is made apparent when the elastic and plastic components of the experimentally obtained J-integral are compared. This is done in Figure 4-10, where (J_{el}, J_{pl}) data pairs are plotted. Figure 4-10 (a) and (c) show continuous functions for the values obtained from the AS steel and the HSLA specimens. Nonetheless, the non-continuous relationship between relative crack length a/W and Γ_J^E for bi-material specimens leads to a sudden drop in the estimated J_{el}. This relationship is shown in Figure 4-10 (b). Given the sample geometry, pre-crack length and loading conditions of the method chosen, this drop accounts for about 15 to 19 kJ/m^2 of elastic energy, or between 4 and 7 % of the total J value measured at the position where $a = Z(BM)$.

Although a discontinuity is observed in the function describing J_{el}, the relationship that describes the crack length as a function of compliance shows to be continuous. Data points relating these two values are presented in Figure 4-10 (d-f). The effect that the bi-material interface has on the elastic compliance curves is that each curve is offset from the others. Consequentially, larger values of $Z(BM)$ entail that the specimen becomes less stiff and thus more compliant in the presence of a crack. This has in turn a small effect on the evaluation of crack length. For example, given the specimens BB and BC under the same measured CMOD compliance of $2.0 \cdot 10^{-8}$ N/mm, a difference in position of $Z(BM)$ of 1.27 mm yields a difference of estimated crack length of 0.244 mm, or about 2.4 % relative error.

Alongside the intricacies derived from the mathematical description of J, other testing difficulties arise while trying to obtain and interpret data adequately. In terms of the pre-fatigue process, it is a non-trivial task to accurately estimate the crack depth before the fracture toughness test is completed. This opens the possibility to start the test within an unintended material domain. Such is the case for sample BA. Pre-fatiguing the sample up to an unnecessarily long crack leads to a smaller amount of material at the interface layer available to evaluate J_Q.

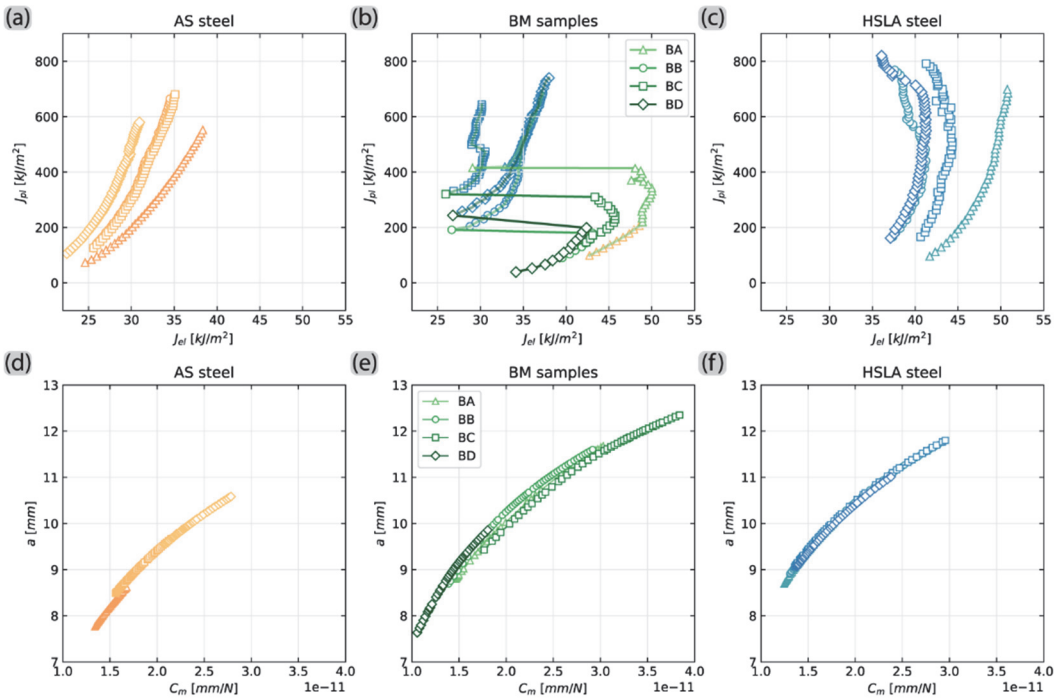

Figure 4-10 Elastic vs. plastic components of J for (a) AS steel, (b) bi-material specimens and (c) HSLA steel and corresponding elastic compliance vs. crack length for each material condition (d-f).

A particular challenge is derived from the geometry of the dissimilar fusion line itself. Standard testing methods use a provision to ensure the validity of the linear-elastic solution for J_{el}. As mentioned in section 4.2.3, it is required for the crack front to stay straight and perpendicular to the faces of the sample. This is enforced within a deviation of $0.1 \cdot (b_o \cdot B_N)^{1/2}$ at any point along the average positions of a_0 and a_p lines. This value is about 950 µm given the pre-fatigue crack length and the sample dimensions used in this study. All bi-material specimens comply with this provision when applied to the geometry of the interface layer. However, as the crack approaches the bi-material fusion line, local crack acceleration originating from the change in elastic domain is expected, in turn compromising the crack front straightness. The method implemented is considered sufficient to discern between the three material domains along a bi-material fusion line, although an accurate estimation on the position of the crack front, and with it, a direct correlation of defects found is challenging.

A closer look at the data used for regression is carried out to compare the differences in fracture behaviour of each material domain. To process the R-curve data shown in

Figure 4-5, the $J - \Delta a$ data pairs are used to fit an exponential function. It is from this fitted function that values J_Q and Δa_q are later derived. This entails that it possible to compare increments in J per increments in a in a log-log space at different test stages. The data is plotted as such in Figure 4-11 for the mono-material specimens of (a) AS steel and (c) HSLA steel. The data plotted in (b) for the bi-material specimens is limited to those crack extension steps measured within the bi-material interface. On the one hand it is made visible in the plots that both the AS steel and the HSLA mono-material data fall neatly together, displaying comparatively low dispersion. This can be correlated to the homogeneity in the crack propagation process across the different layers of the additively manufactured material. The diluted interface layer in the bi-material specimens, on the other hand, is more disperse. This speaks to the degree of variability in local fracture toughness. Although data clusters mostly at lower values of $\log(a_{i+1}/a_i)$, a standard deviation an order of magnitude higher than that of the mono-material specimens is obtained from the diluted interface layer. The fracture performance of the interface is thus the effect of a highly heterogeneous microstructure interacting with itself.

Shear banding, twinning, and metastable austenite transformation

The main strengthening mechanism at play across this bi-material part is revealed by the crack flanks of the cracked SENB specimens. It is observed that plastic strain is accommodated through shear banding, both on the undiluted AS steel and the diluted interface material volumes. For AS steels, specifically for 316L, this is well in line with the available literature. Twinning gives way to the exceptional work hardening providing this excellent mechanical performance [3], [21], [22]. However, this observation entails a non-trivial process along the diluted interface layer due to its heterogeneous chemistry. Instead of twinning, martensite is observed at the crack flanks. This does not relate clearly to the fracture deformation mechanisms typically observed across acicular ferrite [20], but better resembles the observations made on the deformation mechanisms controlling plasticity in metastable austenite [23]. Thus, a deeper discussion on the underlying mechanisms of shear banding is necessary.

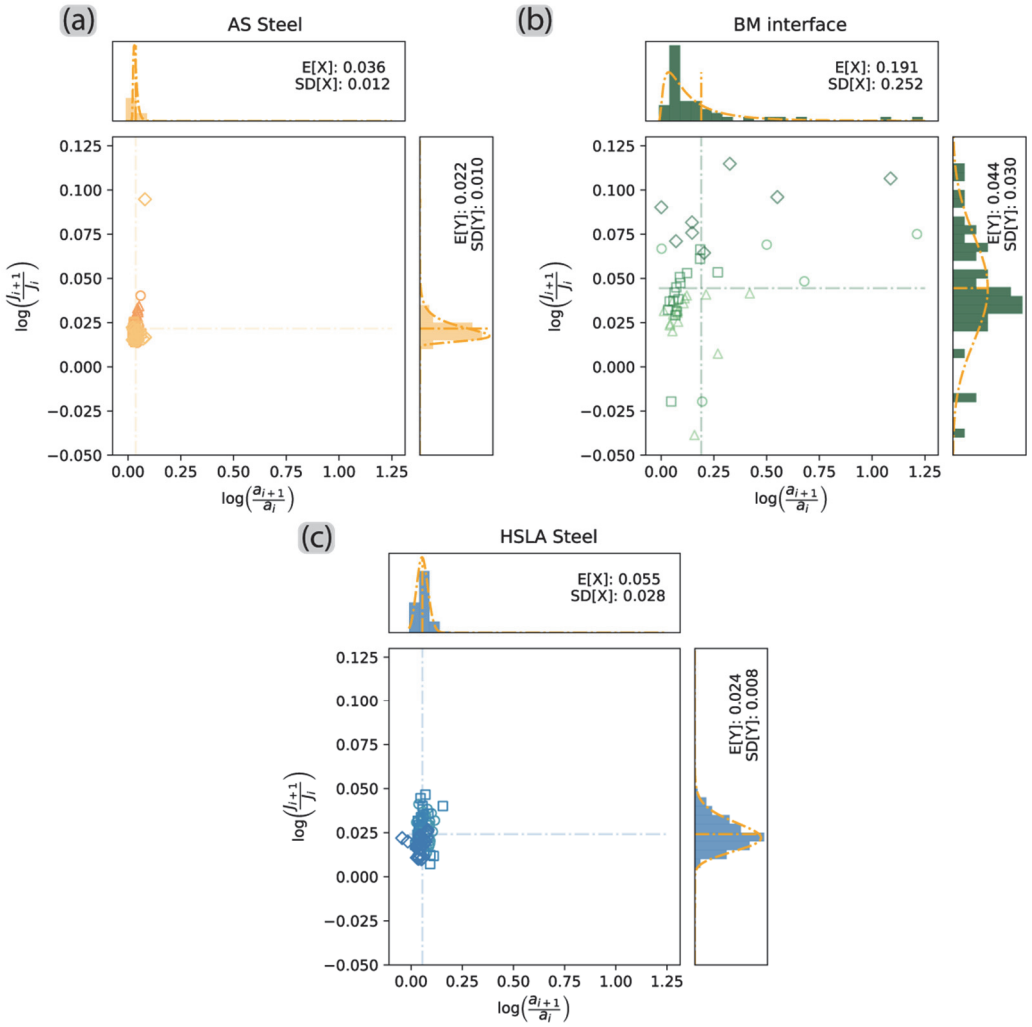

Figure 4-11 Δ in log (a) vs. Δ in log (J) for (a) AS steel (b) bi-material specimens, constrained within the diluted interface layer, and (c) HSLA steel. Means (E[X]) and standard deviations (SD[X]) used to fit the scattered data to log-norm distributions are provided along each axis.

Since stacking fault energy (SFE) has been extensively correlated to the occurrence of either mechanical twinning or transformation-induced plasticity of metastable austenite, it is discussed in the context of this work. The SFE of different regions along the bi-material build as well as the nominal composition of the ER316L wire are presented in Table 4-3. The values for chemical composition are obtained from a previous related study [24], as measured through electron probe microanalysis. A distinction is made between the bulk

of the diluted interface layer and the martensite bands running along it. This is done due to their distinct level of dilution. Martensite start temperature is included as a metric to emphasise this difference. Empirical models have been developed to estimate the SFE based on chemical composition. Although this method of estimating SFE is limited by the constrained nature of the data modelled [25], it serves as useful approximate indication. Thus, the random-intercept model presented by Meric de Bellefon et al. [26] is used, as it integrates data from many of the frequently cited models available in literature. The lower SFE values derived from the diluted chemistry of the interface support the notion that much of the martensite observed at the crack flanks originated from a TRIP effect.

Table 4-3 Chemical composition in wt%, martensite start temperature (M_s) and room temperature stacking fault energy (SFE) for regions of interest across the bi-material part, and the nominal composition of the AS wire consumable. Data provided ± 1 standard deviation.

	[C]	[Si]	[Cr]	[Mn]	[Mo]	[Ni]	Other	M_s * °C	SFE† mJ/m^2
Diluted interface layer, excluding martensite bands	0.02 ±0.01	0.56 ±0.05	14.49 ±0.88	1.63 ±0.16	2.11 ±0.23	8.65 ±1.09	-	-84 ±60	20 ±2
Martensite band within diluted interface layer	0.03 ±0.02	0.7 ±0.06	10.48 ±1.52	1.64 ±0.08	1.5 ±0.23	6.54 ±0.93	-	83 ±62	16 ±2
AS steel layer 2	0.01 ±0	0.41 ±0.04	16.87 ±0.78	1.52 ±0.12	2.52 ±0.26	8.97 ±0.95	-	-153 ±42	21 ±2
ER316L Nom. Comp. ‡	0.02	0.45	18.50	1.60	2.60	12.00	[N]: 0.04	-326	27

* $M_s = 526 - 354[C] - 29.7[Mn] - 31.7[Si] - 12.5[Cr] - 17.4[Ni] - 20.8[Mo]$ [27]

† $SFE = 2.2 + 1.9[Ni] - 2.9[Si] + 0.77[Mo] + 0.5[Mn] + 40[C] - 0.016[Cr] - 3.6[N]$ [26]

‡ [28]

EBSD mapping provides a useful path to map the extent of TWIN and TRIP effects on the deformed specimens through grain boundary analysis. In order to identify the TWIN effect, a practical approach is to map the $\Sigma 3$ boundary which most commonly follows a <111>/60° axis-angle relationship [21], [29], [30]. Alternatively, the TRIP effect can be highlighted through the martensite-austenite orientation relationship (OR). A Nishiyama-Wasserman (N-W) OR measured within a tolerance angle of 5° will include most Kurdjumov-Sachs (K-S) and Greninger-Troiano OR's [31], [32] obtained from this transformation. To do this, the axis-angle values of N-W OR used for EBSD mapping are <0.98 0.08 0.20>/45.98° [33], [34]. To distinguish martensite from ferrite, an additional relationship is necessary. Helpful OR's have been established between the packages within martensite laths. Martensite packages in Mn-alloyed TWIP steels were observed to follow either K-S or N-W OR's. Morito et al. [35] identified an axis-angle of <101>/60° for martensite packages with a common <111> planes, although K-S OR foresees additional variants. Measurements by Suikkanen et al. [36] in Mn-Si-Cr steel show a preferential misorientation angle of <343>/59.8° between martensite laths. This indicates that mapping axis-angle relationships at 60° can help to distinguish contiguous martensite packages.

It is possible to correlate the SFE values with the OR discussed and examine the spatial distribution of these boundaries across the regions of interest. Given a value SFE of 27 $mJ \cdot m^{-2}$, the AS steel mono-material sample is expected to show extensive signs of twinning [29], [37], [38]. Taylor factors and axis-angle misorientations are mapped in Figure 4-12 and Figure 4-13. These maps are complimented with the calculated Taylor factor, as crystal orientation plays an important role on its capacity to accommodate strain by twinning [39], [40]. Figure 4-12 (b) shows disagreement between preferable crystal orientations and the mapped $\Sigma 3$ boundaries. Grains oriented closest to <111> || LD show banding as obtained by the overlayed IQ values. Some of these bands are indicated by grey markers. Taylor factors are thus highest on what is suspected to be densely twinned grains. The necessary resolution to map these boundaries accurately is not sufficient under the EBSD setting chosen, and it seems to be a frequently face problem for mechanically-induced twins [40], [41]. Nonetheless, a very high value of the misorientation distribution function (MDF) for the <111>/60° between FCC phases shows a high occurrence of this OR, as shown in Figure 4-13 (c). The MDF values around <111>/60° between BCC phases and <001>/45 between FCC-BCC phases matches the apparent lack of martensite in the mapped region.

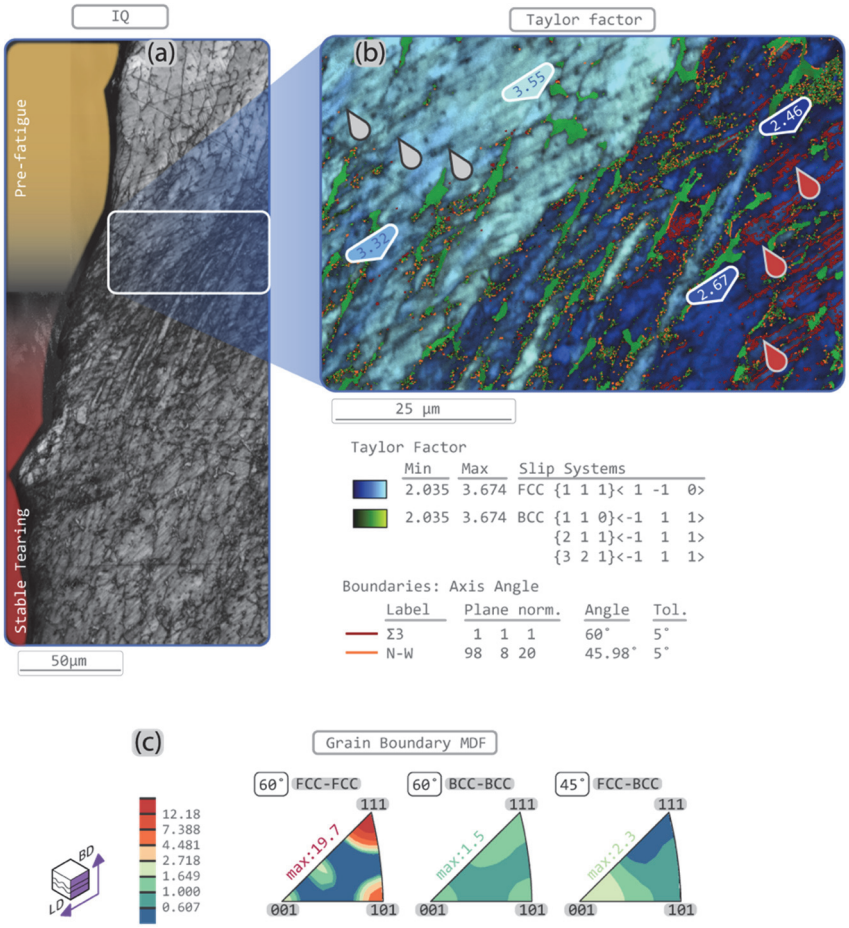

Figure 4-12 (a) Low-magnification IQ map of AS steel crack flank about a_0. The location matches that in Figure 4-8 (e). (b) Taylor factor map (blue colour scale indicates FCC phase, green colour scale indicates BCC phases) annotated with the specific values calculated at representative locations. Colour scales and slip systems are included in the legend. IQ mapping is overlayed as grey scale. Grain boundaries indicating Σ3 OR suggesting twinning and N-W OR for $\gamma \rightarrow \alpha$ transformation are shown in color. (c) Grain boundary ODF shown for axis/angle relationships of interest, within a misorientation tolerance of 5°.

The shear banding nature of the diluted interface layer is now discussed. With an estimated value SFE of 1627 mJ·m^{-2}, transformation to martensite by plastic deformation is expected. To obtain a quantitative measure of the TRIP effect across the heterogeneous diluted interface, three metrics are used. Firstly, the fraction of FCC on the maps increases as a function of position away from the crack flank, from 13.7 % in Figure 4-9 (g) to 42.7 % in Figure 4-9 (q). Due to lattice similarities, the body-centred tetragonal (BCT)

crystal structure of martensite is often mapped as BCC. The phase fraction measured is thus convoluted by the fraction of ferrite originating from solidification. As it was observed previously in Chapter 3 under un-deformed conditions a BCC phase fraction of 40 % is expected for this specific part, although this number is subject to local heterogeneities.

Secondly, the effect of TRIP-assisted deformation is quantified by grain boundary analysis. Unlike the elusive twin boundaries in the undiluted AS steel, Bain-like N-W OR is extensively observed. This condition is met across most FCC-BCC boundaries mapped in Figure 4-9. It shows an agreement between the expected parent-child couples but makes it difficult to distinguish between strain-induced martensite and allotropic martensite, if any is present. Also, the high angle grain boundary fraction between mapped BCC phases decreases as a function of distance, as it is measured through the MDF value shown for <111>/60°. This high angle relationship decreases as a function of distance from the crack flank, giving an indication of a similar trend of the amount of martensite packages adjacent to each other.

The trend observed on the misorientation distribution function (MDF) values of FCC phases about the <111>/60° misorientation requires further attention. As observed on TRIP-assisted steels, [42], [43] the strain hardening capacity is affected by both the interactions between harder and softer phases, as well as by the mechanical transformation of metastable austenite. Multiple studies noted that the austenite to martensite transformation rate would depend on the loading mode, the crystal orientation, and the grain size [44]. The larger, more favourably oriented austenite grains would then be expected to offer lower resistance to transformation than small grains less-favourably oriented. On the one hand, the austenite crystal shown in Figure 4-9 (c) displays a high Taylor value and low FCC-FCC <111>/60° value on the MDF. Interestingly, the crystal in Figure 4-9 (c) shows similar IQ banding as the one observed in Figure 4-9 (b). Figure 4-9 (b, d, e) shows on the other hand lower Taylor values and higher MDF values for the same axis-angle relationship. These boundaries could then signify the effect of strain mismatch between a hard and a soft phase [44]. This needs to be confirmed nevertheless in a more detailed study.

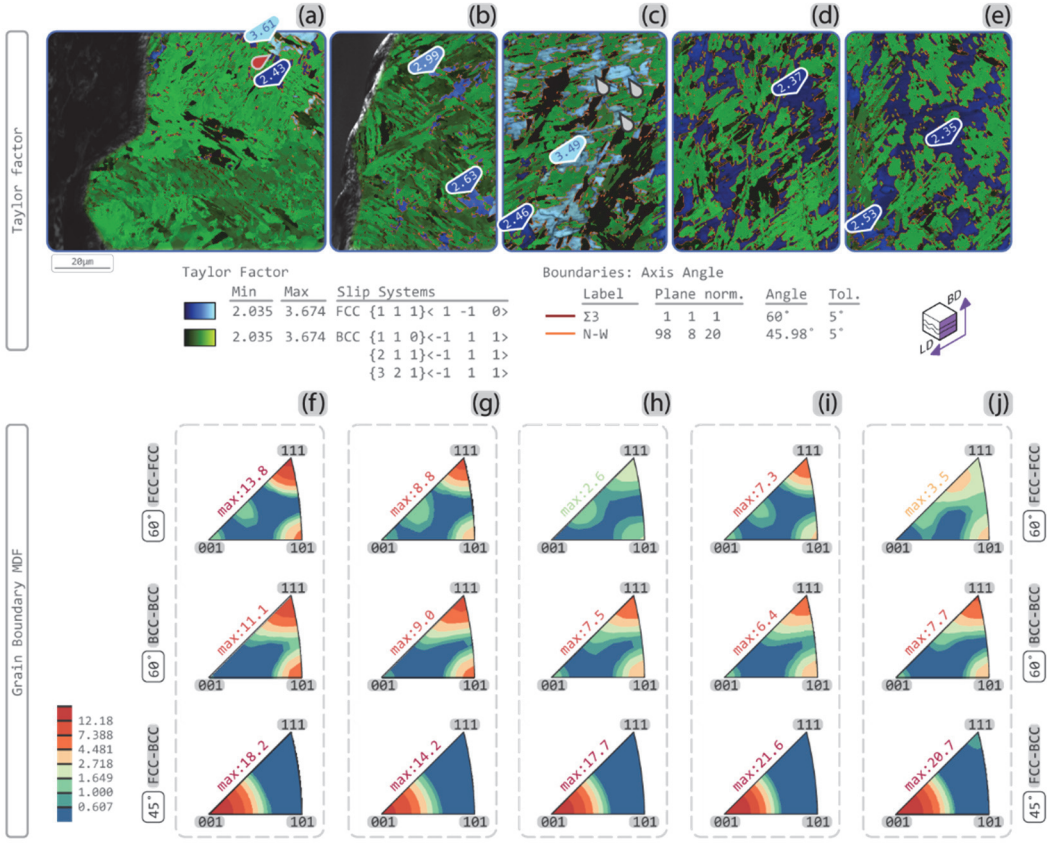

Figure 4-13 (a-e) Taylor factor maps of areas shown in Figure 4-9 (c, f, i, l o). Blue color scale indicates FCC phase, green colour scale indicates BCC phases. Maps are annotated with the specific values calculated at representative locations. Color scales and slip systems are included in the legend. IQ maps are overlayed as greyscale. Grain boundaries indicating Σ3 OR for twinning and N-W OR for $\gamma \rightarrow \alpha$ transformation are shown in color. (f-j) Grain boundary ODF shown for axis/angle relationships of interest, within a misorientation tolerance of 5 ° for each corresponding area mapped in figures (a-e).

Thirdly, a useful quantitative measure to characterize the TRIP effect is through KAM values. Opposite to the FCC phase fraction, KAM values decrease as a function of distance away from the crack flank. This is shown in Figure 4-9 (g-p). It is helpful to note the findings by Shamsujjoha [45], where it is shown that KAbM values of martensite do no tend to increase after deformation. Nevertheless, as noted by Jacques et al. [46], in order to accommodate the transformation of austenite into de martensite phase, dislocations pile up in the surrounding phases. Depending on the extent, this effect can be measured by KAM values. This reasoning also helps explain the low average KAM value obtained in Figure 4-9 (d) and the high value observed in Figure 4-9 (g). It matches the observation

by Due et al. [47] in dual-phase and TRIP-assisted steels, where it was concluded that lath martensite accommodates plastic deformation by boundary slipping. The authors also observed that the slippage of martensite packages caused strain in softer surrounding phase. Given the lack of work-hardening capacity of martensite, and its effect as a strain concentrator, it is necessary to discuss its effects on the crack propagation process.

4.4.2. Fracture after TRIP, allotropic martensite, and type II boundaries

Distinguishing itself from the bulk of the diluted interface layer, allotropic martensite is observed to promote brittle fracture. The location of cleavage features shown in Figure 4-7 (c, g) matches that of the martensite typically found along the dissimilar fusion line, $Z(BM)$. The difference in fracture morphology between these two locations is attributed to the martensite fraction at each location. In both cases, the material cannot deform like its surroundings. As it is shown in Figure 4-9, allotropic martensite retains only a very small amount of austenite. In the absence of austenite, two contiguous lath packages have no apparent work-hardening mechanism [42]. The mechanisms for plastic deformation are thus limited to the morphology of the laths, their dislocation density and their content of interstitials [44]. Controlling carbon content, tempering, or designing a heat treatment process that allows for a higher content of austenite could help overcome this problem. Tempered martensitic stainless steel, for example, yields a J_Q value of about 265 ±17 kJ/m^2 for compact tensile specimens with a retain austenite volume fraction of 15 % [48].

The effect of type II boundaries as a brittle feature is now brought into discussion. A type II boundary is understood to be caused by the migration of an austenite-austenite grain boundary across the fusion line at very high temperatures, and successive heterogeneous allotropic transformations during cooling [49]. While characterizing the toughness of different regions around a dissimilar metal weld, Kumar et al. [50] demonstrated that the fusion line between Inconel and low-alloy steel produces type-II boundaries, and that this region exerts the least resistance to fracture. Ming et al. [51] show a similar result obtained through bending tests of dissimilar welds between a low-alloy steel and a Fe-Ni alloy. Type II boundaries may promote crack formation at lower strain levels than that of the surrounding matrix, although this effect may not be directly observed under monotonic tensile loading along the fusion line [52]. Ming et al. [51] also show that this type of boundary can promote intergranular fracture modes, similar to the ones found on the secondary crack highlighted in Figure 4-7 (b).

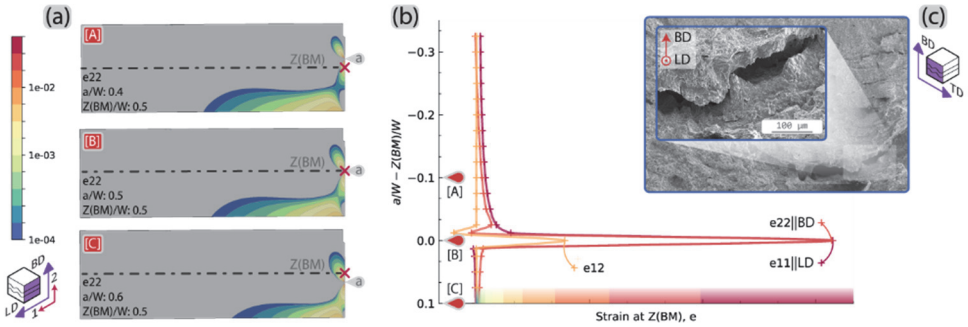

Figure 4-14 FEM results mapping e_{22} strain for values $a/W - Z(BM)/W$ equal to -0.1, 0.0 and +0.1. (b) Principal strain components e_{11} and e_{22}, as well as shear strain e_{12} as measured at the intersection between the crack plane and $Z(BM)$. Values plotted as a function of $a/W - Z(BM)/W$, to understand the effect of an approaching crack on the measured local strain. (c) Fracture surface at the location where a type II boundary is expected.

Type II boundaries are detrimental defects found along the dissimilar fusion line of the bi-material block presented in this work. As shown in Chapter 3, the fusion line between the chosen AS and the HSLA steels show this feature occasionally. This type of boundary was found typically at the root of the welding tracks in the diluted interface layer. It matches the location shown in Figure 4-7 (b), where a large secondary crack was formed. The fracture surface within this crack shows large extents of cleavage fracture accompanied by a few dimples oriented towards the BD direction. These features are shown in detail in Figure 4-14 (c). The geometry of the crack and the orientation of the few dimples found suggest that this feature did not fail due to strain perpendicular to the plain of the main crack. In turn, these features suggest failure by strain parallel to the crack plane. This strain develops as the crack front approached, but had not yet reached, the dissimilar fusion line. This observation is supported by the magnitude of strain e_{22} || BD, which is shown to be of comparable magnitude to the strain e_{11} || LD, the leading strain component resulting in mode I loading. This is shown in Figure 4-14 (b) as obtained from the FEM models detailed in Annex B.

4.5. CHAPTER CONCLUSIONS

Wire arc additive manufacturing provides a unique solution to manufacture compositionally graded parts of large dimensions. This compositional grading can be exploited to manufacture optimized parts in load bearing applications. Thus, it is necessary to understand the deformation and fracture behaviour of these heterogeneous parts. Through the extent of this work, the deformation and fracture toughness behaviour of

wire arc additively manufactured ER70S-6-ER316L bi-material specimens was studied. As reported previously in Chapter 3, the interface created by incomplete mixing of both alloys in a single weld pool shows a heterogeneous chemistry, and with it, a highly heterogeneous microstructure. Digital image correlation was used in the current study to investigate the local strain behaviour of this bi-material interface region during quasi-static tensile loading. Based on the results obtained from DIC measurements, FEM analysis was used to provide correction functions for a J-integral solution specific for bi-material specimens. Fracture toughness values were obtained to measure the layer's resistance to crack extension and scanning electron microscopy with electron back-scatter diffraction were used to inspect the deformation around the crack flanks and at the fracture surface. From this work, the following conclusions are drawn:

- The elastic modulus of the diluted bi-material interface is shown to closely match that of the un-diluted AS steel at a value of 157 ±17 GPa. Digital image correlation exposed also macroscopic shear banding and a variable strain-hardening development in at this interface region.
- The sharp change in elastic modulus of a bi-material sample entails also a discontinuity in the J-integral formulation.
- Fracture toughness of the interface is shown to yield a J_{IC} value of 180 kJ·m^{-2}. The value is lower than that measured of mono-material AS steel specimens (458 kJ·m^{-2}) and HSLA steel (408.1 kJ·m^{-2}). The value obtained from the interface value is nevertheless comparable with other TRIP steels and tempered martensitic stainless steels.
- The fracture surface of the interface shows mostly ductile behaviour, with features of quasi-cleavage fracture. It should be noted that type II boundaries and martensite are observed to cause large amounts of dispersion in the measured toughness values of the interface layer.
- Post-mortem inspection through EBSD mapping of the crack flanks confirms a change in governing deformation mechanism from twinning induced plasticity to transformation induced plasticity, as suggested by the DIC results. This is attributed to the diluted chemistry obtained during deposition.

Through the extent of this chapter, the effect of chemical dilution on the deformation mechanisms and fracture toughness of bi-material component is evaluated. The correlative use of microscopic, mechanical and FEM analysis proved necessary to understand the underlying fracture micro-mechanisms governing the behaviour of such complex interface

layer. The results indicate that the interface develops a lower resistance to fracture if compared to the un-mixed alloys, which needs to be accounted for in the design of parts composed by this bi-metal couple. Subsequent layers of AS steel cladding show adequate monotonic and fracture behaviour, demonstrating that multi-layer cladding would be advisable for structural applications. The work on this chapter thus provides empirical evidence on the effects of manufacturing compositionally graded steel structures through WAAM. While doing so, it establishes a baseline for the evaluation of quasistatic and fracture toughness performance of HSLA-AS steel bi-metal parts. The following chapter delves further into the mechanisms controlling fracture propagation, this time in the context of fatigue.

4.6. CHAPTER REFERENCES

[1] P. Dirisu, S. Ganguly, A. Mehmanparast, F. Martina, and S. Williams, "Analysis of fracture toughness properties of wire + arc additive manufactured high strength low alloy structural steel components," *Materials Science and Engineering A*, vol. 765, no. June, p. 138285, 2019, doi: 10.1016/j.msea.2019.138285.

[2] A. Ermakova, "Structural Integrity Assessment of Wire Arc Additively Manufactured Low Carbon Steel Components for Marine Applications by," University of Strathclyde, Glasgow, 2023.

[3] D. Kumar, S. Jhavar, A. Arya, K. G. Prashanth, and S. Suwas, "Mechanisms controlling fracture toughness of additively manufactured stainless steel 316L," *Int J Fract*, vol. 235, no. 1, pp. 61–78, 2022, doi: 10.1007/s10704-021-00574-3.

[4] T. Sang Byung, T. Lach, and D. Collins, "Effect of Thermal Aging in Stainless Steel Welds: 2nd Year Progress Report of I-NERI Collaboration," 2017.

[5] W. J. Mills, "Fracture toughness of type 304 and 316 stainless steels and their welds," *International Materials Reviews*, vol. 42, no. 2, pp. 45–82, 1997, doi: 10.1179/imr.1997.42.2.45.

[6] J. Talonen and H. Hänninen, "Formation of shear bands and strain-induced martensite during plastic deformation of metastable austenitic stainless steels," *Acta Mater*, vol. 55, no. 18, pp. 6108–6118, 2007, doi: 10.1016/j.actamat.2007.07.015.

[7] ISO, *NEN-ISO 12135:2021 Metallic materials - Unified method of test for the determination of quasistatic fracture toughness*. Switzerland, 2022.

[8] ASTM, "E1820 - 20b Standard Test Method for Measurement of Fracture Toughness," 2020, *ASTM International, West Conshohocken*.

[9] J. R. Rice, "A path independent integral and the approximate analysis of strain concentration by notches and cracks," *Journal of Applied Mechanics, Transactions ASME*, vol. 35, no. 2, pp. 379–388, 1968, doi: 10.1115/1.3601206.

[10] Z. H. Jin and N. Noda, "Crack-tip singular fields in nonhomogeneous materials," *Journal of Applied Mechanics, Transactions ASME*, vol. 61, no. 3, pp. 738–740, 1994, doi: 10.1115/1.2901529.

[11] F. Erdogan and B. H. Wu, "The surface crack problem for a plate with functionally graded properties," *Journal of Applied Mechanics, Transactions ASME*, vol. 64, no. 3, pp. 449–456, 1997, doi: 10.1115/1.2788914.

[12] J. Chen, L. Wu, and S. Du, "A modified J integral for functionally graded materials," *Mech Res Commun*, vol. 27, no. 3, pp. 301–306, May 2000, doi: 10.1016/S0093-6413(00)00096-3.

[13] T. Honein and G. Herrmann, "Conservation laws in nonhomogeneous plane elastostatics," *J Mech Phys Solids*, vol. 45, no. 5, pp. 789–805, May 1997, doi: 10.1016/S0022-5096(96)00087-7.

[14] D. Weichert and M. Schulz, "J-integral concept for multi-phase materials," *Comput Mater Sci*, vol. 1, no. 3, pp. 241–248, 1993, doi: 10.1016/0927-0256(93)90016-G.

[15] S. Ghorbanpour *et al.*, "Effect of microstructure induced anisotropy on fatigue behaviour of functionally graded Inconel 718 fabricated by additive manufacturing," *Mater Charact*, vol. 179, Sep. 2021, doi: 10.1016/j.matchar.2021.111350.

[16] NEN-ISO, *EN-ISO 6892-1:2019 Metallic materials - Tensile Testing - Part 1: Method of test at room temperature*, no. december 2019. Belgium, 2019.

[17] S. Ghorbanpour *et al.*, "Effect of microstructure induced anisotropy on fatigue behaviour of functionally graded Inconel 718 fabricated by additive manufacturing," *Mater Charact*, vol. 179, no. July, p. 111350, 2021, doi: 10.1016/j.matchar.2021.111350.

[18] W. J. Mills, "Heat-to-heat variations in the fracture toughness of austenitic stainless steels," *Eng Fract Mech*, vol. 30, no. 4, pp. 469–492, 1988, doi: 10.1016/0013-7944(88)90058-6.

[19] A. Ermakova, A. Mehmanparast, S. Ganguly, J. Razavi, and F. Berto, "Investigation of mechanical and fracture properties of wire and arc additively manufactured low carbon steel components," *Theoretical and Applied Fracture Mechanics*, vol. 109, no. May, p. 102685, 2020, doi: 10.1016/j.tafmec.2020.102685.

[20] W. L. Costin, O. Lavigne, and A. Kotousov, "A study on the relationship between microstructure and mechanical properties of acicular ferrite and upper bainite," *Materials Science and Engineering: A*, vol. 663, pp. 193–203, 2016, doi: 10.1016/j.msea.2016.03.103.

[21] M. S. Pham, B. Dovgyy, and P. A. Hooper, "Twinning induced plasticity in austenitic stainless steel 316L made by additive manufacturing," *Materials Science and Engineering A*, vol. 704, no. April, pp. 102–111, 2017, doi: 10.1016/j.msea.2017.07.082.

[22] F. K. Yan, G. Z. Liu, N. R. Tao, and K. Lu, "Strength and ductility of 316L austenitic stainless steel strengthened by nano-scale twin bundles," *Acta Mater*, vol. 60, no. 3, pp. 1059–1071, Feb. 2012, doi: 10.1016/j.actamat.2011.11.009.

[23] J. Talonen, *Effect of strain-induced α′-martensite transformation on mechanical properties of metastable austenitic stainless steels*, vol. PhD. 2007.

[24] J. L. Galán Argumedo, M. Mahmoudiniya, T. E. Reinton, L. A. I. Kestens, M. J. M. Hermans, and V. A. Popovich, "Functional grading of low alloy steel to 316 L by wire arc additive manufacturing – Microstructural and mechanical characterization of bi-metal interface," *J Mater Process Technol*, vol. 325, p. 118305, Apr. 2024, doi: 10.1016/j.jmatprotec.2024.118305.

[25] A. Das, "Revisiting Stacking Fault Energy of Steels," *Metall Mater Trans A Phys Metall Mater Sci*, vol. 47, no. 2, pp. 748–768, 2016, doi: 10.1007/s11661-015-3266-9.

[26] G. Meric de Bellefon, J. C. van Duysen, and K. Sridharan, "Composition-dependence of stacking fault energy in austenitic stainless steels through linear regression with random intercepts," *Journal of Nuclear Materials*, vol. 492, pp. 227–230, 2017, doi: 10.1016/j.jnucmat.2017.05.037.

[27] J. A. Self, D. L. Olson, and G. R. Edwards, "The stability of austenitic weld metal," in *Proceedings of IMCC*, Kiev, Ukraine, 1984.

[28] "3Dprint AM 316L," 2019, *Böhler Welding by Voestalpine*. [Online]. Available: https://www.vabw-service.com/voestalpine/

[29] A. Saeed-Akbari, L. Mosecker, A. Schwedt, and W. Bleck, "Characterization and prediction of flow behavior in high-manganese twinning induced plasticity steels: Part i. mechanism maps and work-hardening behavior," *Metall Mater Trans A Phys Metall Mater Sci*, vol. 43, no. 5, pp. 1688–1704, 2012, doi: 10.1007/s11661-011-0993-4.

[30] M. Madivala, A. Schwedt, S. L. Wong, F. Roters, U. Prahl, and W. Bleck, "Temperature dependent strain hardening and fracture behavior of TWIP steel," *Int J Plast*, vol. 104, no. February, pp. 80–103, 2018, doi: 10.1016/j.ijplas.2018.02.001.

[31] P. Thome, M. Schneider, V. A. Yardley, E. J. Payton, and G. Eggeler, "Crystallographic Analysis of Plate and Lath Martensite in Fe-Ni Alloys," *Crystals (Basel)*, vol. 12, no. 2, pp. 11–13, 2022, doi: 10.3390/cryst12020156.

[32] T. Maki, *Morphology and substructure of martensite in steels*. Woodhead Publishing Limited, 2012. doi: 10.1533/9780857096111.1.34.

[33] K. Verbeken, L. Barbé, and D. Raabe, "Evaluation of the crystallographic orientation relationships between FCC and BCC phases in TRIP steels," *ISIJ International*, vol. 49, no. 10, pp. 1601–1609, 2009, doi: 10.2355/isijinternational.49.1601.

[34] V. Tari, A. D. Rollett, and H. Beladi, "Back calculation of parent austenite orientation using a clustering approach," *J Appl Crystallogr*, vol. 46, no. 1, pp. 210–215, 2013, doi: 10.1107/S002188981204914X.

[35] S. Morito, X. Huang, T. Furuhara, T. Maki, and N. Hansen, "The morphology and crystallography of lath martensite in alloy steels," *Acta Mater*, vol. 54, no. 19, pp. 5323–5331, Nov. 2006, doi: 10.1016/j.actamat.2006.07.009.

[36] P. P. Suikkanen, C. Cayron, A. J. DeArdo, and L. P. Karjalainen, "Crystallographic Analysis of Martensite in 0.2C-2.0Mn-1.5Si-0.6Cr Steel using EBSD," *J Mater Sci Technol*, vol. 27, no. 10, pp. 920–930, Oct. 2011, doi: 10.1016/S1005-0302(11)60165-5.

[37] S. Allain, J. P. Chateau, O. Bouaziz, S. Migot, and N. Guelton, "Correlations between the calculated stacking fault energy and the plasticity mechanisms in Fe-Mn-C alloys," *Materials Science and Engineering: A*, vol. 387–389, no. 1-2 SPEC. ISS., pp. 158–162, 2004, doi: 10.1016/j.msea.2004.01.059.

[38] S. Curtze and V. T. Kuokkala, "Dependence of tensile deformation behavior of TWIP steels on stacking fault energy, temperature and strain rate," *Acta Mater*, vol. 58, no. 15, pp. 5129–5141, 2010, doi: 10.1016/j.actamat.2010.05.049.

[39] I. Gutierrez-Urrutia and D. Raabe, "Dislocation and twin substructure evolution during strain hardening of an Fe-22 wt.% Mn-0.6 wt.% C TWIP steel observed by electron channeling contrast imaging," *Acta Mater*, vol. 59, no. 16, pp. 6449–6462, 2011, doi: 10.1016/j.actamat.2011.07.009.

[40] H. Beladi, I. B. Timokhina, Y. Estrin, J. Kim, B. C. De Cooman, and S. K. Kim, "Orientation dependence of twinning and strain hardening behaviour of a high manganese twinning induced plasticity steel with polycrystalline structure," *Acta Mater*, vol. 59, no. 20, pp. 7787–7799, 2011, doi: 10.1016/j.actamat.2011.08.031.

[41] D. Barbier *et al.*, "EBSD for analysing the twinning microstructure in fine-grained TWIP steels and its influence on work hardening," *Journal of Microscopy2*, no. hal-02402444, 2009.

[42] P. J. Jacques, Q. Furnémont, F. Lani, T. Pardoen, and F. Delannay, "Multiscale mechanics of TRIP-assisted multiphase steels: I. Characterization and mechanical testing," *Acta Mater*, vol. 55, no. 11, pp. 3681–3693, 2007, doi: 10.1016/j.actamat.2007.02.029.

[43] P. Jacques, Q. Furnémont, A. Mertens, and F. Delannay, "On the sources of work hardening in multiphase steels assisted by transformation-induced plasticity," *Philosophical Magazine A: Physics of Condensed Matter, Structure, Defects and Mechanical Properties*, vol. 81, no. 7, pp. 1789–1812, 2001, doi: 10.1080/01418610108216637.

[44] G. Krauss, "Martensite in steel: Strength and structure," *Materials Science and Engineering: A*, vol. 273–275, pp. 40–57, 1999, doi: 10.1016/s0921-5093(99)00288-9.

[45] Md. Shamsujjoha, "Evolution of microstructures, dislocation density and arrangement during deformation of low carbon lath martensitic steels," *Materials Science and Engineering: A*, vol. 776, p. 139039, Mar. 2020, doi: 10.1016/j.msea.2020.139039.

[46] P. J. Jacques, Q. Furnémont, F. Lani, T. Pardoen, and F. Delannay, "Multiscale mechanics of TRIP-assisted multiphase steels: I. Characterization and mechanical testing," *Acta Mater*, vol. 55, no. 11, pp. 3681–3693, 2007, doi: 10.1016/j.actamat.2007.02.029.

[47] C. Du, R. Petrov, M. G. D. Geers, and J. P. M. Hoefnagels, "Lath martensite plasticity enabled by apparent sliding of substructure boundaries," *Mater Des*, vol. 172, pp. 1–12, 2019, doi: 10.1016/j.matdes.2019.107646.

[48] J. Chen, Y. Verreman, and J. Lanteigne, "On fracture toughness JIC testing of martensitic stainless steels," *13th International Conference on Fracture 2013, ICF 2013*, vol. 5, pp. 3561–3569, 2013.

[49] T. W. Nelson, J. C. Lippold, and M. J. Mills, "Investigation of boundaries and structures in dissimilar metal welds," *Science and Technology of Welding and Joining*, vol. 3, no. 5, pp. 249–255, 1998, doi: 10.1179/stw.1998.3.5.249.

[50] S. Kumar, P. K. Singh, K. N. Karn, and V. Bhasin, "Experimental investigation of local tensile and fracture resistance behaviour of dissimilar metal weld joint: SA508 Gr.3 Cl.1 and SA312 Type 304LN," *Fatigue Fract Eng Mater Struct*, vol. 40, no. 2, pp. 190–206, 2017, doi: 10.1111/ffe.12484.

[51] H. Ming, J. Wang, and E.-H. Han, "Comparative study of microstructure and properties of low-alloy-steel/nickel-based-alloy interfaces in dissimilar metal weld joints prepared by different GTAW methods," *Mater Charact*, vol. 139, pp. 186–196, May 2018, doi: 10.1016/j.matchar.2018.02.044.

[52] H. Ming *et al.*, "Microstructure, local mechanical properties and stress corrosion cracking susceptibility of an SA508-52M-316LN safe-end dissimilar metal weld joint by GTAW," *Materials Science and Engineering: A*, vol. 669, pp. 279–290, Jul. 2016, doi: 10.1016/j.msea.2016.05.101.

5. FATIGUE CRACK PROPAGATION ACROSS FUNCTIONALLY GRADED BI-METAL STEEL

This study concentrates on the fatigue crack propagation behaviour of a high-strength low-alloy (HSLA) steel and austenitic stainless (AS) steel bi-material part, as obtained by wire arc additive manufacturing (WAAM). Due to partial mixing in the weld pool, the first layer of AS steel laid onto the previously deposited HSLA steel results in a diluted interface layer of distinct chemical and microstructural characteristics. To characterise crack propagation, Paris parameters are obtained for the interface layer along transverse and longitudinal planes to the deposition direction (BD-LD plane: $m = 2.79$, $\log_{10}(C) = -7.83 \log_{10}(da/dN)$) (BD-TD plane: $m = 3.47$, $\log_{10}(C) = -8.39 \log_{10}(da/dN)$). However, it is observed that this interface layer manifests an intriguing crack propagation behaviour. Fatigue crack growth rate consistently drop as the crack front transitions from undiluted AS steel to the interface. At $\Delta K = 20$ MPa·m$^{0.5}$, the greatest Δ is -0.77 $\log_{10}$ steps (R=0.1). As cracks near the HSLA fusion line, rates re-accelerate up to +0.75 $\log_{10}$ steps (R= 0.5). The phenomenon is attributed to the interplay between deformation-induced martensitic transformation and pre-existing allotropic martensite. Our findings, derived from a series of fatigue tests in correlation with multiscale microstructural and fracture characterization, offer insights into the damage-tolerant behaviour of these bi-material structures.

This chapter is an adaptation from the publication Galán Argumedo, J. L., Suresh, A., Ding, Z., Bertolo, V., Reinton, T. E., Riemslag, A. C., Hermans, M. J. M., & Popovich, V. A. (2025). Fatigue crack propagation in functionally graded bi-material steel obtained through wire-arc additive manufacturing. *International Journal of Fatigue*, *194*(September 2024), 108819. https://doi.org/10.1016/j.ijfatigue.2025.108819

5.1. INTRODUCTION

Limited work has been done to characterize the mechanical behaviour of HSLA-AS steel bi-material additively manufactured structure (BMAS). Tensile tests of bi-metal tensile coupons shown by Ahsan *et al.* in two related studies [1], [2] show that necking and failure are typically localized away from the interface layer. This is confirmed in similar studies by Ayan *et al.* [3], and Suárez *et al.* [4]. Repetition of quasi-static mechanical testing with the aid of digital image correlation shows a change in the work-hardening behaviour at the interface. Instead of a monotonic decay in work-hardening rate, the interface develops a local minimum and subsequent strengthening originating from strain-induced martensitic transformation. This is otherwise known as a Transformation-Induced Plasticity (TRIP) effect and is attributed to the local chemical constitution of the interface material [5]. In terms of fatigue, Ayan *et al.* [3] showed that HSLA-AS steel bi-material parts display adequate behaviour under bending stresses, as failure typically originated on the HSLA material volume. Nonetheless, no further research is apparently available on the fatigue crack propagation behaviour. This is necessary, as the mechanisms controlling deformation ahead of a crack tip across the interface layer are observed to be different from the parent materials.

It is crucial to understand the fatigue crack propagation behaviour for a reliable application of HSLA-AS steel bi-material additively-manufactured (BMAS) parts. The intention of this study is to establish empirical evidence on the fatigue behaviour of bi-metal components specific to the metallurgical conditions obtained from the WAAM process. Benchmarking results are carried out for mono-material specimens of ER70S-6 (HSLA steel) and ER316L (AS steel) and are used to establish a performance baseline. Fatigue crack propagation studies are then carried out across interface layer to understand its behaviour in the context of a bi-metal part. Microscopy, fractography and electron backscatter diffraction are used to understand the relationship between microstructure and fatigue performance. Special attention is placed on the martensite found along the interface as an outcome of the AM process, and its effect as a crack-accelerating microstructural feature. These results are fundamental to establish workable reliability levels, and to adequately estimate their fatigue life performance.

5.2. MATERIALS AND METHODS

5.2.1. Wire-Arc Additive Manufacturing

Wire arc additive manufacturing of a bi-material bock was carried out with a 6-degree of freedom robot and a CMT-capable Fronius power source. The reader is directed to Chapter 3 for a detailed specification of wire consumables, block dimensions, and deposition parameters. Chapter 4 gives a detailed description of the quasi-static mechanical properties as obtained from a comparable bi-material block.

5.2.2. Fatigue specimens, testing apparatus and programme

Single edge notched bending (SENB) specimens were extracted from the bi-material block for fatigue testing. Prisms with dimensions of length 60 mm, width W of 10 mm, and thickness B of 5 mm were obtained by cutting and milling. Dimensions are intentionally chosen small to minimize the effect of residual stresses on the fatigue crack growth rate (FCGR) measurements [6]. The prisms were obtained in two orientations designated transverse and longitudinal to capture the anisotropic effect caused by the deposition strategy. Mono-material specimens were extracted from the HSLA and AS steel material volumes. This was done at a minimum distance of 10 mm away from the dissimilar fusion line to avoid any effect of dilution. Bi-material specimens were extracted in such way that a portion of the interface would be contained within their volume, and such that the dissimilar fusion line would be located at a maximum distance of 6 mm from the face intended for notching. A starter notch of 1.5 mm length and 0.4 mm width was fabricated through electric discharge machining. The top face was notched on all specimens, intending a consistent crack propagation direction opposite to the building direction (BD). The specimen dimensions, orientations and distribution within the bi-material parent block are pictured in Figure 5-1 (b).

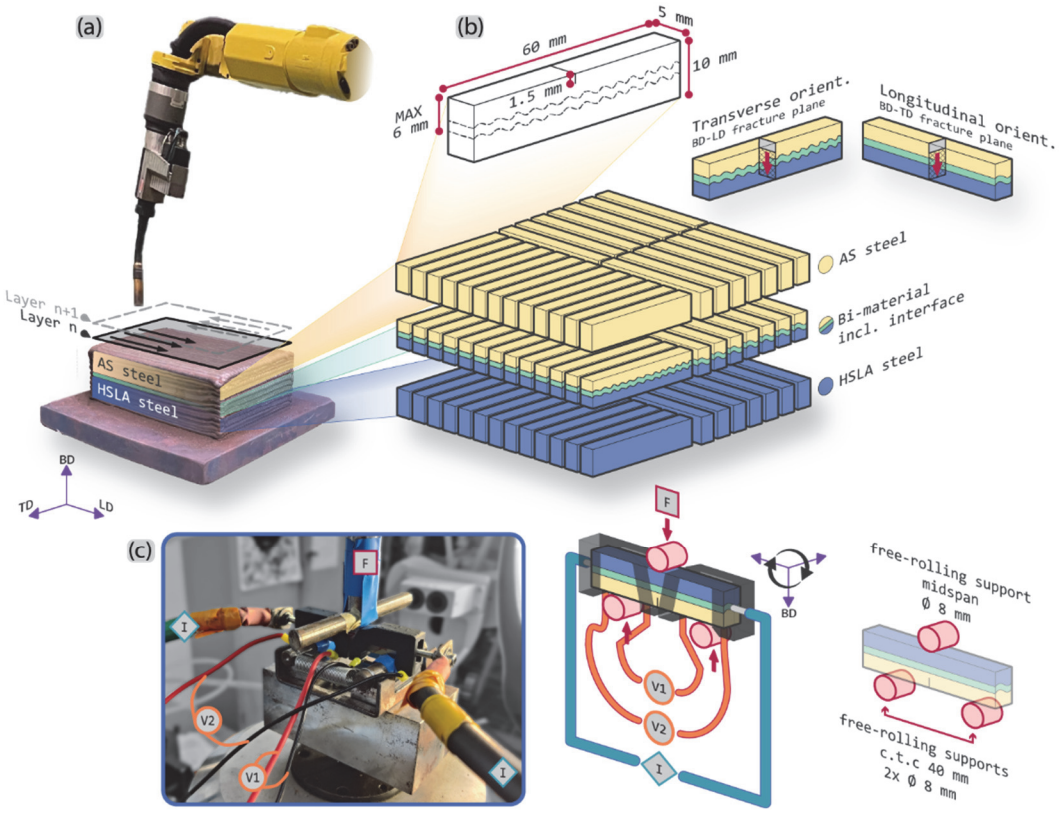

Figure 5-1 (a) WAAM layer deposition strategy of bi-material block. (b) Sample distribution within parent block, as well as dimensions, materials, and orientations used for testing. (c) Testing set-up used for FCGR measurement for single edge notched 3-point bending specimens with DCPD measurement probes connected. Note the specimen is placed upside-down during testing. Diagram indicates potential drop measurement location about the crack tip (V1) and reference circuit (V2), alongside location of current-carrying leads (I). Contact rollers belonging to the load train (F) are also shown for context. Sketches are not to scale.

A fatigue-rated testing apparatus was used to carry out the fatigue testing program. Force-controlled dynamic loading was applied using a servo-hydraulic MTS frame with a dynamic load range of ±25 kN. The frame was controlled with an MTS MultiPurpose TestWare and Flextest electronic control unit. Direct current potential drop (DCPD) measurements were done with dedicated DCPD Howden hardware at a crack length extension resolution of 50 µm. A polymer clamp system was used to facilitate stable and consistent connection points of four M2 brass screws attached to the DCPD probes. The specimen, polymer clamp, electrical probes and loading frame are pictured in Figure 5-1 (c). DCPD set-up calibration was done per material (HSLA steel/AS steel/bi-material). In

the case of the bi-material specimens, calibration was also carried out based on specimen orientation. Calibration involved the polynomial regression of the data pairs voltage vs. crack extension, as measured every 0.5 mm. Crack increments were observed with a long-distance stereo microscope and physical markings on a polished face of the specimen. DCPD measurements were done in agreement with ISO 12108 [7]. While testing, data was recorded continuously at a frequency of 100 Hz. An averaging data algorithm was used to reduce data to every 0.01 mm of crack extension, either based on time-voltage acquisition or peak-valley computations, as deemed more appropriate depending on the nature of fatigue test being performed.

A sharp fatigue crack tip was obtained by means of pre-fatigue. Specimen pre-fatiguing was done following a reducing ΔK procedure. To do so, a decreasing ΔK relationship was employed following:

$$\Delta K = \Delta K_0 \exp[C(a - a_0)] \qquad (Eq. 5.1)$$

where ΔK is the applied stress intensity range, ΔK_0 is the initial ΔK value set at 25 MPa·m$^{0.5}$, C is the reduction gradient set at an approximate value of -0.02 mm^{-1}, a_0 is the starting notch length and a is the instantaneous crack length. For single-material specimens, $\Delta K = K_{MAX} - K_{MIN} = K(P_{MAX}) - K(P_{MIN})$ was determined based on standard relationships such that,

$$K = \left[\frac{P \cdot S}{B \cdot W^{3/2}}\right] \cdot f\left(\frac{a}{W}\right) \qquad (Eq. 5.2)$$

where P is either the MAX or MIN applied load, and S is the span between supports equal to $4 \cdot W$. The function $f(a/W)$ is the geometry-dependent relation between the load applied and the stress intensity value, as provided on ISO 12108 [7]. For mono-material specimens, these relationships are sufficient to determine every value of K. For bi-material specimens, a modification of the standard relationship is necessary, such that:

$$K_{BM} = \sqrt{\Gamma_J^E} \cdot K \qquad (Eq. 5.3)$$

given that Γ_J^E is a correction function derived from the numerical FEM analysis of bi-material SENB specimens. Γ_J^E is a function of elastic moduli E of the materials involved, crack length a, and position of the bi-material dissimilar fusion line $Z(BM)$. The derivation and function values of Γ_J^E are provided in Annex C. In every case, K_{MAX} at the end of the

pre-fatigue procedure was lower than the K_{MAX} at the start of the fatigue test, as dictated by standard procedure [7].

Three testing programmes were carried out to characterize the fatigue crack propagation behaviour of the bi-material block. These programmes encompassed constant force amplitude ΔF, constant stress intensity amplitude ΔK, and stress intensity threshold ΔK_{th} testing. Constant ΔF tests were carried out to obtain the Paris parameters. Preliminary testing was used to establish workable ΔK ranges that would result in a linear Paris relationship. All tests were undertaken with an R ratio of 0.1. A complimentary constant ΔK testing programme was carried out to isolate the effect of material heterogeneities on the measured FCGR. ΔK values were set to 20 MPa·mm$^{0.5}$. For this purpose, two R ratios were used (0.1 and 0.5) to distinguish the effect of increased loading. Both constant ΔF and constant ΔK testing programmes were carried out at a loading frequency of 15 Hz. A final test programme involved the determination of the ΔK_{th} through a decreasing ΔK approach. This was achieved by maintaining K_{MAX} constant and gradually increasing K_{MIN}. The decreasing ΔK rate was determined by the same relationship as the one stated in Eq. 5.1. An initial R ratio of 0.5 and C value of -0.4 mm^{-1} were used for this purpose. ΔK_0 was set at 14 MPa·mm$^{0.5}$ and ΔK was adjusted every 0.1 mm of crack increment, until no increment was measured after 1×10^6 cycles. ΔK_{th} and the Paris parameters $\log_{10}$(C) and m were finally determined by the procedure set by Ohta *et al.* [8]. ΔK_{th} testing was carried out at a loading frequency of 60 Hz. All test experiments were repeated 3 times per material and specimen orientation, except were indicated.

5.2.3. Fractography, microscopy and crystallography

Fractographic analysis was carried out to establish a correlation between the specimen's features and the measured fatigue crack propagation behaviour. After fatigue testing, the bi-material and HSLA steel specimens were cooled with liquid nitrogen, cracked open through 3-point bending, and brought back to room temperature through subsequent submersions in water and isopropanol alcohol. The latter step was done to minimize the effect of corrosion during de-frosting. AS steel specimens were heat-tinted at 350 °C for 15 min. and cracked open. Macroscopic imaging of the fracture surfaces was carried out with an optical microscope Keyence VHX-700. Partial illumination (quadrants top and left) was used to accentuate fracture features. Features like the crack extension after pre-fatigue a_p, the position of the bi-material dissimilar fusion line $Z(BM)$, and the

crack extension after test completion a_f were obtained as an average of 5 measurements equally spaced across the full width of each specimen. Scanning electron microscopy of the fracture surfaces was done with a JEOL JSM-IT100 InTouchScope™ instrument at an accelerating voltage of 20 kV.

Fractography is complimented with crystallographic analysis of the crack flanks to better understand the crack propagation process. Standard metallographic sample preparation was used with a final polishing step in colloidal silica (OPS) for a minimum of 30 minutes. Electron back-scatter diffraction (EBSD) mapping was carried out with a FEI® SEM-Quanta FEG 450 SEM from ThermoFischer Scientific with an integrated EDAX detector. An accelerating voltage of 20 kV and a current of 13 nA was used for all mapping purposes. Mapping step sizes are indicated in the caption under each figure in the results and discussion sections. Post-processing was done with the EDAX OIM Analysis software v8.6. Martensite variant analysis was performed to distinguish between deformation-induced and allotropic martensite. EBSD maps obtained with a step size of 0.1 µm about the crack flanks of two different specimens were cropped and coarsened. This was done to avoid noise derived from mis-indexed points across the crack void, and to reduce computational load. Variant and packet identification was carried out with the open-source MATLAB toolboxes MTex and ORTools, following the grain graph procedure. A step-by-step procedure is explained in detail elsewhere [9]. In every case, the parent phase was considered face-centred cubic and the child phase body-centred cubic. The re-construction of Parent Austenite Grains (PAG's) was carried out assuming a Kurdjumov-Sachs (K-S) $\{1\,1\,1\}_\gamma || \{1\,1\,0\}_{\alpha'}$ and $\langle 1\,1\,0\rangle_\gamma \,||\langle 1\,1\,1\rangle_{\alpha'}$ orientation relationships (OR).

Lastly, Transmission Kikuchi Diffraction (TKD) was used to establish the relationship between the martensite lath orientations and the fatigue fracture plane. Specimen preparation involved the conventional lift out method of electron-transparent lamella with a xenon plasma focused ion beam Helios G4 PFIB UXe. To avoid ion milling of the fracture features at the region of interest, beam-induced platinum deposition was used. After ion milling and polishing, the lamellae were inspected under scanning transmission electron microscopy (STEM) at 30 kV. Subsequently, specimens were tilted 40° from horizontal and mapped with transmission-EBSD (t-EBSD). Mapping was done with a step size of 0.01 µm for this purpose.

5.3. RESULTS

5.3.1. Constant force and near-threshold FCGR

The results obtained from ΔF testing experiments are presented in Figure 5-2, while those results obtained from constant ΔK_{th} experiments are presented in Figure 5-3. Due to the experimental design, the data obtained from the ΔF experiments does not overlap with the data obtained from the ΔK_{th} programme. Constant force experiments ran for ΔK values above 15 MPa·m$^{0.5}$, threshold tests ran for values below 10 MPa·m$^{0.5}$. For ease of representation, data is binned every 2.5 MPa·m$^{0.5}$ along the linear Paris regime and every 0.5 MPa·m$^{0.5}$ in the near ΔK_{th} regime. Error bars at each data point indicate one standard deviation. The results obtained from the regression analysis proposed by Ohta *et al.* [10] are shown graphically for the joint ΔK_{th} data, with 90% confidence interval bands. The result of a log-log regression for each constant force data set is presented, showing the m and c values derived therefrom.

As indicated on the figure legend, the data in Figure 5-2 and Figure 5-3 is distinguished by material and the specimen orientation. In both cases, (a-b) show the data obtained for AS steel mono-material specimens; (c-d) from bi-material specimens; and Figure 5-3 (e-f) for HSLA-steel specimens. Figure 5-2 (c-d) and Figure 5-3 (c-d) show results for bi-material specimens containing also data shown in blue and yellow, as these data points were measured across the un-diluted regions of the bi-material specimens. However, all regression values are reported only for points belonging to the interface. Tabulated results of the regression analysis are shown in Table 5-1.

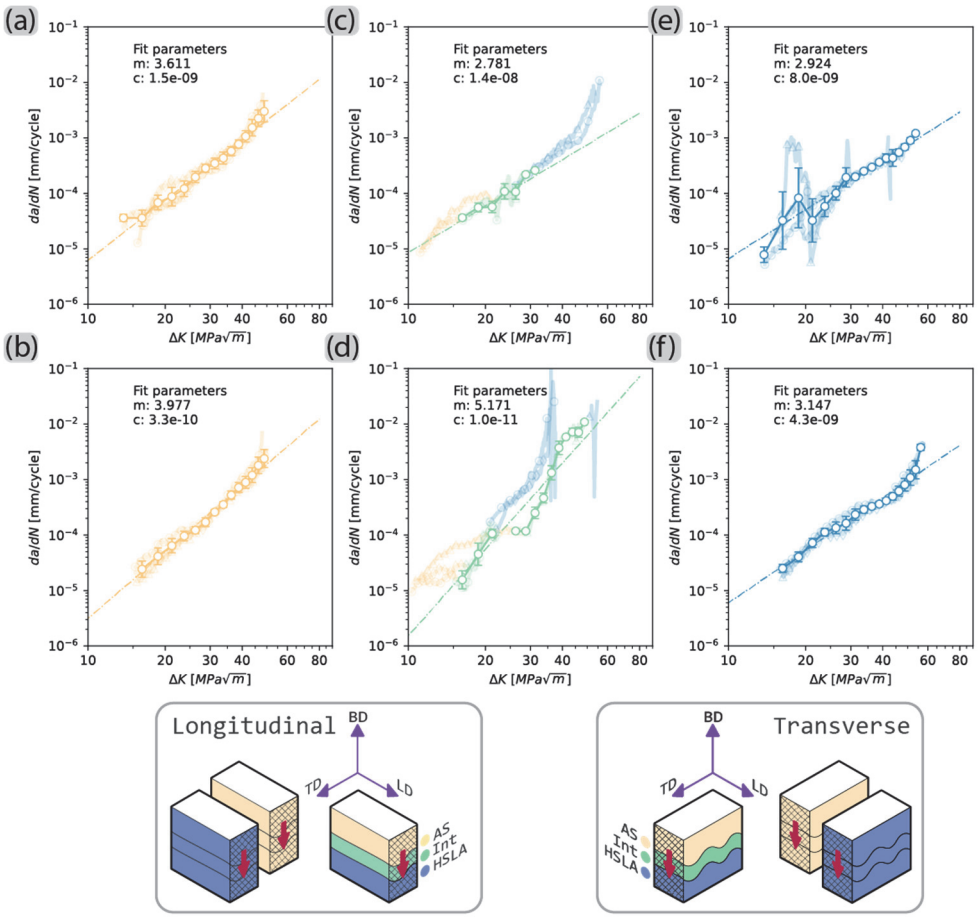

Figure 5-2 Paris regimes for SENB samples for (a-b) AS steel specimens, (c-d) bi-material specimens and (e-f) HSLA steel specimens. (a), (c) and (e) belong to the longitudinal specimen orientation, while (b), (d) and (f) belong the transverse orientation.

Mono-material specimens show overall consistent results. The mono-material AS steel and the mono-material HSLA steel results show overall good agreement with the regression analysis. Also, the regression values show negligible differences between the different orientations, suggesting no relevant anisotropy in terms of fatigue crack propagation. Nevertheless, Figure 5-3 (b) shows a higher degree of dispersion for the data points obtained in the near ΔK_{th} specimens. This could be attributed to the R ratio effect and is discussed in detail in section 5.4.1. Moreover, Figure 5-3 (e) shows an important degree of dispersion across the higher ΔK values for the transverse HSLA steel specimens. These features are related to process-induced defects, mostly consisting of lack of fusion. These defects are presented in greater detail in section 5.3.3.

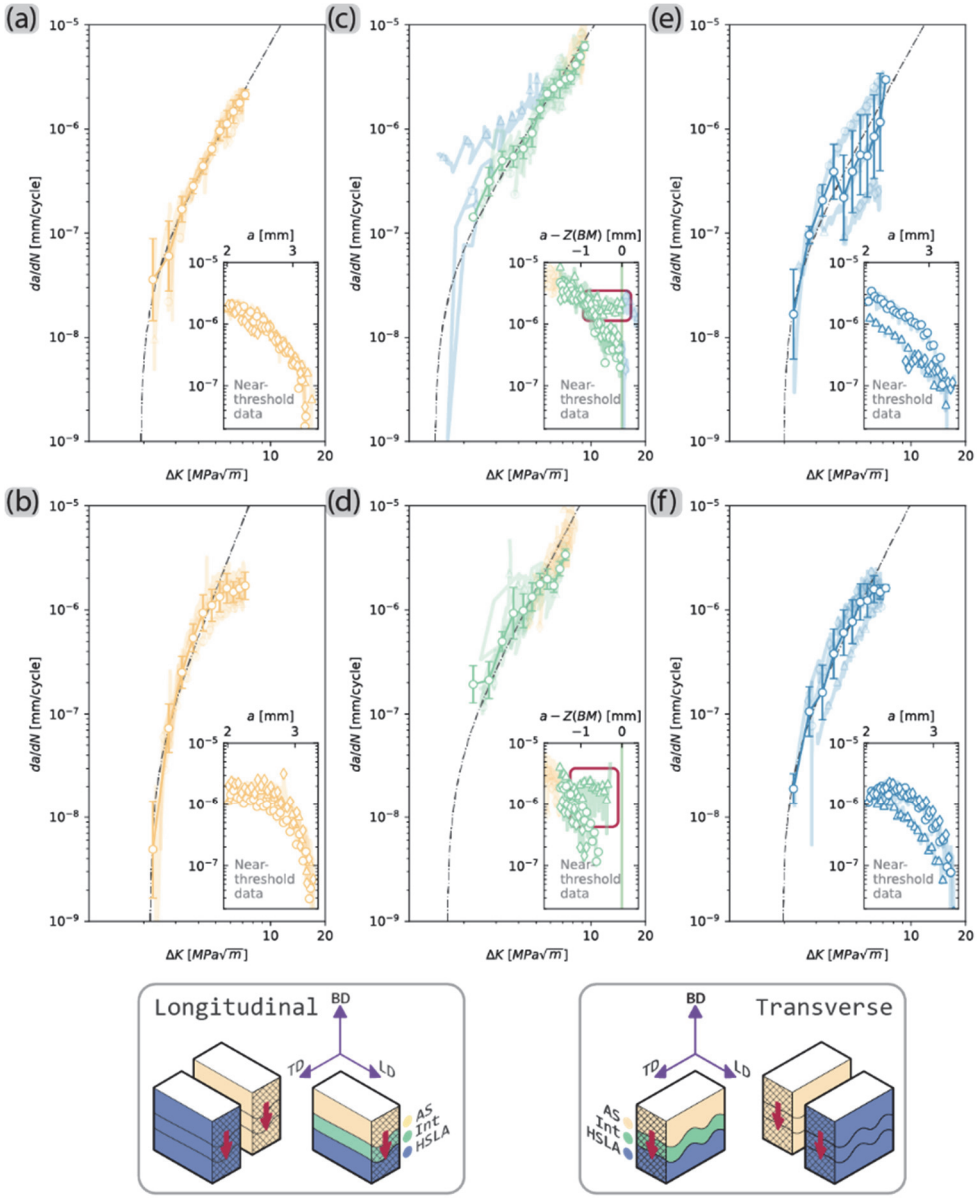

Figure 5-3 Near-threshold Paris regimes for SENB samples for (a-b) AS steel specimens, (c-d) bi-material specimens and (e-f) HSLA steel specimens. (a), (c) and (e) belong to the longitudinal specimen orientation, while (b), (d) and (f) belong the transverse orientation.

Bi-material specimen results contrast from their mono-material counterparts through a few important features. Both the transverse and longitudinal results show higher dispersion than their mono-material counterparts. The source of this dispersion appears to be twofold. First, in Figure 5-3 (d) a large dispersion in FCGR is measured for the highest ΔK values. If Paris parameters are derived solely from the data obtained in this regime, the results suggest a very high sensitivity to ΔK, much higher than the mono-material counterparts. This is easily appreciated by the m values presented between brackets in Table 5-1. Second, in both transverse and longitudinal directions, the near-ΔK_{th} data shows strong discrepancies between different specimens. Inserts in all subfigures show the measured crack propagation rate as a function of crack length. For mono-material specimens, a clear decreasing tendency is observed. On the bi-material specimens, nonetheless, some specimens show decreasing FCGR as they approach $Z(BM)$, but certain specimens do not. Although the stress intensity amplitude is consistently decreased, the crack propagation rate re-accelerates as the crack front approaches $Z(BM)$. This phenomenon is highlighted in red on the inset figures in Figure 5-3 (c) and Figure 5-3 (d). To better distinguish this phenomenon, it is best to isolate it under constant stress intensity and R ratio parameters. This is done in the following section.

Table 5-1 Regression parameters for Paris regime and ΔK_{th} values. Regression values solely obtained from the Paris regime are shown between brackets ± standard error.

	Transverse specimen orientation			**Longitudinal specimen orientation**		
	ΔK_{th}	**m**	**$\log_{10}$(C)**	**ΔK_{th}**	**m**	**$\log_{10}$(C)**
	MPa·m$^{0.5}$	$\frac{\log_{10}(\mathrm{mm/cycle})}{\log_{10}(\mathrm{MPa \cdot m^{0.5}})}$	$\log_{10}(\mathrm{mm/cycle})$	*MPa·m$^{0.5}$*	$\frac{\log_{10}(\mathrm{mm/cycle})}{\log_{10}(\mathrm{MPa \cdot m^{0.5}})}$	$\log_{10}(\mathrm{mm/cycle})$
AS Steel	2.07	3.40 (3.61 ±0.03)	-8.49 (-8.82 ±0.04)	2.04	3.28 (3.97 ±0.02)	-8.43 (-9.48 ±0.03)
BM interface	1.40	2.79 (2.78 ±0.13)	-7.83 (-7.85 ±0.15)	1.90	3.47 (5.17 ±0.09)	-8.39 (-10.98 ±0.13)
HSLA steel	2.00	3.08 (2.92 ±0.06)	-8.34 (-8.10 ±0.09)	1.99	3.20 (3.15 ±0.02)	-8.37 (-8.37 ±0.03)

5.3.2. FCGR under constant ΔK

To clearly distinguish the effect that the interface might impose on FCGR across the bi-material specimens, constant ΔK experiments are carried out. Figure 5-4 shows the results for this fatigue testing programme, distinguishing data based on material condition, orientation, and R ratio. In this case, FCGR results are shown binned every 0.25 mm of crack extension. Error bars on each point show a single standard deviation, as obtained from the binning process. Bi-material crack extension results are normalized to the position of the interface, where negative values show data points measured on the undiluted AS steel and interface layers, and positive values belong to points measured across $Z(BM)$ and into the HSLA steel layers. Average values are shown as a dotted line alongside 90% confidence interval bands. For the bi-material specimens, only data belonging to the interface layer is considered for statistical analysis. Numerical results are shown in Table 5-2.

Under a constant ΔK loading scheme, a clearer relationship can be established between the different materials and their individual response to crack propagation. For a given specimen orientation and R ratio, AS steel typically shows higher crack propagation rates than HSLA steel. In every case, R ratios of 0.5 result in higher growth rates than their 0.1 R ratio counterparts. A slight difference is appreciated between the transverse and longitudinal specimens, typically leading to marginally higher fatigue crack growth rates for longitudinal specimens. Nonetheless, this difference lies within the range of the estimated measurement error. Dispersion of the HSLA steel data is attributed to the lack of fusion defects. These have a more noticeable and adverse effect when the crack lies on the BD-LD plane (transverse specimens). These defects are described in detail in section 5.4.2. None of the mono-material test results indicate a periodic effect that could be related to microstructural differences between the root and the top of each material layer. This indicates that for practical purposes in terms of fatigue crack resistance the mono-material specimens are homogeneous across their layers.

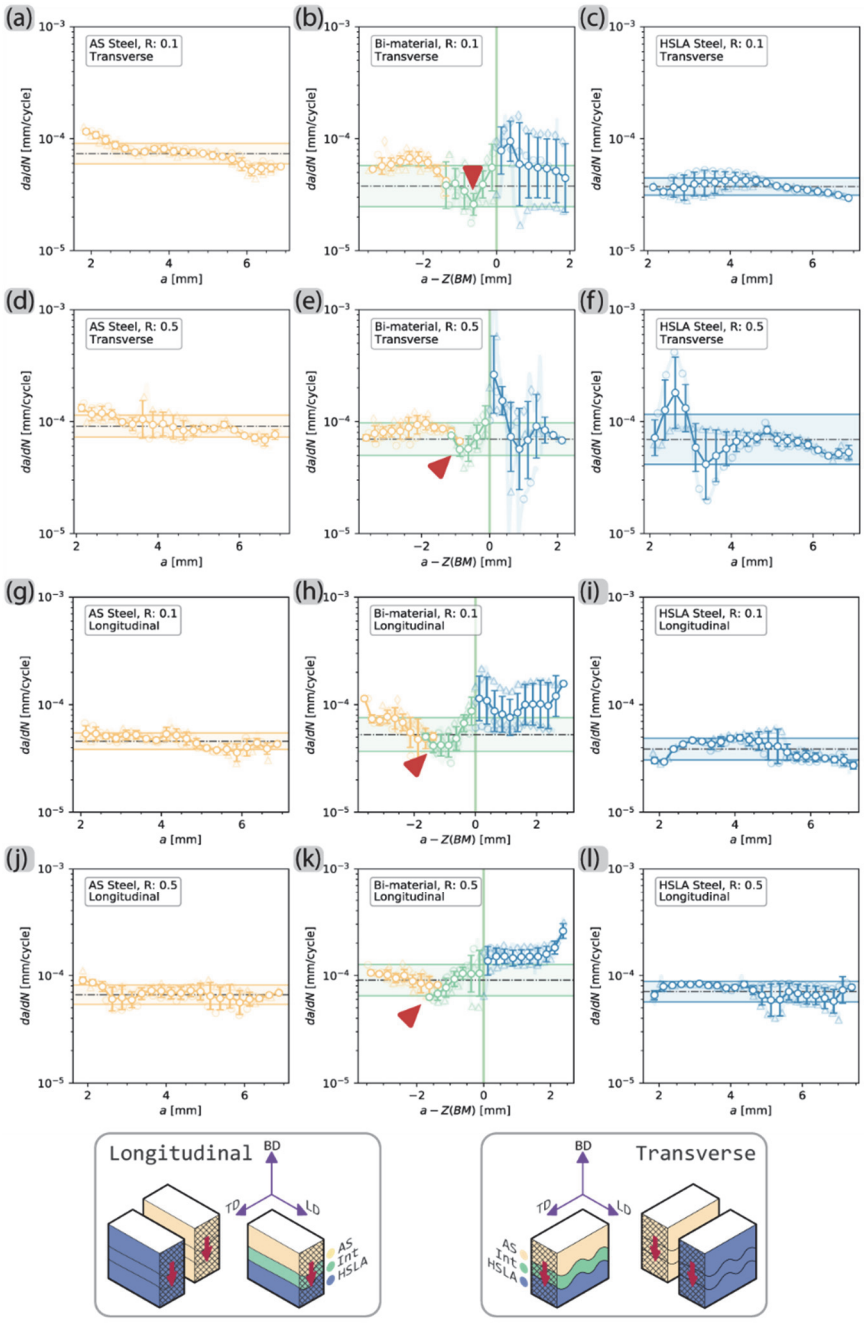

Figure 5-4 Constant ΔK=20 MPa·m0.5 crack propagation rates for (a, d, g, j) AS steel specimens, (b, e, h, k) bi-material specimens and (c, f, I, l) HSLA steel specimens. For bi-material specimens, the position of the crack front is normalized to the position of the dissimilar fusion line, such that a-Z(BM) = 0.

Distinctively, the interface layer shows a variable resistance to crack growth as a function of the position. Bi-material specimens show a clear tendency to arrest crack propagation as the crack front progresses. The position of the lowest measured average growth rates is indicated with a red marker in Figure 5-4 (b, e, h, k). The crack arrest is most notorious on the transverse specimens under an R ratio of 0.1. These specimens shows an average Δ in crack propagation rate of -6.10E-05 mm/cycle (-0.77 $\log_{10}$ steps), when compared to the average propagation rate of the preceding AS steel layers. This tendency is less pronounced but common for the rest of the R ratios and specimen orientations.

As the crack approaches $Z(BM)$, the crack arresting effect is lost. The highest average rate change is measured on the transverse-oriented specimens at a loading ratio of 0.5, where a Δ of + 3.20E-04 mm/cycle (+0.75 $\log_{10}$ steps) was observed. This entails propagation rates almost an order of magnitude higher reached within a crack propagation length of ~1 mm. Growth rates subsequently slow down as the crack front crosses the dissimilar fusion line. $Z(BM)$ is thus the position at which highest rates are measured. This is not immediately clear in all specimens, as lack of fusion defects populate the HSLA steel material volume across many specimens. Nonetheless, this trend is consistent with all material groups in all orientations and R ratios, typically showing the most pronounced effect on transverse-oriented specimens with higher R ratios.

Constant ΔK is ensured through the calibration of ΔK as a function of the elastic moduli and the position of the bi-material interface, as stated in Eq. 5.3 in the method section. Assuming that the calibration is sufficient to control this experimental procedure, the crack arrest and acceleration effects may be attributed to the microstructural constitution of the interface *in-lieu* of the macroscopic effect derived from mismatching elastic moduli. Thus, a closer look is taken into the fracture features in section 5.4.1.

Table 5-2 Average fatigue crack propagation rates as a function of R ratio, material condition and orientation. All data is provided as log10 (mm/cycle) ± one standard deviation.

	Transverse specimen orientation		**Longitudinal specimen orientation**	
	R 0.1	**R 0.5**	**R 0.1**	**R 0.5**
AS steel	-4.134 ±0.09	-4.041 ±0.10	-4.339 ±0.08	-4.178 ±0.09
BM interface	-4.424 ±0.19	-4.156 ±0.15	-4.277 ±0.16	-4.042 ±0.15
HSLA steel	-4.428 ±0.22	-4.159 ±0.22	-4.412 ±0.10	-4.150 ±0.10

5.3.3. Fractography

To establish a relationship between the measured fatigue crack growth rates and the geometrical features of the specimen, macroscopic fractography is carried out. For each specimen, the position of the crack front by the end of the pre-fatigue procedure a_p, the position of $Z(BM)$, and the position of the crack by the end of the fatigue test a_f are highlighted in Figure 5-5. Both fracture surfaces are shown for each specimen. Two reference specimens are shown in Figure 5-5 (a) and Figure 5-5 (b), to highlight the differences in geometry of the interface layer on the crack plane; Figure 5-5 (c) and Figure 5-5 (d) provide examples of the location and geometry of the lack of fusion defects cited in sections 5.3.1 and 0. The measured FCGR as a function of crack position are shown for every specimen presented and approximately scaled to fit between the average position of a_p and a_f.

Differences on the appearance of the fracture surface are attributed to the different material regions and load levels. Crack initiation at the notch is typically achieved with large ΔK values. As the crack approaches a_p, the ΔK values are reduced to a level below the one intended to start the fatigue test, effectively reducing the plastic work imposed on the AS steel material. This is reflected on the four samples shown in Figure 5-5, where a distinctly faceted fracture geometry populates the region adjacent to the notch. These facets become less apparent as the crack progresses up to a_p, and across the rest of the AS steel material volume. The crack then crosses into the interface layer, developing distinct fracture features. The large facets in the AS steel are less apparent, giving place to a predominantly flat surface. Faint facets are however still perceivable. As the crack crosses the dissimilar fusion line into the HSLA steel layers, the fatigued fracture surface

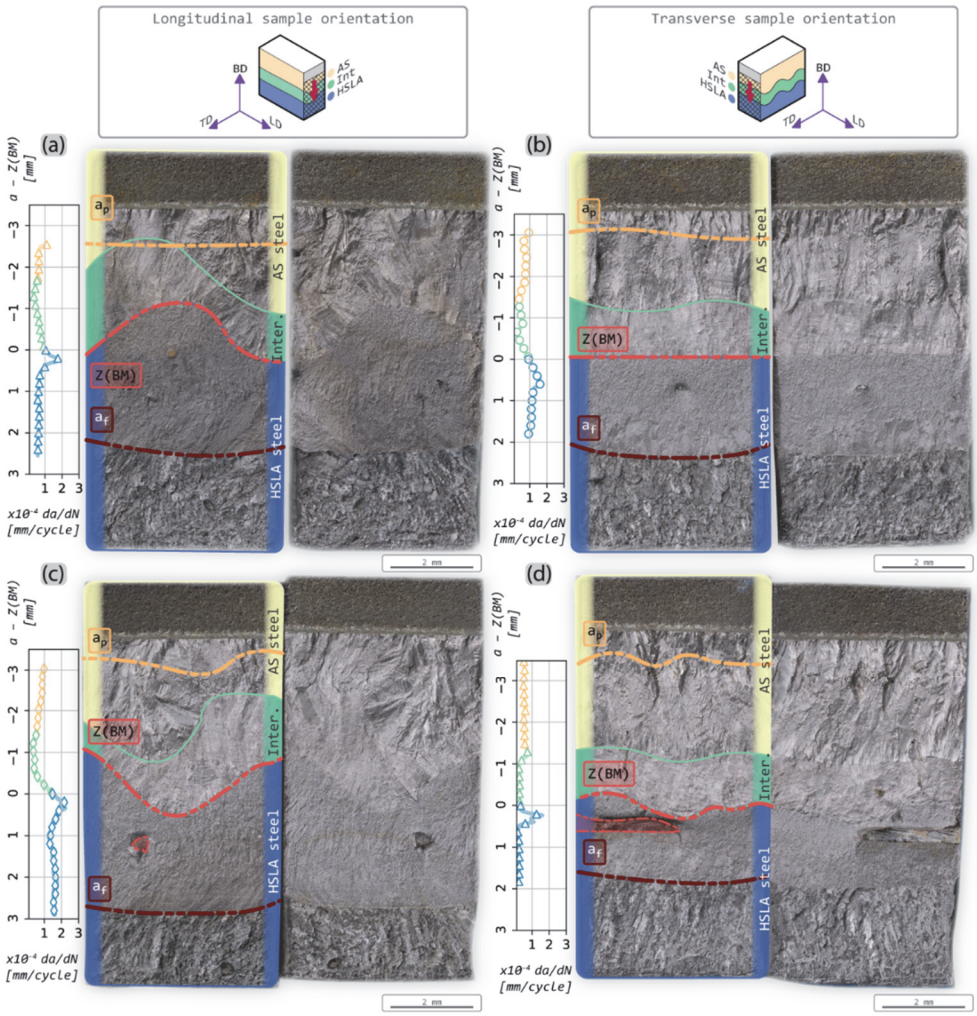

Figure 5-5 Typical macroscopic fracture features of selected specimens, as observed under optical microscopy. Samples were tested under a constant stress intensity range of ΔK: 20 MPa·m0.5 and R: 0.1. Fracture surfaces are presented alongside their corresponding measured fatigue crack propagation rates. (a) and (b) show typical features for longitudinal and transverse oriented samples. (c) and (d) show location of lack-of-fusion defects within the HSLA steel material volume.

becomes duller, and features becomes unperceivable at a macroscopic scale. The surfaces corresponding to final tearing beyond a_f fracture show tortuous detachment, characteristic of HSLA steel alloys.

Microscopic characterization of the fracture surface provides detailed insights on the different mechanisms controlling crack propagation. Figure 5-6 (a) and (b) show low magnification features of two different samples, used to provide context to the features

observed in Figure 5-6 (c-h). The macroscopic facets observed on the AS steel fracture surface are shown under high magnification in Figure 5-6 (c). The faces of these facets are populated by densely packed tearing features related to ductile mixed-mode fracture. Indications of striations across this material volume are not clear. Orange markers indicate locations where secondary cracks are identified. Although most of the fracture surface across the AS steel volume shows similar traits, the region in the vicinity of the fusion line shows occasionally distinct features. The red marker in Figure 5-6 (d) indicates a band of transgranular cleavage combined with tearing fracture, most resembling the mixed fracture modes observed across the interface layer shown in Figure 5-6 (e) and Figure 5-6 (f). This feature most likely originates from unmixed material as obtained during deposition.

Having established the features typically observed across the AS steel layer, it is simpler to identify how unique the fracture features are across the interface layer. At the interface layer, the transformation of metastable austenite into martensite makes itself apparent across the fracture surface features. Figure 5-6 (e) and Figure 5-6 (f) show transgranular cleavage combined with tearing traits obtained from the fracture of martensite. The features in Figure 5-6 (f) converge neatly in a single orientation, whereas the location shown in Figure 5-6 (e) shows tear traits in a multitude of orientations. The origin to this difference can be attributed to the combination of two factors: load direction and the crystal orientation of the grain being fractured. This is discussed in depth in section 5.4.2. Markers in Figure 5-6 (e) and Figure 5-6 (f) indicate the location of small cleavage surfaces. At $Z(BM)$, in line with the features observed in Figure 5-6 (e) and Figure 5-6 (f), shows combined transgranular cleavage and tear fracture, with tear features neatly oriented together. These features are shown in Figure 5-6 (g) and fit with the location of the band of martensite typically formed along this dissimilar fusion line. The red markers show the location of cleavage surface. Across $Z(BM)$, a tearing topography surface is obtained from the HSLA steel layers. This accompanied by secondary cracks (orange markers).

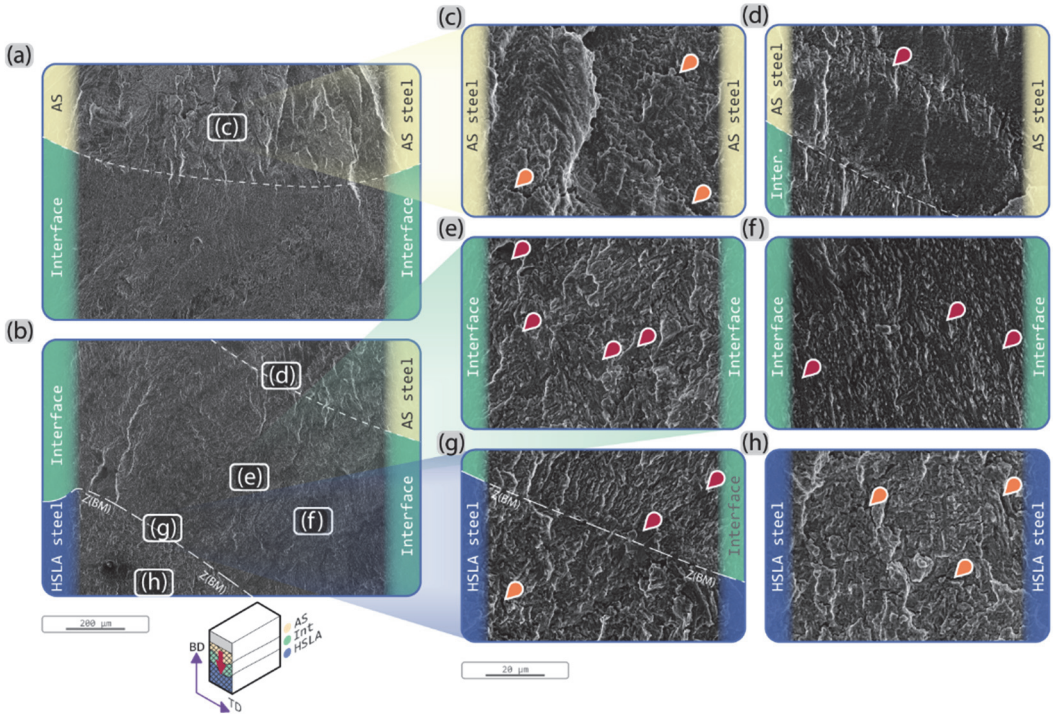

Figure 5-6 Fracture features as observed under scanning electron microscopy. (a) and (b) show a general overview of the regions of interest under low magnification, and specific location of the features shown on (c-h).

5.3.4. EBSD mapping

A practical approach to confirm the presence of martensite along the fracture surface is through EBSD mapping. For this purpose, two different samples were chosen. Figure 5-7 shows the image quality (IQ) and phase maps of two samples tested under constant ΔK. The difference between both samples lies on the R ratio, namely 0.5 for Figure 5-7 (a-d) and for 0.1 Figure 5-7 (e-h). Figure 5-7 (a) and Figure 5-7 (e) show the IQ maps under low magnification. Since the maps are obtained from arbitrary planes across the sample, a considerable difference in size of the interface can be appreciated. This is simply due to the varying geometry of the interface. IQ maps are useful to characterize the degree of clarity with which Kikuchi patterns are obtained. The quality of such patters can be attributed to different factors including sample preparation, mapping parameters, dislocation density and crystal deformation, between others. Given that sample preparation was carefully performed, and the mapping parameters consistent, the changes in grayscale can most likely be attributed to the degree of crystal defects: large crystals

without appreciable deformation appear lighter, while regions with a high density of crystal imperfections and grain boundaries appear darker. In this case, martensite appears dark due to its high dislocation and grain boundary density [11].

Figure 5-7 (a) shows the crack flank region of a specimen with low amount of disperse ferrite banding across the interface layer. The grains thus appear mostly clear, except for a band of martensite along the fusion line pointed with a green marker, and a band of ferrite on the upper region of the interface. Figure 5-7 (b) through (d) show that although the material volume surrounding this region is mainly undeformed, the locations closest to the crack flanks have indeed transformed into martensite. Distinction of ferrite and martensite is not possible simply through phase mapping, but it is understood that most of this mapped bcc phases are bcc' instead based on the grain morphology and the lack of ferrite in their vicinity. The map in Figure 5-7 (b) shows the boundary between the diluted interface and the undiluted AS steel layer. Only the map shown in Figure 5-7 (d) includes the martensite band at the fusion line and the idiomorphic ferrite formed immediately beneath it.

Figure 5-7 (e) offers a contrasting example. The map shows a dense ferrite population, with three clear bands of very low IQ values across the interface layer and an additional band along the fusion line. These are shown with green markers. Under higher magnification, it is easier to confirm the martensitic nature of these low IQ bands. Phase maps shown in Figure 5-7 (g) and Figure 5-7 (h) help identify this phase constituent to be martensite based on the grain morphology and size. The location shown in Figure 5-7 (h) also provides evidence of appreciable crack deflection. The map in Figure 5-7 (f) shows a clear example on this cut plane of martensite obtained from the TRIP effect of metastable austenite. Although this location is found within the undiluted AS steel, an intrusion of the underlying interface layer can lead to local regions of metastable austenite. This matches the observation made in Figure 5-6 (d).

The appearance of martensite across the interface has been presented by us in Chapter 3. Nevertheless, the effect that the martensite had on the crack propagation process is to be further discussed, both in terms of crack propagation speed and orientation. This is done in detail in the following section.

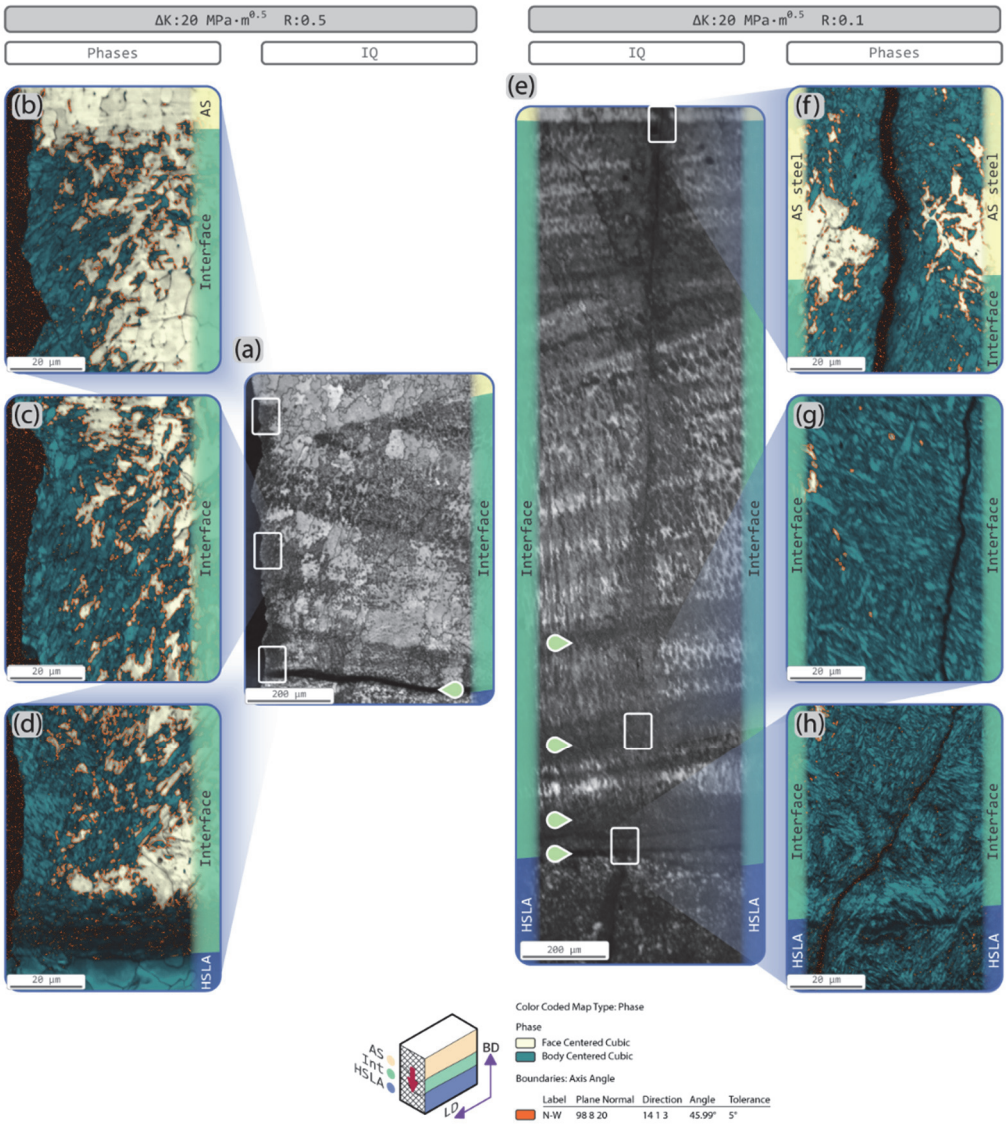

Figure 5-7 EBSD mapping in the vicinity of the crack flank for specimens tested under constant ΔK. (a) shows the crack flank of a specimen loaded under an R ratio of 0.5 as an IQ map, alongside detailed phase mapping of regions showing deformation-induced martensite (b, c), and a region combining both deformation-induced and allotropic martensite (d). (e) shows IQ mapping of the interface layer of a specimen tested under an R ratio of 0.1. Detailed phase maps show deformation-induced martensite in (f) and substantial allotropic martensite found across the rest of the interface's material volume (g, h). Figures (a) and (e) were obtained with a step size of 1.5 µm; figures (b-d) and (f-h) were obtained with a step size of 0.1 µm. Phase maps show points indexed as bcc in teal and fcc in tan. Due to the locations of the maps, most index bcc points are considered martensite.

5.4. DISCUSSION

The results of this work show that fatigue behaviour of this 3D-printed bi-material structure is affected by a complex interplay between macroscopic and microscopic effects, where behaviour of interface layer is of most interest. At a macrostructural scale, the fatigue crack growth rates across the interface show a unique behaviour compared to the parent materials. Crack retardation at the top of the interface layer is consistently accompanied by crack acceleration as the crack front approaches the dissimilar fusion line $Z(BM)$. Changes in specimen orientation and R ratio are also shown to cause measurable differences. These phenomena are discussed in detail in section 5.4.1.

The uniqueness of the interface layer is confirmed at a microstructural scale. Fracture surface analysis demonstrates that there is a fundamental difference between the undiluted and the diluted stainless steel material volumes. This observation is supported by EBSD analysis, where the crack front is demonstrably accompanied by martensite throughout the entire width of the interface layer. The interplay between the previously formed allotropic martensite and deformation-induced martensite is interesting and may help clarify the dual competing effect of crack arrest and acceleration at the interface. Microstructural aspects on fatigue crack growth are discussed in detail in section 5.4.2.

5.4.1. Macrostructural aspects on FCG at the interface

The Dissimilar Interface Effect

Contrary to what was expected, in this work we observe an initial crack retardation followed by a discernible crack acceleration because of a plastically mis-matched interface. This observation does not agree to what would have been expected from a perfectly joint plastically mismatched bi-material structure. Suresh *et al.* [13] propose that dislocation emission from the crack tip is restricted by the harder material, obstructing cyclic slip and therefore obstructing fatigue crack growth. The authors confirmed their results experimentally in a later study [14]. Pippan and Riemelmoser [15] made a similar observation through their numerical analysis, indicating that crack tip opening displacement gradually decreases as the crack approaches the dissimilar fusion line. The authors point out that crack closure effects should become more predominant as the crack front transits from the softer to the harder material, leading to retardation in crack propagation. Work by Jian *et al.* [16] agrees with this observation experimentally. The authors draw this conclusion from a mild steel and AS steel bi-material joint obtained

through explosive cladding. The results obtained from our work under constant ΔK testing in this work show nevertheless an opposite trend.

The variable FCGR across the interface must be thus attributed to its heterogeneous microstructure. The dilution of the AS steel alloy on the HSLA steel substrate layers leads to an interface layer with a unique chemical and microstructural constitution, as characterized Chapter 3. In large, the interface layer is formed by a metastable austenite phase populated by a considerable fraction of ferrite [2]. As the metastable austenite deforms, it transforms into martensite to accommodate large plastic strain. Nevertheless, the heterogeneous chemical constitution of the interface layer also leads to certain regions of high martensite start temperature. This material volume is located mostly alongside the fusion line and in the form of islands (as observed from a BD-TD cross section) or bands (as observed from a BD-LD cross section). Thus, a distinction is necessary between the martensite obtained from allotropic transformations, heron referred to as allotropic martensite, and that obtained from the deformation of metastable austenite at room temperature, hereon referred to as deformation-induced martensite. A correlation can be drawn between the location of metastable austenite, allotropic martensite and the measure fatigue crack propagation rates obtained through ΔK experiments. Within the interface layer, the fatigue crack propagation will be mostly controlled by the deformation of metastable austenite and subsequent fracture of deformation induced martensite, while the root of each bead within the layer will be most affected by the presence of allotropic martensite.

R-ratio effect

As observed under constant ΔK experiments, higher R ratios have a detrimental effect on the crack propagation rates. These results are presented in Figure 5-4 and Table 5-2. The physical effect of the R ratio on the fatigue crack growth process is extensively debated, nonetheless. This dependency on R is often associated with the crack-closure effect [17]. The fracture morphologies presented in Figure 5-6 could be explained at least in part because of crack closure, most evident across the fracture surface of the AS steel and HSLA steel layers. Evidence presented by various studies [18], [19] suggests a nuanced relationship, as quantifying this closure effect is problematic in the presence of material plasticity and non-linear compliance of the testing apparatus.

As an alternative, Kujawski [20] offered an unbiased approach. By means of a normalizing K^* variable, the FCGR data may be homogenized. The homogenization

principle relies on the product of two load parameters, namely ΔK and K_{MAX}, and a material-dependant exponent α, such that:

$$K^* = {K_{MAX}}^{\alpha} \Delta {K^+}^{(1-\alpha)} \qquad (Eq. 5.6)$$

where ΔK^+ is the positive part of the applied K range. This relationship can also be re-stated in terms of R, such that:

$$K^* = \frac{\Delta K^+}{(1-R)^{\alpha}}. \qquad (Eq. 5.7)$$

The proposed method to obtain the value of α involves the determination of two set of Paris parameters obtained with two different R ratios. This can be also achieved by estimating the Paris parameters that would fit the measured FCGR data obtained from the constant-ΔK test. It is done under the assumption that minimal error is incurred if the variation of m as a function of R [21] is small. The assumption is necessary since α is obtained by evaluating ΔK at a common da/dN value. The estimated α parameters, and the resulting K^* values and the relative error between $\log \Delta K$ and $\log K^*$ are presented in Table 5-3.

The approach proposed by Kujawski seems to adequately capture the sensitivity of the materials tested to the R ratio. The highest values of α are obtained from the material volume most sensitive to K_{MAX}. In this case, the largest α exponent is obtained from the bi-material interface layer as measured from transverse-oriented specimens. A high sensitivity of the HSLA material volume to α is also observed, althought this has been attributed to the roughness-induced crack closure [22]. The relative difference between the applied ΔK and the estimated K^* is thus presented in Table 5-3 as relative error in $\log_{10}$ step. This is done, since FCGR data is assumed to be distributed log-norm. Under R=0.1, the relative error between ΔK As the K^* is barely apparent. The relative error incurred under an R ratio of 0.5, though, is more relevant. This is sustained especially for the material conditions most susceptible to the R ratio effect, namely the bi-material interface and the HSLA steel layer (under a constant ΔK of 20 MPa·m$^{0.5}$, K^*=25.96 MPa·m$^{0.5}$ for the transverse oriented BM interface at an R ratio of 0.5, and K^*=25.35 MPa·m$^{0.5}$ for the same orientation and R ratio tested on HSLA steel specimens). Hence, a higher relative induced error is conducive to a more exacerbated R ratio effect.

Previous work has demonstrated a satisfactory relationship between Kujawski's K^* parameter and the crack growth behaviour in metastable austenite [23], [24]. For ductile

materials, the crack driving force is mostly affected by ΔK, as it is correlated to cyclic damage. On the contrary, K_{MAX} best correlates to fatigue crack growth of brittle materials as the parameter relates to the applied monotonic damage [20]. Demonstrably, it also correlates closely to TRIP-aided alloys due to the correlation between K_{MAX} and the size of the process zone ahead of the crack tip. It has been noted previously in this discussion that the deformation-induced martensitic transformation is related to the low stacking fault energy of the interface layer. Thus, a higher dependency of the interface material to α is expected. The α parameter serves thus as a quantitative measure on the sensitivity of K^* on K_{MAX}.

Table 5-3 Kujawski α parameters, estimated K^* values for ΔK-controlled fatigue tests, and relative induced error.

	$\boldsymbol{\alpha}$	$\boldsymbol{K^*}$ $(\mathbf{R\ 0.1})$	$\frac{\log K^* - \log \Delta K}{\log K^*}$	$\boldsymbol{K^*}$ $(\mathbf{R\ 0.5})$	$\frac{\log K^* - \log \Delta K}{\log K^*}$
	-	$MPa \cdot m^{0.5}$	%	$MPa \cdot m^{0.5}$	%
Transverse specimen orientation					
AS steel	0.107	20.23	0.4	21.54	2.4
BM interface	0.376	20.81	1.3	25.96	8.0
HSLA steel	0.342	20.73	1.2	25.35	7.3
Longitudinal specimen orientation					
AS steel	0.192	20.41	0.7	22.85	4.3
BM interface	0.209	20.44	0.7	23.12	4.6
HSLA steel	0.321	20.69	1.1	24.98	6.9

Specimen Orientation and Lack of Fusion Defects

The different crack planes prove useful to characterize the effect of the interface geometry on the FCGR. Differences in the rate of change in FCGR across the interface can be attributed to the geometry of the layer. Figure 5-5 (a) and Figure 5-5 (c) show how much the boundaries of the interface layer may vary across the specimen width. For

example, the average position of $Z(BM)$ on the specimen shown in Figure 5-5 (a) is at about 4.5 mm from the notched surface, whereas its position varies within a range of 1.3 mm. This in turn is related to more nuanced changes in terms of FCGR. For the same specimen, a gradual acceleration in FCGR is measured across the interface as it approaches $Z(BM)$, developing through a length matching ~1.3 mm. Transverse-oriented specimens tend to show clearer changes. The specimen shown in Figure 5-5 (d) is a good example, showing how FCGR decrease sharply after the crack front crosses from the un-diluted AS steel layers into the interface layer. Although it could be reasonable to suspect that the crack may lose considerable straightness as it approaches the dissimilar fusion line, specimens tested under near-threshold loading conditions at the interface show straight cracks compliant with curvature conditions set by ISO 12108 [7].

While transverse specimens provide a clearer picture of the relationship between the geometrical features and the measured FCGR, lack of fusion defects makes it difficult to distinguish the actual magnitude of crack acceleration. Specimens shown in Figure 5-5 (c) and Figure 5-5 (d) show a similar defect in two perpendicular orientations. Their geometry is close to cylindrical, with their long dimension parallel to LD. They typically measure ~0.4 mm in diameter and a few millimetres in length. Regardless of the defect occurrence, the trends in FCGR are comparable to the specimens without defects and are considered useful for analysis.

Limited examples are available in literature addressing this orthotropic effect. Extensive work has been done in this study to characterize the differences between FCGR along the build direction and perpendicular to it. The anisotropy observed in this work is in turn derived from the deposition strategy. Nonetheless, the anisotropy observed may be attributed to the geometrical features of the interface layer. Some parallels can be drawn however with work done on a similar alloy pair. Ayand and Kahraman [25] characterized the mechanical properties of a bi-material wall built by alternating the alloys ER70S-S and 308LSi. By changing the specimen orientation, they observed a clear improvement in fatigue performance through constant load amplitude testing. Fatigue life was improved when the crack plane crossed both materials and $Z(BM)$, instead of a single homogeneous cross section. The observation is not derived from direct fatigue crack propagation rates, thus further work is necessary to address this anisotropy derived from the geometry of the dissimilar fusion line.

5.4.2. Microstructural aspects of FCG through the interface

Metastable Austenite

A fundamental change in the crack driving force is apparent across the interface layer. As observed on constant ΔK experiments, the change in propagation rates amounts up to -6.10E-05 mm/cycle as the crack front crosses the fusion line between the AS steel layers into the interface. Across the AS steel material volume, the faceted nature of the crack front is clearly shown on macroscopic fractography, as shown in Figure 5-5 and Figure 5-6. These facets are a product of the crack front interaction with millimetre-sized grains. It has been observed that twinning and slipping control as deformation mechanism across this material volume under quasi-static fracture [26]. Fracture across austenite grains has been confirmed to occur along low index slip planes, grain and twin boundaries [27]. Thus, crystal orientations of millimetre-size crystals dictate the fracture plane through which the crack propagates, demonstrably yielding a fracture surface showing millimetre-size facets. Alternatively, the faceted fracture is lost as the crack crosses into the interface layer. The fracture morphology shown in Figure 5-6 (e) and (f) is entirely populated by mixed quasi-cleavage and tear features, belonging to the martensite formed ahead of the crack tip. The presence of martensite is confirmed through the EBSD mapping shown in Figure 5-7.

Available literature can give an indication on the underlying differences in fracture mode between the two material volumes. With the use of sub-millimetre CT specimens, Matsushita *et al.* [28] characterized two fundamentally different fatigue crack propagation processes distinguished by the (meta-)stability of austenite grains. For stable austenite, damage accumulation is developed as shear bands form along low-index slip systems. When enough damage is sufficiently accumulated, a shear crack propagates in a short burst along a close-packed plane, only to be slowed down while further damage is accumulated. This observation is congruent with earlier work published by Hanz and Neumann [29] and more recently by Yang *et al.* [30].

Opposingly, Matsushita *et al.* [28] also studied the fatigue crack propagation process across metastable austenite. Through their work they show how the formation and intersection of shear bands leads to the formation of α'-martensite. Further deformation leads to growth of the martensite phase fraction, with most martensite laths oriented along similar crystallographic orientations. This martensite nucleation and propagation process consequently decreases the crack propagation rate. This effect is apparently only effective under stage I cracking, where ΔK is small. Wang *et al.* [31] explain that during

stage II cracking, secondary cracks are formed along martensite packet boundaries ahead of the crack tip. These secondary cracks promote crack coalescence and rapid crack propagation. Ultimately, numerous studies show that crack propagation across metastable austenite is slower compared to stable austenite under comparable loading and environmental conditions [32], [33]. This observation agrees with the results obtained from constant ΔK testing, presented in section 5.3.2.

Martensite Variant Selection

The deformation induced martensite is different from the allotropic martensite in crystallographic terms. Based on the observations by Wang *et al.* [31] metastable austenite will transform into martensite readily arresting the crack propagation process. The susceptibility of the austenite crystal to transform, and the selection of the child martensite phase variant will depend on the crystal and load orientations [34]. Across a material with large austenite grain sizes and strong texture such as the interface layer, under the influence of a single dominant mode of loading, strong variant selection is expected. Opposingly, the martensite derived from allotropic transformations is obtained by the thermomechanical strain derived from solidification and cooling. The strain conditions under which allotropic martensite is formed promote more and more diverse child variants, leading to a more ambiguous variant selection, if at all.

Distinguishing allotropic from strain induced martensite can help clarify differences in crack propagation processes. From the martensitic regions shown in Figure 5-7, a distinction is made between based on the surroundings of the maps. Regions shown in Figure 5-7 (a) through (c) show deformation induced martensite, while Figure 5-7 (d) through (f) show regions populated by allotropic martensite. Figure 5-7 (c) and (e) share the same region of interest, but a distinction is made since this region seemingly contains both allotropic and deformation-induced martensite, as obtained from a single parent austenite grain. Mapping of the identified variants assuming a K-S OR to their parent austenite grain is shown in Figure 5-8. Alongside the variant maps, pole figures indicate the crystal directions of the twenty-four theoretically possible K-S variants about the predicted orientation of the parent austenite grain. Lastly, the histogram shows the relative frequency of the variants identified. Colour coding is consistent on the maps, pole figures and histograms.

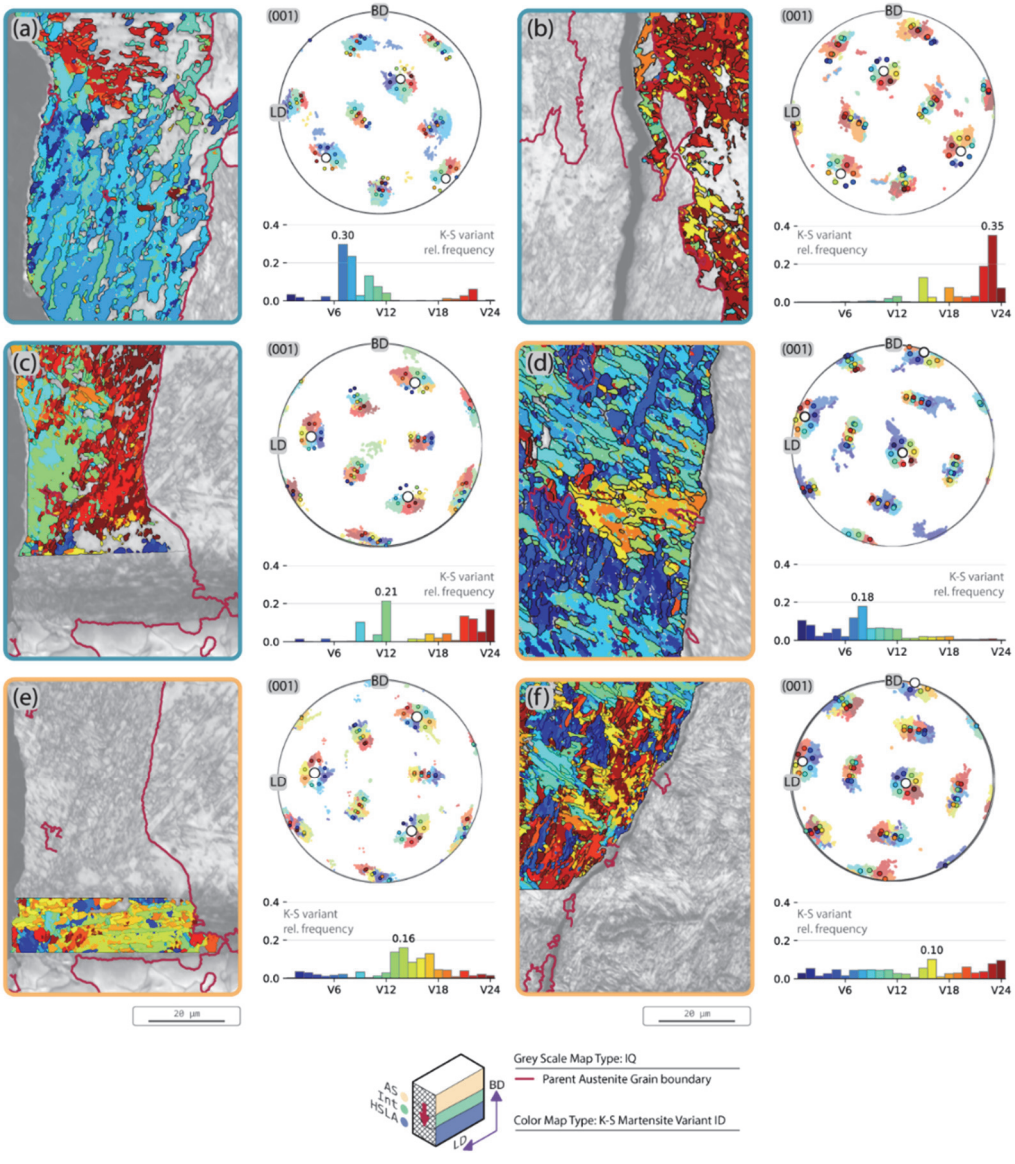

Figure 5-8 Spatial distribution, (001) pole figures and relative frequency histograms of every individual K-S child variant as measured in single PAG's at the flanks of constant ΔK fatigue cracks. All regions of interest match those shown in Figure 5-7. Examples of deformation-induced martensite are shown in (a-c); examples of allotropic martensite are shown on (d-f). Variant maps (a-f) were obtained with a step size of 0.4 µm.

The maps shown in Figure 5-7 indicate a clear distinction in variant selection between allotropic and deformation induced martensite. On one hand, relative frequencies of deformation-induced martensite are consistently higher for the individual variants present. On the other hand, regions of allotropic martensite show lower relative frequencies for single variants, but a more homogeneous distribution across all variants. Each region reflects in turn a selection of specific grain boundary orientation relationship between the different martensite laths. This observation is supported by the histogram presented in Figure 5-9 (a). The figure shows the relative frequencies of all sixteen possible axis-angle relationships between martensite laths belonging to a single parent-austenite grain [35]. In accordance with the data shown on variant selection, grain boundaries show a tendency to select specific orientation relationships across the deformation induced martensite, whereas a better distribution across all possible relationships is observed across allotropic martensite. Figure 5-9 (b) and (c) show in turn that no significant difference in terms of grain size or grain misorientation angle can be derived from the data presented. Arguably, the selection of martensite variants leads to a smaller amount of high angle packet boundaries that may restrict crack propagation. To confirm this, the fracture planes of martensite laths observed across the interface layer are studied in detail in the following subsection.

Fracture Across Martensite

The microstructural mechanisms controlling fracture across martensite are now addressed. It has been discussed that the process zone ahead of the crack front induces martensite transformation across metastable austenite. Alternatively, the crack front may reach a material volume populated by allotropic martensite. In either case, crack extension will be dictated by the mechanisms governing fracture of across that phase constituent. A close inspection of the relationship between the crack path and the crystal orientation can give some indication of the mechanisms ultimately leading to fracture.

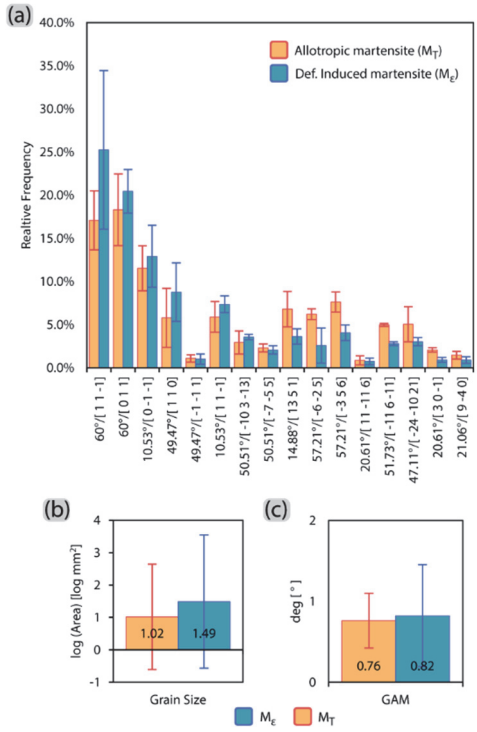

Figure 5-9 (a) Relative frequency of measured axis-angle relationships possible between martensite variants, alongside grain size (b) and grain average misorientaiton (GAM) (c) values. Data is shown as polled from maps (a-c) for deformation-induced martensite and (d-f) for allotropic martensite.

The fracture planes through which the crack propagates are analysed at select locations. Figure 5-10 (a) and Figure 5-10 (f) show the location on the fracture surface where ion-milled lamellae were extracted for this purpose. Transmission Kikuchi Diffraction (TKD) is used to analyse the crystal orientations of the grains subjacent to the fracture surface, as shown in Figure 5-10 (e) and Figure 5-10 (j). Vectors normal to the fracture trace are shown at select locations in Figure 5-10 (b) through Figure 5-10 (d) for the region exemplifying allotropic martensite, and Figure 5-10 (g) through Figure 5-10 (i) for the region exemplifying deformation-induced martensite. The crystal indices parallel to the normal vectors are shown on each corresponding IPF. All points that agree with the proposed <crystal index> || [fracture trace normal] relationship within a tolerance of 5° are colour-plotted. Although the tolerance angle is large, it allows some room to account for the possible error induced by the lack of perpendicularity between the section plane

and the fracture surface. Indexed points outside the tolerance range are not colour-plotted.

Distinct preferences on fracture planes can be associated to the crystal structure of the adjacent martensite. The region of interest shown in Figure 5-10 (b-d) involves two martensitic packets on the fracture plane. A packet is defined as a hierarchical structure containing several blocks of martensite with the same habit plane [36]. Packet id 1 sustains a $(111)_\gamma||(011)_\alpha$, relationship to its parent austenite grain. Alternatively, packet id 3 sustains a $(\bar{1}11)_\gamma||(011)_\alpha$, relationship. Across packet id 1, the fracture plane agrees largely with the crystal plane family {334}. The adjacent martensite grains in Figure 5-10 (b-d) belong to a packet id 3. At this location, the fracture path becomes tortuous, with fracture planes closely approximating the densely packed plane families {3 2 1} and {1 1 2}. The differences between the two packets in fracture surface development is not attributed simply to the different packets, but the habit plane that defines them [37]. The definition of the habit plane is a non-trivial task, but the trace of the habit plane suggests a 40° deviation to the notch plane. Under this condition, closed pack planes appear to be selected as fracture planes. The emergence of different martensite packets is thus beneficial, as high angle packet boundaries have been confirmed to cause crack arrest [36]. Tabulated values between the proposed fracture planes and the most proximal densely packed plane are shown on Table 5-4.

The region of interest shown in Figure 5-10 (g-i) shows contrasting traits, that can similarly be attributed to the relationship between the martensite and apparent habit plane. The martensite packet in this region appears larger to those of allotropic martensite, and the misorientaiton between the fracture plane and the habit plane trace of the martensite packages appears to be smaller (~5.7°). As fracture develops across this single martensite packet, the crack propagates along high-index planes, which do not necessarily resemble any closed-packed planes. On the contrary, the crack appears to follow the block boundaries. These results agree with the observations made by Ueki et al. [62], where it is pointed out that this relationship between load and microstructure is in fact more detrimental than the one observed across allotropic martensite.

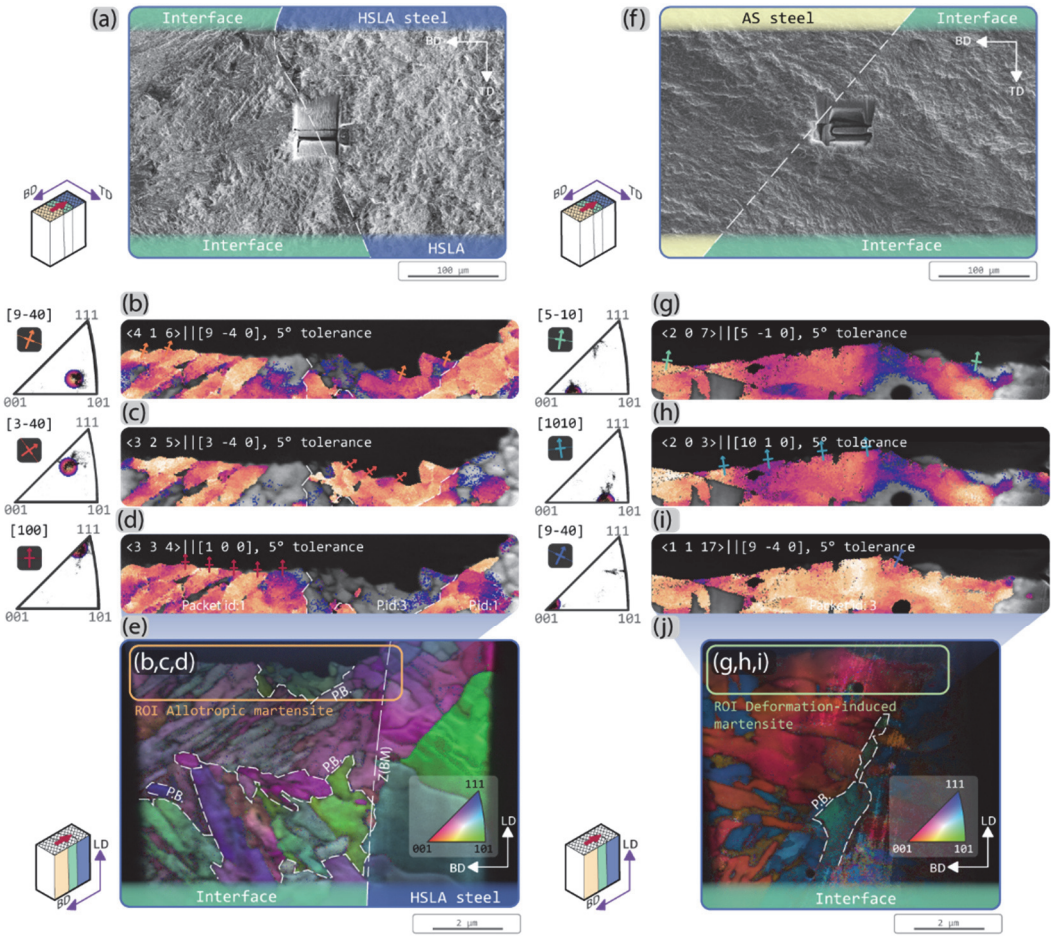

Figure 5-10 TKD of FIB-milled lamella obtained from the fracture surface at the fusion line between the interface layer and the HSLA steel substrate. (a) and (f) show the locations on the fracture surface from which the lamellae were lifted (b) though (d) and (g) through (i) show the colour-mapped correspondence between proposed crystal plane and the fracture surface trace normal. Maps are shown within a 5° tolerance angle. Inverse pole figure shows colour-coding and distribution of points considered about the proposed fracture planes. (e) and (j) show the IPF mapping of the same regions as (b-d) and (g-h) and their surroundings. P.B indicates a packet boundary.

Results of this work are further supported by previous observations made on the fracture of martensite. Lindborg *et al.* [39] made early observations that tempered martensite fractured in well-defined planes, most frequently observed across {100}, {321}, {211} and {110}. This in turn depends on the carbon content and tempering conditions of the martensite laths. These cleavage fracture planes have been experimentally confirmed along the {110} and {100} planes across lath and block

boundaries by Cho *et al.* [40] in the context of hydrogen-embrittled martensite. Moreover, the latter authors point out that the slip plane {112} tends to allocate deformation through dislocation accumulation. Although certain mechanisms in lath martensite have been shown to accommodate plastic deformation [41], [42], TKD results confirm that transgranular fracture across close-packed planes remains the dominant mechanism controlling fracture across the allotropic martensite. The lack of capacity to accommodate and dissipate large strain results ultimately in crack acceleration, as observed in the FCGR measured through this work. Although small, the capacity to accommodate strain in lath martensite will be dependent on the relationship between the habit plane and the load direction [43]. This observation agrees with the work of Ueki et al. [61], where the authors point out that the angle between the martensite habit plane and the notch plane will dictate the fatigue crack propagation rates across this microstructural constituent. This suggests that in the context of this work, the large packets of martensite and the few variants formed ahead of the crack front across regions of metastable austenite favour crack propagation. This observation suggests e.g. that very high overloads could ultimately have an unproportionally detrimental effect in crack propagation rates across the interface layer.

Table 5-4 Observed crystal fracture planes, their most proximal densely packed plane, and their deviation from the notch plane for ROIs shown in Figure 5-10 (e) and Figure 5-10 (j). Angle between the crystal plane parallel to the fracture plane and the closest densely packed plane is shown between parentheses.

ROI exemplifying allotropic martensite			**ROI exemplifying deformation-induced martensite**		
Crystal plane parallel to fracture plane	**Closest densely packed plane**	**Deviation of trace normal from notch plane**	**Crystal plane parallel to fracture plane**	**Closest densely packed plane**	**Deviation from notch plane**
{416}	{213} (err. 7.61°)	-24.0°	{207}	{001} (err. 15.95°)	-11.3°
{325}	{213} (err. 4.31°)	-53.1°	{203}	{101} (err 11.31°)	5.7°
{334}	{111} (err. 8.05°)	0°	{117}	{001} (err. 11.42°)	-24.0°

5.5. CHAPTER CONCLUSIONS

Understanding the fatigue crack propagation behaviour is essential for the reliable application of HSLA-AS steel bi-material components produced by WAAM. This study provides empirical evidence on their fatigue performance. To establish a baseline, mono-material specimens of ER70S-6 (HSLA steel) and ER316L (AS steel) were benchmarked. Subsequently, fatigue crack propagation was studied across the interface layer to assess its behaviour in a bi-metal context. Techniques such as microscopy, fractography, and electron backscatter diffraction were employed to explore the relationship between microstructure and fatigue performance. Special focus is given to the martensite formed at the interface and its role, both as the product of a crack-arresting process through TRIP effect, and as a crack accelerator in the form of allotropic martensite. Based on the results obtained, the following conclusions are drawn:

- Paris parameters and K_{th} values are provided for the interface material volume, as obtained from single edge notched bending specimens. HSLA and AS steel mono-material specimens are used to provide benchmark values. The interface is shown to have comparable Paris parameters to the mono-material counterparts (BD-LD plane: m = 2.79, $\log_{10}(C) = 7.83 \log_{10}(da/dN)$) (BD-TD plane: m = 3.47, $\log_{10}(C) = 8.39 \log_{10}(da/dN)$), but a lower ΔK_{th} value (1.4 MPa·m$^{0.5}$ compared to the ca. 2.0 MPa·m$^{0.5}$of the undiluted parent materials).
- Under constant ΔK, the effect of the interface on the overall fatigue crack propagation performance of the bi-material specimens is made more apparent. The interface displays both a crack retardation effect at the top of the layer, and a crack accelerating effect in the vicinity of the dissimilar fusion line.
- The crack retardation effect at the interface originates from the deformation-induced martensitic transformation of metastable austenite. This process is also shown to drive variant selection on the product martensite.
- The crack acceleration process is confirmed to originate from transgranular fracture across allotropic martensite found in the vicinity of the dissimilar fusion line. It is argued that the lack of metastable austenite restricts the work hardening capacity of the material.
- An anisotropic effect derived from the geometry of the interface layer is observed. The crack propagation process on the plane normal to the bead

deposition direction (longitudinal specimen orientation, plane BD-TD) shows milder changes in FCGR.

- R ratios are shown to have an effect both on the interface layer and the HSLA steel. The driving mechanism leading to this difference is ambiguous, but a normalizing K^* parameter is used to encompass both sensitivity to K_{MAX} and ΔK.

The results of this study contribute to the empirical evidence on the performance of functional graded bi-metal parts obtained through WAAM. By examining the transformation of the diluted interface layer into martensite and its subsequent impact on FCGR, the research elucidates the complex interplay of microstructural changes leading to crack propagation. The findings highlight the conditions under which the interface exhibits both enhanced and detrimental fatigue properties, providing crucial insights for improving the design and reliability of WAAM structures with dissimilar metal interfaces.

5.6. CHAPTER REFERENCES

[1] M. R. U. Ahsan, A. N. M. Tanvir, T. Ross, A. Elsawy, M. S. Oh, and D. B. Kim, "Fabrication of bimetallic additively manufactured structure (BAMS) of low carbon steel and 316L austenitic stainless steel with wire + arc additive manufacturing," Rapid Prototyp J, vol. 26, no. 3, pp. 519–530, 2019, doi: 10.1108/RPJ-09-2018-0235.

[2] M. R. U. Ahsan et al., "Heat-treatment effects on a bimetallic additively-manufactured structure (BAMS) of the low-carbon steel and austenitic-stainless steel," Addit Manuf, vol. 32, pp. 1–25, 2020, doi: 10.1016/j.addma.2020.101036.

[3] Y. Ayan and N. Kahraman, "Fabrication and Fatigue Properties of Dissimilar Steel Functionally Graded Material Structure Through Wire Arc Additive Manufacturing," J Mater Eng Perform, vol. 32, no. 24, pp. 11285–11295, 2023, doi: 10.1007/s11665-023-07914-5.

[4] A. Suárez, A. Panfilo, E. Aldalur, F. Veiga, and P. Gomez, "Microstructure and mechanical properties of mild steel-stainless steel bimetallic structures built using Wire Arc Additive Manufacturing," CIRP J Manuf Sci Technol, vol. 38, pp. 769–773, 2022, doi: 10.1016/j.cirpj.2022.06.018.

[5] S. Allain, J. P. Chateau, O. Bouaziz, S. Migot, and N. Guelton, "Correlations between the calculated stacking fault energy and the plasticity mechanisms in Fe-Mn-C alloys," Materials Science and Engineering: A, vol. 387–389, no. 1-2 SPEC. ISS., pp. 158–162, 2004, doi: 10.1016/j.msea.2004.01.059.

[6] W. Jiang, W. Woo, G.-B. An, and J.-U. Park, "Neutron diffraction and finite element modeling to study the weld residual stress relaxation induced by cutting," Mater Des, vol. 51, pp. 415–420, Oct. 2013, doi: 10.1016/j.matdes.2013.04.053.

[7] ISO, NEN-ISO 12108 (en) Metallic materials - Fatigue crack growth mehod. Switzerland, 2018.

[8] A. Ohta, I. Soya, S. Nishijima, and M. Kosuge, "Statistical evaluation of fatigue crack propagation properties including threshold stress intensity factor," Eng Fract Mech, vol. 24, no. 6, pp. 789–802, 1986, doi: 10.1016/0013-7944(86)90265-1.

[9] F. Niessen, T. Nyyssönen, A. A. Gazder, and R. Hielscher, "Parent grain reconstruction from partially or fully transformed microstructures in MTEX," J Appl Crystallogr, vol. 55, no. 1, pp. 180–194, Feb. 2022, doi: 10.1107/S1600576721011560.

[10] A. Ohta, I. Soya, S. Nishijima, and M. Kosuge, "Statistical evaluation of fatigue crack propagation properties including threshold stress intensity factor," Eng Fract Mech, vol. 24, no. 6, pp. 789–802, 1986, doi: 10.1016/0013-7944(86)90265-1.

[11] J. Wu, P. J. Wray, C. I. Garcia, M. Hua, and A. J. Deardo, "Image quality analysis: A new method of characterizing microstructures," ISIJ International, vol. 45, no. 2, pp. 254–262, 2005, doi: 10.2355/isijinternational.45.254.

[12] J. L. Galán Argumedo, M. Mahmoudiniya, T. E. Reinton, L. A. I. Kestens, M. J. M. Hermans, and V. A. Popovich, "Functional grading of low alloy steel to 316 L by wire arc additive manufacturing – Microstructural and mechanical characterization of bi-metal interface," J Mater Process Technol, vol. 325, p. 118305, Apr. 2024, doi: 10.1016/j.jmatprotec.2024.118305.

[13] S. Suresh, Y. Sugimura, and E. K. Tschegg, "The growth of a fatigue crack approaching a perpendicularly-oriented, bimaterial interface," Scripta Metallurgica et Materiala, vol. 27, no. 9, pp. 1189–1194, 1992, doi: 10.1016/0956-716X(92)90597-8.

[14] Y. Sugimura, P. G. Lim, C. F. Shih, and S. Suresh, "Fracture normal to a bimaterial interface: Effects of plasticity on crack-tip shielding and amplification," Acta Metallurgica Et Materialia, vol. 43, no. 3, pp. 1157–1169, 1995, doi: 10.1016/0956-7151(94)00295-S.

[15] R. Pippan and F. O. Riemelmoser, "Fatigue of bimaterials. Investigation of the plastic mismatch in case of cracks perpendicular to the interface," Comput Mater Sci, vol. 13, no. 1–3, pp. 108–116, 1998, doi: 10.1016/s0927-0256(98)00051-2.

[16] F. Jiang, Z. L. Deng, K. Zhao, and J. Sun, "Fatigue crack propagation normal to a plasticity mismatched bimaterial interface," Materials Science and Engineering: A, vol. 356, no. 1–2, pp. 258–266, 2003, doi: 10.1016/S0921-5093(03)00142-4.

[17] W. Elber, "The significance of fatigue crack closure," ASTM Special Technical Publication, vol. STP 486, pp. 230–242, 1971, doi: 10.1520/STP26680S.

[18] J. K. Donald, "Introducing the compliance ratio concept for determining effective stress intensity," Int J Fatigue, vol. 19, no. SUPPL.1, pp. 191–195, 1997, doi: 10.1016/s0142-1123(97)00024-8.

[19] K. Sadananda, M. Nani Babu, and A. K. Vasudevan, "A review of fatigue crack growth resistance in the short crack growth regime," Materials Science and Engineering: A, vol. 754, no. March, pp. 674–701, 2019, doi: 10.1016/j.msea.2019.03.102.

[20] D. Kujawski, "A fatigue crack driving force parameter with load ratio effects," Int J Fatigue, vol. 23, no. 21, pp. 239–246, 2001, doi: 10.1016/S0142-1123(01)00158-X.

[21] Y. Li, H. Wang, and D. Gong, "The interrelation of the parameters in the Paris equation of fatigue crack growth," Eng Fract Mech, vol. 96, pp. 500–509, 2012, doi: 10.1016/j.engfracmech.2012.08.016.

[22] Y. Zhong, F. Xiao, J. Zhang, Y. Shan, W. Wang, and K. Yang, "In situ TEM study of the effect of M/A films at grain boundaries on crack propagation in an ultra-fine acicular ferrite pipeline steel," Acta Mater, vol. 54, no. 2, pp. 435–443, 2006, doi: 10.1016/j.actamat.2005.09.015.

[23] D. F. Martelo, A. M. Mateo, and M. D. Chapetti, "Fatigue crack growth of a metastable austenitic stainless steel," Int J Fatigue, vol. 80, pp. 406–416, 2015, doi: 10.1016/j.ijfatigue.2015.06.029.

[24] D. F. Martelo, A. Mateo, and M. D. Chapetti, "Crack closure and fatigue crack growth near threshold of a metastable austenitic stainless steel," Int J Fatigue, vol. 77, pp. 64–77, 2015, doi: 10.1016/j.ijfatigue.2015.02.016.

[25] Y. Ayan and N. Kahraman, "Fabrication and characterization of functionally graded material (FGM) structure containing two dissimilar steels (ER70S-6 and 308LSi) by wire arc additive manufacturing (WAAM)," Mater Today Commun, vol. 33, no. September, p. 104457, 2022, doi: 10.1016/j.mtcomm.2022.104457.

[26] D. Kumar, S. Jhavar, A. Arya, K. G. Prashanth, and S. Suwas, "Mechanisms controlling fracture toughness of additively manufactured stainless steel 316L," Int J Fract, vol. 235, no. 1, pp. 61–78, May 2022, doi: 10.1007/s10704-021-00574-3.

[27] A. S. Hamada, L. P. Karjalainen, and J. Puustinen, "Fatigue behavior of high-Mn TWIP steels," Materials Science and Engineering: A, vol. 517, no. 1–2, pp. 68–77, 2009, doi: 10.1016/j.msea.2009.03.039.

[28] A. Matsushita, S. Ueki, Y. Mine, and K. Takashima, "Comparative Study of Microstructure-sensitive Fatigue Crack Propagation in Coarse- and Fine-grained Microstructures between Stable and Metastable Austenitic Stainless Steels Using Miniature Specimen," ISIJ International, vol. 61, no. 5, pp. 1688–1697, May 2021, doi: 10.2355/isijinternational.ISIJINT-2020-659.

[29] A. Heinz and P. Neumann, "Crack initiation during high cycle fatigue of an austenitic steel," Acta Metallurgica et Materialia, vol. 38, no. 10, pp. 1933–1940, 1990, doi: https://doi.org/10.1016/0956-7151(90)90305-Z.

[30] H. K. Yang, V. Doquet, and Z. F. Zhang, "Fatigue crack growth in two TWIP steels with different stacking fault energies," Int J Fatigue, vol. 98, pp. 247–258, 2017, doi: 10.1016/j.ijfatigue.2017.01.034.

[31] X. Wang, C. Liu, B. Sun, and D. Ponge, "The dual role of martensitic transformation in fatigue crack growth," pp. 1–7, 2022, doi: 10.1073/pnas.2110139119/-/DCSupplemental.Published.

[32] Z. Mei and J. W. Morris, "Influence of deformation-induced martensite on fatigue crack propagation in 304-type steels," Metallurgical transactions. A, Physical metallurgy and materials science, vol. 21 A, no. 12, pp. 3137–3152, 1990, doi: 10.1007/BF02647310.

[33] E. Hornbogen, "Martensitic transformation at a propagating crack," Acta Metallurgica, vol. 26, no. 1, pp. 147–152, 1978, doi: 10.1016/0001-6160(78)90211-0.

[34] D. De Knijf, T. Nguyen-Minh, R. H. Petrov, L. A. I. Kestens, and J. J. Jonas, "Orientation dependence of the martensite transformation in a quenched and partitioned steel subjected to uniaxial tension," J Appl Crystallogr, vol. 47, no. 4, pp. 1261–1266, 2014, doi: 10.1107/S1600576714011959.

[35] A. Mirzaei et al., "The role of parent austenite grain size on the variant selection and intervariant boundary network in a lath martensitic steel," Materials Science and Engineering: A, vol. 889, no. August 2023, p. 145793, 2024, doi: 10.1016/j.msea.2023.145793.

[36] M. Tsuboi, A. Shibata, D. Terada, and N. Tsuji, "Role of Different Kinds of Boundaries Against Cleavage Crack Propagation in Low-Temperature Embrittlement of Low-Carbon Martensitic Steel," Metall Mater Trans A Phys Metall Mater Sci, vol. 48, no. 7, pp. 3261–3268, Jul. 2017, doi: 10.1007/s11661-017-4107-9.

[37] S. Ueki, Y. Mine, and K. Takashima, "Microstructure-sensitive fatigue crack growth in lath martensite of low carbon steel," Materials Science and Engineering: A, vol. 773, p. 138830, Jan. 2020, doi: 10.1016/j.msea.2019.138830.

[38] S. Ueki, T. Matsumura, Y. Mine, S. Morito, and K. Takashima, "Microstructural fatigue crack growth in single-packet structures of ultra-low carbon steel lath martensite," Scr Mater, vol. 173, pp. 80–85, Dec. 2019, doi: 10.1016/j.scriptamat.2019.08.004.

[39] U. H. Lindborg and B. L. Averbach, "Crystallographic aspects of fracture in martensite," Acta Metallurgica, vol. 14, no. 11, pp. 1583–1593, 1966.

[40] L. Cho et al., "Characteristics and mechanisms of hydrogen-induced quasi-cleavage fracture of lath martensitic steel," Acta Mater, vol. 206, p. 116635, 2021, doi: 10.1016/j.actamat.2021.116635.

[41] S. Ueki, Y. Mine, X. Lu, Y. L. Chiu, P. Bowen, and K. Takashima, "Effect of geometric lath orientation on fatigue crack propagation via out-of-plane dislocation glide in martensitic steel," Scr Mater, vol. 203, p. 114045, Oct. 2021, doi: 10.1016/j.scriptamat.2021.114045.

[42] C. Du, J. P. M. Hoefnagels, R. Vaes, and M. G. D. Geers, "Plasticity of lath martensite by sliding of substructure boundaries," Scr Mater, vol. 120, pp. 37–40, Jul. 2016, doi: 10.1016/j.scriptamat.2016.04.006.

[43] Y. Mine, K. Hirashita, H. Takashima, M. Matsuda, and K. Takashima, "Micro-tension behaviour of lath martensite structures of carbon steel," Materials Science and Engineering: A, vol. 560, pp. 535–544, Jan. 2013, doi: 10.1016/j.msea.2012.09.099.

[Page intentionally left blank]

6. GENERAL DISCUSSION

Chapters 2 through 5 present the scientific framework aimed to answer the research question presented in Chapter 1. The work extensively deals with the relationship between the processing conditions, the microstructural development, and the derived mechanical properties of HSLA-AS steel bi-materials produced by WAAM. However, it might be useful to explicitly establish the relationships between the conclusions drawn in each chapter across a comprehensive discussion. The discussion presented in the following pages is intended to contextualize Chapters 2 through 5 into a broader scientific and technical context, otherwise intended to provide a "helicopter view". The discussion is thus structured in two main sections. First, an evaluation of the research objectives formulated in Chapter 1 is given. It is then followed by a contextualization of our results is presented for the broader readership, concentrating on the utilization of the results for the design of functionally graded parts through additive manufacturing.

6.1. EVALUATION OF RESEARCH OBJECTIVES

The first research objective stated in Chapter 1 reads as follows:

> *"To develop a comprehensive understanding of microstructural evolution at the interface layer, which is crucial for correlating microstructural features with the mechanical performance of bi-material components."*

One of the central challenges in dissimilar metal additive manufacturing is understanding the microstructure that forms at the interface between alloys. This work systematically characterized the interface layer formed between ER70S-6 (HSLA steel) and ER316L (AS steel) through wire arc additive manufacturing. The investigation was carried out at multiple length scales to gain critical insights into the microstructural complexity of this region. This objective is addressed through Chapters 2 and 3. Figure 6-1 offers a visual representation of the major microstructural components found at the diluted interface layer, summarized hereunder.

At the millimetre scale, macroscopic examination revealed a visibly heterogeneous interface layer, shaped by the dynamics of the molten metal weld pool during deposition. Features such as protrusion of unmixed material provided direct evidence of partial mixing—a phenomenon predicted in previous literature [1], and here confirmed experimentally. These observations underscored the first challenge: for the process parameters chosen, the interface does not form as a uniform transition, but rather as a heterogeneous material volume with chemically distinct regions.

At the micron scale, the focus shifted to understanding how chemical segregation influenced phase development. Through a combination of metallography, crystallography, and EPMA, it became evident that regions of low Ni and Mn content—elements known to stabilize austenite—were associated with the presence of martensite. The crystallographic orientation relationships derived from EBSD analysis identified between underlying ferrite, martensite at the dissimilar fusion line, and adjacent austenite, strongly suggest epitaxial growth during solidification. However, this level of analysis revealed a new challenge: certain ferritic regions could not be readily distinguished from martensite or bainite, making phase identification uncertain.

To resolve this ambiguity, nano-scale characterization was undertaken. TEM confirmed the presence of both α' (bcc) and ε (hcp) martensite, clarifying the identity of the previously ambiguous structures. The remaining ferritic regions were predominantly

idiomorphic in nature, though rare instances of acicular morphology pointed to possible bainitic lath formation.

All together, these results present a comprehensive, empirical description of the interface microstructure, addressing in the first objective. The layer is defined by chemical heterogeneity, solidification dynamics, allotropic phase transformations, and thermal cycling induced by successive layer deposition. Although complex, the microstructural constitution uncovered through this multi-scale approach is crucial for establishing meaningful correlations between the interface and its mechanical response. While doing so, this work lays the foundation establish structure-property relationships in dissimilar metal WAAM components.

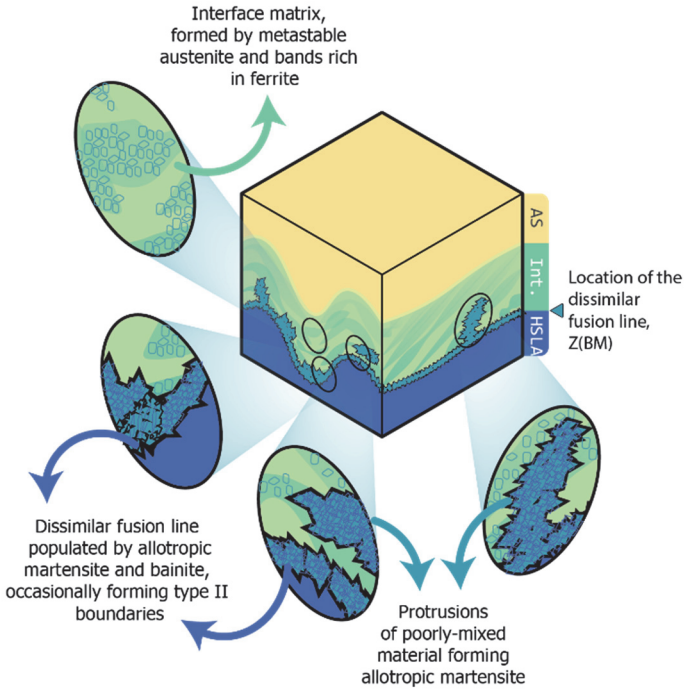

Figure 6-1 Main microstructural components constituting the material volume of the diluted interface layer between and HSLA steel substrate and a AS steel cladding in a bi-material wire-arc additively manufacture part.

As stated in Chapter 1, the second research objective is:

> *"To investigate the quasi-static deformation and fracture behaviour of the bi-material part, combining mechanical testing and microstructural analysis to elucidate the mechanisms driving plastic deformation and failure, while addressing challenges in testing anisotropic specimens."*

Establishing a clear link between microstructural features and mechanical performance is particularly challenging in compositionally graded materials. This objective focused on understanding how the unique microstructure of the bi-material interface, shaped by partial mixing, governs its deformation and fracture behaviour under quasi-static loading. The work related to this objective is presented in Chapter 4.

The first step involved monotonic tensile testing, designed to assess the mechanical performance across three distinct material regions: the undiluted HSLA steel, the undiluted AS steel, and the chemically diluted interface layer between them. Benchmark tests on mono-material specimens confirmed expected behaviour based on existing literature. In contrast, the bi-material specimens revealed unexpected insights. Using Digital Image Correlation (DIC), the strain distribution during loading was visualized, highlighting regions of macroscopic shear banding across both the interface and the AS steel regions. The interface layer demonstrated an unforeseen work-hardening mechanism, which allowed it to sustain strain without premature failure. This behaviour ultimately led to fracture occurring in the adjacent undiluted AS steel region, suggesting that under monotonic loading, the interface can develop superior mechanical strength.

To probe deformation mechanisms at a more localized scale, fracture toughness testing was conducted. Unlike tensile testing, this method concentrates stress at the crack tip, making it ideal for identifying microstructural influences on strain accommodation and failure. However, the heterogeneous nature of the bi-material specimens posed significant barriers for standard analysis. A custom methodology was developed using Finite Element Modelling (FEM) to calculate elastic J-integral correction functions tailored to the properties of the bi-material couple. This enabled the distinction of the elastic component of the J-integral value, making it possible to distinguish the plastic contribution during testing.

Fractographic and post-mortem microstructural analyses revealed familiar deformation mechanisms in the parent materials. In AS steel, plasticity was accommodated through twinning in large austenitic grains, resulting in crack blunting. Opposingly, deformation occurred through slip of the fine acicular ferrite crystals in the

HSLA steel material volume, leading to exceptional toughness through crack deflection along grain boundaries.

The interface layer, however, exhibited a fundamentally different behaviour. DIC and post-mortem crystallographic characterization confirmed the development of Transformation-Induced Plasticity (TRIP) as the dominant strain accommodation mechanism. The dilution of AS steel into HSLA steel produced a metastable austenite phase. Under strain, this phase transformed sequentially into ε-martensite and then α'-martensite, accommodating deformation until saturation, after which the material fractured. This strain-induced phase transformation explains the enhanced work hardening observed under tensile loading.

In contrast, fracture toughness measurements revealed that the same martensitic transformation mechanisms that enhance strength can limit resistance to crack propagation. As strain energy accumulates ahead of the crack tip, it is partially dissipated by austenite transformation. However, this beneficial effect competes with brittle fracture across pre-existing allotropic martensite islands formed during deposition in regions depleted of austenite-stabilizing elements. These hard but brittle regions, often near the dissimilar fusion line, act as crack accelerators, resulting in scattered and generally lower J-integral values. The presence of Type II boundaries, which facilitate secondary crack paths, further contributes to the variability in fracture toughness measurements.

These findings offer valuable insight into the dual nature of the interface layer. They provide a description of the main mechanism driving plastic deformation, directly addressing the second objective stated in Chapter 1. While the metastable microstructure enhances strength through strain-induced transformation, it also introduces local brittleness that reduces resistance to crack propagation. These results underscore the importance of balancing strength and toughness when designing bi-material components. Moreover, they highlight the need to tailor processing conditions to control the microstructural development and distribution at the diluted interface layer.

As stated in Chapter 1, the third research objective reads as follows:

> *"To characterize the fatigue behaviour of the bi-material couple for its reliable application, focusing on the relationship between the interface microstructure and fatigue crack propagation."*

While strength and fracture toughness are essential for qualifying structural materials, the long-term reliability of bi-metallic components, particularly in cyclic service conditions, is governed by their fatigue performance. For functionally graded structures produced by WAAM, this concern is especially pronounced at the interface layer. Addressing this challenge, the third objective of this work was to characterize FCGR across the bi-material interface of AS steel and HSLA steel.

The investigation, presented in Chapter 5, began with establishing baseline fatigue behaviour for the undiluted AS steel and HSLA steel materials using SENB specimens. Paris curves and ΔK_{th} values were generated at constant R-ratios, providing a benchmark that aligned with values presented in existing literature. To capture subtler effects, such as crack closure sensitivity, constant ΔK testing at two different R-ratios was employed. This approach provided a more nuanced understanding of how crack propagation responds to microstructural transitions across a bi-material specimen.

An important insight emerged when examining fatigue crack propagation across the diluted interface layer. Unlike the more predictable behaviour in the monolithic alloys, the interface exhibited a non-linear, multi-stage propagation process. As the fatigue crack approached from the AS steel region, its growth rate initially slowed upon entering the interface layer, then sharply accelerated as it advanced toward and crossed the dissimilar fusion line. This complex behaviour could only be understood by integrating findings from the preceding objectives—specifically, the metastable microstructure and deformation mechanisms active within the interface.

At the microstructural level, this variability is rooted in the transformation of metastable austenite during cyclic loading. As the crack front advances into the interface layer, the TRIP-effect plays a critical role in retarding crack growth. In this region, the applied strain drives the austenite-to-martensite transformation within the crack process zone, absorbing energy and slowing propagation. However, once the austenite is fully transformed, this mechanism becomes exhausted. The crack then accelerates, leaving behind a fully martensitic fracture surface as evidence of brittle fracture response.

The crack propagation behaviour becomes further convoluted as the crack approaches the dissimilar fusion line. As the fatigue process progresses across the interface layer, the crack front meets islands of pre-existing allotropic martensite that offer little capacity to accommodate strain. This reduced deformation capacity in the crack's process zone leads to a sharp increase in crack growth rate. The result is both a macroscopically measurable spike in FCGR and the formation of fracture features indicative of brittle failure. Contrasting to the fracture toughness test outcomes, the influence of Type II boundaries was less evident across this testing programme.

These findings confirm that fatigue behaviour across the bi-material interface cannot be inferred from the performance of its constituent materials alone. Instead, the local microstructure and active deformation mechanisms must be directly considered. The testing carried out in Chapter 5 reveals the key fatigue parameters required to model crack growth in such heterogeneous structure, while also identifying the microstructural features that govern this response, addressing the third objective of this thesis. Ultimately, the insights gained from this objective can offer practical guidance for the design of WAAM bi-metal components, particularly in structural and fatigue-critical applications.

Figure 6-2 offers a visual summary of the deformation and fracture processes under the load scenarios studied across this thesis. Section 6.3 draws on these findings to propose design considerations and process strategies that account for the microstructural transitions at the interface, ensuring improved reliability and performance.

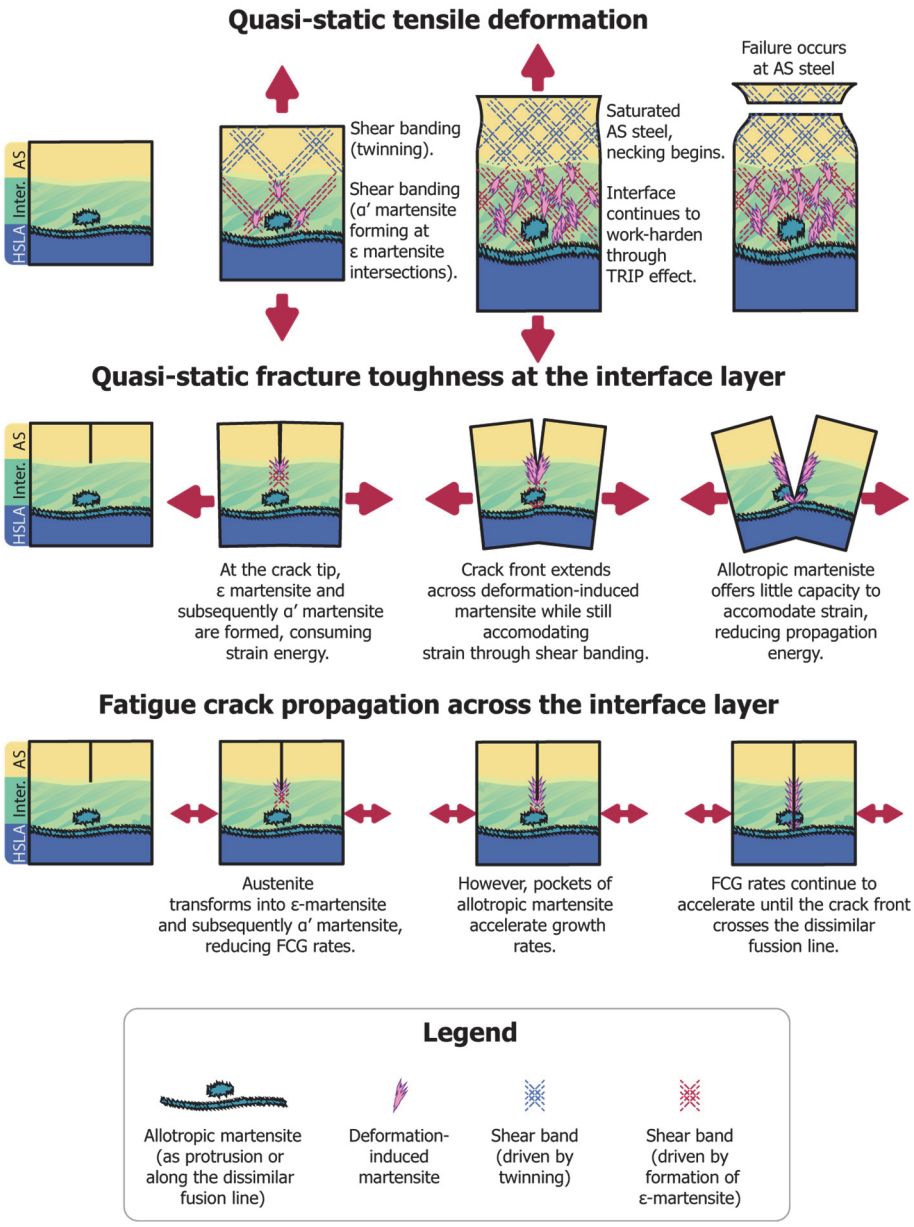

Figure 6-2 Multi-stage process of deformation, transformation and crack growth during tensile testing, fracture toughness testing and fatigue crack propagation testing

6.2. CONTRIBUTION TO THE DESIGN OF FUNCTIONALLY GRADED PARTS

6.2.1. Bi-material steel parts with a sharp interface

The results presented in this thesis provide valuable insights for the design and validation of bi-material steel parts featuring a sharp interface. Two major considerations emerge from the findings: the nuanced role of microstructural homogeneity, and the influence of process parameters on the microstructural evolution of the interface layer.

Typically, the formation of a homogeneous microstructure across joints or interfaces would be preferred under the assumption that chemical and phase uniformity leads to superior performance. However, the findings of this thesis challenge this assumption, at least in the context of functionally graded bi-material steels. A perfectly homogeneous martensitic interface—where chemical heterogeneity is eliminated by full dilution and mixing, and where phases are uniformly distributed—may miss the beneficial mechanisms such as transformation-induced plasticity (TRIP). The mechanical testing presented shows that metastable austenite within the otherwise heterogeneous interface provide a valuable strain accommodation mechanism under quasi-static and cyclic loading conditions. This localized transformation to martensite enables enhanced work-hardening, improving strength without compromising ductility of the bi-metal part.

Therefore, engineering a controlled degree of heterogeneity—rather than eliminating it—may be more advantageous for the long-term reliability of sharp-interface bi-material parts. Process design should aim to balance mixing and phase distribution to optimize both strength and damage tolerance, rather than pursuing homogeneity as an end in itself.

Based on the microstructural differences observed in this study compared to existing literature, it is evident that the microstructural constitution of the interface layer is highly sensitive to the thermal conditions present during deposition. The formation and characteristics of the interface depend not only on the welding parameters (such as current, voltage, and travel speed) but also on the local heat extraction capacity of the adjacent material. In practice, this means that designers and engineers must account for both the thermal input and the heat extraction properties of the material underlying the weld being deposited, especially when working with thick sections or complex geometries where heat dissipation pathways vary. A large thermal sink may promote rapid cooling, while a less conductive or massive substrate may extend the thermal cycle, promoting mixing and altering the phase constitution at the interface.

Thus, validation of functionally graded bi-material parts must include consideration of local heat flow conditions during manufacturing. It is insufficient to rely solely on nominal process parameters; instead, predictive modelling or empirical validation must account for how the adjacent material mass and properties impact the evolution of the interface layer

In summary, for bi-material steel parts with a sharp interface, the local heat gradient and extraction capacity are critical design parameters that influence interface microstructure, and controlled heterogeneity may, in fact, offer functional advantages for mechanical performance and durability. These findings advocate for a nuanced, performance-driven approach to interface design and validation in functionally graded metallic structures.

6.2.2. Bi-material steel parts with transitional chemical gradients

Building upon the findings presented in this thesis, important guidance can be drawn for the design and validation of bi-material steel parts featuring a transitional chemical gradient, either achieved across multiple deposition layers or using a buttering layer. These approaches offer alternative strategies to mitigate the challenges inherent to sharp interfaces by introducing a controlled compositional transition between dissimilar materials.

For the specific case of austenitic stainless steel (ASS) and high-strength low-alloy (HSLA) steel combinations, the research findings suggest that the abrupt change in chemical composition at the sharp interface is a key driver of both microstructural heterogeneity and mechanical variability. As demonstrated in this work, incomplete mixing at the interface leads to localized formation of metastable austenite.

One promising strategy to address these hurdles is the intentional introduction of a third, intermediate alloy designed to smooth the chemical transition between HSLA and ASS. This concept is supported by industrial welding practices in reactors, where buttering layers are commonly used to bridge differences in chemical potential and mechanical properties. Candidate alloys could include duplex stainless steels or low-Cr, Ni-based alloys specifically designed for dissimilar metal welding [23], [24]. These materials could enable a layered transition, reducing chemical gradients and thus minimizing the extent of martensitic transformation, carbon migration risks, and strength mismatches across the joint.

By implementing such a strategy, future WAAM builds of AS–HSLA bi-metallic structures could achieve enhanced reliability, particularly in applications subject to thermomechanical cycling. Validation would need to include assessment of gradient design parameters (e.g., number of layers, thickness of each transition) and their influence on residual stress profiles, phase stability, and mechanical integrity.

Beyond the specific case of AS–HSLA joints, the broader field of functionally graded steel structures offers successful precedents for chemical gradient design across major stainless-steel families. Recent studies have demonstrated that graded transitions between martensitic stainless steels and low alloy ferritic steels can develop adequate toughness [25]. Other studies show that multi-layer deposition of mixed powder consumables in LPB-F have been effectively employed to transition from ferritic stainless steels to austenitic grades, carefully managing Ni and Cr content to suppress deleterious phase formations such as sigma-phase [26], [27], with the caveat of forming multiple layers of hard martensite. Finally, laser-based directed energy deposition (L-DED) has been used to achieve continuous chemical gradients between AS steel and Cr/Ni alloys across several millimetres, yielding graded structures with minimal hardness discontinuities [28].

These examples reinforce the concept that chemical gradients, whether linear or tailored, can provide significant benefits for functionally graded steel components. These strategies are summarized visually on Figure 6-3, where the effect of each strategy on the distribution of diluted material is made apparent. The key lies in carefully engineering the transition path, ensuring that gradual changes in composition are matched by gradual changes in microstructure and mechanical properties. The findings of this thesis support these approaches by illustrating how sharp chemical transitions exacerbate microstructural instability, while also showing the potential for localized strain-accommodation mechanisms. Informed by this understanding, future design strategies for graded steel structures should aim to balance chemical continuity, phase stability, and functional mechanical properties through deliberate gradient engineering.

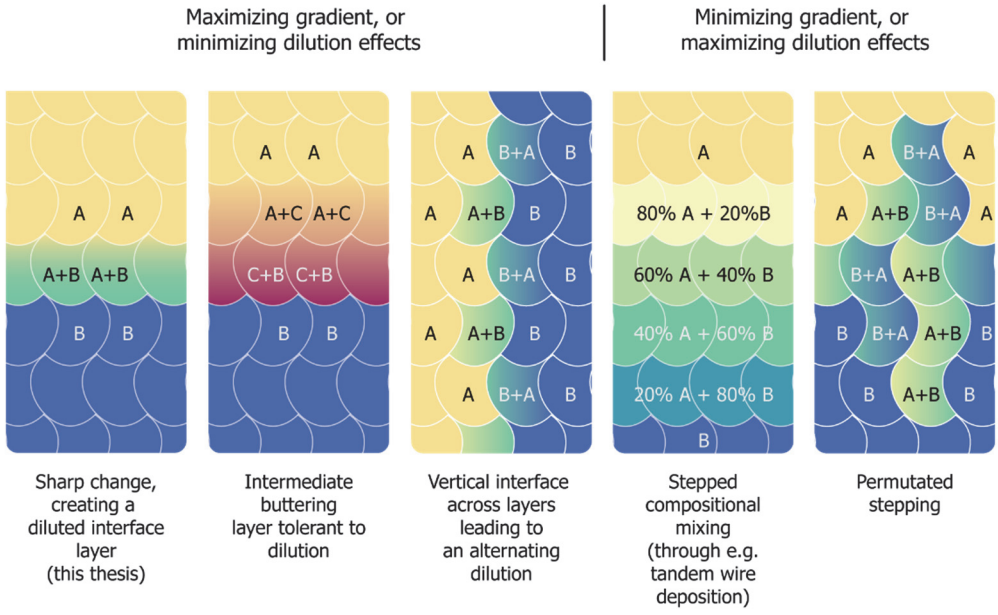

Figure 6-3 Different strategies for fusion-welding AM to achieve compositional grading through sharp, buttered, and stepped interfaces. B+A conveys a bead of alloy B laid (and diluted) onto a bead of previously deposited alloy A; A+B conveys the opposite procedure. For some material-process parameter combinations, it is noteworthy that several layers may be necessary to obtain the undiluted composition of the cladding material.

6.2.3. For the broader additive manufacturing industry

Although this thesis focuses on a bi-material steel system, its findings offer broader insights into the design and validation of functionally graded materials (FGMs), especially those involving dissimilar alloys. The challenges observed, such as carbon migration, chromium depletion, and brittle intermetallic formation, are not unique to AS–HSLA steel but are common to many metallurgical transitions in FGMs.

These chemical gradients can lead to mechanical heterogeneity, introducing stress concentrators that may compromise structural integrity. The studies presented here, highlighting metastable microstructures, thermal sensitivity, and degradation mechanisms, illustrate the complexity of managing dissimilar alloy interfaces in additive manufacturing (AM).

While recognizing these challenges, the AM community is actively developing standards to guide the qualification of FGMs. Two key efforts include [29] ASTM Committee F42 on Additive Manufacturing Technologies and ISO/TC 261 Additive

Manufacturing is collaborating closely with ASTM F42. While current standards do not yet explicitly address bi-material parts, they emphasize principles highly relevant to FGMs, such as:

- Localized property assessment (e.g., hardness, tensile, fatigue testing);
- Microstructural characterization at critical zones;
- Robust process monitoring and control;
- Consideration of service-specific conditions (e.g., temperature, fatigue).

These principles apply to both homogeneous and graded parts. The experimental work in this thesis supports the rationale behind these emerging standards and underscores the need for rigorous validation pathways for FGMs in structural applications. Ultimately, successful adoption of FGMs in industries like aerospace, energy, and transportation will depend not only on advanced manufacturing techniques but also on robust, empirically informed qualification frameworks.

The results obtained throughout this thesis provide critical insights into the design and validation of functionally graded steel components. They highlight the essential relationship between the process, microstructure and functional performance within the context of functional grading through additive manufacturing. These findings emphasize that successful deployment of functionally graded materials requires not only innovative manufacturing strategies but also a deep, empirical understanding of process-microstructure-gproperty relationships. Building on these foundations, the conclusions in the following chapter consolidate the key contributions and implications of this research work.

6.3. CHAPTER REFERENCES

[1] S. Kou and Y. K. Yang, "Fusion-boundary macrosegregation in dissimilar-filler welds," Welding Journal (Miami, Fla), vol. 86, no. 10, pp. 303–312, 2007.

[2] Z. Lin et al., "Deposition of Stellite 6 alloy on steel substrates using wire and arc additive manufacturing", doi: 10.1007/s00170-020-06116-w/Published.

[3] M. Dinovitzer, X. Chen, J. Laliberte, X. Huang, and H. Frei, "Effect of wire and arc additive manufacturing (WAAM) process parameters on bead geometry and microstructure," Addit Manuf, vol. 26, pp. 138–146, Mar. 2019, doi: 10.1016/j.addma.2018.12.013.

[4] U. Gürol, B. Turgut, H. Kumek, S. Dilibal, and M. Koçak, "Fabrication and Characterization of Wire Arc Additively Manufactured Ferritic-Austenitic Bimetallic Structure," Metals and Materials International, vol. 30, no. 5, pp. 1342–1355, May 2024, doi: 10.1007/s12540-023-01568-7.

[5] M. R. U. Ahsan et al., "Heat-treatment effects on a bimetallic additively-manufactured structure (BAMS) of the low-carbon steel and austenitic-stainless steel," Addit Manuf, vol. 32, Mar. 2020, doi: 10.1016/j.addma.2020.101036.

[6] F. Marefat, J. De Pauw, A. Kapil, N. Chernovol, P. Van Rymenant, and A. Sharma, "Design strategies for bi-metallic additive manufacturing in the context of wire and arc directed energy deposition," Mater Des, vol. 215, Mar. 2022, doi: 10.1016/j.matdes.2022.110496.

[7] T. Watanabe, M. Shiroki, A. Yanagisawa, and T. Sasaki, "Improvement of mechanical properties of ferritic stainless steel weld metal by ultrasonic vibration," J Mater Process Technol, vol. 210, no. 12, pp. 1646–1651, Sep. 2010, doi: 10.1016/j.jmatprotec.2010.05.015.

[8] W. Zhao, Y. Wei, X. Zhang, J. Chen, and W. Ou, "Comparative investigation of wire arc additive manufacturing of Al-5%Mg alloy with and without external alternating magnetic field," International Journal of Advanced Manufacturing Technology, vol. 119, no. 3–4, pp. 2571–2587, Mar. 2022, doi: 10.1007/s00170-021-08466-5.

[9] B. Wu et al., "Effects of synchronized magnetic arc oscillation on microstructure, texture, grain boundary and mechanical properties of wire arc additively manufactured Ti6Al4V alloy," Addit Manuf, vol. 54, Jun. 2022, doi: 10.1016/j.addma.2022.102723.

[10] Y. Cui, C. L. Xu, and Q. Han, "Effect of ultrasonic vibration on unmixed zone formation," Scr Mater, vol. 55, no. 11, pp. 975–978, Dec. 2006, doi: 10.1016/j.scriptamat.2006.08.035.

[11] T. Yuan, S. Kou, and Z. Luo, "Grain refining by ultrasonic stirring of the weld pool," Acta Mater, vol. 106, pp. 144–154, Mar. 2016, doi: 10.1016/j.actamat.2016.01.016.

[12] C. R. Cunningham, V. Dhokia, A. Shokrani, and S. T. Newman, "Effects of in-process LN2 cooling on the microstructure and mechanical properties of type 316L stainless steel produced by wire arc directed energy deposition," Mater Lett, vol. 282, Jan. 2021, doi: 10.1016/j.matlet.2020.128707.

[13] C. Goulas et al., "The Effect of Cryogenic Cooling on the Microstructure and Mechanical Properties of Wire Arc Additively Manufactured Steels," in 2023 TMS Annual Meeting & Exhibition: Additive Manufacturing of Large-scale Metallic Components, TMS, 2023.

[14] W. Li et al., "Microstructure evolution and mechanical properties of 308L stainless steel coatings fabricated by laser hot wire cladding," Materials Science and Engineering: A, vol. 824, Sep. 2021, doi: 10.1016/j.msea.2021.141825.

[15] J. Talonen and H. Hänninen, "Formation of shear bands and strain-induced martensite during plastic deformation of metastable austenitic stainless steels," Acta Mater, vol. 55, no. 18, pp. 6108–6118, Oct. 2007, doi: 10.1016/j.actamat.2007.07.015.

[16] J. Talonen, Effect of strain-induced α'-martensite transformation on mechanical properties of metastable austenitic stainless steels, vol. PhD. 2007.

[17] C. Zheng and W. Yu, "Effect of low-temperature on mechanical behavior for an AISI 304 austenitic stainless steel," Materials Science and Engineering: A, vol. 710, pp. 359–365, Jan. 2018, doi: 10.1016/j.msea.2017.11.003.

[18] S. Curtze and V. T. Kuokkala, "Dependence of tensile deformation behavior of TWIP steels on stacking fault energy, temperature and strain rate," Acta Mater, vol. 58, no. 15, pp. 5129–5141, Sep. 2010, doi: 10.1016/j.actamat.2010.05.049.

[19] N. I. Vazquez-Fernandez et al., "Adiabatic Heating of Austenitic Stainless Steels at Different Strain Rates," Journal of Dynamic Behavior of Materials, vol. 5, no. 3, pp. 221–229, Sep. 2019, doi: 10.1007/s40870-019-00204-z.

[20] J. M. Race, "Carbon Diffusion Across Dissimilar Welds," University of Cambridge, Cambrdge, UK., 1992. doi: https://doi.org/10.17863/CAM.14227.

[21] J. N. DuPont, "Microstructural evolution and high temperature failure of ferritic to austenitic dissimilar welds," Jul. 2012. doi: 10.1179/1743280412Y.0000000006.

[22] F. Gauzzi and S. Missori, "Microstructural transformations in austenitic-ferritic transition joints," 1988.

[23] A. K. Bhaduri, S. Venkadesan, P. Rodriguez, and P. G. Mukunda, "Transition metal joints for steam generators An overview," 1994.

[24] A. Asadollahi, A. Bahrami, and M. Shamanian, "The effects of filler metal and butter layer on the microstructure and mechanical properties of API 5L X65/AISI 304L joint," Journal of Materials Research and Technology, vol. 23, pp. 4148–4166, Mar. 2023, doi: 10.1016/j.jmrt.2023.02.063.

[25] E. Tenuta, A. Nycz, M. Noakes, S. Simunovic, and M. H. A. Piro, "Material properties and mechanical behaviour of functionally graded steel produced by wire-arc additive manufacturing," Addit Manuf, vol. 46, Oct. 2021, doi: 10.1016/j.addma.2021.102175.

[26] W. Woo, D. K. Kim, E. J. Kingston, V. Luzin, F. Salvemini, and M. R. Hill, "Effect of interlayers and scanning strategies on through-thickness residual stress distributions in additive manufactured ferritic-austenitic steel structure," Materials Science and Engineering: A, vol. 744, pp. 618–629, Jan. 2019, doi: 10.1016/j.msea.2018.12.078.

[27] G. Shin et al., "Microstructural evolution and mechanical properties of functionally graded austenitic–low-carbon steel produced via directed energy deposition," Mater Des, vol. 227, Mar. 2023, doi: 10.1016/j.matdes.2023.111681.

[28] C. H. Zhang, H. Zhang, C. L. Wu, S. Zhang, Z. L. Sun, and S. Y. Dong, "Multi-layer functional graded stainless steel fabricated by laser melting deposition," Vacuum, vol. 141, pp. 181–187, Jul. 2017, doi: 10.1016/j.vacuum.2017.04.020.

[29] G. Moroni, S. Petrò, and H. Shao, "On Standardization Efforts for Additive Manufacturing," 2020, pp. 156–172. doi: 10.1007/978-3-030-46212-3_11.

[Page intentionally left blank]

7. CONCLUSIONS AND RECOMMENDATIONS

7.1. MAIN FINDINGS PER RESEARCH OBJECTIVE

Wire-Arc Additive Manufacturing (WAAM) offers a feasible path to manufacture functionally graded metallic components, while inheriting the benefits of additive manufacturing. Among the different possibilities, the pairing of austenitic stainless steel (AS) and high-strength low-alloy (HSLA) steel is particularly attractive due to the potential combination of corrosion resistance, fatigue performance, and mechanical soundness. While prior research has explored this material combination, a detailed understanding of the microstructural evolution and its implications for mechanical performance at the critical interface layer remained limited in the context of AM through WAAM. Based on the results obtained in this study, the following key conclusions can be drawn:

Objective 1: To develop a comprehensive understanding of microstructural evolution at the interface layer, which is crucial for correlating microstructural features with the mechanical performance of bi-material components

The first objective was to develop a comprehensive understanding of microstructural evolution at the interface layer, as it was deemed crucial for correlating microstructural features with mechanical performance. Through systematic characterization across multiple length scales, the interface layer formed between ER70S-6 (HSLA steel) and ER316L (AS steel) was found to be highly heterogeneous. Incomplete mixing led to Ni- and Mn-depleted zones forming martensite, while other regions retained austenite and ferrite. Advanced characterization through EBSD, EPMA and TEM confirmed the presence of bcc', hcp martensite, and sparse bainite. Alongside these observations, it was found that:

- For the heat input used (0.22 kJ/mm), the cladding austenitic stainless steel reaches a level of dilution of 25% from its original composition, as measured by the average chromium value across the diluted layer.
- The degree of dilution obtained yields an interface layer with Vickers hardness values ranging from 220 and up to 371 $HV_{0.2}$. This spread is attributed to the heterogeneous microstructural constitution. The combination of ferrite and martensite material volumes increases from the typical 8-10% for SS316L to almost 40% in this region. The highest hardness

value was typically measured within a range of 250 μm, as this region is most often populated by martensite.

These findings reveal the complex interplay of chemistry, solidification, and thermal cycling in shaping the interface.

The second objective reads:

> **Objective 2:** To investigate the quasi-static deformation and fracture behaviour of the bi-material part, combining mechanical testing and microstructural analysis to elucidate the mechanisms driving plastic deformation and failure, while addressing challenges in testing anisotropic specimens.

This objective aimed to link interface microstructure with mechanical performance under static loading. Tensile tests with Digital Image Correlation (DIC) revealed that the interface layer strengthens via the TRIP effect, enabling plastic deformation through strain-induced martensite. However, brittle martensitic islands, formed during post-deposition transformations, reduced fracture toughness. Supporting these findings, it was observed that:

- The elastic modulus of the interface layer resembles that of the austenitic stainless steel in the build direction, achieving a value of 157±17 GPa for the set of parameters and materials chosen in this thesis.
- Yielding of the interface layer was accompanied by macroscopic shear banding, as it recorded through DIC measurements. Yield values reached 412±13MPA in the build direction. Subsequent hardening mechanisms enhanced by the TRIP effect yielded a work hardening exponent n equal to 0.210 ±0.020 log(MPa), higher than either undiluted parent material.
- Opposingly, low fracture toughness values were measured. Under 3-point single-edge notch bending, the interface yielded J_Q = 236 ±78 kJ/m^2, comparable to the typical performance of martensitic stainless steels, and about 49% lower than the value measured for the undiluted AS steel parent material.

As a result, the interface exhibited enhanced strength but also localized brittleness, highlighting its "double-edged sword" effect on the macroscopic mechanical performance.

The third, and last, objective reads:€

> **Objective 3:** To characterize the fatigue behaviour of the bi-material couple for reliable application, focusing on the relationship between the interface microstructure and fatigue crack propagation, and establishing reliable performance levels for bi-material components.

The third objective entailed the characterization of the fatigue behaviour of the bi-material couple, focusing on the influence of the microstructure on the crack propagation mechanisms. A Fatigue Crack Growth Rate (FCGR) testing programme revealed a multi-stage propagation mechanism across the interface layer. Initially, crack growth is hindered by the TRIP effect, with strain-induced transformation of metastable austenite absorbing strain energy. However, once transformation was exhausted, crack growth accelerated sharply, particularly upon encountering regions of allotropic martensite near the dissimilar fusion line. Supporting these findings it was measured that:

- Paris parameters derived from the diluted interface material volume under single-edge notched 3-point bending for two specimen orientations (BD-LD plane: m = 2.79, $\log_{10}(C) = 7.83 \log_{10}(da/dN)$) (BD-TD plane: m = 3.47, $\log_{10}(C) = 8.39 \log_{10}(da/dN)$), similar to that of the parent materials.
- However, ΔK_{th} value are shown to be lower (1.4 MPa·m$^{0.5}$ compared to the ca. 2.0 MPa·m$^{0.5}$of the undiluted parent materials).
- FCGR consistently drop as the crack front transitions from undiluted AS steel to the interface. At ΔK = 20 MPa·m$^{0.5}$, the greatest Δ is -0.77 $\log_{10}$ steps (R=0.1). As cracks near the HSLA fusion line, rates re-accelerate up to +0.75 $\log_{10}$ steps (R= 0.5).

This complex behaviour, distinct from that of the homogeneous parent materials, underscores the critical role of local microstructural evolution in governing fatigue performance.

7.2. SCIENTIFIC AND TECHNICAL CONTRIBUTIONS

This work challenges the assumption that microstructural homogeneity always yields better mechanical performance. In functionally graded bi-material steels, controlled heterogeneity, specifically the retention of metastable austenite, activates TRIP

mechanisms under both static and cyclic loading. This enhances work hardening and strain accommodation, improving strength without compromising ductility.

The study also highlights the critical role of thermal conditions during deposition, which are influenced not just by process parameters but also by local heat extraction from the substrate. Effective process design at the interface region must therefore account for both thermal management and dilution control to ensure mechanical reliability.

Beyond the AS–HSLA system, these findings support broader efforts in the AM community to establish qualification standards. They reinforce the need for localized property testing, microstructural analysis, and robust process monitoring. Ultimately, this research contributes a detailed case study that underscores the importance of empirical validation in advancing the industrial adoption of functionally graded materials.

The research presented in this thesis advances the understanding of microstructural evolution and mechanical performance at dissimilar interfaces manufactured by WAAM. Through systematic investigation of the AS–HSLA steel system, the work uncovers critical relationships between process parameters, phase transformations, and mechanical properties across multiple length scales. These findings not only address key challenges in the design of functionally graded components but also establish a baseline methodology for future exploration of multi-material systems. As additive manufacturing continues to evolve toward the production of larger and more complex structures, the ability to engineer graded interfaces with predictable, tuneable properties will be vital. By deepening our empirical understanding of the process–structure–property linkages in WAAM-fabricated bi-material components, this thesis work lays the groundwork for further technological development. Continued efforts in this field promise to unlock new design freedoms, enabling the development of highly optimized, resilient structures tailored to the demands of next-generation industries—from civil, maritime and nuclear applications to aerospace and beyond.

7.3. RECOMMENDATIONS FOR FUTURE WORK

While the research presented in this thesis provides valuable insights into the process–microstructure–property relationships of WAAM-fabricated AS–HSLA bi-material components, several limitations arising from the experimental design must be acknowledged.

The first challenge involves the description of process-microstructure-properties relationships through a window of workable process parameters. WAAM processes inherently allow wide flexibility in parameters such as heat input, travel speed, and interpass temperature. Variations in heat input or heat extraction capacity could influence solidification dynamics, dilution behaviour, phase formation, and defect occurrence. While this study provides a strong baseline, future work should explore broader parameter ranges to fully map the process window for optimized interface properties. This limitation leads to the following recommendation:

⇒ **Future research should systematically investigate how deposition parameters affect the interface microstructure and mechanical properties**. This will support the development of a processing window tailored to the heat extraction capacity of the underlying substrate, including parameters like heat input, deposition path and even part geometry.

The second opportunity for future work involves the use of ancillary methods. Despite some ability to tune deposition parameters, WAAM alone imposes limits on microstructural control at dissimilar interfaces. The potential use of ancillary technologies, such as mechanical stirring, magnetic oscillation, cryogenic cooling, or hybrid laser-wire approaches, is identified a potential path to further refine interface structure. They could even have an effect on the residual stress development. However, these enhancements were outside the scope of this study and should be considered in future investigations aiming to achieve more tailored or homogeneous graded regions. The opportunity leads to the following recommendation:

⇒ **Future studies should explore the integration of ancillary technologies**, such as mechanical stirring, magnetic arc oscillation, and cryogenic cooling to achieve finer control over dilution, grain structure, and phase stability at dissimilar interfaces over a wide range of thermal conditions during deposition.

The third opportunity involves mechanical characterization at a temperature different than room temperature. The TRIP effect, central to interface strengthening, is known to diminish at elevated temperatures and to vary with strain rate. As service environments often involve thermal fluctuations and dynamic loading, additional testing across a range of temperatures and strain rates is needed to fully understand the stability and reliability

of the interface under practical conditions. This observation leads to the following recommendation:

⇒ **Extend mechanical testing across a range of temperatures and strain rates.** This will help confirm the stability of the TRIP effect and determine the operational boundaries under dynamic service conditions.

Finally, the potential degradation mechanisms associated with long-term high-temperature exposure, particularly carbon migration across the bi-metal interface, were not experimentally addressed in this work. Such diffusion-driven degradation could lead to embrittlement and localized loss of mechanical integrity. Insights from dissimilar metal welds in high-temperature power systems suggest that time-dependent effects could be critical for service performance, highlighting the need for extended aging and creep testing of WAAM-fabricated bi-material components. This insight leads to the following recommendation:

⇒ **Long-term aging experiments and creep testing at elevated temperatures** should be conducted to assess time-dependent degradation mechanisms such as carbon migration, grain growth, and embrittlement, providing critical data for qualifying bi-material components for high-temperature applications.

[Page intentionally left blank]

ANNEXES

A

ANNEX A. TRUE STRESS, TRUE STRAIN, AND WORK-HARDENING RELATIONSHIPS OBTAINED FROM DIC

True strain is obtained based on the Holloman relationship [79], given that:

$$\varepsilon = \ln(1 + e) \qquad (Eq.\ \text{A1})$$

where e is the engineering strain as measured by the digital DIC strain gauges, s is the engineering stress, σ is the true stress and ε the true strain. Similarly, the true stress values are derived from the digital strain gauge measurements as follows:

$$\sigma = s \cdot (1 + e)\,. \qquad (Eq.\text{A2})$$

Since necking occurs away from the region measured, this relationship stays true through all measured points. Having obtained the true strain-stress relationships, it is possible to obtain the work hardening rate (WHR), such that:

$$\Theta = \frac{d\sigma}{d\varepsilon}. \qquad (Eq.\text{A3})$$

For the data given, $d\sigma$ and $d\varepsilon$ are computed based on the numerical differences of two subsequent data points. The values obtained are plotted in Figure 4-3 (c) and (d) for the two set of tensile specimens measured. Due to the noise derived from the numerical operation to obtain the WHR, a moving average regression of order 5 is provided with an error band equivalent to ±1 standard deviations. In the case of bi-metal specimens, the moving average regression is applied only on values where $\varepsilon > 3\ \%$ to emphasize the work-hardening behaviour caused by the TRIP effect.

ANNEX B. LE-FEM ANALYSIS IN DETAIL

The intention of this annex is to elaborate on the finite element model used to obtain $J_{el,FEM,BM}$ and $C(a/W)_{FEM,BM}$ mentioned in Section 4.2.4 (Eq. 4.1) and (Eq. 4.3).

The dimensions and boundary conditions of the modelled specimen were representative to those of the physical specimens tested. Exploiting the symmetry around the crack plane, a model was defined in ABAQUS consisting of half an SENB sample. The material properties chosen are isotropic and linear elastic. As it is demonstrated in section 4.3.1, the diluted interface layer and the AS steel show an elastic modulus of 160 GPa, whereas the HSLA steel shows an elastic modulus closer to 210 GPa. The FEM models were thus fully described by two regions with different elastic moduli. Models were built for values of a/W and $Z(BM)/W$ ranging between 0.175 to 0.850, at increments of 0.0125 in both cases. The model features a width W of 10 mm and a support span S equal to $4{\cdot}W$. A prescribed displacement (δ) of 0.1 mm parallel to the negative BD was set on an edge segment of 0.2 mm length at a distance $S/2$ away from the crack plane. To counter the prescribed displacement, a 0.1 mm support was modelled fixed with a 0 mm displacement directly ahead of the crack front. The mesh topology, boundary conditions and elastic property assignment are shown in Figure B.1 (a). Figure B.1 (b) shows the location of half the CMOD measurement at the crack mouth by superimposing the deformed and undeformed modelling results. To give an indication of the strain values obtained through this numerical analysis, the strain component e_{11} || LD is mapped on the latter figure.

Adequate meshing and section definitions are necessary to obtain reliable J-integral values. Quadrilateral eight-node plane strain elements with full integration were used. Symmetry boundary conditions are set along the ligament up to the crack front to reduce the number of elements. The elements around the crack tip consist of collapsed quadrilateral elements with single nodes around the tip vertex, as shown on Figure B.1 (c). Strain singularity around the crack tip is controlled as a function of $1/\sqrt{r}$ by moving the mid-side nodes to the 1/4 points. The J-integral calculation relies on a series of concentric paths around the crack tip. For every geometry modelled, the J-integral is evaluated at the 10th concentric path, described by a radius approximately equal to $0.002 \cdot W$.

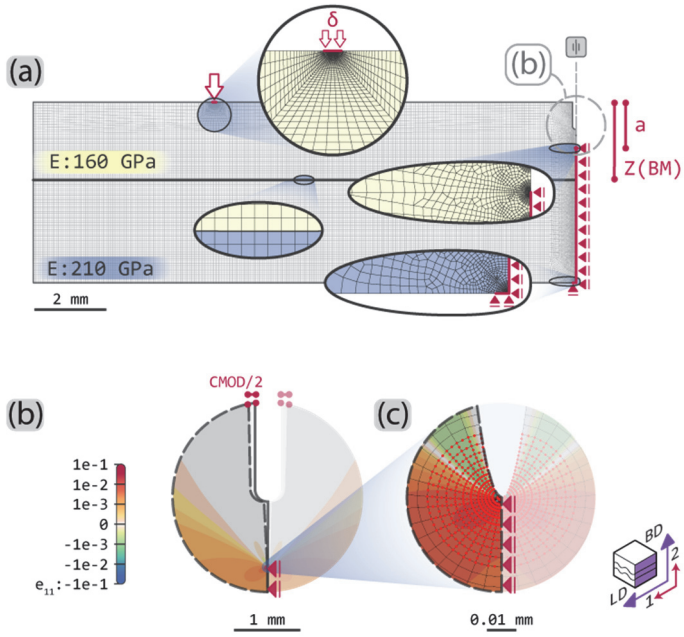

Figure B.1 Finite element model showing (a) boundary conditions, material assignments and mesh topology, as well as the definition of the variables a and $Z(BM)$. (b) Measurement location for CMOD, on undeformed and deformed geometries. (c) Detail on mesh topology and J-integral integration nodes at the crack front on a deformed geometry. (b - c) show geometries 5x exaggerated with e_{11} strain values plotted for a/W=0.25 and $Z(BM)/W$=0.6.

As observed in section 4.3.1, the elastic response of the diluted interface layer shows small variability for the loading condition studied. Moreover, the elastic properties of the diluted interface layer fairly resemble those of an un-diluted ER316L all-weld-metal deposit. As a result, and under these simplified conditions, both materials are expected to behave homogeneously under linear-elastic deformation. Consequently, the only interface considered is that between the diluted interface layer and the HSLA steel material volume. The elastic values obtained are taken as an input to study the effect of elastic heterogeneity across a bi-material interface.

The results obtained from the linear-elastic J-integral FEM calculations are provided on Figure B.2. Figure B.2 (a) shows the values obtained of J-integral as a function of the crack depth, a, and the position of the bi-material fusion line $Z(BM)$ as measured from the notched surface. The values of J-integral are plotted against the FEM results for a mono-material SENB sample of identical dimensions of elastic moduli of 160 GPa and 210 GPa independently. Given that analytical solutions for the J-integral values exist for mono-material conditions, this $a - J$ relationship is also presented, given that [34]:

$$J_{I,el} = G_I = \frac{K_I^2 \cdot (1 - \nu^2)}{E} \qquad (Eq.\,\mathrm{B1})$$

for plain strain conditions, where G is the strain energy release rate, K is the stress intensity factor, ν is the Poisson's ratio and E is the elastic modulus. The index I is used to indicate mode I loading. Given the loading conditions at the quasi-static crack front region for a 3-point single edge notched bending specimen (SENB3), this is the only load mode considered. Thus, this index is not used further for brevity. The relationship between a and J is made explicit if it is considered that [34]:

$$K = \left[\frac{P \cdot S}{(B \cdot B_n)^{1/2} \cdot W^{3/2}}\right] \cdot f\left(\frac{a}{W}\right) \qquad (Eq.\,\mathrm{B2})$$

where P is the total load, S is the span between supports, B and B_n are the un-grooved and the grooved sample thicknesses correspondingly, and W is the sample's width. The function $f(a/W)$ is the geometry-dependent relation between the load applied and the stress intensity factor. For a standard SENB3 specimen, this function is formulated as [34]:

$$f\left(\frac{a}{W}\right) = \frac{3 \cdot \left(\frac{a}{W}\right)^{1/2} \cdot \left[1.99 - \left(\frac{a}{W}\right) \cdot \left(1 - \left(\frac{a}{W}\right)\right) \cdot \left(2.15 - 3.93 \cdot \left(\frac{a}{W}\right) + 2.7 \cdot \left(\frac{a}{W}\right)^2\right)\right]}{2 \cdot \left(1 + 2 \cdot \frac{a}{W}\right) \cdot \left(1 - \frac{a}{W}\right)^{3/2}}. \qquad (Eq.\,\mathrm{B3})$$

The values of J-integral are thus demonstrated to vary between the boundaries of the mono-material solutions for the elastic moduli considered. This is true with exception of the J values obtained near the bi-material interface. When the depth of the crack front approaches $Z(BM)$, the values of J rapidly drop. This can be interpreted as less energy input being necessary to achieve an infinitesimal extension of the crack front as it approaches the bi-material boundary. Having crossed the bi-material boundary, the values rapidly increase. The J value then gradually approaches that of the mono-material condition of the underlying metal.

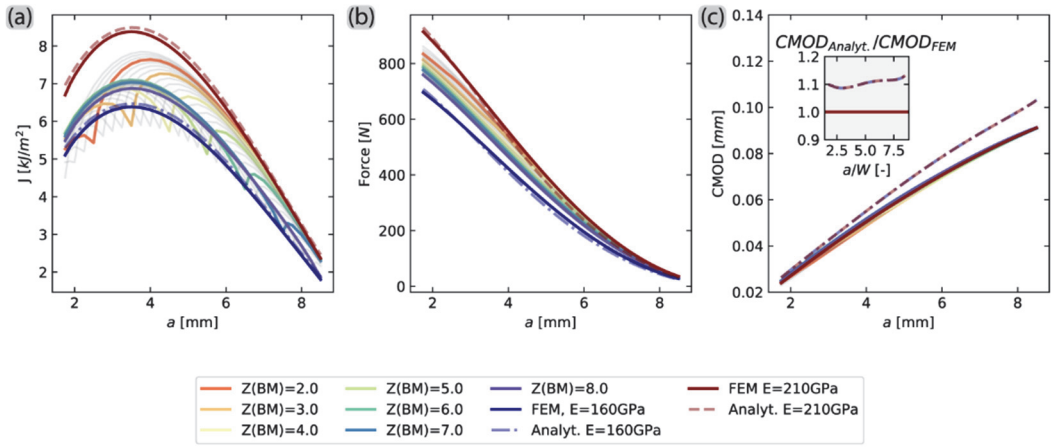

Figure B.2 (a) J integral, (b) resultant force and (c) CMOD measurements obtained from linear-elastic composite SENB specimen under a 0.1 load-line displacement for different positions of the bi-material interface Z(BM). Results are shown in colour for every 1 mm increment of Z(BM), and in grey for every 0.25 mm increments. Analytical and FEM solutions for mono-material specimens are provided as a reference. Inset in (c) shows ratio between CMOD values for the analytical solution with respect to the FEM calculations.

The force compliance as a function of a and $Z(BM)$ is presented in Figure B.2 (b). Like the results presented for J-integral, the results for bi-material geometries are accompanied by FEM results of mono-material conditions for the 2 elastic moduli of interest, and two analytical solutions. In this case, the analytical solution is provided by [34]:

$$P = \frac{v_{LL}}{C_{LL}} \qquad (Eq.\,\mathrm{B4})$$

where v_{LL} is the load-line displacement and the force vs. load-line compliance, C_{LL}, is defined analytically as follows [34]:

$$C_{LL} = \frac{1}{E \cdot B_e} \cdot \left(\frac{S}{W-a}\right) \cdot \left[1.193 - 1.98 \cdot \left(\frac{a}{W}\right) + 4.478 \cdot \left(\frac{a}{W}\right)^2 - 4.443 \cdot \left(\frac{a}{W}\right)^3 + 1.739 \cdot \left(\frac{a}{W}\right)^4\right] \qquad (Eq.\,B5)$$

where $B_e = B - (B - B_n)^2/B$. The load can then be easily estimated, given that the modelling conditions impose a load-line displacement of 0.1 mm in all instances. For the FEM models, the load is simply obtained as the global reaction force. The compliant loads obtained from the bi-material sample models neatly fall within the boundaries set by the mono-material models. However, the FEM solutions appear to overestimate the resulting

load for crack depth values larger than 3 mm when they are compared to the analytical solutions.

The opposite problem is observed when analysing the results of CMOD vs. crack depth values. On this occasion, the FEM results underestimate the CMOD values when compared to the analytical solution. The latter is taken from the relationship between load and CMOD, such that:

$$v_m = CMOD = P \cdot C_m \qquad (Eq.\,\mathrm{B6})$$

where v_m is the crack-mouth opening displacement and C_m is the load-CMOD compliance relationship. The analytical solution for C_m is stated as follows [34]:

$$C_{m,analyt} = \frac{6 \cdot S}{E \cdot W \cdot B_e} \cdot \left(\frac{a}{W}\right) \cdot \left[0.76 - 2.28 \cdot \left(\frac{a}{W}\right) + 3.87 \cdot \left(\frac{a}{W}\right)^2 - 2.04 \cdot \left(\frac{a}{W}\right)^3 + \frac{0.66}{(1 - a/W)^2}\right] \qquad (Eq.\,B7)$$

The relationship of CMOD vs. a is identical for both elastic moduli of interest. This is true, given that to compute the analytical value of v_m, the corresponding mono-material P values were used as obtained from the FEM analyses. To overcome this difference between analytical and FEM formulations, an error function is obtained as a 4th order polynomial regression which is independent of the elastic modulus, namely:

$$e_m\left(\frac{a}{W}\right) = \frac{CMOD_{Analyt.}}{CMOD_{FEM}} = 0.0003 \cdot \left(\frac{a}{W}\right)^4 - 0.0061 \cdot \left(\frac{a}{W}\right)^3 + 0.048 \cdot \left(\frac{a}{W}\right)^2 - 0.1498 \cdot \left(\frac{a}{W}\right) + 1.2467. \qquad (Eq.\,\mathrm{B8})$$

This regression result is shown graphically in the inset of Figure B.2 (c). The bi-material solutions obtained through FEM closely resemble the solution obtained from mono-material conditions. Nonetheless, for all values of $Z(BM)$ a similar trend is found: CMOD values are typically higher when $a < Z(BM)$, and lower when the opposite relationship is true. Also, the largest relative difference $CMOD_{BM}/CMOD_{MM}$ ranges between 1.05 to 0.99 for $Z(BM)$ = 6 mm, under a non-linear relationship with a/W.

ANNEX C. NUMERICAL EVALUATION OF CORRECTION FUNCTIONS, Γ_J^E AND Γ_C^E

Figure C.1 (a) and (b) show the ratio between the results obtained from FEM analysis of a bi-material sample and the analytical expressions for J-integral available in the literature. This is done through the normalized error functions Γ_J^{160} and Γ_J^{210} defined on Eq. 4.1. Since $G_{Analyt,MM}^E$ is a function of the elastic modulus, a superscript 210 or 160 is used to denote the value of E used. Figure C.1 (a) gives the ratio between the J_{el} and G values as a function of crack tip and bi-material interface positions. The values are normalized by the analytical solution of G describing an isotropic sample with an elastic modulus of 160 GPa. Figure C.1 (b) shows the same relationship for a sample with an elastic modulus of 210 GPa. The domain of Figure C.1 (a) is constrained to values were $a/W < Z(BM)/W$. Similarly, the Figure C.1 (b) is constrained to a domain of $a/W > Z(BM)/W$. These two conditions are set considering the geometry and loading direction of the bi-material specimens tested in this work.

Fracture toughness results are derived from the evaluation of the crack length as a function of CMOD compliance. Hence the need for such relationship to be established. Eq. 4.B5 provides a useful solution to obtain the compliance values as a function of relative crack depth. Nonetheless, during testing the inverse relationship between C_m and a is necessary. An analytical relationship is available in literature, such that [34]:

$$C(a/W)_{Analyt,MM} = 0.999748 - 3.9504 \cdot u + 2.9821 \cdot u^2 - 3.21408 \cdot u^3 + 51.51564 \cdot u^4 - 113.031 \cdot u^5 \quad (Eq.\,\mathrm{C1})$$

where:

$$u = \frac{1}{\left[\frac{B_e \cdot W \cdot E \cdot C_m}{S/4}\right]^{1/2}}. \quad (Eq.\,\mathrm{C2})$$

$$e_m^{-1}\left(\frac{a}{W}\right) = e_{a/W}(C_m). \quad (Eq.\,\mathrm{C3})$$

This function is solved numerically through interpolation of the function e_m^{-1} for the known value pairs of $(C_m, a/W)$.

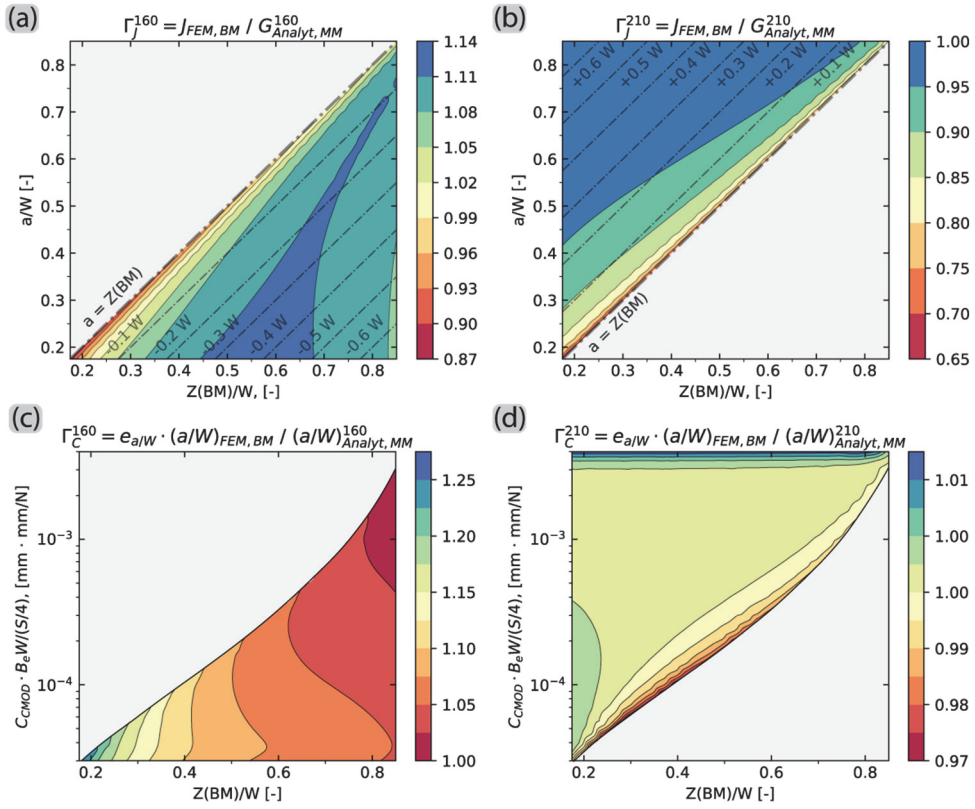

Figure C.1 (a) J-integral values obtained from bi-material SENB FEM model normalized by G values of a mono-material specimen with E=160 GPa as a function of crack position a/W, and position of bi-material interface $Z(BM)$ (b) J-integral values normalized by G with E=210 GPa. Iso-distant curves of the crack front position with respect to the bi-material interface are provided each 0.1W. (c-d) a/W as a function of CMOD compliance and bi-material interface position, normalized by the analytical solution for mono-material specimens.

Having established the necessary relationship between C_m and a, an error function can be defined to relate the standard analytical relationships with the experimental data obtained from a bi-material sample. The sought relationship establishes the connection between the predicted values of $(a/W)_{BM}$ and $(a/W)_{MM}$ as a function of compliance and position of the bi-material interface. The numerical solution is presented in Figure C.1 (c) and (d), following the relationship established in Eq. 4.3. Figure C.1 (c) shows the values to this function for the domain where $(a/W) = e_{a/W}(C_m) \cdot (a/W)_{FEM,BM} < Z(BM)/W$ and Figure C.1 (d) for the domain where $(a/W) = e_{a/W}(C_m) \cdot (a/W)_{FEM,BM} > Z(BM)/W$.

[Page intentionally left blank]

ACKNOWLEDGEMENTS

Whoever said that a PhD is an individual effort had clearly a different experience than mine. The path to completion of a doctoral dissertation is often unclear, paved with uncertainty and frustration. It is the people in the doctoral candidate's environment that help make the unclear, clear; the uncertain, manageable; and the frustrating, bearable. If one is as lucky as I consider myself, the work even becomes enjoyable.

First and foremost, I would like to thank my co-promotors **Vera Popovich** and **Marcel Hermans**. I know I have tried to communicate it often and clearly, that I am truly grateful for your help and guidance. You provided consistent and timely support, space for error and discovery, and invaluable critical input necessary to complete this doctoral work. Thank you for the time invested, thank you for the attention given to the work and to me as a person, and thank you for giving me the opportunity to work with you in this unique scientific endeavor.

This thesis was conceived within the framework of **Grade2XL**. This is a project initiative financed by the European Commission **Horizon2020** initiative, involving outstanding academics, technical and validation experts, industry leaders, science communicators, and project managers. Your collective effort was an inspiration, jointly driving the development of WAAM to an industrial reality. Within this cohort of outstanding professionals, I would like to specially acknowledge three teams: the team at RAMLAB, and more specifically **Wei Ya** and **Vincent Wagner**; the team at Ghent University, specifically **Leo Kestens** and **Mahdi Mahmoudiniya**; and the team at Eindhoven University, specifically **Constantinos Goulas**. Thank you for the time and trust invested in this project, thank you for the disposition to lend a hand when needed, and thank you for the countless discussions that shaped blurry ideas into tangible results.

Any person who attempts to become an expert in every field will soon be faced with their own relentless incompetence. Expertise is achieved through dedicated, conscious and consistent hard work. To complete a complex task such as a doctoral dissertation, the best strategy is certainly to rely on the extraordinary people that have already developed unvaluable expertise. Thanks to the technical team at TU Delft, specially **Remko Seijffers**, **Jurrian van Slingerland**, **Ton Riemslag**, **Elise Reinton**, **Sean Scott**, and **Raymond Dekker**, as well as **Kees Kwakernaak** and **Durga Mainali**. Through work iterations, trial an error and driven often by intellectual curiosity, I also had the chance to

work with an extended technical team. This team includes **Agnieszka Kooijman**, **Hans Brouwer**, **Richard Huizenga**, and **Ruud Hendrikx**. Thank you for helping me explore new paths.

There is a group of people that were not involved directly to the Grade2XL project, however contributed deeply valuable work to the completion of the present thesis. Thanks to the co-authors **Virginia Bertolo** and **Zhaoying Ding** for your invaluable expertise, as well as **Aswin Suresh** for your excellent work.

The academic environment can be deeply rewarding, but it is not exempt of very real institutional challenges. I was lucky enough to be entrusted with two representative positions, where I could elucidate the challenges faced by my peers at higher organizational levels within the university. Firstly, thanks to the team of the ME PhD council, including **Jette, Iris, Robin, Vishal, Hugo, Andrea, Katy, Vasu, Bob, Sietske, Kirsten, Suriya, Yujie, Martin, Pieter, Anna, Paulina, Steven, Athina, Leila,** and **Alina**, as well as old and new council members. Working with you helped me connect with the organization within which we found ourselves, and have fun while doing so. This connection would not have been possible without the champion aid of **Paul Breedveld** and **Mascha Toppenberg**. Thank you for lending your ears to hear our concerns, and lending your voices to make them loud and clear across the faculty. Secondly, I would like to thank the team at the University PhD council, most specially thanking **Berend van Veldhuizen** and **Israel Carrete**. Working with you to identify and follow up on university-wide challenges was truly a pleasure.

A doctoral dissertation presents a compilation of scientific contributions that support the construction of a thesis. It does not, however, present the compilation of personal experiences and connections that support the construction of a person. I would like to thank those people that supported me personally. Thanks to my colleagues at MSE for immense laughter, especially **Can** and **Arjun,** and those sitting every lunch pause at the 3rd floor table. The dozens of cake moments made the PhD trajectory a sweet and fraternal experience. Thanks to my family, **Flor, Enrique, Rocío, Sofía** and **José**, for helping me stay grounded, and for helping me feel loved, and connected to myself. Thanks to my Dutch family, **Huco, Marleen, Koen, Esther, Linda, Omar, Michiel**, and **Floor**, for welcoming me with arms and hearts wide open. And finally, thanks to my wife, the amazingest **Lotte de Vos**. You show up, you care, you listen, you advise - every time, full of love. And you brought María Isabel to this world. Thank you.

ABOUT THE AUTHOR

José Luis Galán Argumedo (05 Nov. 1993 - Torreón, Mexico) obtained the degree of Civil Engineer with Honorable Mention from the *Instituto Tecnológico y de Estudios Superiores de Monterrey*, in Monterrey, Mexico (2017). The completion of this degree was partially supported by the *Deutscher Akademischer Austauschdienst* (DAAD) through the financing of an academic and professional exchange program at Ruhr Universität Bochum, in Bochum, Germany (2015).

José then continued his academic trajectory at Delft University of Technology, obtaining the degree of MSc Civil Engineer with *Cum Laude* (2020). The degree was awarded after the completion of the thesis entitled 'Fatigue behaviour and mechanical characterization of austenitic stainless-steel components produced through Wire+Arc Additive Manufacturing'. The degree was fully financed through the academic grant *CONACYT-Alianza FiiDEM 2017* provided by the Mexican public entity *CONACYT*.

[Page intentionally left blank]

LIST OF PUBLICATIONS

Journal publications pertaining to this thesis

Galán Argumedo, J. L., Riemslag, A. C., Hermans, M. J. M., & Popovich, V. A. (2025). Fracture behaviour of functionally graded bi-material interface produced by wire arc additive manufacturing. *Materials Science and Engineering: A*, *928*(February). https://doi.org/10.1016/j.msea.2025.148034

Galán Argumedo, J. L., Suresh, A., Ding, Z., Bertolo, V., Reinton, T. E., Riemslag, A. C., Hermans, M. J. M., & Popovich, V. A. (2025). Fatigue crack propagation in functionally graded bi-material steel obtained through wire-arc additive manufacturing. *International Journal of Fatigue*, *194*(September 2024), 108819. https://doi.org/10.1016/j.ijfatigue.2025.108819

Galán Argumedo, J. L., Mahmoudiniya, M., Reinton, T. E., Kestens, L. A. I., Hermans, M. J. M., & Popovich, V. A. (2024). Functional grading of low alloy steel to 316 L by wire arc additive manufacturing – Microstructural and mechanical characterization of bi-metal interface. *Journal of Materials Processing Technology*, *325*, 118305. https://doi.org/10.1016/j.jmatprotec.2024.118305

Additional journal publications

Babu, A., Trodini, E., Galán Argumedo, J. L., Richardson, I. M., & Hermans, M. J. M. (2025). Correlating geometry, microstructure and properties of High Strength Steel thin wall structures fabricated with WAAM. *Journal of Advanced Joining Processes*, *11*, 100292. https://doi.org/10.1016/j.jajp.2025.100292

List of international conference presentations

Galán Argumedo, J.L., Suresh, A., Hermans, M.J.M., Popovich, V.A. (2024). Fatigue and Fracture of Bi-metallic Parts Produced through Wire Arc Additive Manufacturing. *2024 TMS Annual Meeting & Exhibition: Additive Manufacturing of Large-Scale Metallic Components*.

Galán Argumedo, J.L., Mahmoudiniya, M., V., Hermans, M.J.M., Popovich, V.A. (2023). WAAM of Functionally-graded HSLA and Austenitic SS bi-material Structures. *2023 TMS Annual Meeting & Exhibition: Additive Manufacturing of Large-Scale Metallic Components*.

Goulas, C., Akuh, M., Venketa, V., Rook, R., Galán Argumedo, J. L., Michelis, T., Ameye, M., Ya, W., Gibson, I., & Hermans, M. (2023). The Effect of Cryogenic Cooling on the Microstructure and Mechanical Properties of Wire Arc Additively Manufactured Steels. *2023 TMS Annual Meeting & Exhibition: Additive Manufacturing of Large-Scale Metallic Components*.

[Page intentionally left blank]